UNIVERSITY OF
LIVERPOOL

Search for resonances decaying to a Z boson and a photon in the ATLAS Detector using data from the Large Hadron Collider

Thesis submitted in accordance with the requirements of
the University of Liverpool for the degree of Doctor in Philosophy
by

Nathan Peter Readioff

September 2016

Abstract

This thesis presents a search for $Z\gamma$ resonances in the context of both the Standard Model Higgs boson and exotic high mass particles. The search for evidence of a Standard Model Higgs boson undergoing the decay $H \to Z\gamma, Z \to \ell\ell$, where $\ell = e$ or μ, is performed using proton-proton collision data recorded by the ATLAS detector at the LHC corresponding to $4.5\,\text{fb}^{-1}$ at a centre-of-mass energy $\sqrt{s} = 7\,\text{TeV}$ and $20.3\,\text{fb}^{-1}$ at a centre-of-mass energy $\sqrt{s} = 8\,\text{TeV}$. No significant excess over the Standard Model prediction is observed and so exclusion limits on the production cross-section of an SM Higgs boson decaying to $Z\gamma$ are set at 95% confidence level: production of the Higgs boson at $9.0 \times$ SM predictions is excluded. Refinements to the analysis are presented, making use of an alternative event classification based on the mass of the reconstructed Z boson to increase the sensitivity and set improved exclusion limits: production of the Higgs boson at $8.0 \times$ SM predictions is excluded. A search for a new Higgs-like boson, X, with high mass and decaying through $Z\gamma$ to an $\ell\ell\gamma$ final state, where $\ell = e$ or μ, is performed using proton-proton collision data recorded by the ATLAS detector at the LHC corresponding to $3.2\,\text{fb}^{-1}$ at a centre-of-mass energy $\sqrt{s} = 13\,\text{TeV}$. No significant excesses above the SM background are observed and so exclusion limits at 95% confidence level are set on the production cross section times decay branching ratio to $Z\gamma$ for such a boson with mass between 250 GeV and 1.5 TeV.

Acknowledgements

Firstly, I would like to acknowledge that the work presented in this thesis would not have been possible without the efforts of the thousands of people involved in the design, construction, and running of the LHC and the ATLAS detector. The analyses presented in this thesis were developed as part of a close-knit team of researchers whom I have been privileged to have worked with, and my work has contributed to two publications [1, 2].

I would like to thank all of the wonderful staff at the University of Liverpool for their help and support over the last four years. In particular, a special thanks must go to my excellent supervisors, Dr Helen Hayward and Dr Sergey Burdin, for guidance and support throughout the PhD. I am also most grateful to Dr Barry King for his assistance with the statistical methods used in this thesis, and Dr Stephen Maxfield for his help in understanding the Standard Model. A special mention must likewise be made of Dr Tulay Cuhadar Donszelmann from the University of Sheffield for her invaluable advice on all aspects of the $H \to Z\gamma$ analysis.

Over the last four years I've had the pleasure of meeting many amazing and talented people, who have really enriched my experiences. I'd like to thank Kate, Steve, and everyone else from the outreach groups at CERN for their enthusiastic help and support as I developed the Lego LHC project. Markus, Marcel, J.D. and the rest of the gang in the CERN board games club also deserve a mention for the hours of gaming fun we had while I was staying at CERN.

Lastly, I thank those who are never last in my thoughts: my parents, Karen and Mike. For their unstinting love and kindness throughout my entire life, and especially over the last four years, I will be forever grateful.

Contents

List of Figures

List of Tables

To Mum and Dad,
and the home education they gave me

Chapter 1

Introduction

The Higgs boson of mass 125 GeV was discovered by the ATLAS [3] and CMS [4] experiments at the Large Hadron Collider (LHC) in 2012, through study of the $H \to \gamma\gamma$ and $H \to ZZ^*$ decay modes. It remains important to fully characterise the observed boson by measuring its properties in as many different decay channels as possible, since any deviations in behaviour from the predictions of the Standard Model (SM) of particle physics - no matter how slight - would provide vital clues for assessing physics beyond the SM. The $H \to Z\gamma$ decay channel is therefore of interest due to its similarities to the $H \to \gamma\gamma$ decay, as both processes share the same leading order set of Feynman diagrams. Both decays proceed via loops, which could contain new and undiscovered particles - if such particles couple differently to the Z boson and the photon, then the ratio of the measured branching fractions for the two processes could differ from SM predictions and help inform on new physics. The main focus of this thesis is therefore on a search for the Higgs boson decaying via $H \to Z\gamma$ using the 7 and 8 TeV data recorded by the ATLAS detector at the LHC.

It is also possible to perform direct searches for new particles by examining the invariant mass distribution of various final states to search for statistically significant excesses above the expected background. Following the restart of the LHC in June 2015 at an unprecedented centre-of-mass energy of $\sqrt{s} = 13$ TeV, it became possible to directly probe higher mass regions than ever before. Reports of an excess of events at around 750 GeV in the diphoton channel led to a similar search being undertaken for resonances with a $Z\gamma$ state, since any particle coupling to the photon would be expected to couple to the Z boson as well. The thesis concludes with a study of the early Run 2 data, obtained in 2015, and searches for evidence of any new high-mass resonances decaying to a $Z\gamma$ state.

This document is organised as follows. Chapter 1 provides a general introduction and overview of the whole thesis. Chapter 2 introduces the Standard Model of particle physics and the Brout-Englert-Higgs mechanism of electroweak symmetry breaking which gives rise to the Higgs boson. It includes a description of Higgs boson production and decay modes, and a look ahead to other undiscovered particles which could decay to a $Z\gamma$ state. Chapter 3 provides descriptions of both the LHC, which provided a source of proton-proton collisions, and the ATLAS detector, which consists of multiple subdetectors working in concert to record the resultant decay products. An overview of the recorded data samples and simulated Monte-Carlo samples is provided

in Chapter 4, while Chapter 5 describes how physics objects are reconstructed from the detector response. Chapter 6 describes the search for a Higgs boson decaying via $H \to Z\gamma$, $Z \to \ell\ell$, $\ell = e, \mu$, and is split into four main sections. Section 6.1 describes the final stages of object reconstruction that result in the identification of Higgs boson candidates. Section 6.2 describes how events were filtered into categories based on kinematic variables in order to boost the sensitivity of the analysis. This work has contributed directly to the publication listed as Ref. [1], where the author worked on the optimisation of the event categorisation and the validation of the event selection. Section 6.3 presents an attempt to select events where the Higgs boson was produced through the vector boson fusion mechanism outlined in Section 2.5. Section 6.4 then describes an improved analysis using a novel technique whereby events are filtered into categories based on the reconstructed Z mass. Chapter 7 describes a search for new Higgs-like bosons decaying via $Z\gamma$ to an $\ell\ell\gamma$ final state in the high mass region. This work has contributed directly to publications listed as Refs. [2, 5], where the author was involved in modelling the signal and data-driven background distributions, and also performing cross-checks of the computed expected limits. Finally, the conclusions of this work are summarised in Chapter 8.

Chapter 2

Theory

The Standard Model (SM) of particle physics [6–9] is the current best theory for describing the behaviour of matter at a subatomic level. Developed throughout the 1960s and 1970s, it successfully unifies three of the four fundamental forces of Nature and has been verified to an extraordinarily high precision [10]. A brief introduction to the SM and the set of fundamental particles it describes is presented in Section 2.1.

The electroweak theory [7], described in Section 2.2, successfully unifies the electromagnetic and weak interactions by describing them both in terms of a single electroweak interaction. Unfortunately, the theory as originally written predicted that all of the associated force-carrier bosons should be massless and this is known not to be the case. Section 2.3 describes the Brout-Englert-Higgs (BEH) mechanism [11–13], which uses spontaneous symmetry breaking to allow the $W^{\pm}$ and Z bosons to acquire mass while keeping the photon massless. The mechanism achieves this through the introduction of a scalar field (the Higgs field) which also gives rise to an associated scalar boson - the famous Higgs boson, which was discovered in 2012. Section 2.4 describes how interactions between fermions and the Higgs field give rise to their masses, with the exception of neutrinos which do not directly couple to the Higgs field.

The data studied in this thesis came from proton-proton collisions provided by the LHC (see Chapter 3). Such collisions provide several mechanisms for producing a Higgs boson, the most important of which are described in Section 2.5. Following its production, the Higgs boson is capable of decaying in a wide variety of ways and Section 2.6 examines the $H \to Z\gamma$ decay which forms the main focus of this thesis.

Finally, Section 2.7 notes a selection of the properties of Nature that cannot yet be explained by the SM, and examines some techniques that can be used in searching for physics beyond the SM.

2.1 The Standard Model

The Standard Model (SM) of particle physics [6–9] is the theory which currently best explains the behaviour of matter at a subatomic level. Under this theory, matter is described in terms of a set of fundamental spin-$\frac{1}{2}$ fermions that interact via the exchange of spin-1 bosons. The SM provides a description of three out of the four fundamental forces of Nature: electromagnetism, the weak interaction and the strong interaction. The fourth known fundamental force is gravity, which is exceptionally well

described on large scales by general relativity but (to date) has never been successfully incorporated into the SM.

The SM is a quantum field theory where particles of matter are defined as local excitations of fields permeating space. The forces of Nature arise from interactions between these fields, which are introduced into the SM by requiring the Lagrangian describing the matter particles to carry certain symmetries - such symmetries are responsible for conserved physical parameters [14]. The Lagrangian must be locally gauge invariant and therefore unchanging under transformations of the underlying symmetry, even if different transformations are applied at each point in space. The gauge transformations are required to vary smoothly from space-time point to space-point.

The symmetry of the SM is described by:

$$U(1)_Y \times SU(2)_L \times SU(3)_C, \tag{2.1}$$

where $U(1)_Y$ and $SU(2)_L$ together describe the electromagnetic (QED) and weak interactions, and $SU(3)_C$ describes quantum chromodynamics (QCD). QED is a relativistic quantum field theory of electrodynamics that describes the interactions of photons with matter, while the weak interaction enables radioactive decay to occur. Above a unification energy of around 100 GeV, both the electromagnetic and weak interactions can be described by a single "electroweak" interaction. QCD describes the strong nuclear force, which is the interaction between quarks and gluons.

The spin-$\frac{1}{2}$ fermions which form the basic constituents of matter are classified as quarks and leptons. Each type of fermion has an associated anti-particle of identical mass but with all quantum numbers and electric charge multiplied by -1. When equivalent matter and anti-matter particles meet and interact, they immediately annihilate to produce either a pair of photons or other particle and anti-particle pairs. The fermions are organised in three generations, or families, of particles where the only difference between successive generations is the increasing mass of the particles they contain. The mass and charge of all matter particles are summarised in Table 2.1.

Each generation contains an up-type quark (up, charm or top) with a fractional electric charge of +2/3, and a down-type quark (down, strange or bottom) with a fractional electric charge of -1/3. The quarks carry a property termed colour which can be either red, green or blue, and they behave in a manner that is loosely analogous to the mixing of the three primary colours of light. Only colour neutral combinations of quarks are permitted to exist, and so they are always bound together as either mesons or baryons to form hadronic matter - it is impossible for individual quarks to appear in isolation. Mesons are formed from the combination of a quark and an anti-quark, which is acceptable since (for example) red and anti-red colours combine to form a colour neutral state. Baryons are composed of a triplet of quarks, which is also acceptable since (for example) red, green and blue quarks also combine to produce a colour neutral state. The property of colour serves as the origin of the strong nuclear

Generation	Name	Symbol	Mass	Charge
		Quarks		
1^{st}	Up	u	2.3 MeV	2/3
	Down	d	4.8 MeV	−1/3
2^{nd}	Charm	c	1.275 GeV	2/3
	Strange	s	95 MeV	−1/3
3^{rd}	Top	t	173.2 GeV	2/3
	Bottom	b	4.18 GeV	−1/3
		Leptons		
1^{st}	Electron	e	0.51 MeV	−1
	Electron-Neutrino	ν_e	< 2 eV	0
2^{nd}	Muon	μ	105.66 MeV	−1
	Muon-Neutrino	ν_μ	< 2 eV	0
3^{rd}	Tau	τ	1.78 GeV	−1
	Tau-Neutrino	ν_τ	< 2 eV	0

Table 2.1: Summary of the properties of Standard Model fermions [10].

Interaction	Symbol	Mass	Charge
Electromagnetic	γ	0	0
Strong	g	0	0
Weak (charged)	$W^{\pm}$	80.38 GeV	± 1
Weak (neutral)	Z	91.19 GeV	0

Table 2.2: Summary of the properties of Standard Model bosons [10].

force, which binds quarks together inside hadrons and (on a slightly larger scale) binds protons and neutrons together inside atomic nuclei to provide stability of matter.

Each generation also contains two leptons: a particle (electron, muon or tau) with an electric charge of -1, and an associated uncharged neutrino. Neutrinos were originally treated as massless in the SM, but observations of neutrino oscillations [15] have confirmed that they all carry a slight mass that is less than 2 eV [10]. It is not yet known if neutrinos follow a normal hierarchy, with the electron-neutrino lightest and the tau-neutrino the heaviest, or an inverted hierarchy where the tau-neutrino is the lightest and the electron-neutrino the heaviest.

As noted above, the interactions between fermions are accomplished via the exchange of spin-1 gauge bosons, whose properties are summarised in Table 2.2. The photon mediates the electromagnetic force, the $W^{\pm}$ and Z bosons mediate the weak interaction and gluons mediate the strong interaction. The hypothetical graviton is thought to mediate gravity, which affects all particles with mass. All fermions can interact via the weak interaction, while all those with an electric charge can interact via electromagnetism. The quarks and gluons are the only particles to carry the property of colour, and gluons are affected by the strong interaction while also mediating it.

The SM is completed by the spin-0 Higgs boson, which was introduced as part of the mechanism to explain electroweak symmetry breaking. The electroweak theory originally predicted that the photon, $W^{\pm}$ and Z bosons would all be massless, but

experimental observations confirmed large masses for the $W^{\pm}$ and Z bosons [16–19]. The BEH mechanism solved this in a natural way by introducing an additional scalar field (the Higgs field) that the $W^{\pm}$ and Z bosons interacted with in order to acquire their mass, but the photon did not interact with and therefore remained massless. This field also carried an associated scalar boson, the Higgs boson, which was observed experimentally in 2012 and found to have a mass of around 125 GeV [10].

The SM may therefore be fully described in a compact notation by the following Lagrangian [6–9]:

$$\mathcal{L} = -\frac{1}{4}F^a_{\mu\nu}F^{a\mu\nu} + i\bar{\psi}\not{D}\psi + \psi_i\lambda_{ij}\psi_j\phi + \text{h.c.} + |D_\mu\phi|^2 - V(\phi) + \frac{1}{M}L_i\lambda_i j^\nu L j\phi^2, \quad (2.2)$$

where the parameters have the following meanings:

- $-\frac{1}{4}F^a_{\mu\nu}F^{a\mu\nu}$ describes the interactions of gauge bosons,
- $i\bar{\psi}\not{D}\psi$ describes the propagation of fermions and their interactions with the gauge bosons,
- $\psi_i\lambda_{ij}\psi_j\phi$ describes the couplings of fermions to the Higgs field through which they acquire mass,
- h.c. is the hermitian conjugate of the preceding term to account for anti-fermions,
- $|D_\mu\phi|^2$ describes the interactions of bosons with the Higgs field through which they acquire mass, and also the propagation of the Higgs boson,
- $V(\phi)$ is the potential due to the Higgs field,
- $\frac{1}{M}L_i\lambda_i j^\nu L j\phi^2$ is a term to describe the neutrino mass sector.

2.2 Electroweak unification

The electroweak theory [7] is a cornerstone of the SM that models the electromagnetic and weak interactions as two different low-energy aspects of a single "electroweak" interaction. Under this theory, fermions can have either left- or right-handed chirality (apart from the neutrino for which no right-handed equivalent is currently known to exist) that is identified by using the following operator to project out the chiral state:

$$\psi_{L,R} = \frac{1}{2}\left(1 \mp \gamma^5\right)\psi, \quad (2.3)$$

The general form for an interaction between a fermion and a boson consists of a linear combination of a vector (V) and an axial-vector (A) component of equal strength. The weak interaction takes the form $V - A$, which results in parity violation as only left-handed fermions or right-handed anti-fermions interact. The electromagnetic interaction does not observe chirality and interacts with both left- and right-handed particles equally. Particle fields which are left-handed transform as $SU(2)_L$ doublets,

while particle fields which are right-handed transform as $SU(2)_L$ singlets. These fields can be defined as:

$$\psi_L = \begin{pmatrix} u \\ d \end{pmatrix}_L, \begin{pmatrix} \nu_e \\ e^- \end{pmatrix}_L, ..., \tag{2.4}$$

$$\psi_R = u_R, d_R, \nu_{eR}, e_R^-, ..., \tag{2.5}$$

and are valid for particles from all three generations. These fields transform as:

$$\psi_L \to \psi'_L = \exp\left(-\frac{ig}{2}\sigma^i \cdot \Delta^i + i\frac{1}{2}g'\Lambda\right)\psi_L, \tag{2.6}$$

$$\psi_R \to \psi'_R = \exp\left(ig'\Lambda\right)\psi_R, \tag{2.7}$$

where σ^i are the Pauli matrices, Λ specifies the local $U(1)_Y$ gauge transformation, and Δ^i specifies the local $SU(2)_L$ gauge transformations.

The unification of the electromagnetic and weak interactions is based on a model of $SU(2)_L \times U(1)_Y$. An isotriplet of vector bosons (W^i_μ, where $i = 1, 2, 3$) is introduced to gauge the $SU(2)_L$ symmetry with a coupling strength g, and a single vector boson B_μ is introduced to gauge the $U(1)_Y$ symmetry with a coupling strength $g'/2$. The W^i_μ and B_μ fields transform as:

$$W^i \to W^{i\prime} = W^i_\mu + g\epsilon_{ijk}\Delta^j W^k_\mu + \partial_\mu \Delta^i, \tag{2.8}$$

$$B_\mu \to B'_\mu = B_\mu + \partial_\mu \Delta, \tag{2.9}$$

The Lagrangian must remain invariant under all of these transformations, and so it is written as:

$$\mathcal{L} = \bar{\psi}_L i\gamma^\mu \left[\partial_\mu + \frac{ig}{2}\sigma^i W^i_\mu + \frac{ig'Y}{2}B_\mu\right]\psi_L, + \bar{\psi}_R i\gamma^\mu \left[\partial_\mu + \frac{ig'Y}{2}B_\mu\right]\psi_R, \tag{2.10}$$

where the term $Y = 2(Q - I_3)$ is the hypercharge, which is a quantum number linking the electric charge Q and the third component of the weak isospin I_3. The weak isospin can be understood as an eigenvalue of a charge operator, and the $W^\pm$ and Z bosons transform between weak isospin charge states. The third component, I_3, is generally a conserved quantity and must be preserved in all weak interactions.

The above Lagrangian is incomplete, however, and must be extended by adding the following gauge invariant kinetic energy terms:

$$\mathcal{L}_{Kin} = -\frac{1}{4}B_{\mu\nu}B^{\mu\nu} - \frac{1}{4}W^i_{\mu\nu}W^{i\mu\nu}, \tag{2.11}$$

To satisfy gauge invariance, the fields must be:

$$B_{\mu\nu} = \partial_\mu B_\nu - \partial_\nu B_\mu, \tag{2.12}$$

$$W^i_{\mu\nu} = \partial_\mu W^i_\nu - \partial_\nu W^i_\mu - gW^k_\mu W^l_\nu \epsilon_{ikl}. \tag{2.13}$$

It is important to note that the terms W_μ^i and B_μ do not correspond to physical fields - the term B_μ arises from $U(1)_Y$ group of hypercharge, not the $U(1)_{EM}$ group of electric charge, and is not therefore the photon field. However, it is possible to construct linear combinations of these four fields to produce the physical fields observed in Nature. The states W_μ^1 and W_μ^2 mix to form the charged vector bosons:

$$W_\mu^\pm = \frac{1}{\sqrt{2}} \left(W_\mu^1 \pm i W_\mu^2 \right), \tag{2.14}$$

while the states W_μ^3 and B_μ mix via a rotation matrix to produce the Z_μ and A_μ fields that the Z boson and photon are respectively associated with:

$$Z_\mu = -B_\mu \sin\theta_W + W_\mu^3 \cos\theta_W, \tag{2.15}$$

$$A_\mu = B_\mu \cos\theta_W + W_\mu^3 \sin\theta_W, \tag{2.16}$$

where θ_W is the Weinberg angle, alternatively known as the weak mixing angle.

The constructed Lagrangian is therefore able to successfully describe the electromagnetic and the weak interactions in terms of a single electroweak interaction. Unfortunately, it contains no mass terms and therefore predicts that the photon, the $W^\pm$ and the Z bosons are all massless particles. Experimental observation has shown that this not the case, with the $W^\pm$ and Z bosons having precisely measured masses and only the photon being massless. This problem can be resolved through the introduction of the BEH mechanism.

2.3 The Brout-Englert-Higgs Mechanism

The BEH mechanism [11–13] uses gauge invariant spontaneous symmetry breaking to provide a means for particles to acquire mass. An additional scalar field (the Higgs field) is introduced into the Lagrangian which breaks the $SU(2)_L$ and $U(1)_Y$ symmetries in order to allow the $W^\pm$ and Z bosons to acquire mass. However, the symmetry must be broken in such a way that the mechanism remains invariant under $U(1)_{EM}$ transformations to ensure the photon remains massless. In order to understand this mechanism, first consider a doublet of complex scalar fields with hypercharge $Y = 1$:

$$\Phi(x) = \begin{pmatrix} \phi^+ \\ \phi^0 \end{pmatrix} = \frac{1}{\sqrt{2}} \begin{pmatrix} \phi_1 + i\phi_2 \\ \phi_3 + i\phi_4 \end{pmatrix}, \tag{2.17}$$

where the ϕ_i are real scalar fields.

The additional term in the Lagrangian due to these fields is therefore:

$$\mathcal{L} = (D_\mu \Phi)^\dagger (D^\mu \Phi) - V(\Phi), \tag{2.18}$$

where D_μ is the covariant derivative:

$$D_\mu = \partial_\mu + \frac{ig}{2}\sigma^i W_\mu^i + \frac{ig'Y}{2}B_\mu, \tag{2.19}$$

and the term $V(\Phi)$ is a scalar potential. The simplest one for $SU(2)_L \times U(1)_Y$ which is gauge invariant and renormalisable is:

$$V(\Phi) = \mu^2 \Phi^\dagger \Phi - \lambda \left(\Phi^\dagger \Phi\right)^2, \tag{2.20}$$

where μ^2 and λ are real constants.

The potential must be bounded from below to ensure the existence of a ground state, and so λ must be negative. Setting the parameter $\mu^2 > 0$ produces a trivial potential with only one minimum located at $\phi^+ = \phi^0 = 0$, and no symmetry breaking occurs. However, setting $\mu^2 < 0$ produces a more interesting potential, with a local maximum at $\phi^+ = \phi^0 = 0$ and a set of degenerate minima lying in a circle on the ϕ^+, ϕ^0 plane according to:

$$\Phi^\dagger \Phi\Big|_{min} = \frac{1}{2}\left(\phi_1^2 + \phi_2^2 + \phi_3^2 + \phi_4^2\right) = \frac{\mu^2}{2\lambda}. \tag{2.21}$$

A projection of such a potential as a function of two real scalar fields in the complex plane is shown in Figure 2.1. Any combination of the ϕ_i fields that satisfy the above constraint may be chosen, but they are all equivalent owing to the requirement of gauge invariance. It is therefore possible to simplify the mathematics by choosing a specific field configuration where the vacuum expectation values of ϕ_1, ϕ_2 and ϕ_4 are zero:

$$\langle \phi_1 \rangle = \langle \phi_2 \rangle = \langle \phi_4 \rangle = 0, \tag{2.22}$$

but the real component of ϕ^0 has a non-zero vacuum expectation value:

$$\langle \phi_3 \rangle = v^2 = \frac{\mu^2}{\lambda}. \tag{2.23}$$

The complex scalar doublet Φ shown in Equation 2.17 therefore becomes:

$$\Phi = \frac{1}{\sqrt{2}}\begin{pmatrix} 0 \\ v \end{pmatrix}. \tag{2.24}$$

It is then possible to expand Φ around this vacuum configuration by setting $\phi^0 = \phi_3 = H + v$, where H is the neutral scalar Higgs field:

$$\Phi = \frac{1}{\sqrt{2}}\begin{pmatrix} 0 \\ H + v \end{pmatrix}. \tag{2.25}$$

When the covariant derivative shown in Equation 2.19 then acts on this expanded Φ, some mathematical manipulation and substitution of Equations 2.14 to 2.16 results

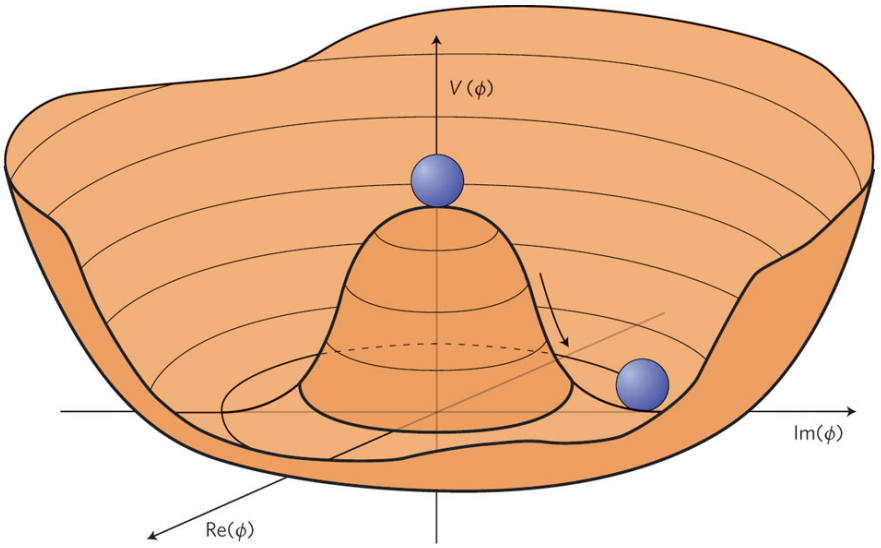

Figure 2.1: Projection of the Higgs potential as a function of two real scalar fields in the complex plane [20].

in:

$$D_\mu \Phi = \begin{pmatrix} \frac{ig}{\sqrt{2}} W_\mu^+ (H+v) \\ \left(\partial_\mu - \frac{i}{2}\left(g\cos\theta_W + g'\sin\theta_W\right) Z + \mu\right)(H+v) \end{pmatrix}. \tag{2.26}$$

After some algebraic manipulation, the gauge invariant Lagrangian shown in Equation 2.18 can therefore be written as:

$$\begin{aligned} \mathcal{L} &= \left(D_\mu \Phi\right)^\dagger \left(D^\mu \Phi\right) - V(\Phi) \\ &= \frac{1}{2}\partial_\mu H \partial^\mu H + \frac{1}{4} g^2 \left(H^2 + 2vH + v^2\right) W_\mu^+ W^{-\mu} \\ &+ \frac{1}{8}\left(g^2 + g'^2\right)\left(H^2 + 2vH + v^2\right) Z_\mu Z^\mu \\ &+ \mu^2 H^2 + \frac{\lambda}{4}\left(H^4 + 4vH^3\right). \end{aligned} \tag{2.27}$$

The photon field A_μ does not appear here and so there can be no mass term for the photon (ensuring it remains massless), but there are explicit mass terms for the $W^\pm$ and Z bosons. For the $W^\pm$ bosons:

$$M_W^2 W_\mu^+ W^{-\mu} = \frac{1}{4} g^2 v^2 W_\mu^+ W^{-\mu}, \tag{2.28}$$

and so they have a mass M_W of:

$$M_W = \frac{1}{2} g v. \tag{2.29}$$

For the Z boson:

$$\frac{1}{2} M_Z^2 Z_\mu Z^\mu = \frac{1}{8}\left(g^2 + g'^2\right) v^2 Z_\mu Z^\mu, \tag{2.30}$$

and so it has a mass M_Z of:

$$M_Z = \frac{1}{2}\sqrt{(g^2 + g'^2)}v = \frac{1}{2}\frac{gv}{\cos\theta_W} = \frac{M_W}{\cos\theta_W}. \tag{2.31}$$

However, this Lagrangian also contains a series of terms in H^2 that correspond to an additional massive boson - the Higgs boson. The terms appear because the scalar potential given in Equation 2.20 acts on the doublet of scalar fields Φ given in Equation 2.25 as follows:

$$V(\Phi) = \frac{\mu^2}{2}(H+v)^2 - \frac{\lambda}{4}(H+v)^4. \tag{2.32}$$

Expanding and gathering the terms that depend on H^2 yields:

$$\left(\frac{1}{2}\mu^2 - \frac{3}{2}\lambda v^2\right)H^2 = \left(\frac{1}{2}\mu^2 - \frac{3}{2}\mu^2\right)H^2 = -\mu^2 H^2. \tag{2.33}$$

It therefore follows that:

$$\frac{1}{2}M_H^2 H^2 = -\mu^2 H^2, \tag{2.34}$$

and so the Higgs boson has a mass of:

$$M_H = \sqrt{-2\mu^2}. \tag{2.35}$$

Since μ is a free parameter of the SM, the value of M_H must be determined through experimental observation. The Higgs boson was discovered in June 2012 with a mass of around 125 GeV, resulting in the Nobel prize being awarded to François Englert and Peter Higgs in 2013.

2.4 Fermion Masses and Couplings

It is impossible to directly add mass terms to the electroweak theory without breaking the $SU(2)_L$ symmetry. However, the masses of fermions can be introduced through Yukawa-type interactions with the Higgs field of the form:

$$\mathcal{L}_f = -G_l\left[\bar{\psi}_L\Phi\psi_R + \bar{\psi}_R\Phi^\dagger\psi_L\right]. \tag{2.36}$$

The simplest case is for the interaction of leptons, when the above Lagrangian acts on the doublet of scalar fields Φ given in Equation 2.25 to become:

$$\mathcal{L}_l = \frac{G_l v}{\sqrt{2}}(\bar{l}l) - \frac{G_l}{\sqrt{2}}(\bar{l}lH). \tag{2.37}$$

This gives rise to a lepton mass $m_l = G_l v/\sqrt{2}$, and a lepton-Higgs coupling which can be expressed as follows (note the substitution of Equation 2.29):

$$\frac{G_l}{\sqrt{2}} = \frac{m_l}{v} = \frac{m_l g}{2M_W}. \tag{2.38}$$

The coupling between a lepton and the Higgs boson is therefore directly proportional to the lepton mass. It is also important to note that since the upper entry in Φ is zero, there is no coupling to the upper entry in the left-handed doublet ψ_L (see Equation 2.4). This means that neutrinos are predicted to be massless, which experimental observation shows is not the case, and leads to the addition of a separate neutrino mass term in the complete SM Lagrangian (see Equation 2.2).

The interactions of quarks represent a more complex case, since the Lagrangian becomes:

$$\mathcal{L}_q \sum_{f=1,2,3} - \left[\bar{\psi}_L^f G_{ff'}^D \Phi D_{f'R} + \bar{\psi}_L^f G_{ff'}^U \Phi^c U_{f'R} + \text{h.c}\right], \tag{2.39}$$

where f denotes the quark generation, $G_{ff'}^U$ and $G_{ff'}^D$ are the matrix of quark Yukawa couplings, and U_f and D_f are the set of up- and down-type quarks, respectively. The term Φ^c is the conjugate scalar field:

$$\Phi^c = \begin{pmatrix} \bar{\phi}^0 \\ -\phi^- \end{pmatrix}, \tag{2.40}$$

and is required to stop the up-type quarks in the upper entries of the left-handed doublet ψ_L (see Equation 2.4) from being massless, in the same way neutrinos were. After spontaneous symmetry breaking, Φ^c becomes:

$$\Phi^c = \begin{pmatrix} H + v \\ 0 \end{pmatrix}, \tag{2.41}$$

which therefore generates masses for up-type quarks while making no contribution to the masses of down-type quarks.

As in the case of the charged leptons, the coupling between a quark and the Higgs boson is directly proportional to the quark mass. Decays of the Higgs boson into fermions will therefore be dominated by top quarks, to which the Higgs boson couples most strongly.

2.5 Higgs Production Mechanisms at the LHC

The Large Hadron Collider (described in Chapter 3) is a proton-proton collider which provides several mechanisms for producing the Higgs boson. The dominant production mechanisms for the SM Higgs boson are through gluon-gluon fusion (ggF), vector boson fusion (VBF), associated production involving a $W^{\pm}$ or Z boson (VH), and associated production with a $t\bar{t}$ pair ($t\bar{t}$H). Figure 2.2 shows a set of Feynman diagrams

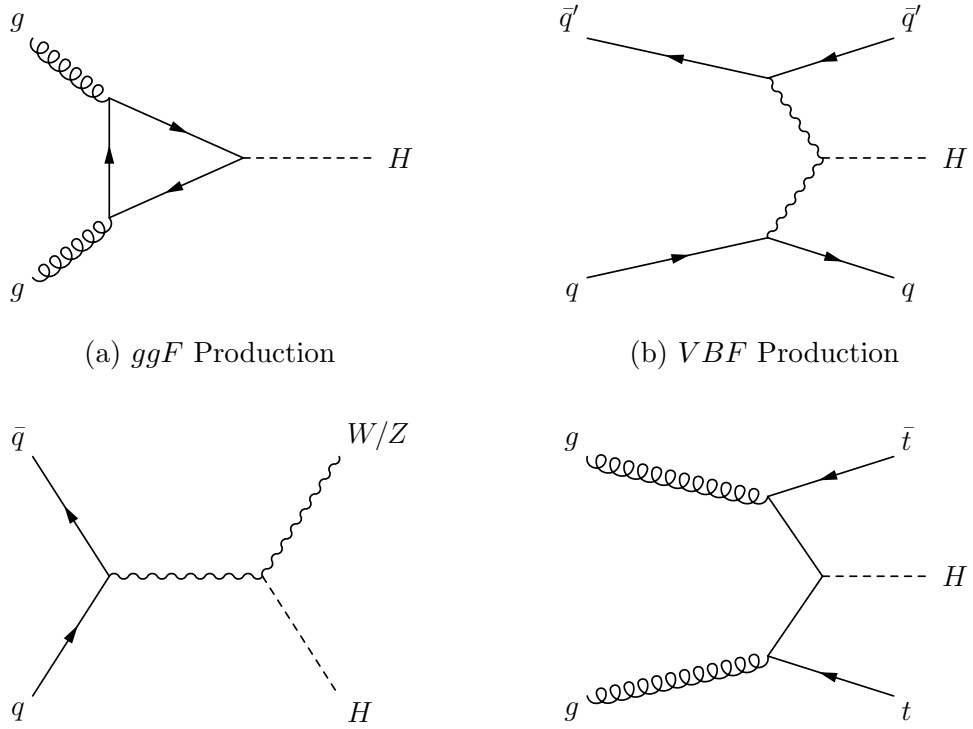

(a) ggF Production (b) VBF Production

(c) VH Production (d) $t\bar{t}$ Production

Figure 2.2: Summary of Higgs boson production mechanisms at the LHC.

for these processes. It should be noted that the VBF production mechanism also creates two quarks that form the seeds of hadronic jets, which are boosted into the forward regions of the ATLAS detector. This provides a useful experimental signature and an attempt was made to select events produced in this manner (described in Section 6.3). Other rarer decay processes are possible, but have not been considered in this analysis due to negligible production cross-section.

The Higgs boson production cross-sections and associated uncertainties that were used in this analysis were taken from Refs. [21, 22]. Full details of the computation of these values and the corrections applied can be found in Ref. [23], but a brief overview is provided in Section 4.2.1.1. Figures 2.3 and 2.4 show the production cross-sections for each mechanism as a function of mass at 7 and 8 TeV, respectively, while Table 2.3 summarises the values for a selection of Higgs boson masses. The ggF and VBF mechanisms make the two greatest contributions to the total production cross-section, and for a Higgs boson of mass 125 GeV account for around 87% and 7% of the total, respectively.

2.6 Higgs Decay Modes

The Higgs boson is an unstable particle with a predicted mean lifetime of around 1.6×10^{-22} s for a mass of 125 GeV [22], and decays primarily into pairs of fermions or gauge bosons. It couples to fermions with a strength proportional to their mass, and

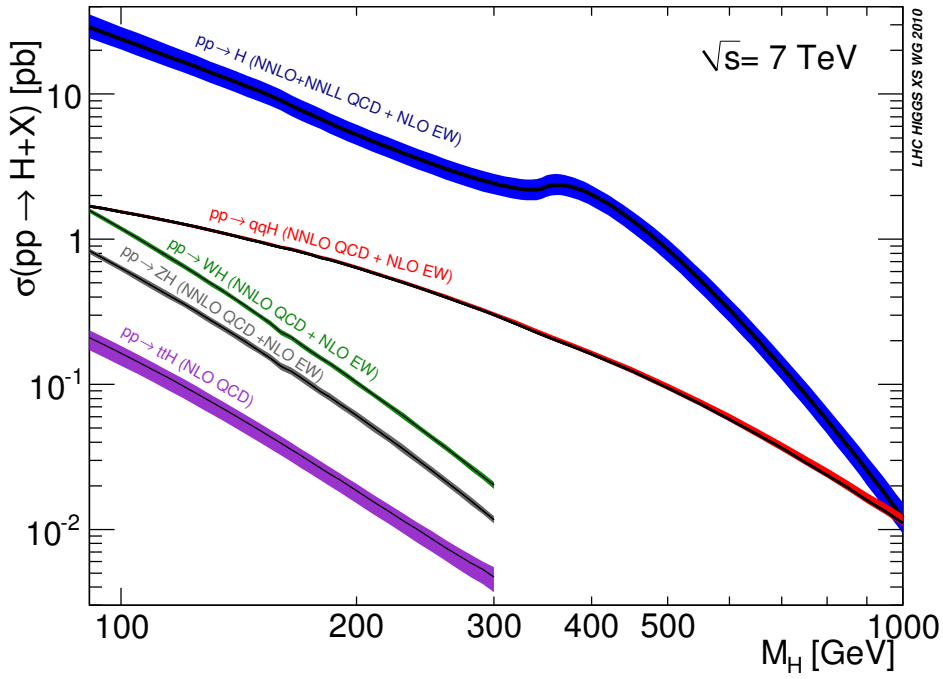

Figure 2.3: SM Higgs boson production cross-section as a function of mass at $\sqrt{s} = 7\,\text{TeV}$ [21].

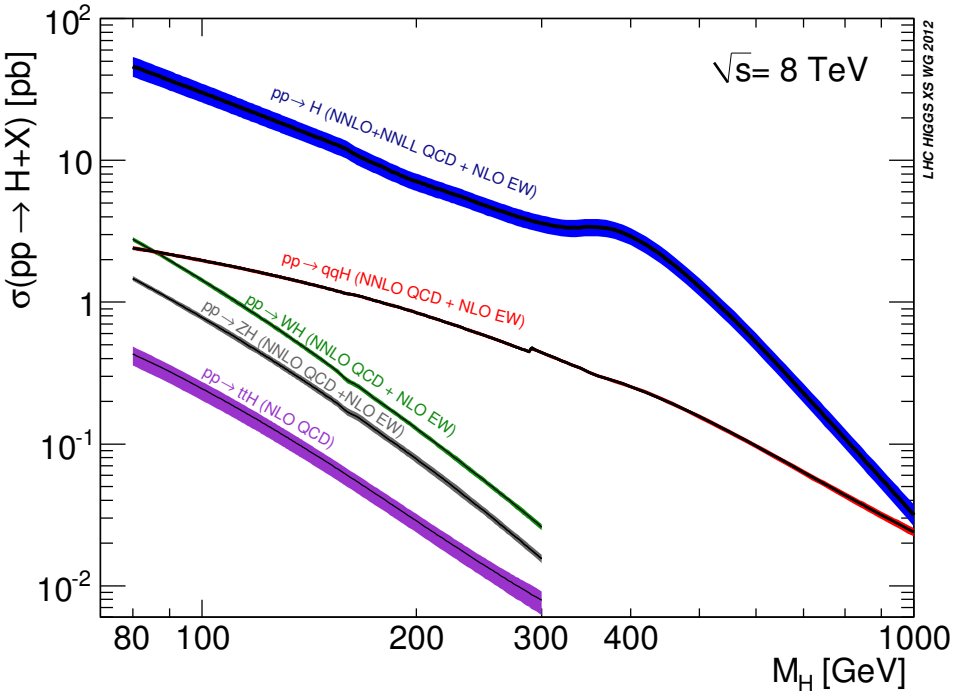

Figure 2.4: SM Higgs boson production cross-section as a function of mass at $\sqrt{s} = 8\,\text{TeV}$ [22].

$\sqrt{s}$ [TeV]	m_H [GeV]	σ_{ggF} [pb]	σ_{VBF} [pb]	σ_{WH} [pb]	σ_{ZH} [pb]	$\sigma_{t\bar{t}H}$ [pb]
	120	16.43	1.28	0.66	0.38	0.10
7	125	15.13	1.22	0.58	0.34	0.09
	130	13.98	1.17	0.51	0.30	0.08
	120	20.86	1.65	0.81	0.47	0.15
8	125	19.27	1.58	0.70	0.42	0.13
	130	17.85	1.51	0.62	0.37	0.11

Table 2.3: SM Higgs boson production cross-sections for various mechanisms, at masses of $m_H = 120$, 125 and 130 GeV and at centre-of-mass energies of $\sqrt{s} = 7$ TeV and $\sqrt{s} = 8$ TeV [21, 22]. An overview of how these values were calculated is provided in Section 4.2.1.1.

also to gauge bosons with a strength proportional to their mass squared. Photons are massless and do not couple directly to the Higgs boson, but $\gamma\gamma$ and $Z\gamma$ final states can still be generated via loops involving massive particles - typically $W^{\pm}$ loops, but also fermion loops dominated by top quarks. The Higgs boson branching fraction depends on either the masses of the final state particles or the mass of the virtual particles appearing within these loops, and is shown as a function of the Higgs mass for different decay channels in Figure 2.5.

The $H \to b\bar{b}$ decay carries the largest branching fraction of 57% for a Higgs boson of mass 125 GeV, but unfortunately the process is dominated by a background from SM di-jet production that dwarfs the signal and makes experimental studies of the channel rather challenging. Preferred channels for study are those with good signal-to-background ratios and where all final state particles can be reconstructed - classic examples are the $H \to \gamma\gamma$ and $H \to ZZ^*$ channels where the Higgs boson was discovered.

The main analysis in this thesis focuses on the relatively rare $H \to Z\gamma$ decay, Feynman diagrams for which are shown in Figure 2.6. The decay proceeds mainly through $W^{\pm}$ boson loops, and the coupling term responsible for this decay is visible in the Lagrangian shown in Equation 2.27. However, the decay can also proceed via fermion loops dominated by top quarks since (as noted in Section 2.4) fermions interact with the Higgs field with a strength proportional to the fermion mass. Table 2.4 summarises the $H \to Z\gamma$ branching fractions for a selection of Higgs boson masses, and provides the corresponding $H \to \gamma\gamma$ branching fractions for reference.

The Z boson is itself an unstable particle, with a width of $\Gamma_Z = 2.4952$ GeV [10], which also rapidly decays in a variety of ways as summarised in Table 2.5. This thesis focuses on the leptonic decays of the Z boson, $Z \to ee$ and $Z \to \mu\mu$. The $Z \to \tau\tau$ decay has not been included since the τ lepton decays mainly hadronically - it is sufficiently rare for both τ leptons to decay to same-flavour electrons or muons that the number of affected events will fall under the statistical uncertainty arising from genuine $Z \to ee$ and $Z \to \mu\mu$ decays. Study of the invisible decays of the Z boson are beyond the

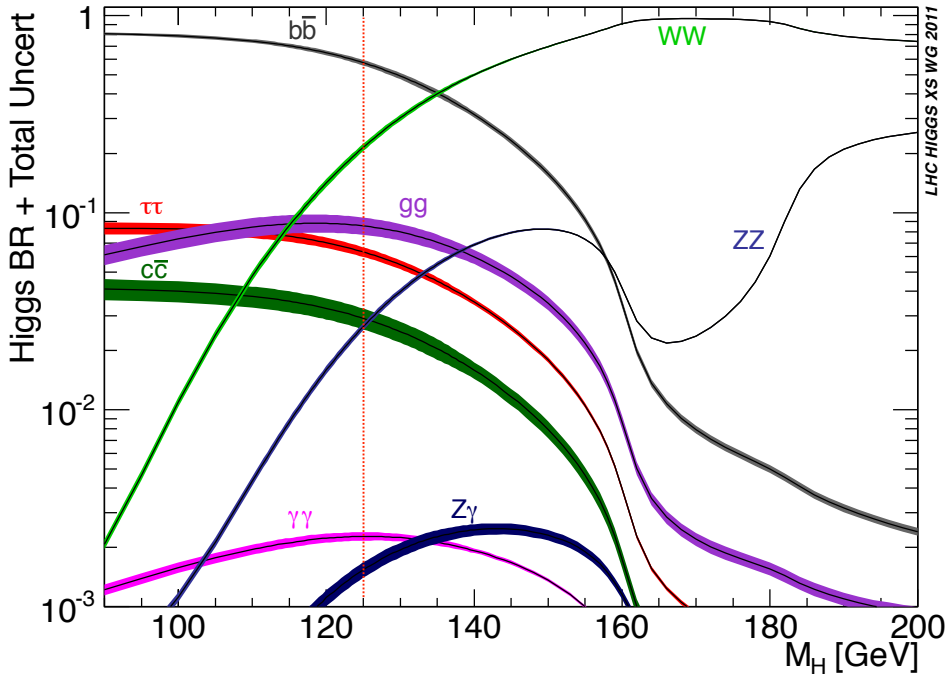

Figure 2.5: Branching fractions of an SM Higgs boson as a function of mass for various final states. The dashed line highlights the branching fractions at the observed Higgs boson mass of 125 GeV.

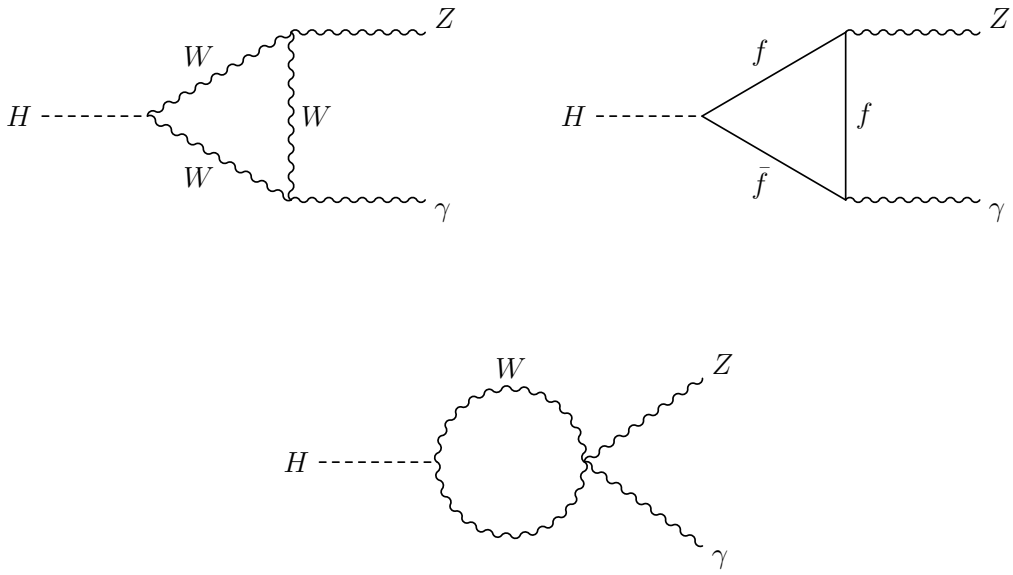

Figure 2.6: Summary of the $H \to Z\gamma$ decay process.

m_H [GeV]	$\mathcal{B}_{H\to Z\gamma}$ [10^{-3}]	$\mathcal{B}_{H\to\gamma\gamma}$ [10^{-3}]
120	1.11	2.23
125	1.54	2.28
130	1.95	2.24

Table 2.4: Branching fractions for a SM Higgs boson of mass $m_H = 120$, 125 or 130 GeV decaying to $Z\gamma$ and $\gamma\gamma$ [22].

Decay Mode	Fraction (Γ_i/Γ)
$\ell^+\ell^-$	(3.3658 ± 0.0023) %
hadronic	(69.91 ± 0.06) %
invisible	(20.0 ± 0.06) %

Table 2.5: Branching fractions for the Z boson under various decay modes [10].

scope of this thesis. Hadronic decays of the Z boson have not been considered in this thesis, since the channel is dominated by large backgrounds and therefore has poor sensitivity unless a very high mass region of over 1 TeV is being probed [2]. Table 2.6 summarises the total cross-section for production of the Higgs boson and decay via $H \to Z\gamma$, $Z \to \ell\ell$ for a selection of Higgs boson masses.

2.7 Beyond the Standard Model

Despite the enormous success of the SM, there are several features of Nature that it did not predict and cannot explain in its current form. The most obvious shortcoming is the absence of gravity in the theory, which has never (to date) been successfully described on a subatomic scale using a quantum field theory approach.

The observation of neutrino oscillations [15] provided direct experimental confirmation that neutrinos carry a small mass, yet it was noted in Section 2.4 that neutrinos do not interact with the Higgs field and should therefore be massless. While the complete SM Lagrangian shown in Equation 2.2 incorporates a dedicated term to describe the neutrino sector, the precise mechanism through which neutrinos acquire their masses remains a mystery.

The SM requires an unnatural fine-tuning of its parameters in order to produce a Higgs boson with a mass of order 100 GeV [24]. Quantum corrections Δm_H to a fermion f with a repetition number N_f and coupling λ_f to the Higgs field can be taken as:

$$\Delta m_H^2 = N_f \frac{\lambda_f^2}{8\pi^2}\left[-\Lambda^2 + 6m_f^2 \log\left(\frac{\Lambda}{m_f}\right) - 2m_f^2\right] + \mathcal{O}\left(\frac{1}{\Lambda^2}\right), \tag{2.42}$$

where Λ is the cutoff scale, $\lambda_f = \sqrt{2}m_f/v$, and v is the vacuum expectation value of the Higgs field. It follows that $\Delta m_H^2 \propto \Lambda^2$, but since the Planck scale is approximately 10^{18} GeV the Higgs mass will be extremely large. The only way of returning the Higgs

$\sqrt{s}$ [TeV]	m_H [GeV]	$\sigma(pp \to H \to Z(\ell\ell)\gamma)$ [fb]
7	120	0.70
	125	0.90
	130	1.05
8	120	0.89
	125	1.15
	130	1.34

Table 2.6: Total cross-section, including the Higgs boson production cross-sections, the branching ratio $\mathcal{B}_{H\to Z\gamma}$ and the branching ratio $\mathcal{B}_{Z\to\ell\ell} = 3.366\%$. This corresponds to the number of SM Higgs boson decaying to $Z(\ell\ell)\gamma$, for each lepton flavour, in $1\,\text{fb}^{-1}$ of pp collisions.

mass to around 100 GeV is to include counteracting terms that are fine-tuned to the order of 10^{-30}, which is highly unrealistic. One possible solution is the introduction of supersymmetry [25], which postulates that each type of fermion has a boson counterpart and vice versa. This introduces the counteracting terms in a natural way, but in order to produce a Higgs boson of the correct mass it is necessary for the symmetry to be broken and the supersymmetric particles to appear at the TeV scale. To date, no supersymmetric particles have been observed, and a wide variety of searches are underway at the LHC [26].

The Universe is also known to contain large amounts of non-baryonic "dark matter" [27], which is so-called because it interacts gravitationally but not electromagnetically. Evidence for the existence of dark matter comes from the study of galaxy rotation curves [28], where stars on the edges of a galaxy rotate faster than predicted, and also from the observation of distant galaxies affected by gravitational lensing [29], where the strength of the lensing effect is greater than predicted. These effects are only possible if the celestial objects contain more mass than their visible output implies, but even the inclusion of neutrino mass in the calculations is insufficient to account for the observed discrepancies. More direct evidence for dark matter comes from the Bullet Cluster, a cluster of galaxies where dark and visible matter have separated out due to the earlier collision of two smaller galaxy clusters [30]. It has been shown from study of the cosmic microwave background that non-relativistic dark matter is also responsible for the large-scale structure of the Universe [31]. The Planck telescope [32] demonstrated that the Universe contains 26.8% dark matter as opposed to just 4.9% of visible matter. Dark matter could be described in terms of undiscovered subatomic particles that were produced in the early Universe and which interact very weakly with the known SM particles. While many potential candidates for dark matter have been proposed [33, 34], its precise nature remains elusive and several experiments are ongoing to try and detect it (see Ref. [35] and its references).

A final point of note is that there is no adequate reason as to why the three gauge couplings of the SM gauge group almost, but do not actually, meet at the grand

unification scale [36]. It is possible that undiscovered heavy particles affect the coupling constants, which might lead them to unify into a single superforce at the unification scale.

The reasons presented above demonstrate why it is essential to search for physics beyond the SM, and one possible method is to measure the $H \to Z\gamma$ decay rate. The $H \to Z\gamma$ decay proceeds via loops that couple to the Higgs boson, as shown in Figure 2.6, and the $H \to \gamma\gamma$ decay shares the same set of leading order Feynman diagrams. However, the two processes could be affected in slightly different ways if there were additional diagrams involving loops of undiscovered particles, whose existence is motivated by the considerations outlined above. Several theoretical models predict enhancements to the $H \to Z\gamma$ branching ratio of up to a few tens of percent [37, 38], or a suppression relative to $H \to \gamma\gamma$ [39]. A measurement of the ratio of the $Z\gamma$ and $\gamma\gamma$ branching fractions could therefore provide some insight into models beyond the SM.

A more direct method of finding new physics is to perform searches for new mass resonances, which are motivated by various theoretical models including extensions to the Higgs sector. One possibility is that the Higgs field described previously is merely one of multiple scalar fields, which could provide a means of explaining how neutrinos acquire mass [40]. Another is that the Higgs boson is not a fundamental particle but is instead a composite of other particles, which provides a solution to the naturalness problem but requires the existence of new particles on the TeV scale [41].

A slight excess of events was seen in the diphoton channel at around 750 GeV [42, 43], and if this is not merely a statistical fluctuation then it will represent a new particle that could be connected to one of the aforementioned theories. A coupling of a new singlet scalar boson, S, with photons could be described through a phenomenological model based on an effective-field-theory (EFT) approach, where the low-energy effective Lagrangian is independent of the underlying dynamical details. Such a model could be written as follows:

$$\mathcal{L}_{eff} = c_g \frac{4\pi\alpha_s}{\Lambda} S G^a_{\mu\nu} G^{a\mu\nu} + c_W \frac{4\pi\alpha_{em}}{\Lambda \cdot \sin^2\theta_W} S W^a_{\mu\nu} W^{a\mu\nu} + c_B \frac{4\pi\alpha_{em}}{\Lambda \cdot \cos^2\theta_W} S B_{\mu\nu} B^{\mu\nu} + \sum_f c_f \frac{m_f}{\Lambda} f\bar{f} S. \quad (2.43)$$

where α_s and α_{em} are the couplings of the strong and electromagnetic interactions, respectively, Λ is the cutoff scale and θ_W is the Weinberg angle. Moreover, c_g, c_W and c_B are the coupling coefficients between the scalar field S and the gluon field strength $G^a_{\mu\nu}$, the $SU(2)$ field strength $W^a_{\mu\nu}$ and the $U(1)$ field strength $B_{\mu\nu}$, respectively [44]. A search for a new high mass resonance decaying to a $Z\gamma$ final state is described in Chapter 7.

Chapter 3

The LHC and the ATLAS Detector

The analyses presented in this thesis were performed using pp collision data recorded by the ATLAS Collaboration using the ATLAS detector [45], which is one of the four main experiments located at the Large Hadron Collider (LHC) [46]. An overview of the LHC accelerator and its associated pre-accelerators, together with a brief summary of the experiments it provides collisions for, is presented in Section 3.1. A description of the ATLAS detector, its many components and their use in recording information on the vast array of particles that can be produced in pp collisions is given in Section 3.2.

3.1 The Large Hadron Collider

The Large Hadron Collider (LHC) [46] at CERN (Centre Européen pour la Recherché Nucléaire) is an approximately circular particle accelerator with a 26.7 km circumference that is located between 50 and 175 m underground, extending across the French-Swiss border near Geneva, Switzerland. The tunnel it occupies was originally constructed between 1983 and 1988 to house the Large Electron-Positron Collider (LEP). The LHC is designed to accelerate two counter-rotating beams of protons up to a nominal energy of 7 TeV per beam, before steering them to collision at the four interaction points where the main experiments are located (as shown in Figure 3.1).

The ATLAS (A Toroidal LHC ApparatuS) [45] and CMS (Compact Muon Solenoid) [47] experiments are general purpose detectors with broad physics programs including studies of the Higgs Boson and searches for supersymmetry. ALICE (A Large Ion Collider Experiment) [48] studies the collision of heavy ions, such as lead nuclei, which can produce a quark gluon plasma. LHCb (Large Hadron Collider beauty) [49] specialises in the study of b-hadrons. Three additional experiments have since been added to the LHC: TOTEM (TOTal Elastic and diffractive cross section Measurement) [50] is a forward detector located near CMS that measures the total pp cross-section, MoEDAL (Monopole and Exotics Detector At the LHC) [51] is located inside the LHCb cavern and specialises in the search for magnetic monopoles, and LHCf (Large Hadron Collider forward) [52] consists of two detectors placed 140 m down the beamline on each side of the ATLAS collision point to measure very forward photons and neutral pions.

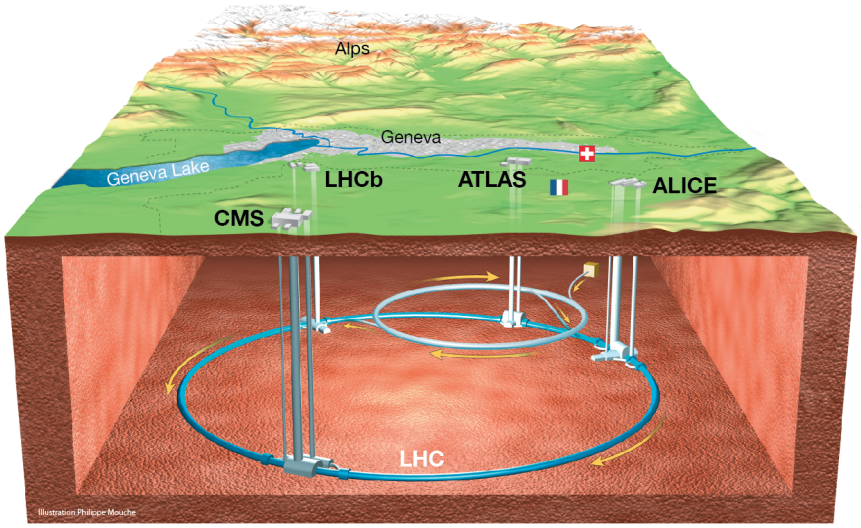

Figure 3.1: Overall view of the LHC [53].

The acceleration and configuration of the LHC proton beams require several steps over multiple pre-accelerators. Molecules of hydrogen gas are stripped of their electrons to create a source of protons, which are then injected into the LINAC2 linear accelerator and taken to an energy of 50 MeV. If the LHC is required to collide heavy ions, then the adjacent LINAC3 accelerator is instead used for this initial step. The protons (or ions) are then fed into the Proton Synchrotron Booster (PSB), where they are accelerated to 1.4 GeV and separated into a series of discrete bunches. The Proton Synchrotron (PS), which first operated in November 1959 and initially served as CERN's flagship accelerator, then accelerates the protons to 25 GeV before passing them to the Super Proton Synchrotron (SPS) where they are further accelerated to 450 GeV. Finally, the proton bunches are injected into the LHC where they are accelerated up to the nominal beam energy of 7 TeV for a centre-of-mass collision energy of 14 TeV. A schematic outline of the accelerator chain is shown in Figure 3.2.

The LHC uses 1232 15m-long superconducting dipole magnets to steer the proton beams around the ring. An additional 392 superconducting quadrupole magnets, each measuring 5 to 7 m long, focus the beam while further hexapole and octupole magnets provide minor corrections. Sixteen superconducting radio-frequency cavities, eight per beam, are located between the ALICE and CMS detectors and provide the acceleration of the protons. All of the superconducting components are operated at a temperature of 1.9 K that is maintained by 19.6 tonnes of liquid helium, which makes the LHC the largest liquid helium cryogenics facility in the world.

The instantaneous luminosity, $\mathcal{L}$, is a measurement of the rate of proton-proton collisions provided by the LHC, and directly affects the volume of data that is available

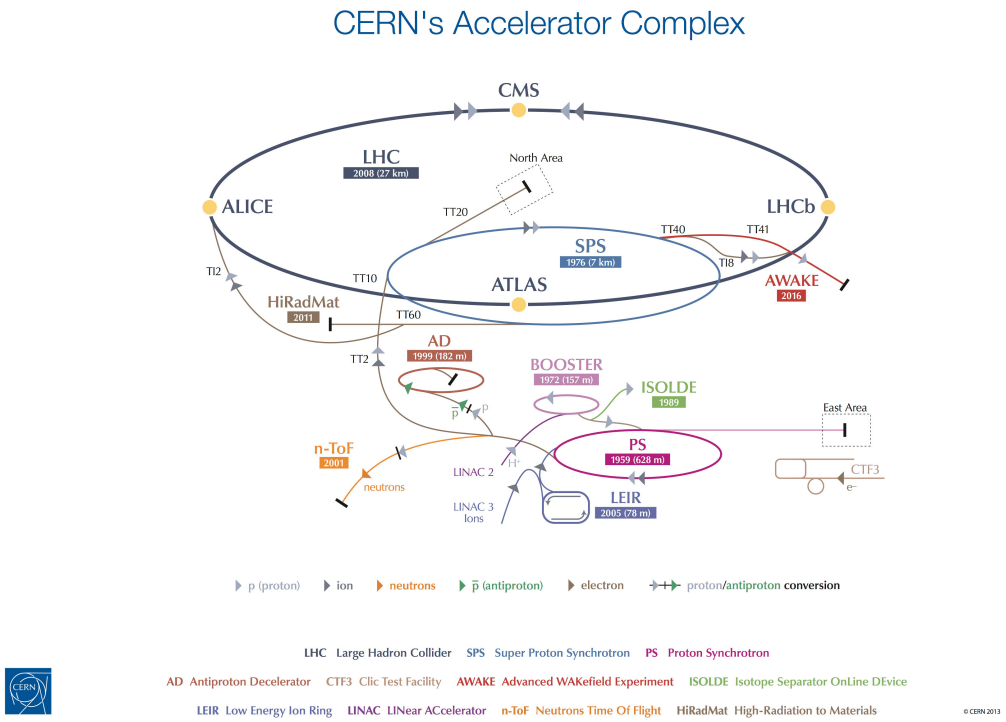

Figure 3.2: The CERN accelerator complex [54].

for physics analysis. It is typically quoted in units of $\mathrm{cm}^{-2}\,\mathrm{s}^{-1}$, and is evaluated using:

$$\mathcal{L} = \frac{n_b f_r n_1 n_2}{2\pi \Sigma_x \Sigma_y}, \tag{3.1}$$

where f_r is the revolution frequency of the LHC (11.245 kHz), n_b is the number of bunch pairs that collide per revolution, and n_1 and n_2 are the number of protons in beams 1 and 2, respectively. The parameters Σ_x and Σ_y characterise the horizontal and vertical beam profiles and can be measured directly through van der Meer scans, whereby the collision rate is measured while the two colliding proton beams are scanned across each other in discrete steps over the horizontal (x) and vertical (y) planes. When the beams are unseparated, these values can be combined with an external measurement of the bunch population product $n_1 n_2$ to directly determine the luminosity [55].

The integrated luminosity, L, over a given data-taking period is therefore given by:

$$L = \int \mathcal{L} dt. \tag{3.2}$$

This is related to the total number of events of a given process with cross-section σ by:

$$N = \sigma \epsilon L, \tag{3.3}$$

where ϵ denotes the detector efficiency and acceptance.

Initially, the LHC was operated with $\sqrt{s} = 7$ TeV and delivered a total of $4.5\,\mathrm{fb}^{-1}$

of data. Following maintenance at the start of 2012, the beam energy was increased slightly to provide collisions at $\sqrt{s} = 8$ TeV and 20.3 fb^{-1} of data was recorded. Figure 3.3 shows the cumulative integrated luminosity delivered over time by the LHC during Run 1. The increased luminosity at 8 TeV was primarily due to an increase in the mean number of proton-proton interactions per bunch crossing (n_b in Equation 3.1). This effect is termed pileup, and can present issues for physics analyses since it results in multiple vertices per bunch crossing and an increased flux of particles with potentially overlapping signals.

In 2013, a two year shutdown termed Long Shutdown 1 (LS1) commenced so that repairs and significant upgrades could be made to the LHC and its main experiments. The LHC successfully restarted in June 2015 at a centre-of-mass collision energy of $\sqrt{s} = 13$ TeV. Figure 3.4 shows the cumulative integrated luminosity delivered over time by the LHC during 2015.

3.2 The ATLAS Detector

The ATLAS detector [45] is a general purpose particle detector with an approximately forward-backward symmetric cylindrical geometry, which provides almost 4π coverage in solid angle around the interaction point. It measures 25 m in diameter and 44 m in length overall, but is composed of several subsystems wrapped in layers around the central beam pipe. The inner detector (ID) comprises a Silicon Pixel Detector, a Silicon Microstrip Tracker (SCT), and a straw-tube Transition Radiation Tracker (TRT). The ID is immersed in a 2 T magnetic field generated by a thin superconducting solenoid, and is surrounded by the electromagnetic and hadronic calorimeters. The outermost sub-system is the muon spectrometer, which is integrated with three large superconducting air-core toroid magnets. A schematic overview of the detector is provided in Figure 3.5.

ATLAS uses a right-handed coordinate system with its origin located on the nominal interaction point at the centre of the detector. The z-axis coincides with the beam pipe passing through the detector, the x-axis points towards the centre of the LHC ring and the y-axis points approximately vertically upwards. The y-axis is not truly vertical since the LHC tunnel was dug at a slight gradient of 1.4% in order to minimise the depth of the vertical access shafts and to facilitate a link-up with the SPS accelerator. The half of the detector on the positive z axis points in the direction of the airport and the Saleve and is referred to as the "A-side"; the other half points in the direction of the Jura and is referred to as the "C-side". Owing to the cylindrical nature of the detector, it is usually more convenient to work in polar coordinates where the azimuthal angle ϕ is measured from the x-axis around the beam pipe and the polar angle θ is the angle from the positive z-axis.

The rapidity, y, is preferred over θ since it is invariant under boosts along the beamline. It is defined as:

$$y = \frac{1}{2} \ln \left[\frac{(E + p_z)}{(E - p_z)} \right], \tag{3.4}$$

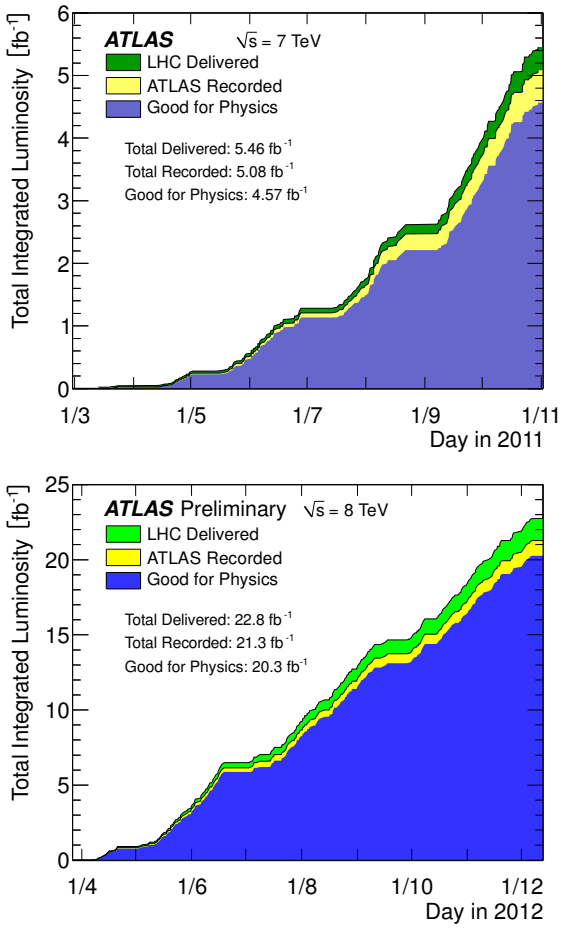

Figure 3.3: Breakdown of the total integrated luminosity delivered to the ATLAS detector by the LHC, recorded by ATLAS and containing data assessed to be of good quality as a function of time, for the 7 TeV (left) and 8 TeV *pp* collisions [56].

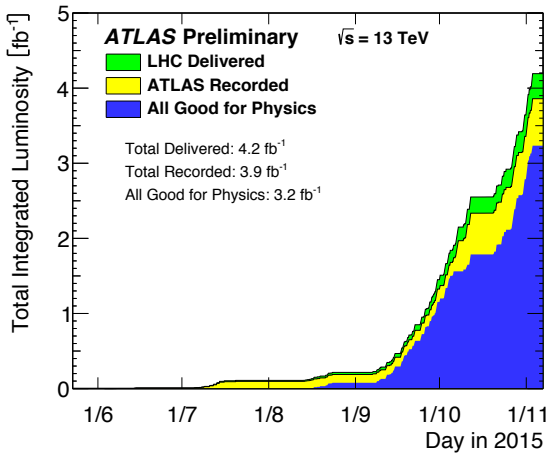

Figure 3.4: Breakdown of the total integrated luminosity delivered to the ATLAS detector by the LHC, recorded by ATLAS and containing data assessed to be of good quality as a function of time, for the 13 TeV *pp* collisions recorded in 2015 [57].

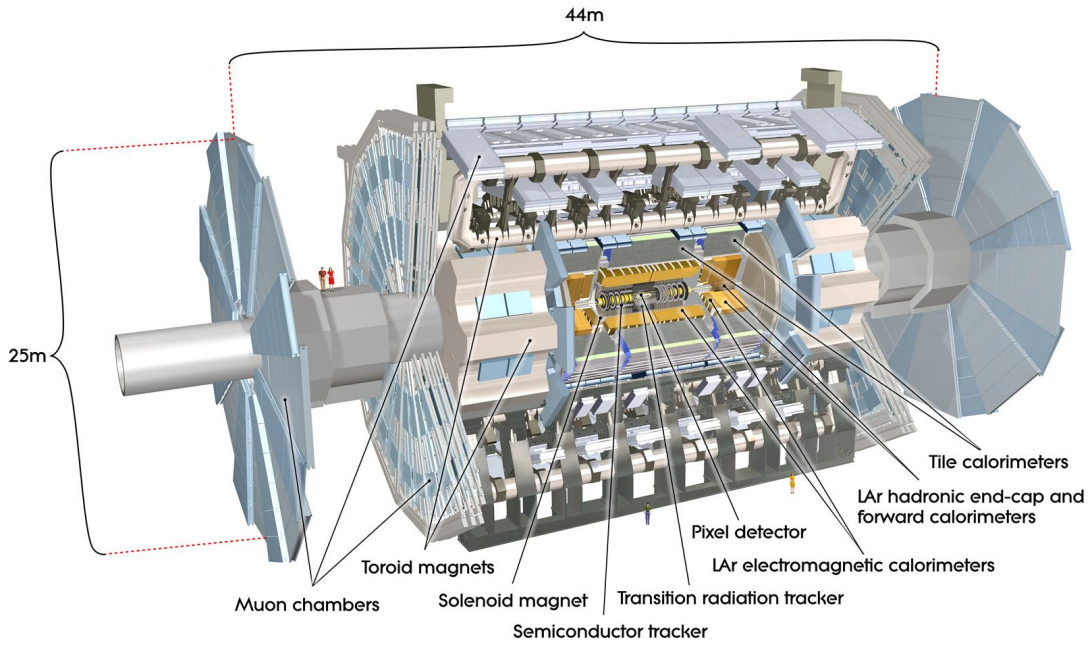

Figure 3.5: Computer generated image of the ATLAS detector, using cutaway walls to highlight the major subsystems [58].

where E is the energy of the particle and p_z is the z-component of its three-momentum. However, the difference between energy and momentum is difficult to measure for highly relativistic particles. In such cases the pseudorapidity, which is equivalent to the rapidity in the highly relativistic limit, is a more useful quantity as it depends only on the polar angle θ. It is defined as:

$$\eta = -\ln\left(\tan\left(\theta/2\right)\right), \tag{3.5}$$

where η varies from zero in the xy-plane to $\pm\infty$ along the beam pipe at $\pm z$. The distance ΔR in the $\eta - \phi$ space is defined as:

$$\Delta R = \sqrt{\Delta\eta^2 + \Delta\phi^2}. \tag{3.6}$$

3.2.1 The Inner Detector

The ATLAS inner tracking volume [45], or ID, is composed of a pixel detector, the SCT and the TRT arranged in a cylindrical volume of radius 1.15 m and length 7 m that is centred over the interaction point, as shown in Figure 3.6. An alternative cross-sectional view of the ID showing the radial location of the elements within each of these subsystems is presented in Figure 3.7. The three systems together provide high-resolution tracking and vertex reconstruction for charged particles within the region $|\eta| < 2.5$, while the TRT provides enhanced electron identification over $|\eta| < 2.0$. This provides a momentum resolution of around 4% for tracks within the central region, deteriorating to 10% or worse at $|\eta| > 2$ [60]. The ID is immersed in a 2 T solenoidal

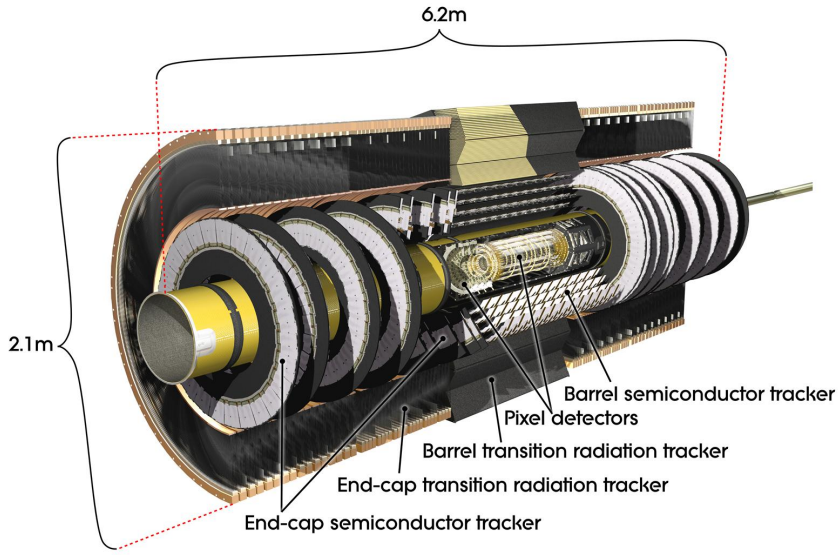

Figure 3.6: Cutaway view of the ATLAS inner detector, showing the layout of the pixel detector, SCT and TRT [59].

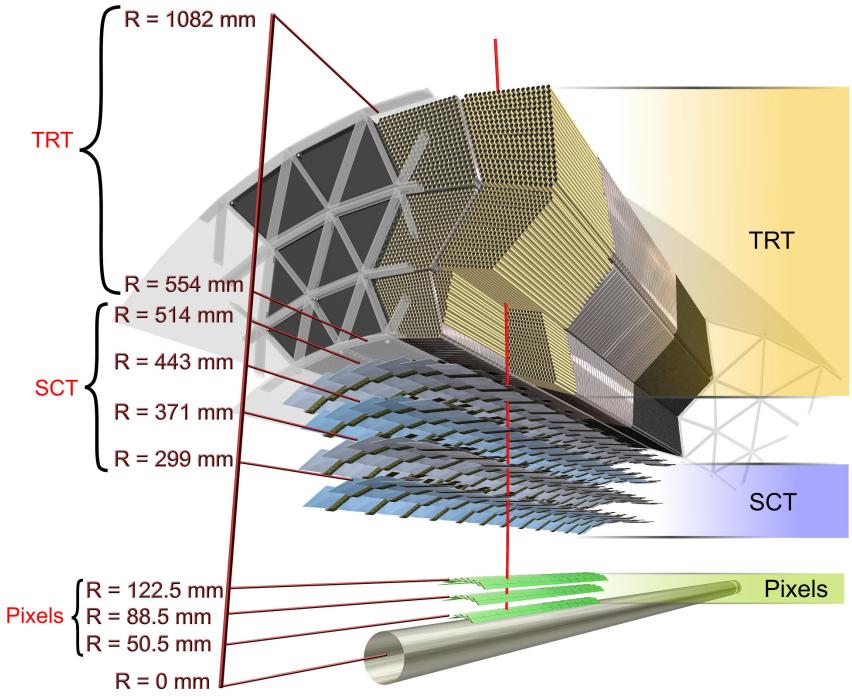

Figure 3.7: Section of the ATLAS inner detector being crossed by a single high energy particle [59].

field along the z-axis, and can reconstruct tracks from particles with a nominal lower p_{T} threshold of 0.5 GeV.

The pixel detector lies closest to the beam pipe and has the highest resolution in order to facilitate accurate vertex reconstruction. It consists of 1744 identical pixel modules arranged into three concentric cylindrical layers at radii of 50.5, 88.5 and 122.5 mm in the central barrel region, and three circular disks in each end-cap at $|z|$ of 495, 580 and 650 mm. The modules have a resolution of 10 µm in $(R-\phi)$ and 115 µm in either z or R, depending on whether the module is located in the barrel or end-cap, respectively. Each module measures $62.4 \times 21.4\,\mu\mathrm{m}^2$ and contains 47 232 pixels, providing the pixel detector with a total of approximately 80.4 million readout channels. During LS1, an additional pixel layer was added to this detector as described in Section 3.2.2.

The SCT surrounds the pixel detector and uses silicon microstrip sensors to provide further precision tracking. Individual sensors measure $6.36 \times 6.40\,\mathrm{cm}^2$ and have a strip pitch of 80 µm, but are only capable of providing position measurements in one direction. Pairs of sensors are therefore mounted back-to-back with an angular separation of 40 mrad, using the small angle stereo effect to record particle trajectories in all three dimensions. In the central barrel region, such pairs of sensors are arranged into four concentric cylindrical layers at radii of 299, 371, 443 and 514 mm, with one set of strips in each layer running parallel to the beam pipe. In the end-cap regions, tapered strips are arranged on nine wheels between $|z|$ of 853.8 and 2 720.2 mm with one set of strips in each wheel aligned radially. This design gives the SCT a resolution of 17 µm in $(R-\phi)$ and 580 µm in z (R) within the barrel (end-cap). Both the pixel detector and the SCT are operated between −5 and −10 °C in order to reduce noise.

The TRT is a straw tube tracker located outside the SCT between radii of 563 mm and 1 067 mm in the barrel. It provides an average of 36 hits per track in the $(R-\phi)$ plane for additional tracking, while also generating and recording transition radiation from charged particles to help distinguish between electrons and charged pions. The 4 mm diameter straw tubes are constructed from a sandwich of two polyimide films bonded by polyurethane, with thin coatings of aluminium and protective graphite-polyimide applied both inside and out. Each tube is fitted with a centrally mounted 30 µm gold-plated tungsten anode wire. The straws are filled with a gas mixture of 70% Xe, 27% CO_2 and 3% O_2, which creates larger signal amplitudes from the transition radiation than from minimal ionising particles, and thus allows for discrimination. In the central barrel region, the straws are 144 cm long and placed parallel to the beam pipe. The anode wires are split electrically at $\eta = 0$ by fused glass capillaries in order to reduce the occupancy. The straws are embedded in a matrix of polypropylene fibres that serve as a source of transition radiation. In the end-caps, the straws are 37 cm long and arranged radially with polypropylene foil between them. All straws have an intrinsic resolution of 130 µm in the $R-\phi$ plane, and no z measurement is possible. Unlike the inner two silicon detectors, the TRT is designed to operate at room temperature. It is therefore maintained in an envelope of CO_2 gas to prevent

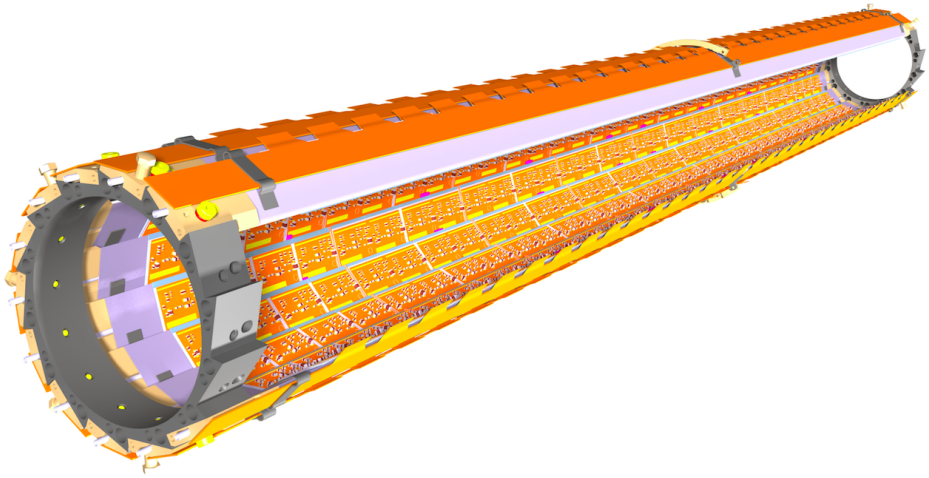

Figure 3.8: Schematic drawing of the ATLAS IBL detector. The single detector modules are mounted on carbon fibre support structures with incorporated CO_2 cooling circuits [61].

contamination from the dry nitrogen used to keep the pixel and SCT detectors at their required operating temperatures.

3.2.2 Insertable B-Layer

The beam pipe that runs through ATLAS is 38 m long and consists of seven pieces bolted together with flanges to form an ultra-high vacuum system that can be baked *in-situ*. The central section is a beryllium tube with an inner diameter of 58 mm and a wall thickness of 0.8 mm, centred around the interaction point. It is an integral part of the pixel detector and the two are installed together. The other six beam pipe sections are made of stainless steel, and are placed symmetrically on each side of the interaction point. During the maintenance performed in preparation for Run 2, the beryllium beam pipe segment was replaced with a new tube of inner diameter 50 mm. This opened up a gap between the beam pipe and the pixel detector, which was filled by a new layer of silicon sensors named the insertable B-layer (IBL) [61].

The IBL consists of 14 carbon fibre staves of sensors that form a cylindrical layer of mean radius 33 mm, with each stave rotated at 25.7° to the preceding one in order to provide hermetic coverage in ϕ. Each stave measures 64 cm in length, making it possible to take measurements up to $|\eta| < 3$, and is fitted with 32 sensor modules that each contain 26 880 pixels, for a total of around 12 million pixels over the whole IBL. This detector adds a fourth layer to the pixel detector to enhance the tracking and vertex performance, and could also be used as a backup to maintain the current performance level if some of the existing pixel detector silicon sensors fail due to age or radiation damage. A schematic overview of the IBL is presented in Figure 3.8.

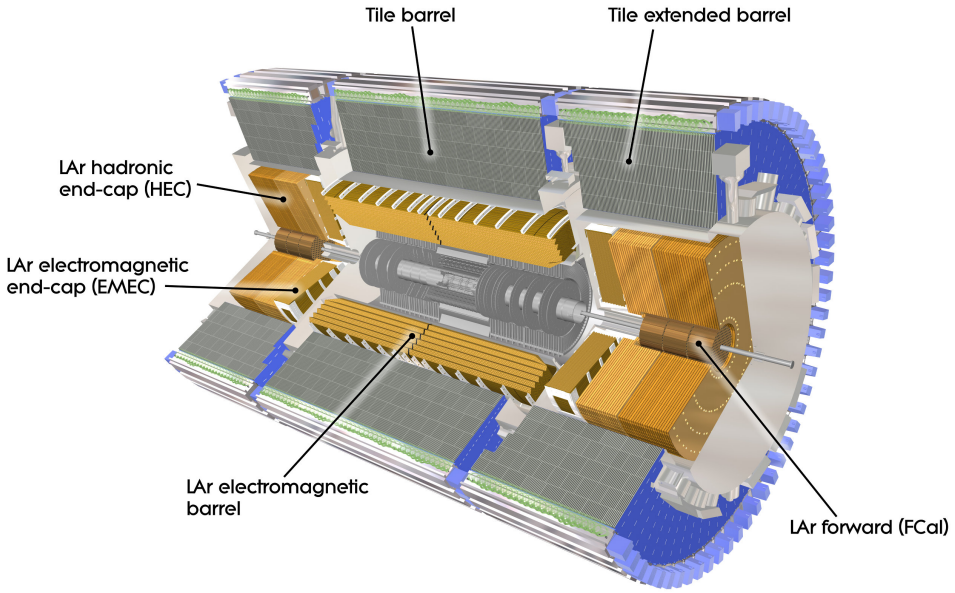

Figure 3.9: Computer generated image of the ATLAS Calorimeters [62].

3.2.3 Calorimeters

The ATLAS detector uses sampling calorimeters, composed of alternating layers of an active sensing material and an absorber, to measure the energy deposited by electromagnetic (EM) and hadronic showers up to $|\eta| < 4.9$ [45]. They are designed to capture the entire shower produced from an incident particle, allowing its total energy to be inferred from the sum of the energy deposits in each sampling layer. The calorimeters play an important role in the measurement of jets and also missing transverse energy, where apparent violations in conservation of energy are used to infer the presence of weakly interacting neutral particles such as neutrinos.

The calorimeters are divided into two main subsystems, which are arranged as shown in Figure 3.9. The liquid argon (LAr) EM calorimeter immediately surrounds the ID and is used to measure the energy of photons and charged particles. In order to optimise performance and reduce material, it shares the same vacuum vessel as the central solenoid. The hadronic tile calorimeter measures the energy of hadrons, which pass through the EM calorimeter relatively undisturbed. For reference, schematic diagrams of the central barrel modules of the electromagnetic and hadronic calorimeters are presented in Figure 3.10.

The EM calorimeter uses steel-clad lead absorber plates and LAr as the sensing element, with accordion-shaped kapton electrodes to provide complete ϕ coverage without any azimuthal cracks. The central barrel covers $|\eta| < 1.475$ and is constructed from two identical half-barrels separated by 4 mm at $z = 0$. The thickness of the lead absorber plates varies with η in order to provide optimum performance with regard to the energy resolution, while the LAr gap between the plates is held at a constant thickness of 2.1 mm.

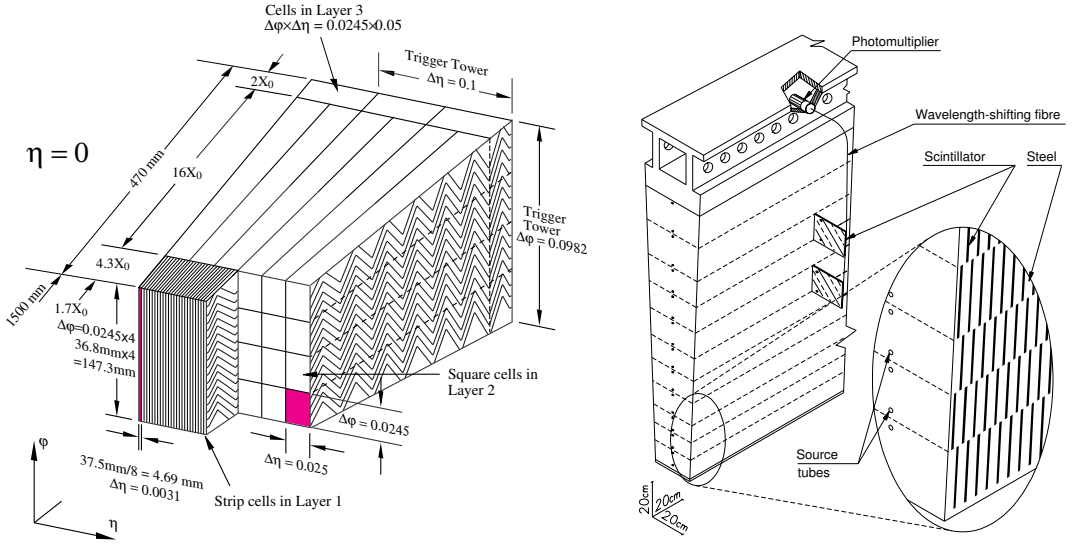

Figure 3.10: Left: Diagram of an electromagnetic calorimeter barrel module showing the segmentation in three layers. The granularity of the cells and trigger towers is also shown. Right: Schematic of a single barrel module in the hadronic tile calorimeter, showing the integration of the tiles, fibres, and photomultipliers [45].

The end-caps take the form of two coaxial wheels, with the outer covering $1.375 < |\eta| < 2.5$ and the inner covering $2.5 < |\eta| < 3.2$. The wheels maintain a constant absorber thickness, leading to a more complex geometry where the amplitude of the accordion waves increases as a function of radius. The EM calorimeter is segmented into three layers in depth within the region $|\eta| < 2.5$, while the inner end-cap wheels are segmented into only two layers. Fine segmentation in η of the first layer allows for position measurements and, if coupled with the second sampling layer, photon pointing. The central region ($|\eta| < 1.8$) is complemented by an active LAr presampler that is used to correct for the energy loss of particles as they traverse the ID.

The hadronic calorimeter uses steel plates as the absorber and plastic scintillating tiles coupled to wavelength-shifting fibres as the sensing material. It extends radially from 2 280 to 4 230 mm and is composed of a 5 640 mm long central barrel flanked by 2 910 mm long barrel extensions on each side, providing coverage over $|\eta| < 1.7$. The central barrel is segmented into three layers, with thicknesses of 1.5, 4.1 and 1.8 interaction lengths. The extended barrels are also segmented into three layers, but with thicknesses of 1.5, 2.6 and 3.3 interaction lengths.

The hadronic end-cap calorimeter (HEC) is located directly behind the EM calorimeter end-cap and covers the region $1.5 < |\eta| < 3.2$. It overlaps slightly with both the tile calorimeter and the forward calorimeter (described below) in order to reduce the drop in material density at the transition boundaries. The HEC consists of two independent wheels per end-cap, constructed from parallel copper plates interleaved with 8.5mm LAr gaps. The copper plates have an inner and outer radius of 475 and 2 030 mm, respectively, except for the overlap region between the HEC and the forward calorimeter where the inner radius drops to 372 mm. The HEC is segmented into two

layers in depth, providing four layers per end-cap in total.

The forward calorimeter serves to increase coverage in the forward region at $3.1 < |\eta| < 4.9$. Each endcap has a depth of approximately 10 interaction lengths and is segmented into three modules. Each module consists of a metal matrix with regularly spaced longitudinal channels that are filled with the electrode structure - a series of concentric rods and tubes running parallel to the beam-pipe, with the gap between the rod and the tube filled with LAr to act as the sensing medium. The innermost module uses a copper matrix and is optimised for electromagnetic measurements, while the outer two layers use a tungsten matrix for hadronic measurements.

The energy resolution of the EM calorimeter, following subtraction of noise due to the electronic gain of the calorimeter cells, can be described by:

$$\frac{\sigma_E}{E} = \frac{a}{\sqrt{E}} \oplus b, \tag{3.7}$$

where a takes into account statistical fluctuations connected with the detection of the EM shower and has been measured as $(10.1 \pm 0.1\% \cdot \sqrt{\text{GeV}})$, and b is a constant term including detector instabilities and mis-calibration that has been measured as $0.17 \pm 0.04\%$ [63]. The symbol $\oplus$ denotes a summation in quadrature of the two terms. The energy resolution of the hadronic calorimeter has a similar functional form, and uses $a = (52.6 \pm 0.9\%/\sqrt{\text{GeV}})$ and $b = 5.7 \pm 0.2\%$ [64].

3.2.4 Muon Spectrometer

The outermost part of the ATLAS detector is the muon spectrometer, which is designed to detect charged particles exiting the barrel and end-cap calorimeters [45]. The only known particles capable of doing this are muons, which generally interact with matter in the same way as minimal ionising particles and can therefore traverse the ID and calorimeters with their trajectories relatively undisturbed.

The spectrometer is fully integrated with three large air-core toroids that provide magnetic deflection of the muon tracks. Each toroid magnet features eight coils arranged radially and symmetrically around the beam pipe. The air-cores minimise the amount of material that the muons must traverse, reducing the possibility of multiple scattering and thereby limiting the loss of signal resolution. The large barrel toroid generates a 0.5 T field over the range $|\eta| < 1.0$, while the two smaller end-cap toroids each generate a 1.0 T field over the range $1.4 < |\eta| < 2.7$. Across the transition region, in the range $1.0 < |\eta| < 1.4$, magnetic deflection is provided by the combination of the overlapping barrel and end-cap fields. In order to optimise the bending power in the transition region, and to provide radial overlap, the end-cap toroids are rotated by 22.5° with respect to the barrel toroid. The resultant magnetic field is mostly orthogonal to the muon trajectories.

The muon spectrometer itself consists of a series of trigger chambers and high-precision tracking chambers. They are arranged into three concentric cylinders at radii of approximately 5.0, 7.5 and 10.0 m in the central barrel region, and large wheels in

each end-cap located at $|z|$ of approximately 7.4, 10.8, 14.0 and 21.5 m. The layout of these chambers is presented in Figures 3.11 and 3.12. The muon spectrometer is capable of measuring the transverse momentum of muons with a resolution of around 4% [45].

Muon tracking comes predominantly from Monitored Drift Tube (MDT) chambers, which provide coverage over $|\eta| < 2.7$ apart from a small break around $|\eta| \approx 0$ to allow access for services to the inner detector, solenoid magnet and calorimeters. The MDT chambers contain three to eight layers of 29.97 mm diameter aluminium tubes that are each fitted with a central 50 µm tungsten-rhenium anode wire. The size of the chambers increase proportionally with distance from the interaction point, causing the tubes to vary in length from 0.7 to 6.3 m based on their location in the spectrometer. The tubes are filled with a gas mixture of 93%Ar and 7% CO_2 that is maintained at an absolute pressure of 3 bar. This mixture was selected for its good ageing properties, since clean samples of the gas prevent the formation of polymers that could lead to deposits on the anode wires and a reduction in the output signal pulse height. The MDT chambers have a resolution of approximately 35 µm per chamber. It should be noted that not all of the muon chambers had been installed when Run 1 commenced, resulting in reduced coverage in some ϕ regions at $1.1 < |\eta| < 1.3$ where muons could only traverse a single layer of chambers. This was corrected during the extended shutdown between Run 1 and Run 2 when the missing chambers were finally installed.

On the innermost end-cap wheel (corresponding to $2.0 < |\eta| < 2.7$) the MDTs are replaced with Cathode-Strip Chambers (CSCs), since they have a higher rate capability and better time resolution. The CSCs are multiwire proportional chambers that each contain four CSC planes to provide four independent measurements of η and ϕ. There are 16 CSCs per end-cap, arranged over two circular disks containing eight large and eight small chambers - the only difference between the large and small chambers is the size of the active area. The chambers are filled with a gas mixture of 80% Ar and 20% CO_2. Each CSC plane contains a series of parallel 30 µm tungsten-rhenium anode wires, with the central wire aligned radially. One cathode is segmented into 48 strips running parallel to the wires and provides the transverse coordinate with a resolution of approximately 5 mm, while the other is segmented into 192 strips running perpendicular to the wires and provides the precision measurement with a resolution of 60 µm.

Trigger information is provided by Resistive Plate Chambers (RPCs) mounted in the barrel region, and Thin Gap Chambers (TGCs) in the end-cap, which together provide coverage up to $|\eta| < 2.4$.

The RPCs are gaseous parallel plate detectors, each consisting of two resistive plates made from phenolic-melaminic plastic laminate that are separated by a 2 mm gap. This gap is occupied by a gas mixture of 94.7% $C_2H_2F_4$, 5% Iso-C_4H_{10} and 0.3% SF_6, which was selected for its relatively low operating voltage, low cost, and because it afforded a good plateau region for electron avalanches. The RPCs are arranged into three concentric cylindrical layers located around the MDT chamber barrel layers, and

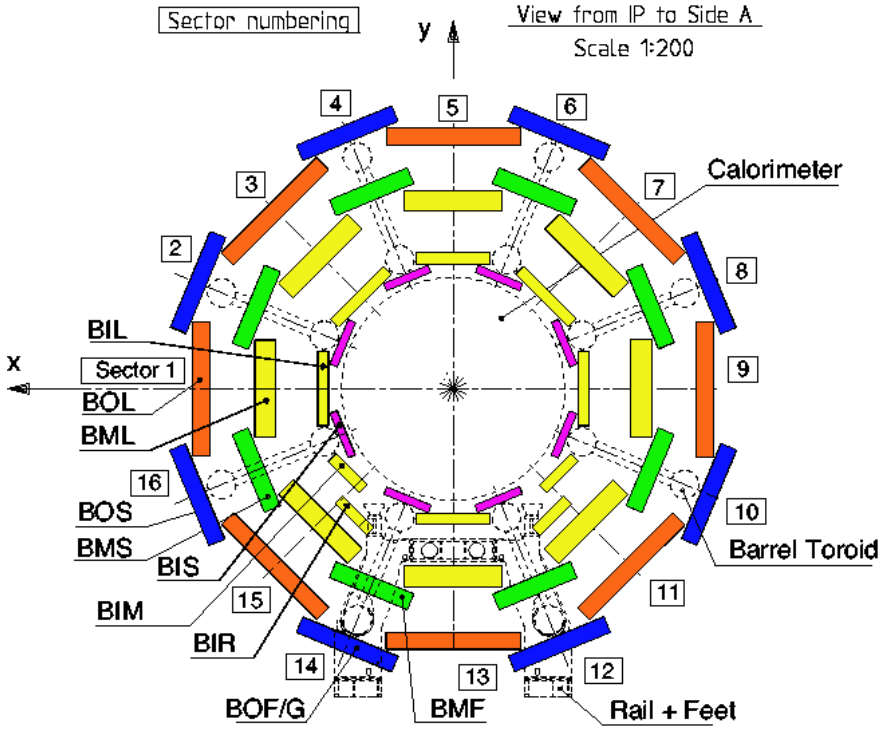

Figure 3.11: Cross-section of the barrel muon system perpendicular to the beam axis (non-bending plane), showing three concentric cylindrical layers of eight large and eight small chambers. The outer diameter is about 20 m [45].

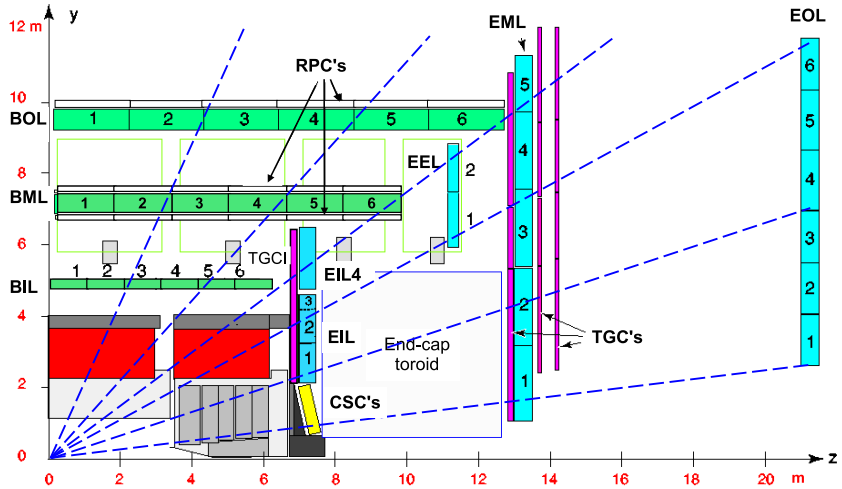

Figure 3.12: Cross-section of the muon system in a plane containing the beam axis (bending plane). Infinite-momentum muons would propagate along straight trajectories which are illustrated by the dashed lines and typically traverse three muon stations [45].

provide coverage up to $|\eta| < 1.05$. The two inner layers provide triggering for low momentum muon tracks, while the outer layer provides triggering for high momentum tracks. They feature good timing resolution, essential for the trigger system, but also carry a good spatial resolution which enables them to provide further tracking.

The TGCs are multiwire proportional chambers that provide coverage over $1.05 < |\eta| < 2.4$. They feature an anode-wire pitch that is greater than the anode-cathode distance, and are filled with a highly quenching gas mixture of 55% CO_2 and 45% n-C_5H_{12}. The MDTs on the middle end-cap layer are complemented by seven layers of TGCs, which provide both trigger information and a measurement of the azimuthal coordinate. The inner end-cap layer features two layers of TGCs and is only capable of measuring the azimuthal coordinate. The information collected by the TGC in the inner and middle end-cap layers is used to extrapolate the azimuthal coordinate in the outer end-cap layer.

3.2.5 Trigger System

When the LHC operates with the nominal bunch spacing of 25 ns, bunch crossings occur at a rate of 40 MHz. However, the volume of data that must be read out from the detector per event, combined with limitations in modern technology and the computing resources available to the experiment, means that it is only possible to record a small fraction of those events. The ATLAS Trigger and Data Acquisition systems (TDAQ) are described in detail in Ref. [45], and are responsible for reducing the flow of data to a manageable rate while safeguarding future discoveries by preserving information that will be of interest in physics analysis. The trigger system is comprised of three levels of selection criteria that impose progressively tighter constraints on an event: Level 1 (L1), Level 2 (L2) and the Event Filter (EF). The L2 and EF triggers collectively form the High Level trigger (HLT).

The L1 trigger is implemented in hardware using custom electronics built into the detector itself. The raw energy deposits from the calorimeters are read out using a reduced granularity, and combined with information from the RPC and TGC elements of the muon spectrometer in order to search for events containing high-p_{T} objects or large amounts of missing transverse energy. The trigger has just 2.5 µs following a bunch crossing to select or reject an event, and the aim is to provide the decision within 2.0 µs to leave some time as a contingency. It is worth noting that around 1 µs of this time alone is spent in simply passing data through the cables of the detector. When an event passes an L1 trigger, any regions of the calorimeter with E_{T} greater than a set of pre-determined thresholds will be marked as regions of interest to be investigated in more detail by the L2 trigger. During 2012, events were typically generated at a rate of 20 MHz and the L1 trigger was capable of reducing this to an average rate of around 40 kHz [65].

The L2 trigger is a software based trigger that is permitted 40 ms to examine each incoming event, allowing more complex selection algorithms to be run. Within the identified regions of interest, particle tracks are reconstructed using the full calorimeter

granularity and all elements of the muon spectrometer. Photons and electrons then become distinguishable from jets, and trigger selections can be made against these objects. As tighter constraints are imposed, the event rate is reduced further to an average rate of 4.7 kHz.

The EF is another software based trigger that takes around 4 s to fully reconstruct each event using the same algorithms that are applied in the offline event reconstruction. Information from every subdetector is used, including track information to finally separate photons from electrons. Additional trigger selection criteria can be imposed at this stage, and any events passing them are permanently stored for future analysis. During 2012, the output rate of this trigger averaged just over 700 Hz and around 700 MB of data was written per second [65].

Chapter 4

Data and Simulated Samples

The data samples used in these analyses were recorded by the ATLAS detector following pp collisions provided by the LHC at various beam energies. During Run 1, data was recorded in 2011 and 2012 at centre-of-mass collision energies of $\sqrt{s} = 7$ and 8 TeV, respectively, as described in Section 4.1.1. Following a long shutdown for maintenance and upgrades to the LHC and its main experiments, Run 2 commenced in June 2015 and data was acquired from collisions with a centre-of-mass collision energy of $\sqrt{s} = 13$ TeV as described in 4.1.2.

In order to evaluate the observed data, a series of simulated signal and background Monte-Carlo (MC) samples were produced as described in Section 4.2. The analysis of the Run 1 data involved a search for the SM Higgs boson decaying via $H \to Z\gamma$, $Z \to \ell\ell$, where $\ell = e, \mu$. The leptons from such a decay are produced with a characteristic p_{T} of 45 GeV, while the photon has a characteristic p_{T} of 35 GeV (for a Higgs boson of mass 125 GeV). Several simulated signal samples were therefore generated, which corresponded to various Higgs boson mass hypotheses and production modes. Additional simulated samples were produced to describe the SM background processes that dominate the data. Since the production cross-sections are energy dependent, separate MC samples were produced for 7 and 8 TeV centre-of-mass collision energies, as described in Sections 4.2.1.1 and 4.2.1.2, respectively.

The analysis of the Run 2 data proceeded in a similar manner, but involved a search for new high mass resonances decaying through $Z\gamma$ to an $\ell\ell\gamma$ final state. The leptons from such a decay are again produced with a characteristic p_{T} of 45 GeV, while the photon p_{T} can be any large value. Signal MC samples were generated for a Higgs-like boson, X, of various masses produced through the ggF mechanism and the relevant background processes were also simulated, as described in Section 4.2.2.

4.1 Data

4.1.1 Run 1 Data

The data samples acquired during Run 1 were recorded by ATLAS following pp collisions provided by the LHC at $\sqrt{s} = 7$ and 8 TeV in 2011 and 2012, respectively, under conditions where the colliding proton bunches had a separation of 50 ns. The events used in this analysis were collected using the lowest-threshold, unprescaled single- and

Trigger Type	Periods	Single lepton trigger	Dilepton Trigger
Electron	B-J	`EF_e20_medium`	`EF_2e12_medium`
	K	`EF_e22_medium`	`EF_2e12T_medium`
	L-M	`EF_e22vh_medium1`	`EF_2e12Tvh_medium`
Muon	B-I	`EF_mu18_MG`	`EF_2mu10_loose`
	J-M	`EF_mu18_MG_medium`	`EF_2mu10_loose`

Table 4.1: List of triggers used to record the 7 TeV data.

Trigger Type	Single lepton trigger	Dilepton Trigger
Electron	`EF_e24vhi_medium1` `EF_e60_medium1`	`EF_2e12Tvh_loose1`
Muon	`EF_mu24i_tight` `EF_mu36_tight`	`EF_mu24i_tight` `EF_mu18_tight_mu8_EFFS`

Table 4.2: List of triggers used to record the 8 TeV data.

di-lepton triggers, as listed in Tables 4.1 and 4.2. It must be noted that the data-taking was split into a number of Periods corresponding to major runs with different beam conditions. The 7 TeV data used a slightly different set of triggers for each Period, while the 8 TeV data used a single set of triggers for all periods, in accordance with official recommendations [66, 67].

The trigger names are an encoded description of the selection criteria that they impose, and the conventions [68] can be most simply explained through the use of an example: `EF_2e12Tvh_medium`. This trigger was applied at the event filter (EF) level, requiring the presence of at least two electrons in the event with $p_{\mathrm{T}} > 12$ GeV. The letters "Tvh" denote that the seed L1 trigger imposed a tighter than default selection in the calorimeter (T), an energy threshold that is variable with η (v), and a hadronic core veto (h). Some of the triggers used in this analysis impose an isolation requirement (i). Finally, for electron triggers the word "medium" or "loose" is used to describe the stringency of the object identification cuts. Some of the 7 TeV muon triggers include "MG" in the name to denote the use of the TrigMuGirl algorithm [69]. From 2012 onwards, the muon trigger was a logical OR of both this and the TrigMuonEF algorithms.

Events failing to satisfy the data quality requirements for physics analysis were rejected through the use of Good Run Lists (GRLs). The GRL[1] for the 7 TeV data set rejected around 13% of recorded events. Out of the total events that were recorded, 1.9% were removed due to tracking problems such as temporary failures of one or more SCT read-out drivers, 2.5% were removed due to calorimetry problems such as LAr readout errors, and around 1% were removed due to problems with the muon chambers such as readout errors [70]. After the trigger and data quality requirements were applied, the integrated luminosity was 4.5 fb^{-1}, with a relative uncertainty of 1.8% [71, 72].

[1] data11_7TeV.periodAllYear_DetStatus-v36-pro10-02_CoolRunQuery00-04-08_All_Good.xml

$Z \to ee\gamma$	$Z \to \mu\mu\gamma$
`HLT_e24_lhmedium_L1EM20VH` (data only)	`HLT_mu20_iloose_L1MU15`
`HLT_e24_lhmedium_L1EM18VH` (MC only)	`HLT_mu50`
`HLT_2e12_lhloose_L12EM10VH`	`HLT_2mu10`

Table 4.3: List of triggers used to record the 13 TeV data.

The GRL[2] for the 8 TeV data set rejected only 4.7% of recorded events. Out of the total events that were recorded, 2.5% were removed due to tracking problems, around 1% were removed due to problems with the calorimeters, and 0.5% were removed due to problems with the muon chambers [70]. After the trigger and data quality requirements were applied, the integrated luminosity was 20.3 fb^{-1}, with a relative uncertainty of 2.8%. The uncertainty was evaluated from a preliminary calibration of the luminosity scale derived from beam-separation scans performed in November 2012, following the same method described in [72].

Following the basic object reconstruction, the data samples were further reduced in size by a factor of approximately 30 by applying the following loose skimming and kinematic selection criteria:

- At least one primary vertex with three associated tracks,
- Lepton transverse momenta and photon transverse energy greater than 10 GeV,
- `loose++` electron identification (see Section 5.3.2) or `loose` muon identification (see Section 5.4),
- At least one same-flavour lepton pair with an invariant mass greater than 10 GeV.

4.1.2 Run 2 Data

The data samples acquired during Run 2 were recorded by ATLAS following pp collisions provided by the LHC at $\sqrt{s} = 13$ TeV in 2015, under conditions where the colliding proton bunches had a separation of 25 ns. The events were collected using the lowest-threshold, unprescaled single- and di-lepton triggers, as listed in Table 4.3.

It should be noted that the trigger naming convention is different from Run 1, and now features greater simplicity and clarity [73]. The electron triggers perform identification of electrons through a likelihood-based selection criteria, using parameters such as the longitudinal and transverse shower profiles from the electromagnetic calorimeter, measures of track quality and track-cluster matching quality, and the transition radiation recorded by the TRT. The single electron triggers have a nominal p_{T} threshold of 24 GeV and must pass what is termed a medium identification requirement, which is tuned to be 90% efficient for electrons with $E_{\text{T}} \approx 40$ GeV [74]. The dielectron trigger requires the presence of two electrons that each have $p_{\text{T}} > 12$ GeV and must pass a

[2] data12_8TeV.periodAllYear_DetStatus-v61-pro14-02_DQDefects-00-01-00_PHYS_StandardGRL_All_Good.xml

loose identification requirement that is 95% efficient for electrons with $E_{\mathrm{T}} \approx 40$ GeV. It should be noted that the identification selection criteria applied here are looser than those applied during the object reconstruction and selection. These high-level triggers are seeded by L1 triggers (see Section 3.2.5) that apply an E_{T}-dependent veto against energy deposits in the hadronic calorimeter located behind the cluster of energy in the electromagnetic calorimeter that was associated with the electron candidate [75].

The single muon trigger `HLT_mu20_iloose_L1MU15` has a nominal p_{T} threshold of 20 GeV and a loose requirement on the muon track isolation, whereby the sum of the transverse momentum of ID tracks located in a cone of radius $\Delta R < 0.2$ around the muon (excluding the track of the muon itself) must be less that 12% of the muon p_{T}. This high-level trigger is seeded from an L1 trigger that requires the candidate muon to have a transverse momentum of at least 15 GeV. The other single muon trigger, `HLT_mu50`, has a nominal p_{T} threshold of 50 GeV and no isolation requirement. The dimuon trigger requires the presence of two muons that each have $p_{\mathrm{T}} > 10$ GeV and does not impose an isolation requirement. Events are selected if they pass any of these three triggers.

The trigger efficiency is greater than 99% in $ee\gamma$, and 96% in $\mu\mu\gamma$ due to the reduced geometrical acceptance at $|\eta| < 1.05$ and $|\eta| > 2.4$ [5]. After the trigger and GRL[3] selections, the integrated luminosity of the data sample corresponds to 3.2 fb^{-1}.

As part of the preparation for Run 2, the ATLAS collaboration initiated a major paradigm shift in the management of computing resources whereby all Run 2 data samples (and also the MC samples) are now produced in a common "xAOD" file format. While this decision has centralised code development and maximised the reuse of software, the resultant xAOD files are too large to process locally and so a derivation framework has been constructed to select small analysis-specific subsets of events. For this analysis, the derivation framework retained events containing:

- at least one photon with $E_{\mathrm{T}} > 9.5$ GeV and $|\eta| < 2.5$;
- at least two electrons or two muons with opposite charge and invariant mass $m_{\ell\ell} > 40$ GeV, passing the following requirements:
  - electrons: $p_{\mathrm{T}} > 9.5$ GeV, $|\eta| < 2.5$, medium identification (logical OR of likelihood and cut-based selectors),
  - muons: $p_{\mathrm{T}} > 9.5$ GeV, $|\eta| < 2.7$, and good muon quality requirements (pass cuts on number of hits).

It should be noted that these selection criteria are only applied to reduce the memory footprint of the data and MC samples, and the object selection is looser than the one applied in the final analysis. The reduced data samples that resulted from this selection process and which were used in this analysis are listed in Table 4.4.

[3] data15_13TeV.periodAllYear_DetStatus-v73-pro19-08_DQDefects-00-01-02_PHYS_StandardGRL_All_Good_25ns.xml

data15_13TeV.periodD.physics_Main.PhysCont.DAOD_HIGG1D2.grp15_v01_p2425
data15_13TeV.periodE.physics_Main.PhysCont.DAOD_HIGG1D2.grp15_v01_p2425
data15_13TeV.periodF.physics_Main.PhysCont.DAOD_HIGG1D2.grp15_v01_p2425
data15_13TeV.periodG.physics_Main.PhysCont.DAOD_HIGG1D2.grp15_v01_p2425
data15_13TeV.periodH.physics_Main.PhysCont.DAOD_HIGG1D2.grp15_v01_p2425
data15_13TeV.periodJ.physics_Main.PhysCont.DAOD_HIGG1D2.grp15_v01_p2425

Table 4.4: List of data samples used in the $X \to Z\gamma$ analysis. The term "HIGG1D2" denotes that the samples contain a subset of the total data set where events have been selected according to the criteria listed in Section 4.1.2.

4.2 Monte Carlo Samples

4.2.1 Run 1 Monte Carlo Samples

4.2.1.1 7 TeV Samples

MC signal samples were generated for SM Higgs bosons produced through various mechanisms and decaying to $Z\gamma$, for seven different Higgs mass points ranging from 120 to 150 GeV in 5 GeV steps. Samples for Higgs bosons produced through the ggF and VBF mechanisms were generated with `POWHEG` [76, 77] interfaced to `PYTHIA` 8.170 [78] for showering and hadronisation, using the CT10 [79] parton distribution functions (PDFs). Additional samples for Higgs bosons produced through the WH, ZH and $t\bar{t}$H mechanisms were generated using `PYTHIA` 8.170 and the CTEQ6L PDFs [80]. Within each sample, the Z boson was forced to decay to charged lepton pairs (e^+e^-, $\mu^+\mu^-$ and also $\tau^+\tau^-$) in equal fractions, up to Poisson fluctuations. Such equal fractions are expected from lepton universality and confirmed by world averages of Z leptonic branching fractions.

The predicted SM cross-sections and branching ratios were discussed in Section 2.5 and a small selection were presented in Tables 2.3 and 2.4. The ggF production cross-section was computed at next-to-next-to-leading order (NNLO) [81–85] in the strong coupling constant α_s and includes next-to-leading order (NLO) electroweak (EW) corrections [86, 87]. The VBF production cross-sections include full NLO QCD and EW corrections [88–90], and approximate NNLO QCD corrections [91]. The WH and ZH cross-sections were calculated at NNLO [92] in α_s, and NLO EW radiative corrections [93] were applied. The full NLO QCD corrections for $t\bar{t}$H were calculated [94, 95].

The theoretical uncertainties on the production cross section originate from the choice of renormalisation and factorisation scales in the fixed-order calculations, and also from the uncertainties on the PDF eigenvalues and the value of α_s used in the perturbative expansion. They depend only mildly on the centre-of-mass energy and on the Higgs boson mass in the range $120 < m_H < 150$ GeV. The scale uncertainties are uncorrelated among the five Higgs boson production modes; for $m_H = 125$ GeV at

$\sqrt{s} = 8$ GeV, they amount to $^{+7}_{-8}$% for ggF, ±0.2% for VBF, ±1% for WH, ±3% for ZH and $^{+4}_{-9}$% for $t\bar{t}$H.

The PDF+α_s uncertainties are correlated among the gluon-fusion and $t\bar{t}$H processes, which are initiated by gluons, and among the VBF and WH/ZH processes, which are initiated by quarks; for $m_H = 125$ GeV at $\sqrt{s} = 8$ GeV, the uncertainties are around ±7−8% for ggF and $t\bar{t}$H and around ±2.5% for the other three Higgs boson production modes. The Higgs boson branching ratios are computed using the HDECAY and Prophecy4f programs [96–98]. The relative uncertainty on the $H \to Z\gamma \to \ell\ell\gamma$ branching ratio varies between ±9.4% for $m_H = 120$ GeV and ±6.2% for $m_H = 150$ GeV.

Samples of $Z + \gamma$ events produced through SM processes were generated with `SHERPA` 1.4.0 [99–101] using the CT10 PDFs, with separate samples produced for Z bosons decaying to $ee\gamma$ and $\mu\mu\gamma$ final states. Up to three partons were produced in the hard scattering processes, with matrix elements implemented at LO. The generated photon transverse momentum had a minimum of 10 GeV and the generated dilepton invariant mass had a minimum of 40 GeV. A minimum distance $\Delta R > 0.1$ between the photon and the leptons and partons was required.

Samples of Z + jet events produced through SM processes were generated with `SHERPA` 1.4.0 using the CT10 PDFs, with separate samples produced for Z bosons decaying to either electron or muon pairs. Event generation made use of the LO matrix elements to produce up to 5 partons, and the dilepton invariant mass was required to be greater than 40 GeV.

A sample of WZ events was generated with `SHERPA` 1.3 using the CTEQ6L1 PDFs, where the $W^{\pm}$ and Z bosons were forced to decay leptonically and up to three partons were produced in the hard scattering process. It was required that the generated dilepton invariant mass be greater than 60 GeV.

Finally, a sample of $t\bar{t}$ events was generated using the CT10 PDFs with `MC@NLO`, interfaced to `HERWIG` 6.510 [102] for parton showering and fragmentation and to `JIMMY` 4.31 [103] to model the underlying-event contributions. A filter was applied between the generation and full simulation of the events requiring that the dilepton invariant mass be greater than 60 GeV.

Lists of the simulated 7 TeV signal and background samples are provided in Tables 4.5 and 4.6, respectively.

4.2.1.2 8 TeV Samples

Signal samples at 8 TeV were produced with the same generators described for the 7 TeV samples, and are listed in Table 4.7.

SM $Z + \gamma$ MC samples were generated with `SHERPA` 1.4.1 [99–101] using the CT10 PDFs. Samples containing Z + jet events were generated using `SHERPA` 1.4.0, with the requirement that the generated dilepton invariant mass be greater than 40 GeV. Less significant background components were also produced, with WZ events generated using `POWHEG` interfaced to `PYTHIA` 8.165, and $t\bar{t}$ events generated using `MC@NLO`. A

Mechanism	DSID	m_H	Production tags	N	σ_{gen} [fb]	$\varepsilon_{\text{filt}}$	eq. lumi [fb^{-1}]
ggF	167480	120	e1749_s1570_s1571_r3108_r3109_p1373	100000	1.8418	1	5.430e+04
	167481	125	e1749_s1570_s1571_r3108_r3109_p1373	100000	2.3531	1	4.250e+04
	167482	130	e1749_s1570_s1571_r3108_r3109_p1373	99999	2.7531	1	3.632e+04
	167484	135	e1749_s1570_s1571_r3108_r3109_p1373	99999	2.9688	1	3.368e+04
	167485	140	e1749_s1570_s1571_r3108_r3109_p1373	99999	2.9741	1	3.362e+04
	167486	145	e1749_s1570_s1571_r3108_r3109_p1373	98900	2.8151	1	3.513e+04
	167487	150	e1749_s1570_s1571_r3108_r3109_p1373	99999	2.4518	1	4.079e+04
VBF	167490	120	e1749_s1570_s1571_r3108_r3109_p1373	100000	0.1434	1	6.975e+05
	167491	125	e1749_s1570_s1571_r3108_r3109_p1373	100000	0.1901	1	5.262e+05
	167492	130	e1749_s1570_s1571_r3108_r3109_p1373	100000	0.2300	1	4.348e+05
	167494	135	e1749_s1570_s1571_r3108_r3109_p1373	100000	0.2561	1	3.905e+05
	167495	140	e1749_s1570_s1571_r3108_r3109_p1373	99899	0.2645	1	3.777e+05
	167496	145	e1749_s1570_s1571_r3108_r3109_p1373	100000	0.2562	1	3.903e+05
	167497	150	e1749_s1570_s1571_r3108_r3109_p1373	100000	0.2286	1	4.374e+05
WH	167500	120	e2016_s1570_s1571_r3108_r3109_p1373	30000	0.0742	1	4.044e+05
	167501	125	e2016_s1570_s1571_r3108_r3109_p1373	30000	0.0900	1	3.334e+05
	167502	130	e2016_s1570_s1571_r3108_r3109_p1373	30000	0.0996	1	3.011e+05
	167504	135	e2016_s1570_s1571_r3108_r3109_p1373	30000	0.1016	1	2.953e+05
	167505	140	e2016_s1570_s1571_r3108_r3109_p1373	30000	0.0964	1	3.112e+05
	167506	145	e2016_s1570_s1571_r3108_r3109_p1373	29500	0.0861	1	3.427e+05
	167507	150	e2016_s1570_s1571_r3108_r3109_p1373	30000	0.0708	1	4.239e+05
ZH	167508	120	e2016_s1570_s1571_r3108_r3109_p1373	30000	0.0427	0.10000	7.028e+06
	167509	125	e2016_s1570_s1571_r3108_r3109_p1373	30000	0.0521	0.10149	5.672e+06
	167510	130	e2016_s1570_s1571_r3108_r3109_p1373	30000	0.0582	0.10053	5.125e+06
	167512	135	e2016_s1570_s1571_r3108_r3109_p1373	30000	0.0600	0.10112	4.947e+06
	167513	140	e2016_s1570_s1571_r3108_r3109_p1373	30000	0.0575	0.10076	5.182e+06
	167514	145	e2016_s1570_s1571_r3108_r3109_p1373	30000	0.0518	0.10071	5.751e+06
	167515	150	e2016_s1570_s1571_r3108_r3109_p1373	30000	0.0430	0.10013	6.972e+06
$t\bar{t}$	167550	120	e2016_s1570_s1571_r3108_r3109_p1373	30000	0.0109	1	2.743e+06
	167551	125	e2016_s1570_s1571_r3108_r3109_p1373	29999	0.0134	1	2.235e+06
	167552	130	e2016_s1570_s1571_r3108_r3109_p1373	29998	0.0151	1	1.989e+06
	167554	135	e2016_s1570_s1571_r3108_r3109_p1373	30000	0.0156	1	1.920e+06
	167555	140	e2016_s1570_s1571_r3108_r3109_p1373	29999	0.0150	1	1.994e+06
	167556	145	e2016_s1570_s1571_r3108_r3109_p1373	30000	0.0136	1	2.206e+06
	167557	150	e2016_s1570_s1571_r3108_r3109_p1373	30000	0.0114	1	2.642e+06

Table 4.5: Simulated signal samples at $\sqrt{s} = 7\,\text{TeV}$, where N is the number of events, σ_{gen} is the cross-section from Ref. [21], $\varepsilon_{\text{filt}}$ is the generator filter efficiency and the equivalent luminosity is computed as $N_{\text{evts}}/(\sigma_{\text{gen}}\varepsilon_{\text{filt}})$.

Mechanism	DSID	Production tags	N	σ_{gen} [nb]	$\varepsilon_{\text{filt}}$	eq. lumi [nb^{-1}]
$Z \to ee\gamma$	145161	e1443_s1372_s1370_r3108_r3109_p1373	389799	2.734E+01	1	1.426E+04
$Z \to \mu\mu\gamma$	145162	e1443_s1372_s1370_r3108_r3109_p1373	399800	2.732E+01	1	1.464E+04
$Z \to ee + jets$	147770	e1443_s1372_s1370_r3108_r3109_p1373	9978665	1.046E+03	1	9.542E+03
$Z \to \mu\mu + jets$	147771	e1443_s1372_s1370_r3108_r3109_p1373	9985488	1.045E+03	1	9.554E+03
WZ	128811	e950_s1310_s1300_r3043_r2993_p1373	299950	3.616E-01	1	8.294E+05
$t\bar{t}$	109345	e961_s1310_s1300_r3043_r2993_p1373	499948	1.452E+02	0.0817	4.214E+04

Table 4.6: Simulated background samples at $\sqrt{s} = 7\,\text{TeV}$, where N is the number of events, σ_{gen} is the cross-section returned by the MC generator, $\varepsilon_{\text{filt}}$ is the generator filter efficiency and the equivalent luminosity is computed as $N_{\text{evts}}/(\sigma_{\text{gen}}\varepsilon_{\text{filt}})$.

list of the simulated 8 TeV background samples used in this analysis is provided in Table 4.8.

All of these MC samples were skimmed in the same way as data and it was verified that this skimming selection is looser than the selection applied offline - all selected signal or $Z\gamma$ background events passing the final selection criteria would also pass the skimming criteria.

4.2.1.3 Corrections applied to MC Samples

Events from MC samples were selected using the same criteria applied to data, apart from the data quality requirements which were not applicable. However, several corrections were applied to the MC samples only, in order to help them better describe the recorded data.

The MC samples were reweighted according to the average number of interactions per bunch crossing, in order to match the distribution observed in data [104]. This process also takes into account the actual luminosity fraction of the various data periods relative to the total luminosity. The MC samples were produced with a beamspot width in z of 6.6 cm and were weighted to have z of 4.8 cm to match that observed in data. Fudge factors to correct for differences between data and simulation were applied on the shower shapes [105, 106]. The photon and electron energies were smeared by around 1% to account for the larger resolution observed using $Z \to e^+e^-$ events in data [107]. Similarly, the muon momentum scale measured in the ID and in the MS was corrected by approximately 0.1% in order to account for the larger resolution observed using $Z \to \mu^+\mu^-$ events in data [108]. The efficiencies of the lepton trigger, reconstruction, and selection requirements were measured using leptons selected from $Z \to ee$ and $Z \to \mu\mu$ decays using the tag-and-probe method, from which scale factors were obtained that corrected the MC samples to match the data selection efficiency.

For 7 TeV MC samples, scale factors provided by the e/γ group [106] for the photon identification efficiency as a function of the photon transverse energy, pseudorapidity and conversion category were applied to the selected events. The scale factors were extracted from data/MC comparisons of the photon identification efficiency measured with radiative Z decays, with a matrix method from inclusive photons, and with an extrapolation based on the distributions of the shower shape variables of electrons selected with a tag-and-probe method from $Z \to ee$.

For 8 TeV MC samples, the track impact parameters were smeared to take into account detector misalignment effects [109, 110].

4.2.2 Run 2 Monte Carlo Samples

As in Run 1, several MC signal samples were generated for use in determining a functional form for the $Z\gamma$ invariant mass distribution, for optimising the event selection criteria and for quantifying the signal efficiency of the final event selection.

Mechanism	DSID	m_H	Production tags	N	σ_{gen} [fb]	$\varepsilon_{\text{filt}}$	eq. lumi [fb^{-1}]
ggF	167480	120	e1746_s1581_s1586_r3658_r3549_p1344	99998	2.3384	1	4.276e+04
	167481	125	e1746_s1581_s1586_r3658_r3549_p1344	99999	2.9970	1	3.337e+04
	167482	130	e1746_s1581_s1586_r3658_r3549_p1344	99999	3.5152	1	2.845e+04
	167484	135	e1746_s1581_s1586_r3658_r3549_p1344	99999	3.7986	1	2.633e+04
	167485	140	e1746_s1581_s1586_r3658_r3549_p1344	99998	3.8153	1	2.621e+04
	167486	145	e1746_s1581_s1586_r3658_r3549_p1344	100000	3.6216	1	2.761e+04
	167487	150	e1746_s1581_s1586_r3658_r3549_p1344	99999	3.1610	1	3.163e+04
VBF	167490	120	e1746_s1581_s1586_r3658_r3549_p1344	99799	0.1849	1	5.399e+05
	167491	125	e1746_s1581_s1586_r3658_r3549_p1344	99900	0.2454	1	4.071e+05
	167492	130	e1746_s1581_s1586_r3658_r3549_p1344	99999	0.2976	1	3.361e+05
	167494	135	e1746_s1581_s1586_r3658_r3549_p1344	100000	0.3320	1	3.013e+05
	167495	140	e1746_s1581_s1586_r3658_r3549_p1344	99997	0.3437	1	2.910e+05
	167496	145	e1746_s1581_s1586_r3658_r3549_p1344	99500	0.3339	1	2.980e+05
	167497	150	e1746_s1581_s1586_r3658_r3549_p1344	98999	0.2986	1	3.315e+05
WH	167500	120	e1978_s1581_s1586_r3658_r3549_p1344	30000	0.0903	1	3.324e+05
	167501	125	e1978_s1581_s1586_r3658_r3549_p1344	30000	0.1096	1	2.738e+05
	167502	130	e1978_s1581_s1586_r3658_r3549_p1344	30000	0.1215	1	2.469e+05
	167504	135	e1978_s1581_s1586_r3658_r3549_p1344	30000	0.1242	1	2.416e+05
	167505	140	e1978_s1581_s1586_r3658_r3549_p1344	30000	0.1180	1	2.543e+05
	167506	145	e1978_s1581_s1586_r3658_r3549_p1344	29999	0.1056	1	2.841e+05
	167507	150	e1978_s1581_s1586_r3658_r3549_p1344	30000	0.0870	1	3.449e+05
ZH	167508	120	e1978_s1581_s1586_r3658_r3549_p1344	30000	0.0528	0.09993	5.686e+06
	167509	125	e1978_s1581_s1586_r3658_r3549_p1344	30000	0.0646	0.10133	4.584e+06
	167510	130	e1978_s1581_s1586_r3658_r3549_p1344	30000	0.0723	0.10045	4.131e+06
	167512	135	e1978_s1581_s1586_r3658_r3549_p1344	30000	0.0747	0.10133	3.963e+06
	167513	140	e1978_s1581_s1586_r3658_r3549_p1344	29999	0.0717	0.10094	4.145e+06
	167514	145	e1978_s1581_s1586_r3658_r3549_p1344	30000	0.0647	0.10069	4.606e+06
	167515	150	e1978_s1581_s1586_r3658_r3549_p1344	30000	0.0538	0.10018	5.562e+06
$t\bar{t}$	167550	120	e1978_s1581_s1586_r3658_r3549_p1344	30000	0.0164	1	1.834e+06
	167551	120	e1978_s1581_s1586_r3658_r3549_p1344	30000	0.0201	1	1.492e+06
	167552	120	e1978_s1581_s1586_r3658_r3549_p1344	30000	0.0226	1	1.326e+06
	167554	120	e1978_s1581_s1586_r3658_r3549_p1344	30000	0.0235	1	1.278e+06
	167555	120	e1978_s1581_s1586_r3658_r3549_p1344	30000	0.0226	1	1.325e+06
	167556	120	e1978_s1581_s1586_r3658_r3549_p1344	29998	0.0205	1	1.461e+06
	167557	120	e1978_s1581_s1586_r3658_r3549_p1344	30000	0.0172	1	1.747e+06

Table 4.7: Simulated signal samples at $\sqrt{s} = 8\,\text{TeV}$, where N is the number of events, σ_{gen} is the cross-section from Ref. [22], $\varepsilon_{\text{filt}}$ is the generator filter efficiency and the equivalent luminosity is computed as $N_{\text{evts}}/(\sigma_{\text{gen}}\varepsilon_{\text{filt}})$.

Mechanism	DSID	Production tags	N	σ_{gen} [fb]	$\varepsilon_{\text{filt}}$	eq. lumi [fb^{-1}]
$Z \to ee\gamma$	145161	e1434_s1499_s1504_r3658_r3549_p1344	3189892	3.230E+01	1	9.876E+04
$Z \to \mu\mu\gamma$	145162	e1434_s1499_s1504_r3658_r3549_p1344	3199894	3.233E+01	1	9.899E+04
$Z \to ee + jets$	147770	e1434_s1499_s1504_r3658_r3549_p1344	9999162	1.207E+03	1	8.282E+03
$Z \to \mu\mu + jets$	147771	e1434_s1499_s1504_r3658_r3549_p1344	9998983	1.207E+03	1	8.282E+03
WZ	129487	e1300_s1469_s1470_r3542_r3549_p1208_p1355	4847	6.293E-01	0.3531	2.181E+04
$t\bar{t}$	110001	e1193_s1469_s1470_r3542_r3549_p1208_p1355	873866	2.077E+02	1	4.208E+03

Table 4.8: Simulated background samples at $\sqrt{s} = 8\,\text{TeV}$, where N is the number of events, σ_{gen} is the cross-section returned by the MC generator, $\varepsilon_{\text{filt}}$ is the generator filter efficiency and the equivalent luminosity is computed as $N_{\text{evts}}/(\sigma_{\text{gen}}\varepsilon_{\text{filt}})$.

DSID	m_X [GeV]	Production tags	N
342208	200	e4217_s2608_r6869_r6282_p2397	29000
342209	300	e4217_s2608_r6869_r6282_p2397	29000
342210	500	e4217_s2608_r6869_r6282_p2397	30000
343577	700	e4735_s2726_r7326_r6282_p2464	30000
343578	750	e4735_s2726_r7326_r6282_p2464	30000
343579	800	e4735_s2726_r7326_r6282_p2464	28000
342211	1000	e4217_s2608_r6869_r6282_p2397	30000
343580	1500	e4735_s2726_r7326_r6282_p2464	30000

Table 4.9: Simulated signal samples at $\sqrt{s} = 13\,\text{TeV}$. Samples were generated for a scalar Higgs-like boson produced through gluon fusion, at masses in the range $200 \leq m_X \leq 1\,500\,\text{GeV}$ using the narrow-width approximation [119].

The simulated signal consisted of a spin-0 Higgs-like boson, X, that was produced in pp collisions through the ggF mechanism and allowed to decay into a Z boson and a photon. The Z was then forced to decay only to charged lepton pairs ($e^+e^-, \mu^+\mu^-, \tau^+\tau^-$) in equal proportions. Interference between the $gg \to X \to Z\gamma$ process and the SM background process of $Z + \gamma$ production through QCD was neglected. The X boson was generated using a fixed intrinsic width of 4.07 MeV, which is the same width as a 125 GeV SM Higgs boson and is much smaller than the resolution of the ATLAS detector. These samples are described as using the narrow width approximation (NWA).

The signal samples were generated using the MC15a settings [111] with POWHEG-BOX [112, 113] interfaced with PYTHIA8 for the underlying event, parton showering and hadronisation. Proton collisions were simulated using a centre-of-mass pp collision energy of 13 TeV and a proton bunch separation of 25 ns. The CT10 [79] PDF set and the AZNLO tune [114] of the underlying event were used. Multiple pp collisions in the same and neighbouring bunch crossings were simulated using the soft QCD processes of PYTHIA 8.186 using the A2 tune [115] and MSTW2008LO PDF set [116], in order to accurately describe the conditions in which real data is acquired. Once the events were generated, they were passed through a detailed GEANT4 [117] model of the ATLAS detector [118] in order to simulate its response. The events were then reconstructed using the same software releases and algorithms that are applied to the collision data.

Several signal samples were generated at various mass points between 200 and 1 500 GeV. Signal samples at higher masses were also generated, but no $m_{\ell\ell\gamma}$ candidates were found in data with an invariant mass greater than 1.5 TeV and so the analysis was limited to this mass range only. Table 4.9 shows the dataset ID number (DSID), mass point, generation and reconstruction tags, and the number of events for each signal sample used in this analysis.

4.2.2.1 Corrections applied to MC Samples

As with the Run 1 MC samples, several corrections were applied to the generated Run 2 MC samples in order to help them better describe the recorded data. The vast majority of the corrections discussed in Section 4.2.1.3 remain applicable in Run 2, but updated values were derived to reflect the changes in ATLAS, the LHC, and the new operating conditions. The MC samples were reweighted according to the average number of interactions per bunch crossing, in order to match the distribution observed in data [120], and also to match the beamspot width observed in data. Fudge factors to correct for differences between data and simulation were applied on the shower shapes [121]. The photon and electron energies were smeared to account for the larger resolution observed in data [122]. The muon momentum scale measured in the ID and in the MS was corrected in order to account for discrepancies observed using $Z \to \mu^+\mu^-$ events in data [123]. The efficiencies of the lepton trigger, reconstruction, and selection requirements were measured using leptons selected from $Z \to ee$ and $Z \to \mu\mu$ decays using the tag-and-probe method, from which scale factors were obtained that corrected the MC samples to match the data selection efficiency [123, 124]. A series of scale factors for the photon identification efficiency as a function of the photon transverse energy, pseudorapidity and conversion category were applied to the selected events [125].

Chapter 5

Object Reconstruction

Once the ATLAS detector records a collision event, it is necessary to reconstruct all of the decay products from the detector response. The process begins by reconstructing the trajectories, or tracks, of charged particles in the inner detector, as outlined in Section 5.1. Section 5.2 describes how the points of origin of those tracks are then used to identify the main collision points. The reconstruction of electrons and photons is outlined in Section 5.3, which proceeds by identifying deposits of energy in the electromagnetic calorimeter and attempting to associate them with tracks from the inner detector (ID). The specific selection criteria imposed on photons and electrons used for the analyses presented in this thesis are described in detail in Sections 5.3.1 and 5.3.2, respectively. The reconstruction of muons is outlined in Section 5.4, and proceeds primarily through the matching of tracks recorded in the muon spectrometer to tracks found in the ID. During the Run 1 $H \to Z\gamma$ analysis, an attempt was made to identify SM Higgs boson candidates produced through the VBF mechanism (see Section 6.3). Such events are characterised by the presence of two hadronic jets located in the forward detector regions, which are reconstructed following the procedure outlined in Section 5.5. A visualisation of the signals produced by all of these various objects is presented in Figure 5.1.

The different algorithms used in these processes can result in the reconstruction of multiple objects from the same tracks and energy deposits. Any ambiguities are resolved by applying an overlap removal, as described in Section 5.6. Finally, Section 5.7 describes the reconstruction of Z bosons from the combination of two same-flavour, opposite-sign leptons, in preparation for use in the $H \to Z\gamma$ and $X \to Z\gamma$ analyses.

5.1 Track Reconstruction

When a charged particle passes through the ID, it interacts with the active sensors to produce a series of hits in the subdetectors. These hits are transformed into three-dimensional space coordinates, termed SpacePoints, which are then used to reconstruct the track describing the trajectory of the particle. Since the ID is immersed in a solenoidal magnetic field, the charged particle will follow a curved trajectory that enables the charge to be determined and facilitates the reconstruction of the momentum three-vector. The high beam luminosity produces multiple interactions per bunch crossing, which results in many hits that require resolving into tracks.

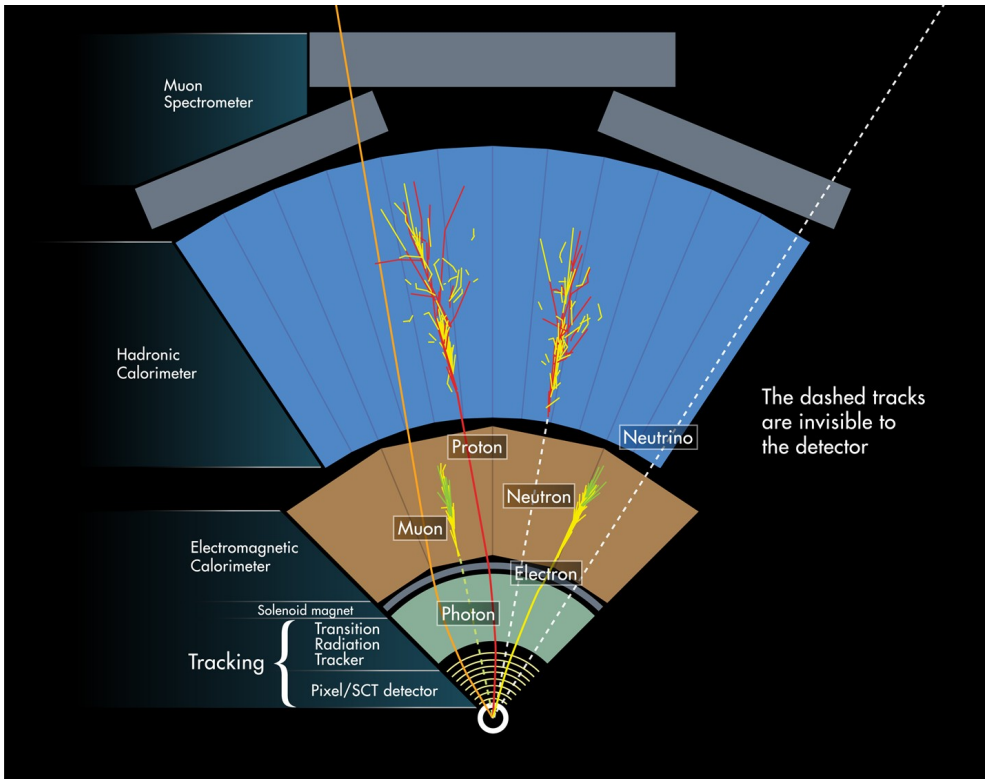

Figure 5.1: Visualisation of the signal left by particles in the various ATLAS subdetectors [126].

It should be noted that the particles will also interact with the inactive material in the ID that was necessary for the physical construction and operation of the detector. Multiple scattering can occur which will cause deviations in the particle trajectory, while ionisation and bremsstrahlung can cause the particle to lose energy, and these effects must be accounted for during the reconstruction.

Two complementary algorithms are used to reconstruct tracks from the set of SpacePoints in an event: one starts from the centre of the ID and works outwards (*inside-out*) while the other starts in the TRT and works inwards (*outside-in*) [127–129].

The inside-out algorithm [130] is used to identify primary particles that were either produced directly in pp interactions and had a mean lifetime longer than 0.03 ns, or that were produced from the decays or interactions of particles with a mean lifetime shorter than 0.03 ns. Pairs of SpacePoints from the pixel detector are used to make a preliminary identification of the pp interaction points, which in turn allow the formation of seed tracks comprising three or more hits. A combinatorial Kalman filter is then used to add successive hits to the track and extend it out towards the TRT. For each new hit that could be a part of the track, the momentum of the particle needed to produce such a revised track is evaluated and if it is compatible with the momentum of the existing track then the hit is added to it. The inside-out algorithm only examines tracks with $p_{\mathrm{T}} > 400\,\mathrm{MeV}$, in order to reduce the algorithm processing time and keep the number of tracks at a manageable level. Many of the reconstructed tracks will be fakes, with the majority of the SpacePoints they contain coming from two or more

different particles. An iterative procedure termed ambiguity resolution is applied to reject fake tracks before they are extended from the SCT into the TRT. All tracks are ranked using a scoring strategy based on criteria such as the number and location of hits on the track candidates, or the presence of holes where hits were expected but not observed. Tracks with a score that falls below a certain threshold are discarded, and the remaining tracks are then refitted to ensure that all hits remain assigned to tracks. These refitted tracks are scored again, and the process repeats until all ambiguities are resolved. The tracks are then extended into the TRT by adding TRT hits that are compatible with the track. Any hits that do not fulfil the basic quality requirements are considered outliers and discarded from the fit.

Secondary particles arising from decay vertices that were displaced along the z axis, such as kaon decays, or resulting from photon conversions may have few or no hits in the silicon detectors. Consequently, they will not be efficiently identified and reconstructed by the inside-out algorithm and so an alternative outside-in algorithm is preferred [130]. Track segments are reconstructed in the TRT using pattern recognition algorithms, and these are then extended backwards into the silicon detectors by sequentially adding hits. In order to avoid double-counting of tracks, the TRT segments are required to have no association with tracks identified by the inside-out algorithm. If no SCT or pixel hits are found matching the track segment, a TRT-only track is recorded.

5.2 Vertex Reconstruction

Following the reconstruction of charged particle tracks, a vertex finding algorithm [131] is used to identify the primary vertices at which the initial pp interactions took place. The algorithm begins by extrapolating all tracks with $p_{\mathrm{T}} > 400\,\mathrm{MeV}$ to the beam line and searching for coordinates with multiple tracks clustered around them, which are then used as vertex seeds. Each vertex seed and the tracks surrounding it are used as inputs to an iterative χ^2 fitting algorithm that progressively lowers the weight of outlying tracks and refits the vertex coordinate. Tracks found to be more than 7σ from the vertex are removed and used to provide new vertex seeds. Each event is usually found to contain multiple primary vertices, which are then ranked according to the sum of p_{T}^2 of all tracks associated with that vertex. The chosen primary vertex in any event is the one for which this value is a maximum and that also has five or more tracks associated with it.

5.3 e/γ Reconstruction

The reconstruction of e/γ objects is performed by taking energy deposits from the electromagnetic calorimeter and attempting to match them to tracks recorded in the ID [132, 133]. The process is designed to separate electrons, unconverted photons, and converted photons (produced when photons interact with the detector material to create electron-positron pairs).

The electromagnetic calorimeter is divided into a grid of $N_\eta \times N_\phi = 200 \times 256$ towers in $\eta - \phi$ space. Each tower is of size $\Delta\eta^{\text{tower}} \times \Delta\phi^{\text{tower}} = 0.025 \times 0.025$, corresponding to the granularity of the middle layer of the electromagnetic calorimeter. The energy of each tower is evaluated from the sum of the energy in cells in the front, middle and back longitudinal calorimeter layers. This summation also includes the energy recorded by the presampler detector if $|\eta| < 1.8$. Clusters of energy are then reconstructed from seeds that were found using a sliding-window algorithm [134] searching for longitudinal towers with $E_{\text{T}} > 2.5\,\text{GeV}$ in windows of size 3×5 towers.

Tracks with $p_{\text{T}} > 0.5\,\text{GeV}$ are then extrapolated from their last measured coordinate in the ID to identify the point where they impact the middle layer of the electromagnetic calorimeter. The η and ϕ coordinates of this impact point are then compared to the positions of seed clusters within that middle layer. A track is considered matched to the cluster if the distance between the track impact point and the cluster barycentre is $|\Delta\eta| < 0.05$. In order to account for energy losses due to bremsstrahlung, the $\Delta\phi$ track cluster matching window is 0.1 on the side where the extrapolated track is bent due to having travelled through the solenoidal magnetic field. In the event of multiple tracks being matched to a single cluster, tracks with hits in the Pixel detector or SCT are preferred and the match with the smallest ΔR is kept. ID tracks that are matched to an electron candidate and (in the 8 and 13 TeV data sets only [135]) tracks from converted photon candidates with at least four associated hits in the silicon detectors are fitted using a Gaussian-Sum filter [136] to account for bremsstrahlung energy losses.

A cluster with a matching ID track is identified as an electron candidate, a cluster without a matching track or conversion vertex is identified as an unconverted photon candidate, and a cluster with a matching vertex reconstructed from one or two tracks is identified as a converted photon candidate. The final cluster is then built using a cluster window of size 3×7 (5×5) towers in the barrel (end-cap) of the calorimeter. The total energy of the cluster is evaluated as the sum of the energy deposited in the calorimeter cluster, the estimated energy deposited in the ID, the estimated energy deposited around the cluster (termed lateral leakage), and the estimated energy deposited outside the cluster in the hadronic calorimeter (hadronic leakage). Note that the energies of the clusters are calibrated separately for electrons, unconverted and converted photon candidates, in order to account for energy losses upstream of the calorimeter and for energy leakage outside of the cluster. The measured energy of converted photons also receives corrections as a function of the conversion radius, which is the distance from the beamline where the photon decays to an electron-positron pair and is evaluated through dedicated MC studies. Electron candidates are then constructed by combining the energy from the cluster with the direction parameters from the associated track.

5.3.1 Photon Selection

Photon candidates reconstructed near regions of the calorimeter affected by read-out or high-voltage failures were rejected. Photons were required to be located at $|\eta| <$

2.37, excluding the transition region between barrel and end-cap LAr calorimeters at $1.37 < |\eta| < 1.52$. This is done to exploit fine segmentation of the first layer of the electromagnetic calorimeter to discriminate between genuine prompt photons and fake photons within jets.

For Run 1, photons were required to have a transverse energy of $E_{\mathrm{T}} > 15\,\mathrm{GeV}$. For Run 2, it was required that the photons satisfy a looser cut of $E_{\mathrm{T}} > 10\,\mathrm{GeV}$, which was subsequently tightened following the $m_{\ell\ell\gamma}$ candidate reconstruction with a selection on the relative photon p_{T} as described in Section 7.2. Figure 5.2 shows the distribution of the photon transverse energy in selected 8 TeV events with an $ee\gamma$ final state.

Photon identification was then performed to help reject fake photons arising from the rapid decay of hadronic particles (typically neutral pions) into pairs of collimated photons. This cut-based selection criteria is based on the transverse shower shapes measured in the first two layers of the electromagnetic calorimeter, exploiting the fine segmentation of the first layer, and also on the energy leakage into the hadronic calorimeter. The criteria have a dependence on the pseudorapidity of the photon, in order to account for the geometry of the electromagnetic calorimeter and the variation in the total thickness of material in the ID. Two official sets of selection criteria are defined. The "loose" selection was harmonised with the corresponding electron selection criteria and used in triggering. The "tight" selection criteria were separately optimised for converted and unconverted photons to give an identification efficiency of 85% for photons with $E_{\mathrm{T}} > 40\,\mathrm{GeV}$ [106]. Photons in the Run 1 analysis were required to satisfy the tight identification criteria. For the analysis of Run 2 samples, photons were initially required to pass the "loose" identification criteria to permit additional studies on the composition of backgrounds; the tight identification criteria was subsequently imposed for the final event selection.

For the Run 1 analysis, it was required at this stage that the photons be isolated from hadronic activity [137, 138]. The isolation energy, $E_{\mathrm{T}}^{\mathrm{iso}}$, was computed from the sum of the positive-energy topological clusters with reconstructed barycentres inside a cone of radius $\Delta R = 0.4$ around the photon candidate. In order to suppress noise, these so-called topoclusters only include cells containing a significant energy deposit and their neighbouring cells. The cells within a region of 0.125×0.175 in $\eta \times \phi$ around the photon barycentre were excluded, in order to remove the energy of the photon candidate itself. The mean value of the photon energy leaking outside this region is evaluated as a function of the photon transverse energy and subtracted from $E_{\mathrm{T}}^{\mathrm{iso}}$. The ambient energy from the underlying event and from pileup was computed for each event from the transverse energy density of low-p_{T} jets as described in [139, 140], and subtracted from $E_{\mathrm{T}}^{\mathrm{iso}}$. Photons were considered to be isolated if the value of $E_{\mathrm{T}}^{\mathrm{iso}}$, after all of these corrections, was less than 4 GeV.

For the Run 2 analysis, as with the choice of identification criteria, the isolation requirement was not imposed at this stage but was required in the final analysis (see Section 7.2 for details).

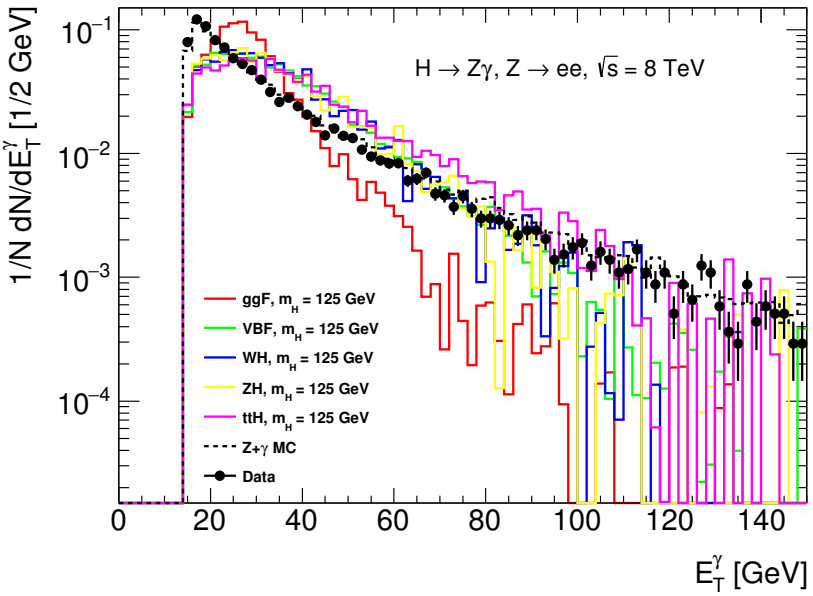

Figure 5.2: Distribution of the photon E_{T} in signal events (for a Higgs boson of mass 125 GeV) from the five considered production processes, in background events selected from a simulated sample of $Z\gamma$ events, and in data. Events with an $ee\gamma$ final state were selected from 8 TeV samples and data sets. Events with a $\mu\mu\gamma$ final state show a similar distribution.

Run 1	Run 2
$\lvert\eta\rvert < 1.37$ OR $1.52 < \lvert\eta\rvert < 2.37$	
$E_{\mathrm{T}} > 15\,\mathrm{GeV}$	
Tight ID	Loose ID (Tight ID applied later)
Corrected topological isolation (in cone of radius $\Delta R = 0.4$) $< 4\,\mathrm{GeV}$	No Isolation (applied later)

Table 5.1: Summary of photon selection criteria in Run 1 and Run 2.

The complete photon selection criteria for both Run 1 and Run 2 are summarised in Table 5.1.

5.3.2 Electron Selection

Electron candidates reconstructed near regions of the calorimeter affected by read-out or high-voltage failures were rejected. Electrons were required to be located at $|\eta| < 2.47$, excluding the transition region between barrel and end-cap LAr calorimeters at $1.37 < |\eta| < 1.52$. As with photons, this was done in order to exploit the fine segmentation of the first layer of the electromagnetic calorimeter and provide discrimination between electrons and jets. All electron candidates were required to have a transverse momentum of $p_{\mathrm{T}} > 10\,\mathrm{GeV}$.

For the Run 1 analysis, it was required that the electrons satisfy a set of cut-based selection criteria termed the "Loose" working point. The selection was based on the

Run 1	Run 2
$\|\eta\| < 1.37$ OR $1.52 < \|\eta\| < 2.37$	
$p_{\mathrm{T}} > 10\,\mathrm{GeV}$	
well reconstructed track	Pass medium ID
Loose++ cluster ID	
Hit in b-layer when expected	
$z_0 < 10\,\mathrm{mm}$	$\|d_0/\sigma(d_0)\| < 6.5$ $\|z_0 \sin\theta\| < 0.5\,\mathrm{mm}$
No isolation applied	Loose track and calorimeter isolation

Table 5.2: Summary of electron selection criteria in Run 1 and Run 2.

transverse shower shapes measured in the first two layers of the electromagnetic calorimeter, the energy leakage into the hadronic calorimeter, the quality of the electron track and also the quality of the matching between the track and the associated calorimeter cluster [132, 141]. The electron track was also required to have a hit in the *b*-layer (the innermost layer of the pixel detector) if the track passed through an active *b*-layer module, which helps reject fake electrons arising from photon conversions, and to have a longitudinal impact parameter $|z_0| < 10\,\mathrm{mm}$.

For the Run 2 analysis, a likelihood-based identification criteria was used to suppress the background due to hadronic jets. The likelihood was evaluated using the longitudinal and transverse shower shapes observed in the electromagnetic calorimeter, measures of the track quality and track-cluster matching quality, and the transition radiation recorded in the TRT [74]. Note that these requirements are tuned to give approximately 85% identification efficiency for electrons with $p_{\mathrm{T}} = 20\,\mathrm{GeV}$ in what is known as the "medium" working point [5]. In order to suppress secondary leptons from the decay chains of heavy-flavour hadrons, electrons were required to have a transverse impact parameter significance $|d_0/\sigma(d_0)| < 6.5$ and longitudinal impact parameter $|z_0 \sin\theta| < 0.5\,\mathrm{mm}$. The electron impact parameter is affected by bremsstrahlung and therefore has a broader distribution than for muons.

A "loose" set of track and calorimeter isolation requirements were then applied to further suppress the background due to hadronic jets. Selections were applied on $E_{\mathrm{T}}^{\mathrm{iso}}$ in a cone of radius $\Delta R = 0.2$ and also on the sum of the transverse momentum of tracks (excluding the track for the electron itself) inside a variable-size cone around the electron of radius $\Delta R = 0.2$ for electrons with $p_{\mathrm{T}} < 50\,\mathrm{GeV}$, and of radius $\Delta R = (10\,\mathrm{GeV})/p_{\mathrm{T}}$ for electrons with $p_{\mathrm{T}} > 50\,\mathrm{GeV}$. The chosen selection requirements follow official recommendations and are tuned to have an efficiency of 99% irrespective of the electron p_{T}.

The electron selection criteria for both Run 1 and Run 2 are summarised in Table 5.2.

5.4 Muon Reconstruction

The ATLAS detector uses several different reconstruction criteria to identify four main "types" of muon, termed Stand-alone (SA), Combined (CB), Segment Tagged (ST) and Calorimeter Tagged (CT) muons [142, 143].

An SA muon is identified through the reconstruction of a track solely within the muon spectrometer. This track is extrapolated back to the interaction point while taking into account the effects of multiple scattering and energy loss in the material the muon had passed through. A track measurement is generally only possible if the muon travelled through at least two layers of MS chambers. However, in order to increase the purity of the tracks, hits are required in all three muon stations that the muon is expected to have passed through. SA muons are primarily used in order to extend coverage from the limit of the inner detector at $|\eta| = 2.5$ up to the geometrical limits of the MS acceptance at $|\eta| = 2.7$.

A CB muon is identified by successfully combining an MS track with an ID track, where both tracks were independently reconstructed. The inner detector measurement provides additional information about the impact parameter of the muon trajectory with respect to the primary vertex.

An ST muon is identified if a track in the ID can be extrapolated to the MS and associated with one or more track segments in the MDT or CSC chambers. This process is generally used for muons with low p_{T}, or that were located in a region with reduced MS acceptance and only crossed one layer of MS chambers.

A CT muon is identified from a trajectory in the ID if the associated energy deposits in the calorimeter is compatible with the hypothesis of a minimum ionising particle. Muons reconstructed in this way have the lowest purity, but are useful in recovering acceptance in the region $|\eta| < 0.1$ where there are no muon chambers to provide full tracking (as described in Section 3.2.4).

The lack of muon chambers around $\eta \approx 0$ also affects the reconstruction of tracks and, consequently, SA and CB muons. The reconstruction of tracks was further impacted in Run 1 by the fact that not all of the muon chambers were installed, and muons could only traverse one layer of chambers in some ϕ regions at $1.1 < |\eta| < 1.3$. This was corrected during the extended shutdown between Run 1 and Run 2 when the missing chambers were finally installed.

For Run 1, the reconstruction of SA, CB and ST muons was performed using two independent software packages, termed chains, for redundancy and robustness [60]. Chain 1 utilised the STACO algorithm to perform a statistical combination of the track parameters of the SA and ID muon tracks using the corresponding covariance matrices [144]. Chain 2 used the MuID algorithm to perform a global refit of the muon track using the hits from both the ID and muon spectrometer sub-detectors [145]. A third chain, combining the best features of the STACO and MuID algorithms, was developed during Run 1 for use as the sole muon reconstruction algorithm in Run 2.

The Run 1 $H \to Z\gamma$ analysis used SA, CB, and ST muons identified using the STACO algorithm (collectively termed STACO muons), and CT muons. The STACO and CT muons were required to pass slightly different sets of hit requirements. The hit requirements were slightly different for the 7 and 8 TeV datasets in order to remove some inconsistencies in the old guidelines for CT muon selection, to fix a problem in 8 TeV data where the status of pixel sensors was not propagated to the offline reconstruction, and to correct for the fact that ID efficiency varied over η. It must also be noted that the TRT hit requirements depend on both the number of TRT hits used to reconstruct the track and also the number of outlier TRT hits located in the vicinity of the track but not used in the reconstruction.

For the Run 1 analysis, all STACO muons were required to have a transverse momentum of $p_{\mathrm{T}} > 10\,\mathrm{GeV}$, while CT muons were selected with $p_{\mathrm{T}} > 15\,\mathrm{GeV}$ to increase their purity. CB and ST muons were required to have $|\eta| < 2.7$, while SA and CT muons were only used in the regions $2.5 < |\eta| < 2.7$ and $|\eta| < 0.1$. STACO muons were identified using a "tight" set of quality cuts as described in Ref. [146]. All CB muon candidates satisfied the requirements, but only ST candidates with at least three TGC ϕ hits or at least two tagging segments passed this selection.

A series of cuts based on the ID track requirements were then applied to help reject background muons, which are mainly due to the production of muons through pion or kaon decays, or from particle showers leaking out of the electromagnetic calorimeter and forming tracks in the muon spectrometer. Three working points are defined, termed loose, medium and tight: the loose working point includes all muon types and requires them to have an isolated track; the medium working point uses CB and ST muons only, requiring them to have isolated tracks and imposing a cut on E_{T} to select high energy muons; the tight working point tightens the isolation requirements. SA muons are not affected by these cuts, since they have no corresponding ID track.

The ID track associated to CB, ST and CT muons also had to have a transverse (longitudinal) impact parameter d_0 (z_0), with respect to the primary vertex, less than 1 mm (10 mm). A summary of the ID hit requirements for STACO and CT muons are presented in Tables 5.3 and 5.4, respectively.

For the Run 2 analysis, the muon reconstruction process was simplified for users with the merging of all four muon types into a single "muon" category. Muons with $|\eta| < 2.5$ were reconstructed by combining ID and MS tracks with consistent trajectories and curvatures but, as in Run1, the acceptance was extended to include the region $2.5 < |\eta| < 2.7$ by using muons reconstructed only in the MS. A summary of the ID hit requirements is presented in Table 5.5. All muon candidates were required to have a transverse momentum greater than 10 GeV. A set of quality requirements termed the "medium" identification criteria were then imposed to help reject background muons from pion or kaon decays, and also misreconstructed hadrons from jets. A series of cuts were made on the number of hits in the muon spectrometer and, for muons located in the region $|\eta| < 2.5$, on the compatibility between the ID and MS momentum measurements. The requirements are tuned to give approximately 97%

	8 TeV
ID Si hit requirement	No. of pixel hits + No. of crossed dead pixel sensors > 0 No. of SCT hits + No. of crossed dead SCT sensors > 4 No. of pixel holes + No. of SCT holes < 3
TRT hit requirement	if $(0.1 < \lvert\eta\rvert \leq 1.9)$ require (Hits + Outliers > 5) AND $\left(\frac{\text{Outliers}}{\text{Hits+Outliers}} < 0.9\right)$
	7 TeV
ID Si hit requirement	expectBLayerHit=false or numberOfBLayerHits ≥ 1 No. of pixel hits + No. of crossed dead pixel sensors > 1 No. of SCT hits + No. of crossed dead SCT sensors > 5 No. of pixel holes + No. of SCT holes < 3
TRT hit requirement	if $(\lvert\eta\rvert < 1.9)$ require (Hits + Outliers > 5) AND $\left(\frac{\text{Outliers}}{\text{Hits+Outliers}} < 0.9\right)$ if $((\lvert\eta\rvert \geq 1.9)$ AND (Hits + Outliers $> 5))$ require $\left(\frac{\text{Outliers}}{\text{Hits+Outliers}} < 0.9\right)$

Table 5.3: List of Run 1 ID hit requirements for muon tracks reconstructed using the STACO algorithm.

	8 TeV
ID Si hit requirement	No. of pixel hits + No. of crossed dead pixel sensors > 0 No. of SCT hits + No. of crossed dead SCT sensors > 4 No. of pixel holes + No. of SCT holes < 3
	7 TeV
ID Si hit requirement	expectBLayerHit=false or numberOfBLayerHits ≥ 1 No. of pixel hits + No. of crossed dead pixel sensors > 1 No. of SCT hits + No. of crossed dead SCT sensors > 5 No. of pixel holes + No. of SCT holes < 3
TRT hit requirement	(Hits + Outliers < 6) OR $\left(\frac{\text{Outliers}}{\text{Hits+Outliers}} < 0.9\right)$

Table 5.4: List of Run 1 ID hit requirements for CT muon tracks.

	13 TeV
ID Si hit requirement	No. of pixel hits + No. of crossed dead pixel sensors > 0 No. of SCT hits + No. of crossed dead SCT sensors > 4 No. of pixel holes + No. of SCT holes < 3
TRT hit requirement	if $(0.1 < \lvert\eta\rvert \leq 1.9)$ require (Hits + Outliers > 5) AND $\left(\frac{\text{Outliers}}{\text{Hits+Outliers}} < 0.9\right)$

Table 5.5: List of Run 2 ID hit requirements for muon tracks.

Run 1	Run 2
Hit requirements for STACO & CT muons	Hit requirements for all muons except SA
STACO $p_{\mathrm{T}} > 10$ GeV CT $p_{\mathrm{T}} > 15$ GeV	All Muons have $p_{\mathrm{T}} > 10\,\mathrm{GeV}$
CB, ST Muons with $\lvert\eta\rvert < 2.7$ CT Muons with $\lvert\eta\rvert < 0.1$	Muons from ID+MS tracks at $\lvert\eta\rvert < 2.5$
SA Muons with $2.5 < \lvert\eta\rvert < 2.7$	SA have $2.5 < \lvert\eta\rvert < 2.7$
STACO muons pass Tight ID	Medium ID
STACO muons have $d_0 < 1\,\mathrm{mm}$, $z_0 < 10\,\mathrm{mm}$	$d_0/\sigma(d_0) < 3.5$, $z_0 \sin\theta < 0.5\,\mathrm{mm}$
Isolation	GradientLoose Track+CaloIsolation

Table 5.6: Summary of muon selection criteria in Run 1 and Run 2.

identification efficiency for muons with $p_{\mathrm{T}} > 10\,\mathrm{GeV}$ [147]. In order to suppress secondary leptons from the decay chains of heavy-flavour hadrons, muons were required to have a transverse impact parameter significance $|d_0/\sigma(d_0)| < 3.5$ and longitudinal impact parameter $|z_0 \sin\theta| < 0.5\,\mathrm{mm}$ [120].

A set of track and calorimeter isolation requirements termed "GradientLoose" was then applied to further suppress the background due to hadronic jets. Selections were applied on $E_{\mathrm{T}}^{\mathrm{iso}}$ in a cone of radius $\Delta R = 0.2$ and also on the sum of the transverse momentum of tracks (excluding the track for the muon itself) inside a cone of radius $\Delta R = 0.3$ for muons with $p_{\mathrm{T}} < 33\,\mathrm{GeV}$, and of radius $\Delta R = (10\ \ \mathrm{GeV})/p_{\mathrm{T}}$ for muons with $p_{\mathrm{T}} > 33\,\mathrm{GeV}$. The chosen selection requirements follow official recommendations and are tuned to have an efficiency that increases with transverse momentum, ranging from 95% for $p_{\mathrm{T}} = 25\,\mathrm{GeV}$ to 99% for $p_{\mathrm{T}} = 60\,\mathrm{GeV}$ [120].

Muons can also appear in the detector from cosmic rays or from beam backgrounds, but these have different timing characteristics from muons produced through pp interactions and should be excluded by the trigger requirements.

The muon selection criteria for both Run 1 and Run 2 are summarised in Table 5.6.

5.5 Jet Reconstruction

Jets are collections of objects that are usually formed through the hadronisation of quarks or gluons, and appear within a conical region originating from the interaction point. Within this thesis, they have been used exclusively in the Run 1 $H \to Z\gamma$ analysis in an attempt to identify events where an SM Higgs boson was produced through the VBF mechanism (see Section 6.3).

The process of jet reconstruction commenced with the formation of topoclusters, which are identified by searching for groups of neighbouring cells in the hadronic calorimeter with significant energy deposits above the background noise [148]. These topoclusters were then used as inputs to a jet finding algorithm - while many exist, the standard one used by the ATLAS Collaboration is the anti-k_t algorithm [149]. This particular algorithm iterates over a set of topocluster objects to evaluate the separation d_{ij} for all pairs of objects i, j, as well as the distance measure d_i of each object i

from the beamline:

$$d_{i,j} = \min\left(\frac{1}{k_{t,i}^2}, \frac{1}{k_{t,j}^2}\right)\frac{\Delta R_{ij}^2}{R^2}, \tag{5.1}$$

$$d_i = \frac{1}{k_{t,i}^2}, \tag{5.2}$$

where $k_{t,i}$ is the transverse momentum of the ith object and R is an input distance parameter that is typically 0.4 or 0.6; within this analysis a value of $R = 0.4$ is used. If $d_{ij} < d_i$, then the two objects i and j are merged into a single object in the list. The process is then repeated until the condition $d_i < d_{ij}$ is satisfied, at which point the object has been fully reconstructed as a jet and is removed from the list. The algorithm then continues until all identified topoclusters have been either recognised as jets or merged into jets. If a high-p_{T} (hard) object has no other hard object within a cone of radius $2R$, then all of the low-p_{T} (soft) objects located in a cone of radius R will be merged with it. If two hard objects are located between R and $2R$ of each other, then the relative momenta of the two objects will determine the location of the boundary between them and the soft objects in this region will be assigned to the nearest hard one. In general, this algorithm will produce conical jets from separated hard objects.

Each jet identified by this algorithm was then given a correction for pile-up, a correction for the origin of the jet, a calibration for the energy and direction of the jet, and (in data only) a residual *in-situ* calibration. The jet energy received η-dependent corrections in order to account for contributions from multiple interactions within the same (in-time pileup) or preceding (out-of-time pileup) bunch crossings [150]. Jets from the 8 TeV data set were given further corrections based on the jet area (defined by the tracks associated with the jet) and the event pileup activity based on the median p_{T} density [151]. The p_{T} and η components of the jet four-vector were calibrated using the jet energy scale, which is derived from comparisons between reconstructed and truth jets in MC simulations.

The $H \to Z\gamma$ analysis required jets to have a transverse momentum of $p_{\mathrm{T}} > 20\,\mathrm{GeV}$ for $|\eta| < 2.4$, or $p_{\mathrm{T}} > 30\,\mathrm{GeV}$ for $2.4 \leq |\eta| < 4.5$. An additional selection was made on the jet vertex fraction (JVF), which is defined as the sum of the p_{T} of the tracks k associated with the jet and matched to the primary vertex, divided by the sum of the p_{T} of all tracks j associated with the jet:

$$JVF = \frac{\sum_k p_{\mathrm{T}}\left(\mathrm{track}_k^{PV}\right)}{\sum_j p_{\mathrm{T}}\left(\mathrm{track}_j\right)}. \tag{5.3}$$

The procedure serves to identify the vertex that a jet is most likely actually associated with - any jets not associated with the primary vertex are likely a result of pileup and can therefore be removed from the event. It should be noted that only tracks with $p_{\mathrm{T}} > 0.5\,\mathrm{GeV}$ are used in the calculation. The requirement for tracks recorded in the ID limits the applicability of this technique to the region $|\eta| < 2.5$, which is the limit of acceptance of the ID, although in practice the region is reduced to $|\eta| < 2.4$ in

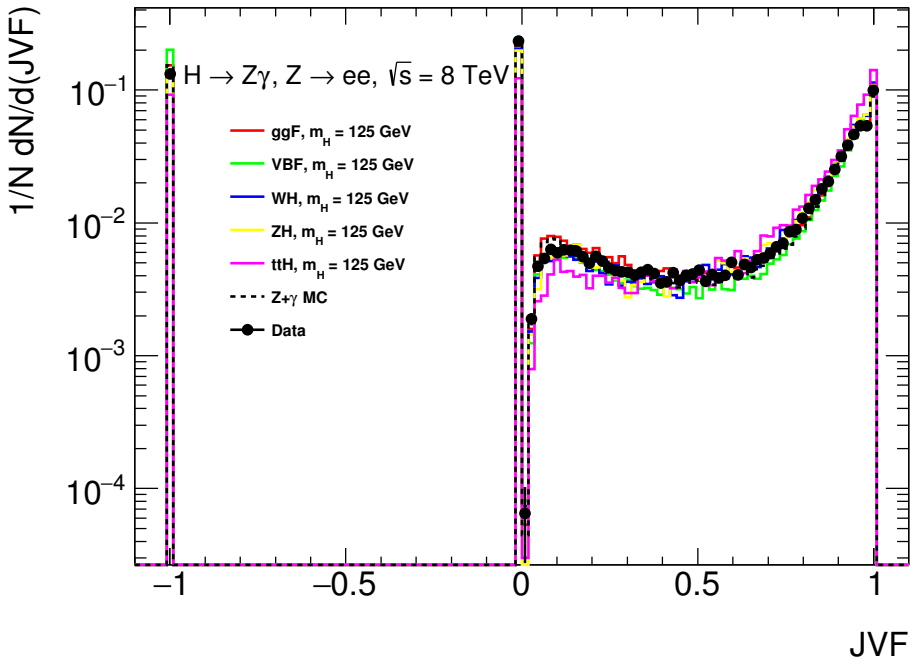

Figure 5.3: Distribution of the jet vertex fraction for selected events in 8 TeV data and MC samples. Note that $JVF = -1$ occurs if the jet falls outside of the ID tracking limits.

order to avoid signal loss when jets fall outside of the ID. For jets with $|\eta| < 2.4$ and $p_{\mathrm{T}} > 25\,\mathrm{GeV}$, it was required that $|JVF|$ was greater than 0.5 (0.25) for events in 7 (8) TeV data. The distribution of the JVF for selected events in 8 TeV data and MC samples is shown in Figure 5.3.

Jets not associated with real energy deposits in the calorimeters (instead arising from sources such as hardware problems, LHC beam conditions and cosmic-ray showers) were rejected using the "Loose Minus" criteria [152]. Further jet cleaning was applied to correct for a hot tile calorimeter cell that had not been masked in the reconstruction for certain runs.

5.6 Overlap Removal

An overlap removal was applied to resolve ambiguities when multiple objects were reconstructed from the same tracks and energy deposits. For Run 1 samples, SA muon candidates within $\Delta R < 0.2$ of a selected ST muon candidate and CT muon candidates within $\Delta R < 0.1$ of a selected STACO muon candidate were rejected in order to correct for multiple muon candidates being reconstructed from the same tracks. For Run 2, all muon candidates were combined into a single category prior to the construction of the derivation samples, and so this selection criteria did not need to be explicitly applied.

If two electron candidates had identical track parameters, only the candidate with the highest E_{T} was retained. In the analysis of 8 and 13 TeV data (because of the greater level of pileup) it was required that if two electron clusters were located within

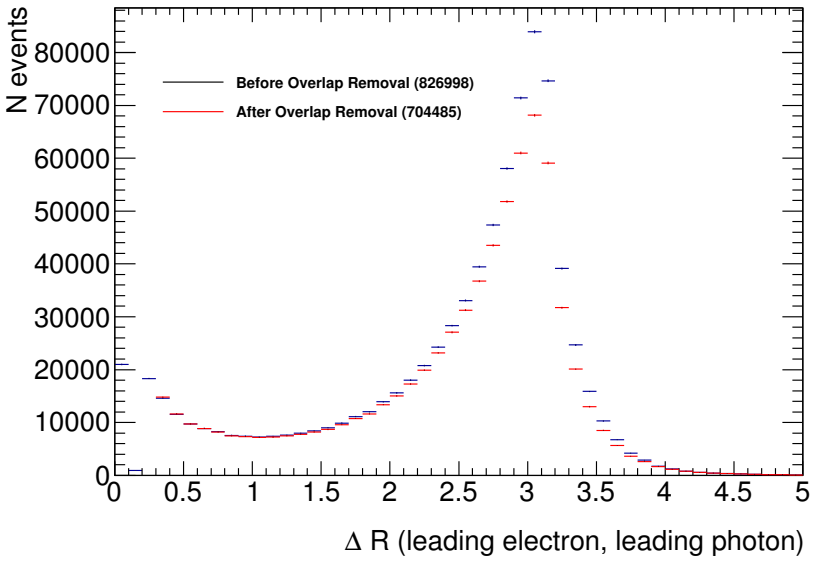

Figure 5.4: Distribution of ΔR between the leading electron and photon, before and after overlap removal, for selected events in 13 TeV MC $Z + \gamma$ events.

a window $|\Delta\eta| < 0.075$ and $|\Delta\phi| < 0.125$ of each other, then only the electron cluster with the highest E_{T} would be kept. If a track associated to an electron candidate was within $\Delta R < 0.02$ of the track associated to a muon candidate (which had passed all of the muon selection criteria), then the electron was rejected and the muon retained.

Photon candidates located within $\Delta R < 0.3$ of a selected lepton candidate were then rejected, in order to suppress the background from FSR $Z + \gamma$ events and the fake signal due to radiation of photons in $H \to \ell\ell$ decays. Finally, if a jet candidate was located within $\Delta R < 0.2$ of an electron candidate, or within $\Delta R < 0.4$ of a muon or photon candidate, then the jet was rejected.

Figure 5.4 shows an example of the effect of the overlap removal process for selected events in 13 TeV MC, illustrating the ΔR between the highest-p_{T} (leading) electron and photon before and after the application of overlap removal.

5.7 Z Boson Reconstruction

Following the selection of lepton candidates, Z boson candidates were reconstructed by making pairs of same-flavour, opposite sign leptons. The invariant mass of these candidates is denoted by $m_{\ell\ell}$ throughout this thesis. In the rare case of multiple Z candidates being identified, only the candidate with mass closest to the true Z mass was retained for further study. Trigger matching was then performed on the leptons used to construct the Z candidate, with the requirement that at least one of those leptons passed the single lepton trigger used to record the event (or both leptons, in the case of events selected by a dilepton trigger). Any events where trigger matching failed were rejected.

Further selection requirements were made on the Z boson, but since these differed between the Run 1 and Run 2 studies they have been detailed separately in Sections 6.1 and 7.2, respectively. Figure 5.5 shows example $m_{\ell\ell}$ distributions of the reconstructed Z boson invariant mass for 8 TeV events with $ee\gamma$ and $\mu\mu\gamma$ final states, after the full Run 1 selection criteria were applied.

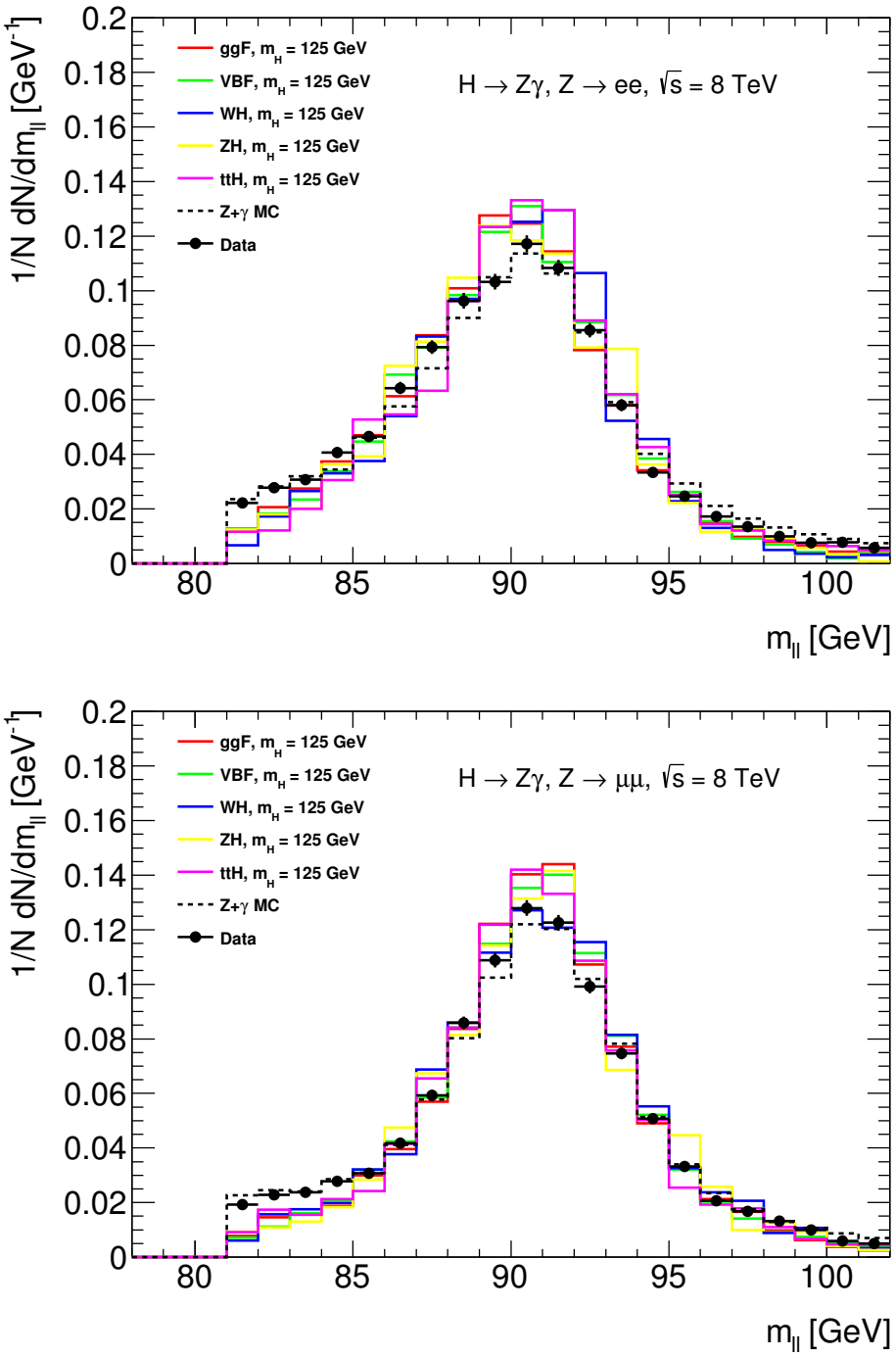

Figure 5.5: Distributions of the reconstructed Z boson mass, $m_{\ell\ell}$, in signal events (for a Higgs boson of mass 125 GeV) from the five considered production processes, in background events selected from a simulated sample of $Z\gamma$ events, and in data. Events were selected from 8 TeV samples and data sets, and the final selection criteria described in Section 6.1 were applied. Note that this criteria includes a requirement that $m_{\ell\ell} > m_Z - 10\,\text{GeV}$, which causes the sharp threshold at 81.12 GeV.

Chapter 6

Search for $H \to Z\gamma$ Decays

This chapter describes a search for evidence of the SM Higgs boson decaying to a Z boson and a photon, by consideration of $ee\gamma$ and $\mu\mu\gamma$ final states. As noted in Chapter 2, the Higgs boson undergoes the $H \to Z\gamma$ decay with a comparable branching fraction to $H \to \gamma\gamma$, and the two states share the same set of leading order Feynman diagrams. However, undiscovered particles appearing in the loops of those diagrams may affect the two processes differently, so a measurement of the ratio of the branching fractions could provide useful clues to physics beyond the SM. Study of this decay mode is also useful to provide additional measurements of the properties of the Higgs boson.

The previous chapter described how standard objects are reconstructed and identified using the ATLAS detector. Section 6.1 continues this theme with a description of the reconstruction of Higgs boson candidates, with further selections imposed on the leptons forming those candidates. Three main corrections to the three-body invariant mass, $m_{\ell\ell\gamma}$, were applied to improve the mass resolution and therefore the sensitivity of the analysis, as described in Section 6.1.1. The number of events passing each main stage of the selection process in signal MC and in data are presented in Section 6.1.2.

Section 6.2 describes the separation of selected events into ten categories based on the centre-of-mass energy, final state, and two kinematic variables, which served to inrease the sensitivity of the analysis. The expected number of signal events were identified as outlined in Section 6.2.1, and their distribution was modelled using a Crystal Ball lineshape summed with a Gaussian function, as described in Section 6.2.2. The background was data-driven, and Section 6.2.3 describes the process of fitting the data in each category with various functional forms to identify the most appropriate model. A variety of systematic uncertainties, arising from both theoretical and experimental sources, were identified and they are summarised in Section 6.2.4. The signal and background models were then used in likelihood-based statistical tests to search for evidence of $H \to Z\gamma$ decays. Technical details of the procedure are given in Section 6.2.5, while the resultant expected limits are presented in Section 6.2.6.

Section 6.3 describes an attempt to increase the sensitivity of the analysis through the introduction of a category containing events where the Higgs boson was produced through the VBF mechanism. As noted in Section 2.5, such events are uniquely characterised by the presence of two jets in the forward regions of the ATLAS detector and therefore present a useful signature.

Section 6.4 describes a novel approach to improving the sensitivity of the analysis where events were separated into a series of categories based on the reconstructed Z boson mass, $m_{\ell\ell}$, termed "Z slices". An initial proof of concept study based on the expected number of signal and background events within a fixed mass window around $m_{\ell\ell\gamma} = 125$ GeV was performed, and is presented in Section 6.4.1. The full limit setting procedure used in the kinematic analysis was then invoked, as described in Section 6.4.2. For simplicity, no systematic uncertainties were included since the analysis was dominated by statistical uncertainties. The study was then repeated with an improved event categorisation that combined the Z slices with a selection of categories from the kinematic analysis, as described in Section 6.4.3. Due to the narrow width of individual Z slices, the possibility of an event migration between categories was investigated and the results are presented in Section 6.4.4. A final comparison of the expected limits for all considered choices of event categorisation is then shown in Section 6.4.5.

6.1 $H \to Z\gamma$ Reconstruction and Selection

For each event, a Higgs boson candidate was reconstructed by combining a Z boson and the photon with the highest transverse energy. The Z boson was selected as outlined in Section 5.7 and in the unlikely event of multiple Z candidates being identified in a single event, only the Z candidate with an invariant mass closest to the true Z mass was used. This safeguard proved unnecessary, however, since no events were ever found to contain more than one Z candidate in either data or the MC samples.

Once the Higgs candidate had been selected, track and calorimeter isolation requirements were imposed on the leptons used to reconstruct it.

The normalised track isolation is defined as the sum of the transverse momenta of good quality tracks within a cone of radius $\Delta R = 0.2$ around the lepton (excluding the track of the lepton itself), divided by the lepton p_{T}. The identification of good quality tracks varied depending on the flavour of lepton used in the reconstruction of the Higgs candidate. For muons, the summation would only include tracks with at least four hits in the pixel and SCT detectors and $p_{\mathrm{T}} > 1$ GeV, while for electrons, the summation would only include tracks with at least nine silicon hits, one hit in the b-layer and $p_{\mathrm{T}} > 0.4\,\mathrm{GeV}$. Each lepton flavour was required to have a normalised track isolation that was less than 0.15.

The normalised calorimetric isolation has slightly different definitions for electrons and muons. For electrons, it is the sum of the positive-energy topoclusters with a reconstructed barycentre located within a cone of radius $\Delta R = 0.2$ around the electron cluster (excluding the cells within 0.125×0.175 in $\eta \times \phi$ around the electron barycentre), divided by the electron E_{T}. It was required that this value be less than 0.30 in 7 TeV data, and less than 0.20 in 8 TeV data. For muons, it is the sum of the energy of the calorimeter cells located within a cone of radius $\Delta R = 0.2$ around the muon. It was

required that this value be less than 0.30, or less than 0.15 in the case of SA muons that do not have an associated ID track.

When applying both the track and calorimeter isolation requirements, any contributions from the other lepton produced in the Z decay were subtracted.

The transverse impact parameter significance $|d_0/\sigma(d_0)|$ of the ID track associated with a lepton located in the region $|\eta| < 2.5$ was then required to be less than 6.5 for electrons, or less than 3.5 for muons with an associated ID track. As noted in Section 5.3.2, the electron impact parameter is affected by bremsstrahlung and therefore has a broader distribution.

Finally, to suppress events from final state radiation (FSR) $Z + \gamma$ events, the dilepton invariant mass was required to be greater than 81.18 GeV (that is, $m_Z - 10\,\text{GeV}$).

6.1.1 Corrections to $m_{\ell\ell\gamma}$

A series of corrections to the three-body invariant mass were then applied, in order to enhance the mass resolution for signal events and improve the discrimination against background events.

6.1.1.1 Photon Correction to Primary Vertex

The point of origin of the reconstructed photon is known only through the extrapolation of the shower recorded in the electromagnetic calorimeter back to the beamline. However, in $H \to Z\gamma$ decays it can be assumed that the photon origin is the same as the primary vertex, whose location is known to a higher precision through the use of multiple tracks in its identification. The photon pseudorapidity, η, and its transverse energy $E_\text{T} = E/\cosh\eta$ were therefore recalculated from the primary vertex and the photon impact point in the calorimeter.

6.1.1.2 QED Final State Radiation correction

When the Z boson decays leptonically, the resultant electrons or muons can radiate photons to produce final state radiation (FSR). The effect of FSR is negligible in the case of $Z \to ee$ decays, since an electron and a radiated photon will produce overlapping electromagnetic showers in the calorimeter that are generally reconstructed as one. However, in the case of $Z \to \mu\mu$ decays the radiated photon represents an energy loss of the muon before any of its properties can be measured in the muon spectrometer. A Z boson reconstructed from such a muon will have its invariant mass erroneously shifted to a lower energy, but this energy loss can be corrected by searching for radiated photons and including them in the Z reconstruction. Full details of the reconstruction of collinear FSR photons in Z decays to muons can be found in Ref. [153], and the technique was successfully applied to the $H \to 4\ell$ analysis [154, 155]. A brief overview of this method is presented here.

FSR photons can be detected and reconstructed from energy deposits in the electromagnetic calorimeter in the same way as regular photons. However, in dimuon events the FSR photons can be identified by searching for electromagnetic clusters within a narrow cone around an axis (termed the neutral line) defined by the muon momentum direction at the interaction point. The longitudinal segmentation of the calorimeter can be exploited to reduce the identification of fake photon clusters produced by muon ionisation or pileup, by using a cut on the fraction f_1 of the cluster energy deposited in the front segment of the calorimeter (the strips) relative to the total energy. Such a cut is very effective against fake photon clusters, and allows high FSR signal purities even at very low cluster energies (with 70% purity found for an energy of $\simeq 1.5\,\text{GeV}$).

Within this analysis, events with a $\mu\mu\gamma$ final state that passed all previous event selections were searched for any FSR candidates, with such photons required to have:

- the cone between the cluster and the muon $\Delta R_{\text{cluster},\mu} = \sqrt{\Delta\eta^2 + \Delta\phi^2} < 0.15$,
- the transverse energy of the cluster $E_{\text{T}} > 1.5\,\text{GeV}$,
- the fraction $f_1 > 0.1$.

If more than one cluster was found within the cone, then only the cluster with the highest E_{T} was used. Candidate Z bosons with $Z_{\mu\mu} > 60\,\text{GeV}$ were then corrected for FSR by recalculating them to include any reconstructed photons with $E_{\text{T}} > 1.5\,\text{GeV}$ and located within $\Delta R < 0.08$ (or 0.15, depending on the photon E_{T}) of the muons. The impact of the correction is only slight, as only 2.5% of all muon events in 8 TeV data were found to be affected by it.

6.1.1.3 Z Boson Mass Constraint

The four-momenta of the leptons was recomputed using a technique developed for the $H \to 4\ell$ analysis [155], whereby a kinematic fit minimised the χ^2 between the lepton 4-momenta and a set of best fit-values. These best fit values were identified by imposing a constraint on the reconstructed Z mass such that it must be the most probable value, as determined using the hypothesis of a genuine $Z \to \ell\ell$ decay and the assumption of an unbiased Gaussian resolution function for the reconstruction of the mass in the detector.

The most likely value of $m_{\ell\ell}$ is determined by finding the value of the true dilepton mass, $m_{\ell\ell}^{\text{true}}$, for which the probability of measuring the observed dilepton mass, $m_{\ell\ell}^{\text{rec}}$, is maximal. This can be achieved by maximising the following likelihood function:

$$L(m_{\ell\ell}^{\text{true}}|m_{\ell\ell}^{\text{reco}}) = P(m_{\ell\ell}^{\text{reco}}|m_{\ell\ell}^{\text{true}}) \times P(m_{\ell\ell}^{\text{true}}), \tag{6.1}$$

where the prior probability distribution function for $m_{\ell\ell}^{\text{true}}$ is assumed to be a Breit-Wigner of the form:

$$P(m_{\ell\ell}^{\text{true}}) = BW(m_{\ell\ell}^{\text{true}}; M_Z, \Gamma_Z) = \frac{N}{\left((m_{\ell\ell}^{\text{true}})^2 - M_Z^2\right)^2 + \Gamma_Z^2 M_Z^2}, \tag{6.2}$$

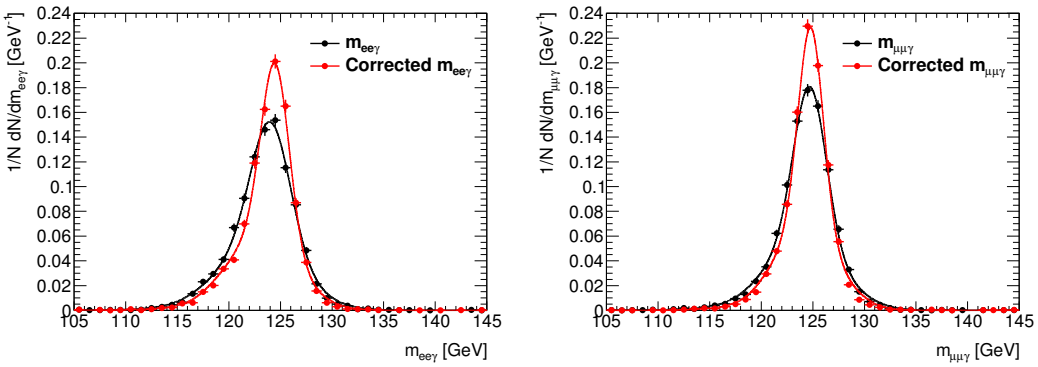

Figure 6.1: Three-body invariant mass distributions (normalised to unity) for selected events from the 8 TeV ggF signal sample at $m_H = 125$, after basic reconstruction (black) and after correcting the photon origin to the primary vertex, applying the FSR correction and applying the Z-mass constraint to the dilepton mass (red). The lines show the results of fits to the distributions using a model composed of a Crystal Ball function summed with a Gaussian function. Left: $Z \to ee$ channel, right: $Z \to \mu\mu$ channel.

with $M_Z = 91.1876\,\text{GeV}$ denoting the true Z boson mass, $\Gamma_Z = 2.4952\,\text{GeV}$ denoting the natural width of the Z [10], and N being a normalisation factor. The conditional probability $P(m_{\ell\ell}^{\text{reco}}|m_{\ell\ell}^{\text{true}})$ is the detector invariant mass response function and is modelled with a Gaussian:

$$P(m_{\ell\ell}^{\text{reco}}|m_{\ell\ell}^{\text{true}}) = G(m_{\ell\ell}^{\text{reco}}|m_{\ell\ell}^{\text{true}}, \sigma_m) = \frac{1}{\sqrt{2\pi}\sigma_m} e^{-\frac{(m_{\ell\ell}^{\text{reco}} - m_{\ell\ell}^{\text{true}})^2}{2\sigma_m^2}}, \tag{6.3}$$

where σ_m is the per-event invariant mass resolution evaluated from the three-momenta of the two leptons and their covariance matrix.

This constraint is particularly useful since it helps recover some of the momentum lost by leptons due to bremsstrahlung, which resculpts the signal peak by shifting it closer to the true Higgs mass and reducing the low-mass tail.

6.1.1.4 Impact of Corrections

Figure 6.1 shows a comparison between the $m_{\ell\ell\gamma}$ distributions with and without the corrections listed in the preceding sections, using simulated signal events from the $gg \to H$ sample at $m_H = 125\,\text{GeV}$.

6.1.2 Summary of Cutflow

Tables 6.1 to 6.4 show the relative number of events passing each main selection step in signal MC (at $m_H = 125\,\text{GeV}$) and data, at 7 and 8 TeV, in $\mu\mu\gamma$ and $ee\gamma$ final states. Various event weights arise from corrections to the MC samples (detailed in Section 4.2.1.3), which are taken into consideration when the relevant stages of the object selection and reconstruction are reached. These help ensure that the MC samples provide an accurate description of what the real detector would record. It

Selection	ggF (%)	VBF (%)	WH (%)	ZH (%)	$t\bar{t}$H (%)	Data (%)
All events	100.00	100.00	100.00	100.00	100.00	100.00
Trigger	81.69	81.94	81.04	81.80	80.62	94.50
γ selection	42.60	42.26	40.05	39.70	32.68	1.13
Z selection	32.69	32.69	26.68	30.05	20.58	0.30
Trigger match	32.26	32.32	26.30	29.56	19.96	0.28
Track isolation	30.49	30.67	24.73	27.77	17.36	0.27
Calorimeter isolation	30.33	30.50	24.64	27.59	17.17	0.27
Impact parameters	30.21	30.35	24.44	27.34	16.96	0.27
$m_{\ell\ell} > 81.18\,\text{GeV}$	28.56	28.51	23.16	25.88	15.92	0.13

Table 6.1: Selection efficiency for $H \to Z\gamma$, $Z \to \mu\mu$ signal events at 7 TeV and $m_H = 125\,\text{GeV}$. The sum of the weights is taken into account: up to the Z selection row, only initial weights (pile-up and z vertex) are considered; in the rows starting with "track isolation", final weights (lepton efficiency scale factors, trigger efficiency scale factors) are also included.

Selection	ggF (%)	VBF (%)	WH (%)	ZH (%)	$t\bar{t}$H (%)	Data (%)
All events	100.00	100.00	100.00	100.00	100.00	100.00
Trigger	61.66	51.47	53.95	51.28	47.91	N/A
γ selection	31.69	26.05	26.08	24.36	19.35	9.99
Z selection	18.95	14.59	12.79	12.91	8.49	0.22
Trigger match	18.91	14.57	12.75	12.90	8.47	N/A
Track isolation	18.25	14.15	12.33	12.48	8.04	0.22
Calorimeter isolation	18.20	14.08	12.23	12.40	7.96	0.22
Impact parameters	18.00	13.93	12.11	12.31	7.88	0.21
$m_{\ell\ell} > 81.18\,\text{GeV}$	16.46	12.83	11.08	11.40	7.21	0.11

Table 6.2: Selection efficiency for $H \to Z\gamma$, $Z \to ee$ signal events at 7 TeV and $m_H = 125\,\text{GeV}$. The sum of the weights is taken into account: up to the Z selection row, only initial weights (pile-up and z vertex) are considered; in the rows starting with "track isolation", final weights (lepton efficiency scale factors, trigger efficiency scale factors) are also included. Note that for data, an issue with the trigger variables prohibited the application of trigger selection or trigger matching.

Selection	ggF (%)	VBF (%)	WH (%)	ZH (%)	$t\bar{t}$H (%)	Data (%)
All events	100.00	100.00	100.00	100.00	100.00	100.00
Trigger	76.71	78.03	77.58	76.18	75.83	49.81
γ selection	46.21	45.90	43.47	41.98	34.25	1.11
Z selection	37.37	36.70	30.61	33.47	23.06	0.34
Trigger match	37.37	36.67	30.35	33.24	22.52	0.34
Track isolation	36.82	36.13	29.65	32.37	20.46	0.32
Calorimeter isolation	36.62	35.92	29.50	32.24	20.11	0.32
Impact parameters	36.41	35.65	29.20	32.06	19.84	0.32
$m_{\ell\ell} > 81.18\,\text{GeV}$	34.27	33.72	27.53	30.14	18.88	0.16

Table 6.3: Selection efficiency for $H \to Z\gamma$, $Z \to \mu\mu$ signal events at 8 TeV and $m_H = 125\,\text{GeV}$. The sum of the weights is taken into account: up to the Z selection row, only initial weights (pile-up and z vertex) are considered; in the rows starting with "track isolation", final weights (lepton efficiency scale factors, trigger efficiency scale factors) are also included.

Selection	ggF (%)	VBF (%)	WH (%)	ZH (%)	$t\bar{t}$H (%)	Data (%)
All events	100.00	100.00	100.00	100.00	100.00	100.00
Trigger	50.29	43.47	45.34	43.35	45.67	65.16
γ selection	29.37	24.05	23.97	22.75	19.90	7.62
Z selection	20.65	15.99	14.22	14.93	10.29	0.22
Trigger match	20.63	15.97	14.21	14.91	10.24	0.21
Track isolation	19.87	15.45	13.62	14.30	9.51	0.20
Calorimeter isolation	19.61	15.28	13.48	14.08	9.30	0.20
Impact parameters	19.41	15.09	13.28	13.90	9.14	0.20
$m_{\ell\ell} > 81.18\,\text{GeV}$	18.05	14.18	12.45	13.06	8.58	0.11

Table 6.4: Selection efficiency for $H \to Z\gamma$, $Z \to ee$ signal events at 8 TeV and $m_H = 125\,\text{GeV}$. The sum of the weights is taken into account: up to the Z selection row, only initial weights (pile-up and z vertex) are considered; in the rows starting with "track isolation", final weights (lepton efficiency scale factors, trigger efficiency scale factors) are also included.

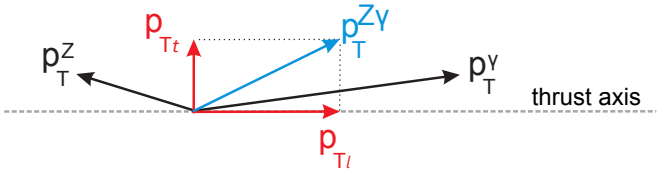

Figure 6.2: Vector diagram of the Higgs p_T^t variable, defined as the component of the Higgs candidate p_{T} that is orthogonal to the thrust axis defined by the difference between the photon and the Z boson momenta [23].

should be also be noted that there was a problem with the trigger variables in the 7 TeV data set with an $ee\gamma$ final state, which prohibited the use of trigger selections or trigger matching. However, this does not affect the final number of events since the criteria used for the offline selection are tighter than those used for the trigger selection.

6.2 Kinematic Event Classification

The sensitivity of an analysis may be enhanced by filtering events into various categories, which each carry their own signal-to-background ratio and invariant mass resolution. In this case, the data was divided into categories based on two kinematic variables: the component of the Higgs boson candidate p_{T} that was orthogonal to the thrust axis defined by the difference in momenta between the photon and the Z boson, termed the Higgs p_T^t (see Figure 6.2); and the absolute value of the difference in pseudorapidity of the photon and the Z boson, $|\Delta\eta_{Z\gamma}|$. The Higgs p_T^t variable was selected because it has been shown to be less sensitive to experimental systematic uncertainties [156], and was used in the $H \to \gamma\gamma$ analysis that led to the discovery of the Higgs [3]. The $|\Delta\eta_{Z\gamma}|$ variable was chosen because the photon and the Z are boosted from the Higgs in signal events, and so this value should be small with respect to that of background events produced through SM $Z + \gamma$ processes.

Distributions of the Higgs p_T^t and $|\Delta\eta_{Z\gamma}|$ from simulated signal samples, simulated background $Z + \gamma$ events, and data are shown in Figures 6.3 and 6.5, respectively. Events were then classified as high- or low-p_T^t if the Higgs p_T^t was greater or less than a given threshold, while low-p_T^t events were further subdivided into high- and low-$|\Delta\eta_{Z\gamma}|$ if this value was above or below a certain threshold. The significance was then evaluated for different threshold values by combining $S/\sqrt{B}$ from each of the three resultant categories in quadrature, where S is the expected number of signal events and B is the expected number of background events taken from data. The results from using 8 TeV data and events with a $\mu\mu\gamma$ final state are shown in Figure 6.6. The significance was a maximum for a p_T^t threshold of around 55 GeV and a $|\Delta\eta_{Z\gamma}|$ threshold of approximately 2.0. However, the p_T^t threshold was lowered to 30 GeV (causing a slight decrease in significance) to prevent the introduction of a peak in the background $m_{\ell\ell\gamma}$ distribution near the signal region for events in the high-p_T^t category [23].

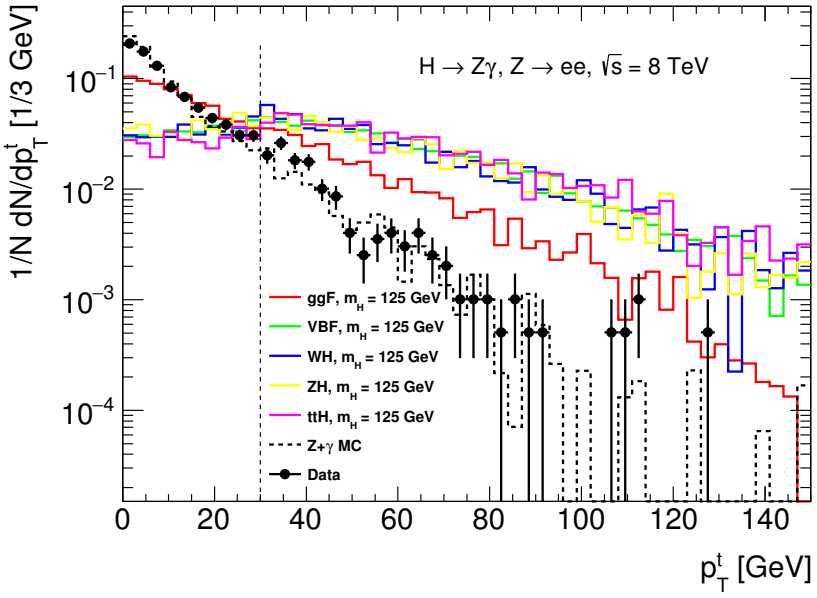

Figure 6.3: Distribution of Higgs p_T^t in signal events (for a Higgs boson of mass 125 GeV) from the five considered production processes, in background events selected from a simulated sample of $Z\gamma$ events, and in data. Events with an $ee\gamma$ final state were selected from 8 TeV samples and data sets in the signal region at $120 < m_{\ell\ell\gamma} < 130$ GeV.

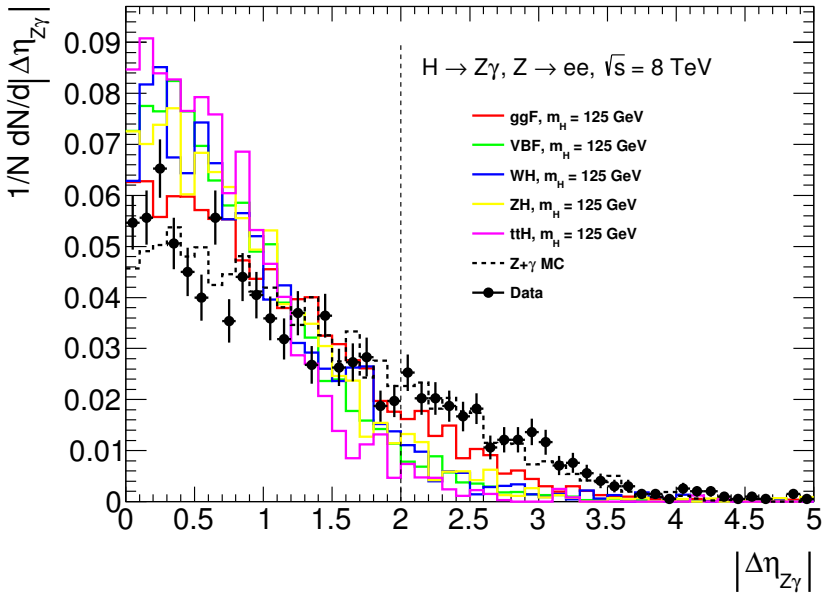

Figure 6.4: Distribution of $|\Delta\eta_{Z\gamma}|$ in signal events (for a Higgs boson of mass 125 GeV) from the five considered production processes, in background events selected from a simulated sample of $Z\gamma$ events, and in data. Events with an $ee\gamma$ final state were selected from 8 TeV samples and data sets in the signal region at $120 < m_{\ell\ell\gamma} < 130$ GeV.

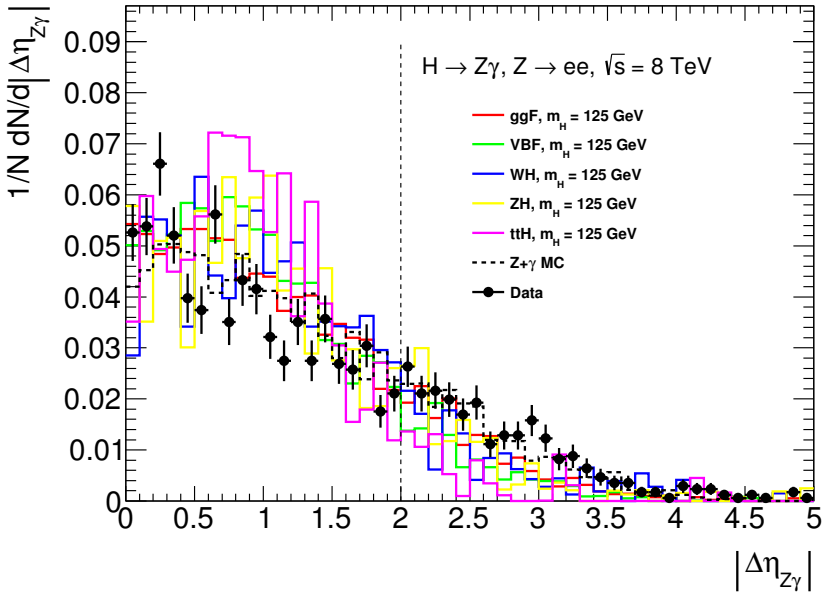

Figure 6.5: Distribution of $|\Delta\eta_{Z\gamma}|$ in signal events (for a Higgs boson of mass 125 GeV) from the five considered production processes, in background events selected from a simulated sample of $Z\gamma$ events, and in data. Events with Higgs $p_T^t < 30$ GeV and an $ee\gamma$ final state were selected from 8 TeV samples and data sets in the signal region at $120 < m_{\ell\ell\gamma} < 130$ GeV.

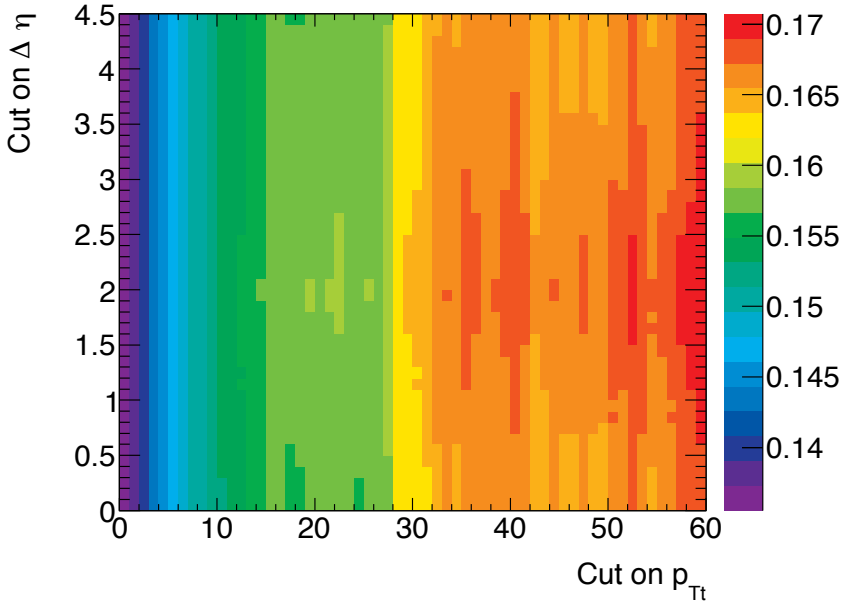

Figure 6.6: Significance as a function of the thresholds used to classify the events into p_T^t and $|\Delta\eta_{Z\gamma}|$ categories, based on 8 TeV $\mu\mu\gamma$ data and signal MC. The significance was evaluated by summing $S/\sqrt{B}$ of each category in quadrature, where S is the expected number of signal events and B is the expected number of background events taken from data [23].

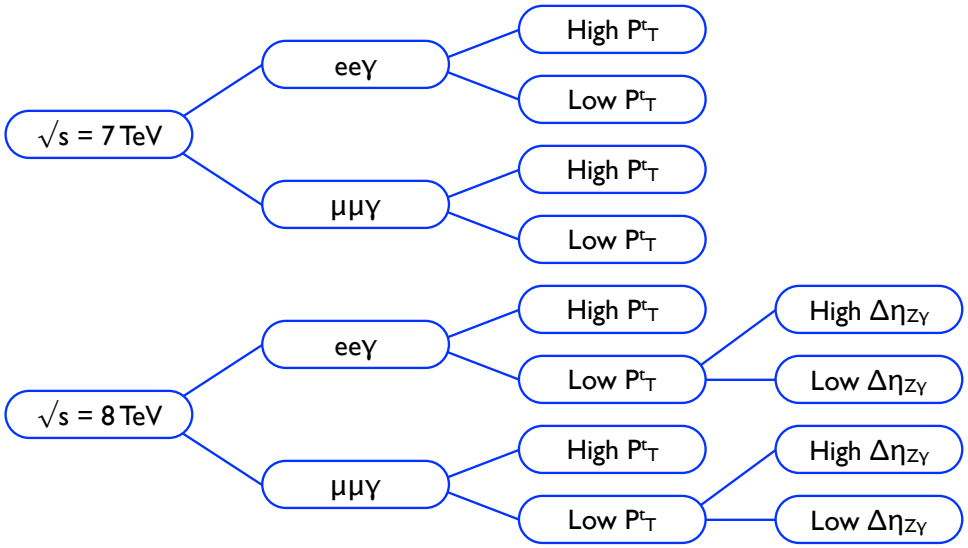

Figure 6.7: Overview of the kinematic event categories. Events are classified by centre-of-mass energy, final state, p_T^t and $|\Delta\eta_{Z\gamma}|$. High and Low p_T^t denote $p_T^t > 30$ and $p_T^t < 30\,\text{GeV}$, respectively. High and Low $|\Delta\eta_{Z\gamma}|$ denote $|\Delta\eta_{Z\gamma}| > 2.0$ and $|\Delta\eta_{Z\gamma}| < 2.0$, respectively.

Higgs boson candidates were therefore classified as high- or low-p_T^t if the Higgs p_T^t was greater or less than 30 GeV, respectively. Events in 8 TeV data with low-p_T^t were separated into high- and low-$|\Delta\eta_{Z\gamma}|$ if this value was greater or less than 2.0. Events in 7 TeV data could not be subdivided into categories based on $|\Delta\eta_{Z\gamma}|$ due to the limited statistics contained in the sample. The complete categorisation scheme is summarised in Figure 6.7.

6.2.1 Evaluating Signal Yields

The production and decay of Higgs bosons at various mass points was simulated using several MC samples, which were then passed through a full detector simulation as described in Section 4.2. This enables evaluation of the signal selection efficiency (and hence the expected signal yield) for $H \to Z\gamma$ decays where the Higgs boson was produced through one of the five considered mechanisms. The expected yield for a given Higgs mass and production mechanism is given by:

$$N_{i,\ell}^{\text{SM}}(m_H) = \int \mathcal{L}dt \times \sigma_i(m_H) \times \mathcal{B}_{H\to Z\gamma}(m_H) \times \mathcal{B}_{Z\to\ell\ell} \times \varepsilon_{i,\ell}(m_H), \qquad (6.4)$$

where:

- $\int \mathcal{L}dt$ is the integrated luminosity of the data sample, (20.3 ± 0.5) fb^{-1} at 8 TeV and (4.5 ± 0.3) fb^{-1} at 7 TeV,
- $\sigma_i(m_H)$ is the production cross-section for a Higgs boson of mass m_H, through the mechanism $i = ggF, VBF, WH, ZH, t\bar{t}H$,

- $\mathcal{B}_{H\to Z\gamma}(m_H)$ is the branching fraction for a Higgs boson of mass m_H decaying to $Z + \gamma$,
- $\mathcal{B}_{Z\to\ell\ell} = (10.0974 \pm 0.0069)\%$ is the $Z \to \ell\ell$ branching fraction, for all three leptonic decay modes,
- $\varepsilon_{i,\ell}(m_H)$ is the selection efficiency for $H \to Z\gamma$, $Z \to \ell\ell$ events.

The production cross sections and $H \to Z\gamma$ branching fractions were taken from [21, 22], as noted in Section 2.5. The selection efficiency at each mass point for which a signal MC sample exists is given by the sum of final weights of all events i with the corresponding $\ell\ell\gamma$ final state that passed the full event selection criteria, divided by the number of generated events in the sample. The final weight is the product of the pileup weight, z vertex weight, and efficiency scale factors for the trigger, the two leptons and the photon. Only events within the range $100 < m_{\ell\ell\gamma} < 170\,\text{GeV}$ were considered.

The expected signal yields for $4.5\,\text{fb}^{-1}$ of data at 7 TeV in the $ee\gamma$ and $\mu\mu\gamma$ final states are shown in Tables 6.5 and 6.6, respectively; the corresponding yields for $20.3\,\text{fb}^{-1}$ of data at 8 TeV in the $ee\gamma$ and $\mu\mu\gamma$ final states are shown in Tables 6.7 and 6.8, respectively. The selection efficiency $\varepsilon_{i,\ell}$ varies with centre-of-mass collision energy, Higgs boson mass point, and Higgs boson production mechanism, and the final state - it varies between 5.7 and 12.1% for 7 TeV samples, and between 6.8 and 13.8% for 8 TeV samples.

The events were then separated into the kinematic categories as described in Figure 6.7. In order to evaluate the yield at any arbitrary mass point, the yield in each category was plotted against the mass point and the resulting distribution was fitted with a 2nd-order polynomial. The results for the 7 and 8 TeV categories are shown in Figures 6.8 and 6.9, respectively. The expected yields from each category and production mechanism for a Higgs boson of mass 125 GeV are presented in Table 6.9. For reference, the selection efficiency $\varepsilon_{i,\ell}(m_H)$ for each category is also presented in Figures 6.10 and 6.11.

The expected total yield, within a given category, is then merely the sum over all production mechanisms:

$$N_\ell^{\text{SM}}(m_H) = \sum_i N_{i,\ell}^{\text{SM}}(m_H). \tag{6.5}$$

6.2.2 Signal Modelling

It has been found [23] that the $m_{\ell\ell\gamma}$ distribution for signal events can be well described by a signal model composed of a Crystal Ball lineshape (to capture the main peak) summed with a wider Gaussian distribution (to improve the description of the tails).

Mass (GeV)	ggF	VBF	WH	ZH	$t\bar{t}$H	Total
120	0.492	0.044	0.019	0.001	0.003	0.559
125	0.744	0.065	0.027	0.002	0.004	0.842
130	0.965	0.086	0.032	0.002	0.005	1.089
135	1.113	0.103	0.035	0.002	0.005	1.259
140	1.208	0.114	0.035	0.002	0.005	1.364
145	1.168	0.117	0.033	0.002	0.005	1.324
150	1.057	0.108	0.029	0.002	0.004	1.201

Table 6.5: Number of expected signal events with an $ee\gamma$ final state in $4.5\,\text{fb}^{-1}$ of 7 TeV data, for SM Higgs bosons of various mass hypotheses produced through each considered mechanism. Only events with $100 < m_{\ell\ell\gamma} < 170\,\text{GeV}$ are considered. The total number of signal events from all five production mechanisms is also presented.

Mass (GeV)	ggF	VBF	WH	ZH	$t\bar{t}$H	Total
120	0.649	0.054	0.025	0.002	0.003	0.733
125	0.950	0.082	0.035	0.002	0.005	1.074
130	1.217	0.110	0.042	0.003	0.006	1.377
135	1.442	0.129	0.046	0.003	0.006	1.626
140	1.509	0.142	0.046	0.003	0.006	1.706
145	1.475	0.143	0.042	0.003	0.006	1.669
150	1.335	0.131	0.036	0.002	0.005	1.509

Table 6.6: Number of expected signal events with a $\mu\mu\gamma$ final state in $4.5\,\text{fb}^{-1}$ of 7 TeV data, for SM Higgs bosons of various mass hypotheses produced through each considered mechanism. Only events with $100 < m_{\ell\ell\gamma} < 170\,\text{GeV}$ are considered. The total number of signal events from all five production mechanisms is also presented.

Mass (GeV)	ggF	VBF	WH	ZH	$t\bar{t}$H	Total
120	3.564	0.306	0.125	0.008	0.023	4.027
125	5.284	0.460	0.176	0.011	0.031	5.963
130	6.672	0.597	0.217	0.013	0.039	7.538
135	7.674	0.710	0.229	0.014	0.043	8.671
140	8.243	0.778	0.225	0.015	0.043	9.304
145	8.000	0.779	0.205	0.014	0.039	9.038
150	7.226	0.726	0.180	0.012	0.035	8.179

Table 6.7: Number of expected signal events with an $ee\gamma$ final state in $20.3\,\text{fb}^{-1}$ of 8 TeV data, for SM Higgs bosons of various mass hypotheses produced through each considered mechanism. Only events with $100 < m_{\ell\ell\gamma} < 170\,\text{GeV}$ are considered. The total number of signal events from all five production mechanisms is also presented.

Mass (GeV)	ggF	VBF	WH	ZH	$t\bar{t}$H	Total
120	4.378	0.364	0.154	0.010	0.027	4.933
125	6.392	0.552	0.216	0.013	0.038	7.212
130	8.102	0.719	0.260	0.016	0.044	9.143
135	9.137	0.834	0.278	0.018	0.048	10.315
140	9.710	0.913	0.270	0.018	0.049	10.960
145	9.437	0.903	0.255	0.016	0.044	10.655
150	8.376	0.839	0.214	0.014	0.039	9.481

Table 6.8: Number of expected signal events with a $\mu\mu\gamma$ final state in $20.3\,\text{fb}^{-1}$ of 8 TeV data, for SM Higgs bosons of various mass hypotheses produced through each considered mechanism. Only events with $100 < m_{\ell\ell\gamma} < 170\,\text{GeV}$ are considered. The total number of signal events from all five production mechanisms is also presented.

$\sqrt{s}$	Final State	Category	ggF	VBF	WH	ZH	$t\bar{t}$H
7 TeV	$ee\gamma$	High p_T^t	0.27	0.044	0.017	0.0011	0.0028
		Low p_T^t	0.49	0.022	0.0089	0.00052	0.0010
	$\mu\mu\gamma$	High p_T^t	0.33	0.056	0.023	0.0013	0.0035
		Low p_T^t	0.64	0.028	0.012	0.00072	0.0012
8 TeV	$ee\gamma$	High p_T^t	1.72	0.31	0.12	0.0071	0.023
		Low p_T^t, High $\lvert\Delta\eta_{Z\gamma}\rvert$	0.58	0.020	0.0076	0.00053	0.00077
		Low p_T^t, Low $\lvert\Delta\eta_{Z\gamma}\rvert$	3.03	0.14	0.051	0.0032	0.0075
	$\mu\mu\gamma$	High p_T^t	2.01	0.37	0.14	0.0086	0.027
		Low p_T^t, High $\lvert\Delta\eta_{Z\gamma}\rvert$	0.76	0.027	0.012	0.00075	0.0010
		Low p_T^t, Low $\lvert\Delta\eta_{Z\gamma}\rvert$	3.68	0.16	0.061	0.0039	0.0088

Table 6.9: Expected signal yields at $m_H = 125\,\text{GeV}$ for each production mechanism in the kinematic event categories.

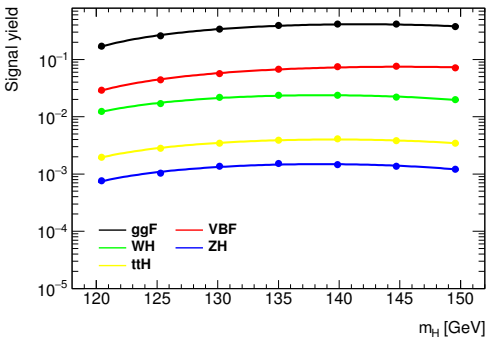

(a) $ee\gamma$ final state, High-p_T^t

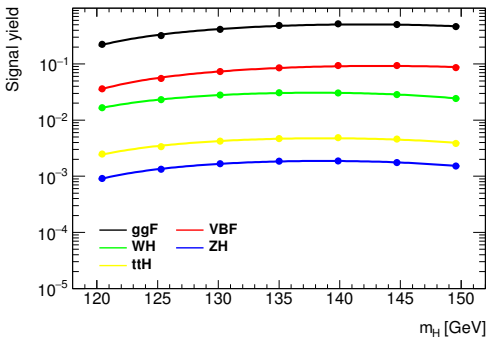

(c) $\mu\mu\gamma$ final state, High-p_T^t

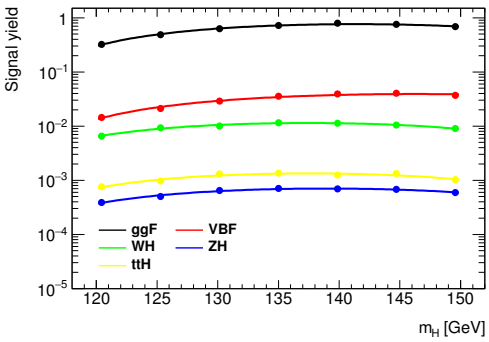

(b) $ee\gamma$ final state, Low-p_T^t

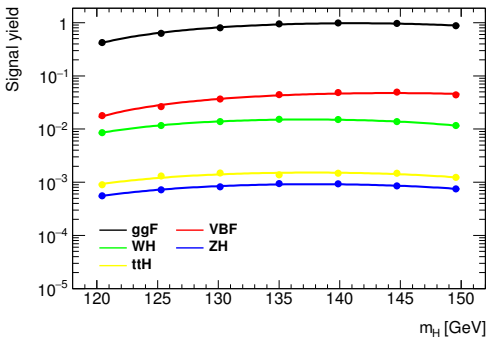

(d) $\mu\mu\gamma$ final state, Low-p_T^t

Figure 6.8: Expected $H \to Z\gamma$ signal yields in $4.5\,\text{fb}^{-1}$ of pp collisions at $\sqrt{s} = 7\,\text{TeV}$. Each distribution is fitted with a second-order polynomial to allow yields to be estimated at arbitrary mass points.

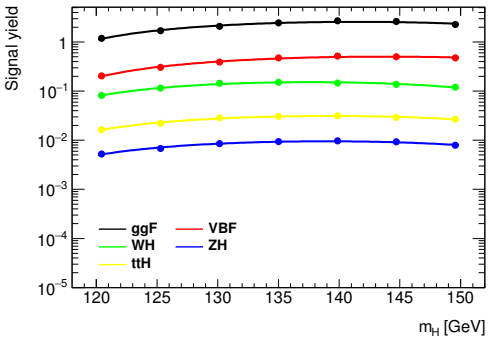

(a) $ee\gamma$ final state, High-p_T^t

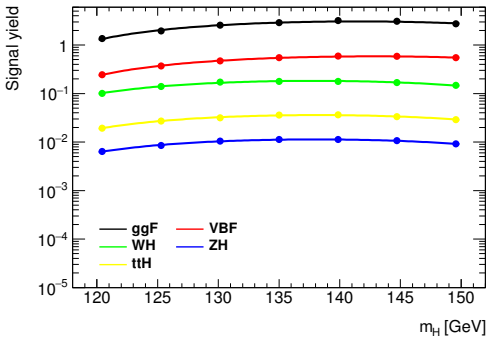

(d) $\mu\mu\gamma$ final state, High-p_T^t

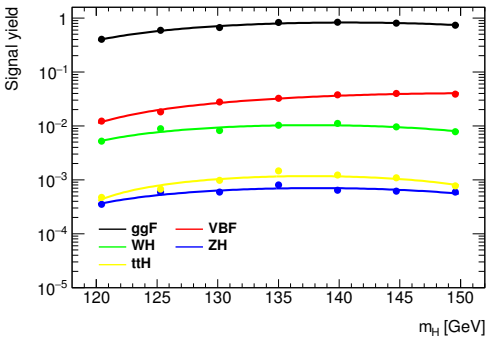

(b) $ee\gamma$ final state, Low-p_T^t, High-$\Delta\eta$

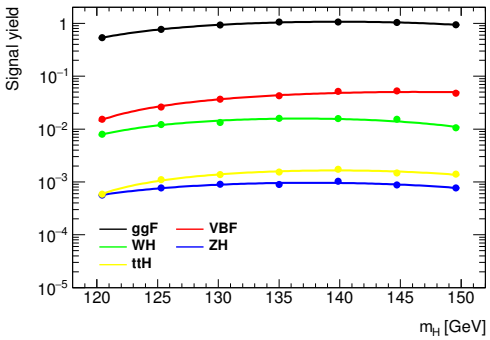

(e) $\mu\mu\gamma$ final state, Low-p_T^t, High-$\Delta\eta$

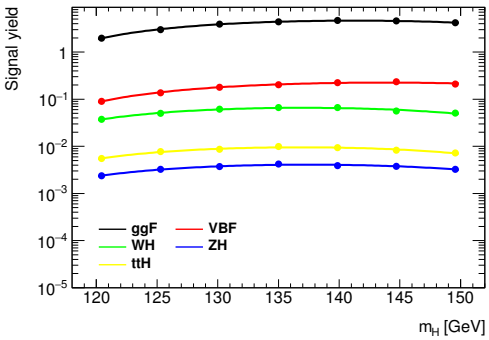

(c) $ee\gamma$ final state, Low-p_T^t, Low-$\Delta\eta$

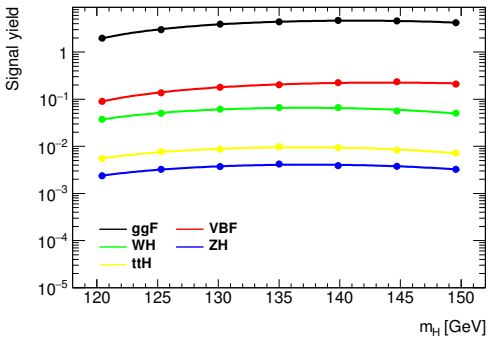

(f) $\mu\mu\gamma$ final state, Low-p_T^t, Low-$\Delta\eta$

Figure 6.9: Expected $H \to Z\gamma$ signal yields in $20.3\,\text{fb}^{-1}$ of pp collisions at $\sqrt{s} = 8\,\text{TeV}$. Each distribution is fitted with a second-order polynomial to allow yields to be estimated at arbitrary mass points.

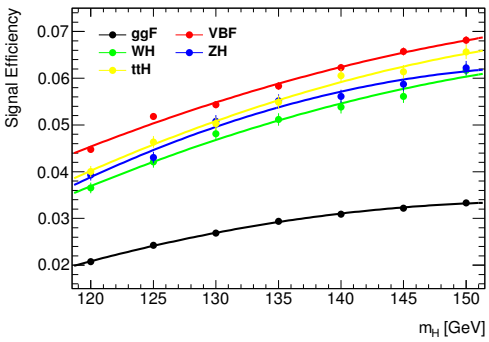

(a) $ee\gamma$ final state, High-p_T^t

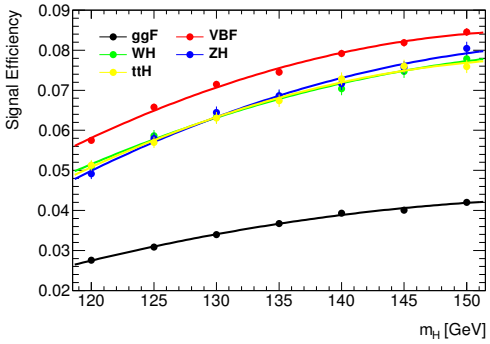

(c) $\mu\mu\gamma$ final state, High-p_T^t

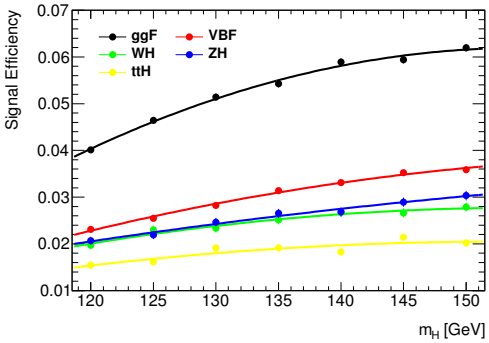

(b) $ee\gamma$ final state, Low-p_T^t

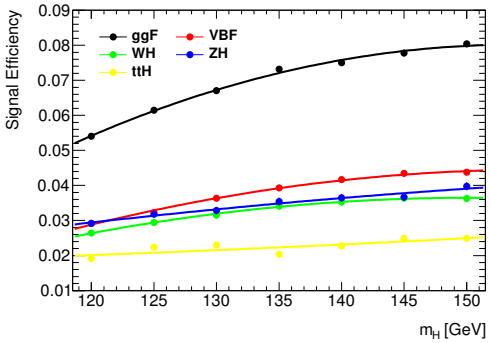

(d) $\mu\mu\gamma$ final state, Low-p_T^t

Figure 6.10: Selection efficiency in 7 TeV $H \to Z\gamma$ signal MC samples. Each distribution is fitted with a second-order polynomial to allow yields to be estimated at arbitrary mass points. Statistical errors were taken into account.

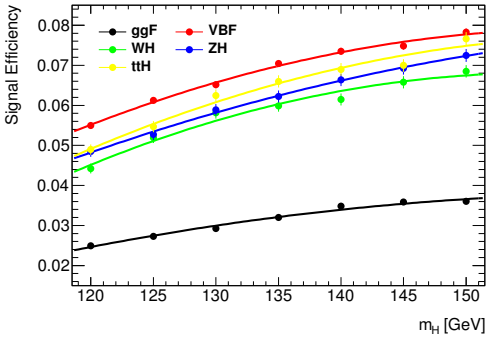

(a) $ee\gamma$ final state, High-p_T^t

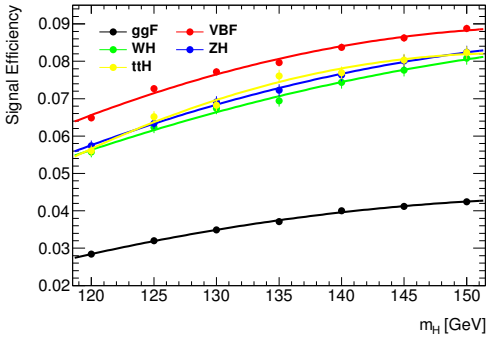

(d) $\mu\mu\gamma$ final state, High-p_T^t

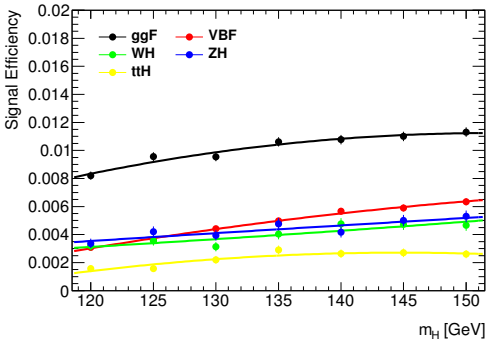

(b) $ee\gamma$ final state, Low-p_T^t, High-$\Delta\eta$

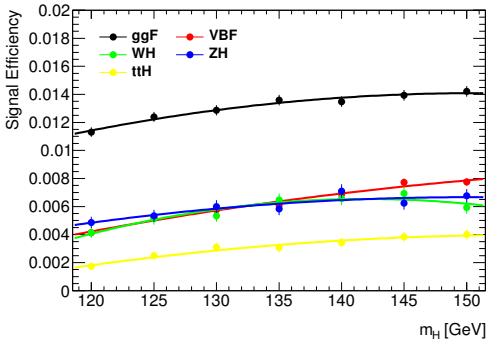

(e) $\mu\mu\gamma$ final state, Low-p_T^t, High-$\Delta\eta$

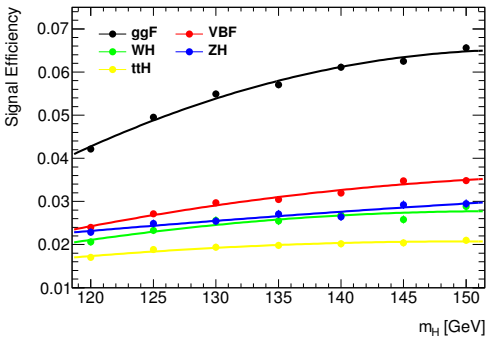

(c) $ee\gamma$ final state, Low-p_T^t, Low-$\Delta\eta$

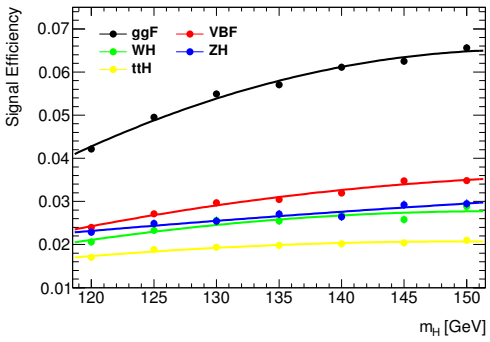

(f) $\mu\mu\gamma$ final state, Low-p_T^t, Low-$\Delta\eta$

Figure 6.11: Selection efficiency in 8 TeV $H \to Z\gamma$ signal MC samples. Each distribution is fitted with a second-order polynomial to allow yields to be estimated at arbitrary mass points. Statistical errors were taken into account.

The Gaussian function has the form:

$$GA\left(x,\mu,\sigma\right) = N\exp\left(-\frac{\left(x-\mu\right)^2}{2\sigma^2}\right), \tag{6.6}$$

where μ and σ define the mean and width of the distribution, respectively, and N is a normalisation parameter designed to scale the integral of the Gaussian to unity. The Crystal Ball function consists of a core Gaussian with a power-law tail, and is given by:

$$CB\left(x,\mu,\sigma,\alpha,n\right) = N\cdot\begin{cases} e^{-t^2/2} & \text{if } t > -\alpha \\ \left(\frac{n}{|\alpha|}\right)^n \cdot e^{-|\alpha|^2/2}\cdot\left(\frac{n}{|\alpha|}-|\alpha|-t\right)^{-n} & \text{if } t \leq -\alpha \end{cases}, \tag{6.7}$$

where $t = (x-\mu)/\sigma$ and N is a normalisation parameter such that the integral of the distribution is unity. The parameters σ and μ denote the mean and sigma of the core Gaussian distribution, α controls how far from μ the Gaussian transitions to the power-law tail, and n affects the slope of the tail.

The full signal model was therefore constructed as:

$$\begin{aligned} R\left(m_{\ell\ell\gamma},\mu_{\text{CB}},\alpha_{\text{CB}},\sigma_{\text{CB}},n_{\text{CB}},f_{\text{CB}},\sigma_{\text{GA}}\right) = {} & f_{\text{CB}}\cdot CB\left[m_{\ell\ell\gamma},\mu_{\text{CB}},\sigma_{\text{CB}},\alpha_{\text{CB}},n_{\text{CB}}\right] \\ & + \left(1-f_{\text{CB}}\right)\cdot GA\left[m_{\ell\ell\gamma},\mu_{\text{CB}},\sigma_{\text{GA}}\right] \end{aligned}, \tag{6.8}$$

where f_{CB} is a mixing fraction that was restricted to the range $0.5 \leq f_{\text{CB}} \leq 1.0$ in order to ensure that the Crystal Ball component dominated the signal model. Note that the Gaussian and Crystal Ball components share a common mean, in order to reduce the complexity of the model and assist in providing stable fits to the $m_{\ell\ell\gamma}$ signal distributions.

In order to construct a signal model at any arbitrary mass point, it is necessary to have some means of interpolating the model parameters between those mass points for which MC samples exist. Certain parameters were found to have a dependence on the nominal Higgs mass (m_H), and so the model was constructed such that μ_{CB}, σ_{CB} and α_{CB} could scale linearly with m_H. The parameters n_{CB} and f_{CB}, and the ratio $\sigma_{\text{GA}}/\sigma_{\text{CB}}$ were found to have a sufficiently mild dependence on m_H that they could be considered independent of it [23].

For each category and production mechanism, the signal MC $m_{\ell\ell\gamma}$ distributions for all available mass points were simultaneously fitted with this model. It was then possible to use the variation of the parameters as a function of m_H to identify the parameters of a signal model at any mass point between 120 and 150 GeV. Within each category, the signal model had nine free parameters: two from each of the three linear variables, and three global variables. The results of the simultaneous fits for events produced through the ggF mechanism are presented in Figures 6.12 and 6.13.

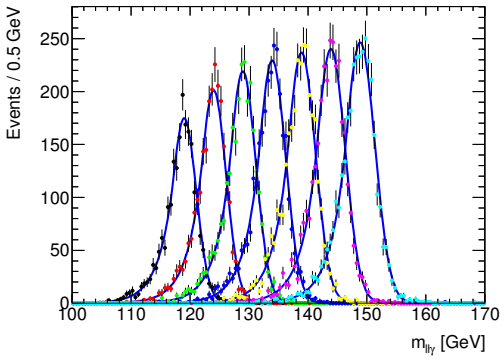

(a) $ee\gamma$ final state, High-p_T^t

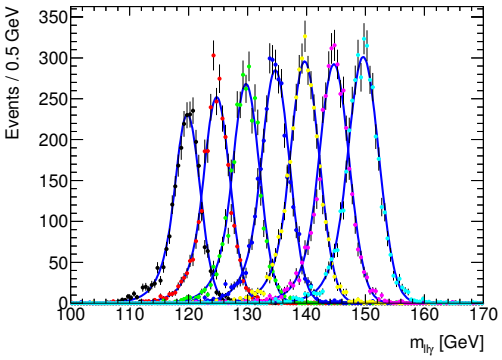

(c) $\mu\mu\gamma$ final state, High-p_T^t

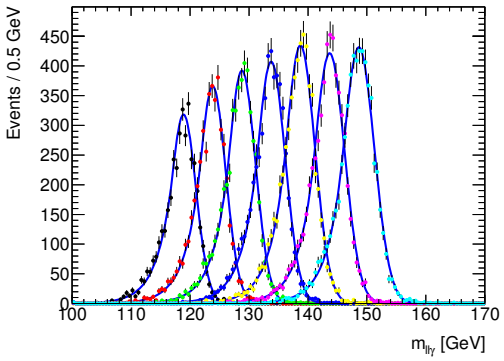

(b) $ee\gamma$ final state, Low-p_T^t

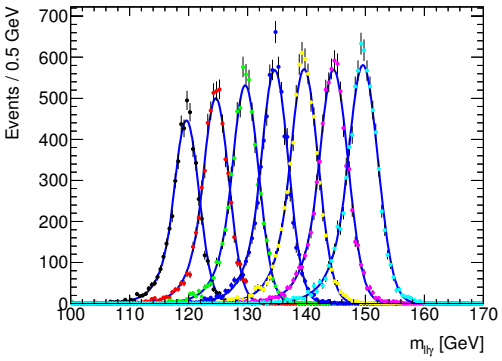

(d) $\mu\mu\gamma$ final state, Low-p_T^t

Figure 6.12: Signal models for the $H \to Z\gamma$, 7 TeV ggF MC samples, for seven different mass points. All mass points were fitted simultaneously with a model composed of a Crystal Ball function summed with a Gaussian function.

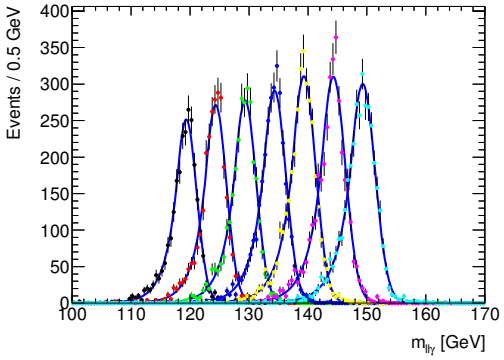

(a) $ee\gamma$ final state, High-p_T^t

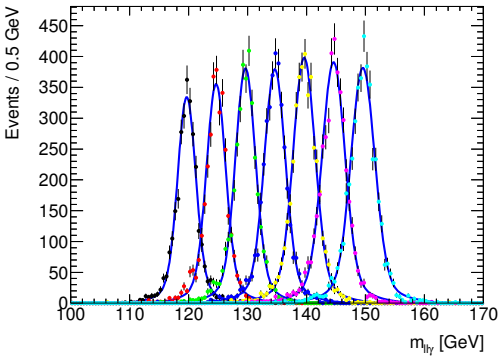

(d) $\mu\mu\gamma$ final state, High-p_T^t

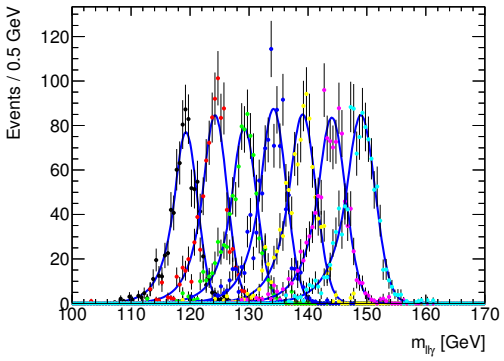

(b) $ee\gamma$ final state, Low-p_T^t, High-$\Delta\eta$

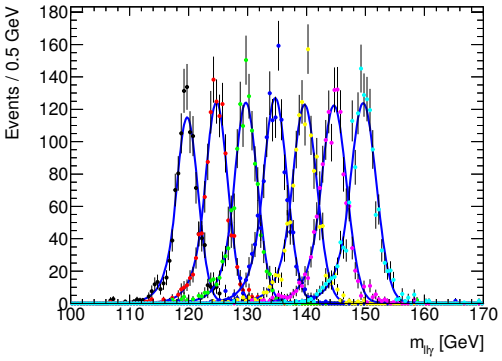

(e) $\mu\mu\gamma$ final state, Low-p_T^t, High-$\Delta\eta$

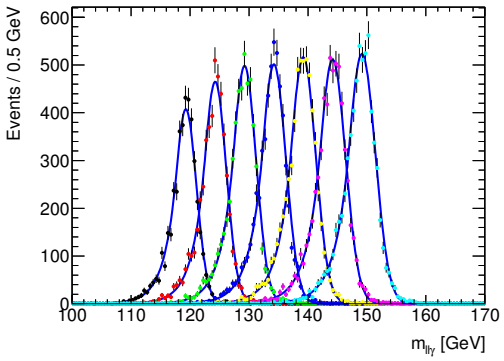

(c) $ee\gamma$ final state, Low-p_T^t, Low-$\Delta\eta$

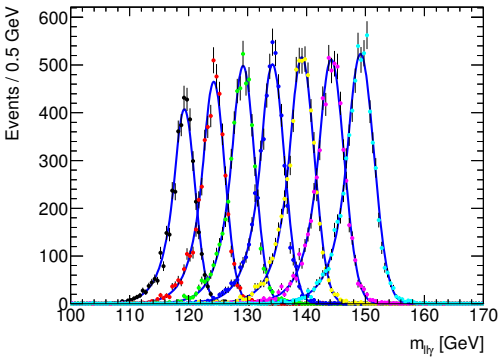

(f) $\mu\mu\gamma$ final state, Low-p_T^t, Low-$\Delta\eta$

Figure 6.13: Signal models for the $H \to Z\gamma$, 8 TeV ggF MC samples, for seven different mass points. All mass points were fitted simultaneously with a model composed of a Crystal Ball function summed with a Gaussian function.

6.2.3 Background Modelling

The invariant mass distributions from the main backgrounds of $Z + \gamma$ and Z + jet combine into a smoothly falling distribution that can be described by an analytical function. In order to remove sources of systematic uncertainty such as the selection efficiencies and the normalisation of individual samples that arise when combining multiple MC background samples, a background model was fitted directly to the data in each category. The functional form of the background model must always be chosen carefully, in order to prevent the introduction of bias that either masks the true signal or creates an artificial peak. The model must also have as few free parameters as possible in order to reduce the uncertainty on the level of background when it is extrapolated into the signal region.

A study was performed [23] using a dedicated high-statistics $Z + \gamma$ Sherpa MC sample (containing 12 million events with $ee\gamma$ and $\mu\mu\gamma$ final states) to test various functional forms for the background distribution in each category. A combined signal and background model was then constructed, and an unbinned likelihood fit to the $m_{\ell\ell\gamma}$ distribution was performed over the range $115 < m_{\ell\ell\gamma} < 170\,\text{GeV}$. This fit should ideally identify zero signal events but, in practice, some level of positive or negative signal (termed spurious signal) will always be reported and this represents a bias in the background model. Figures 6.14 and 6.15 show the level of the spurious signal, divided by its uncertainty, as a function of the Higgs boson mass for various background models in each category. In order to minimise the impact of the spurious signal, the background model selected for each category was taken to be the one with the fewest free parameters for which the level of spurious signal was less than 20% of its fitted uncertainty. Table 6.10 shows the recommended background models for each category, together with the expected signal and background yields for a Higgs boson of mass 125 GeV.

For this analysis, the largest value of the spurious signal across the full mass range was taken to be the signal bias within that category, and was subsequently subtracted from the expected signal yields (see Section 6.2.5). Figures 6.16 and 6.17 show the results of fitting these background models to the data $m_{\ell\ell\gamma}$ distributions in each corresponding category, together with the expected signal distribution for a Higgs boson of mass 125 GeV (scaled by a factor of 50 for visibility).

6.2.4 Systematic Uncertainties

The systematic uncertainties affecting this analysis come from theoretical uncertainties based on the limited knowledge of production cross-sections and branching fractions, and experimental uncertainties based on the way that the data was obtained. The majority of the uncertainties were estimated from the simulated MC samples, before being profiled in the final maximum likelihood fit to the data (as described in Section 6.2.5).

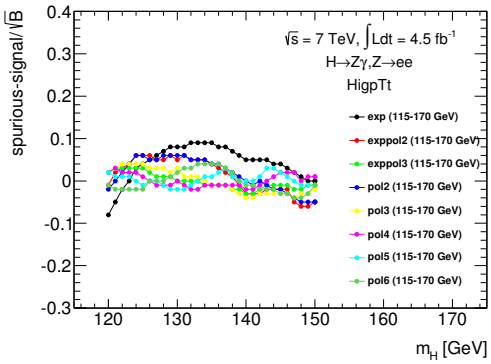

(a) $ee\gamma$ final state, High-p_T^t

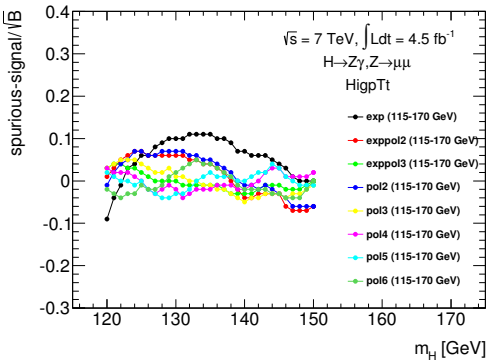

(c) $\mu\mu\gamma$ final state, High-p_T^t

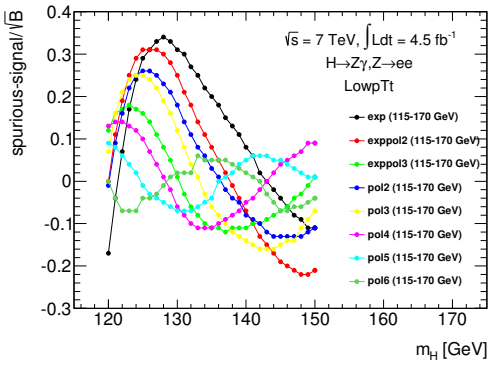

(b) $ee\gamma$ final state, Low-p_T^t

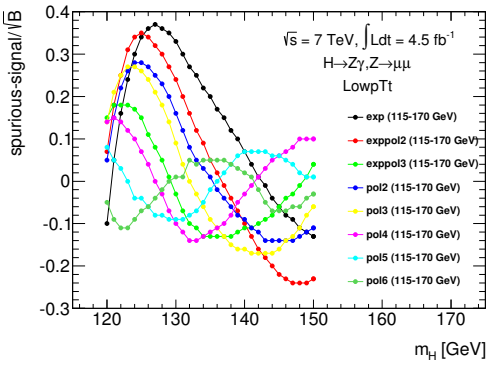

(d) $\mu\mu\gamma$ final state, Low-p_T^t

Figure 6.14: Spurious signal as a function of Higgs boson mass in the 7 TeV categories [23].

$\sqrt{s}$	Final State	Category	Background Model	Degrees of Freedom	$\frac{N_s}{\sqrt{(N_b)}}$
7	$ee\gamma$	High p_T^t	Single expo	1	0.06
		Low p_T^t	Chebyshev 4	4	0.03
	$\mu\mu\gamma$	High p_T^t	Single expo	1	0.06
		Low p_T^t	Chebyshev 4	4	0.03
8	$ee\gamma$	High p_T^t	Expo-poly 2	2	0.12
		Low p_T^t, Low $\Delta\eta$	Chebyshev 5	5	0.08
		Low p_T^t, High $\Delta\eta$	Chebyshev 4	4	0.03
	$\mu\mu\gamma$	High p_T^t	Expo-poly 2	2	0.13
		Low p_T^t, Low $\Delta\eta$	Chebyshev 5	5	0.09
		Low p_T^t, High $\Delta\eta$	Chebyshev 4	4	0.03

Table 6.10: Choice of background model for each kinematic category, together with the signal-to-background ratio of the expected spurious signal. The backgrounds are described by Chebyshev polynomials of various orders, single exponentials, or exponentials of second-order polynomials.

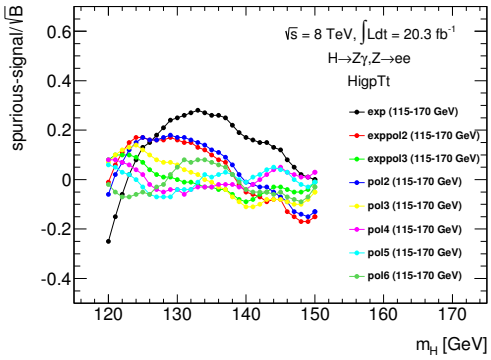

(a) $ee\gamma$ final state, High-p_T^t

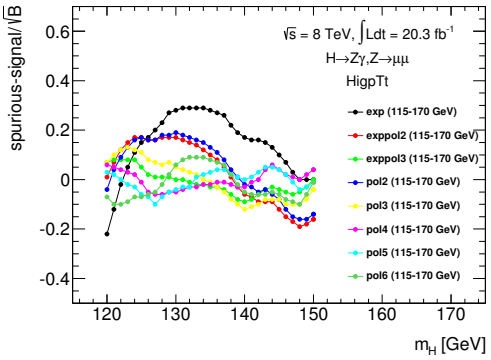

(d) $\mu\mu\gamma$ final state, High-p_T^t

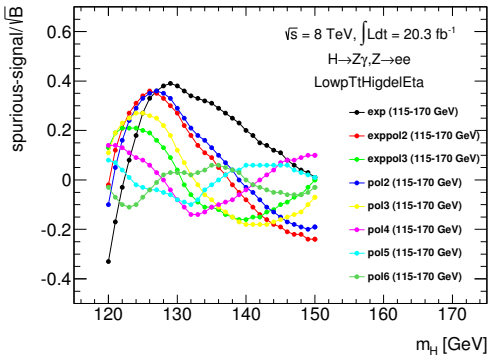

(b) $ee\gamma$ final state, Low-p_T^t, High-$\Delta\eta$

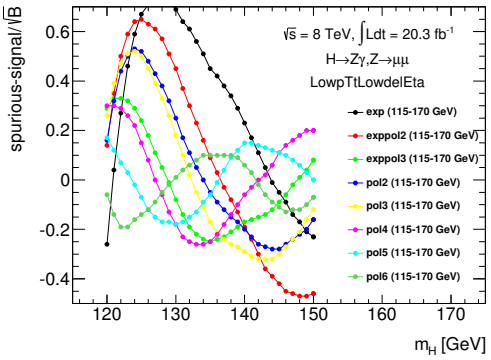

(e) $\mu\mu\gamma$ final state, Low-p_T^t, High-$\Delta\eta$

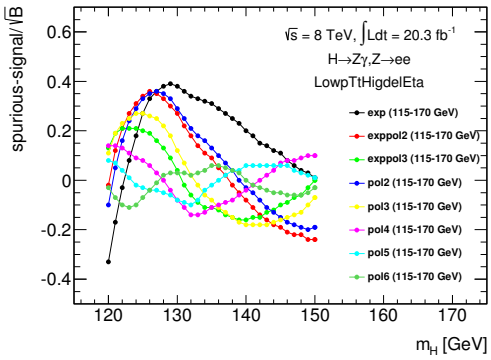

(c) $ee\gamma$ final state, Low-p_T^t, Low-$\Delta\eta$

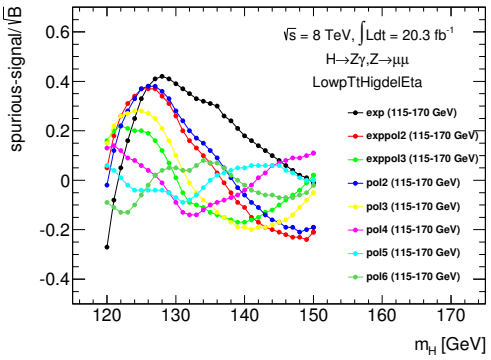

(f) $\mu\mu\gamma$ final state, Low-p_T^t, Low-$\Delta\eta$

Figure 6.15: Spurious signal as a function of Higgs boson mass in the 8 TeV categories [23].

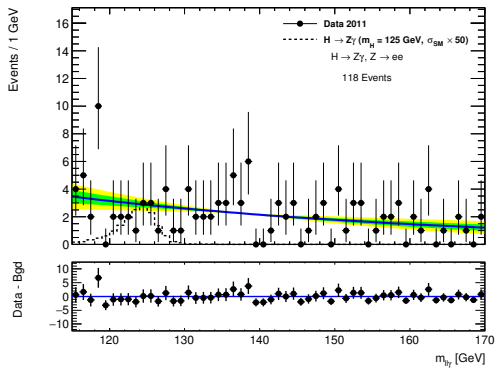

(a) $ee\gamma$ final state, High-p_T^t

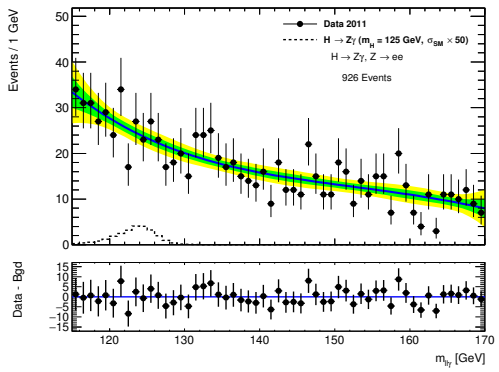

(b) $ee\gamma$ final state, Low-p_T^t, High-$\Delta\eta$

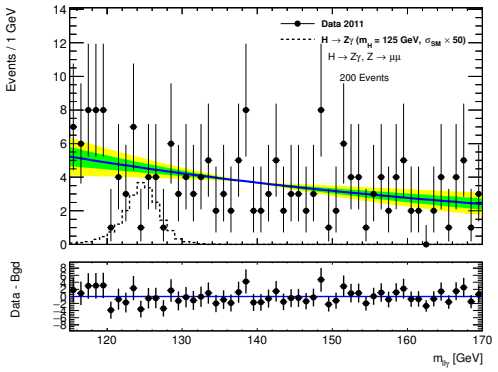

(c) $\mu\mu\gamma$ final state, High-p_T^t

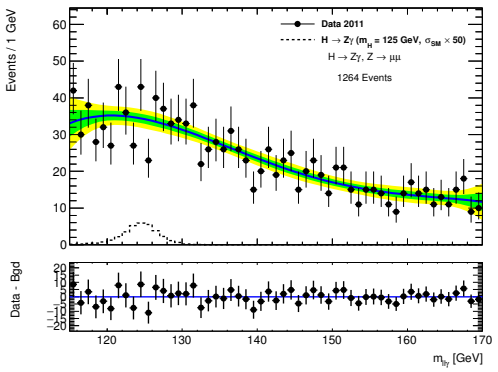

(d) $\mu\mu\gamma$ final state, Low-p_T^t, High-$\Delta\eta$

Figure 6.16: Background-only fit to the $m_{\ell\ell\gamma}$ distribution of events selected from 7 TeV data. The blue line is the fit result, while the green and yellow bands represent the 1σ and 2σ error bands from the uncertainties on the parameters of the fitted functions. The black dashed line is the total expected signal for a Higgs boson of mass 125 GeV, scaled by a factor of 50 for visibility.

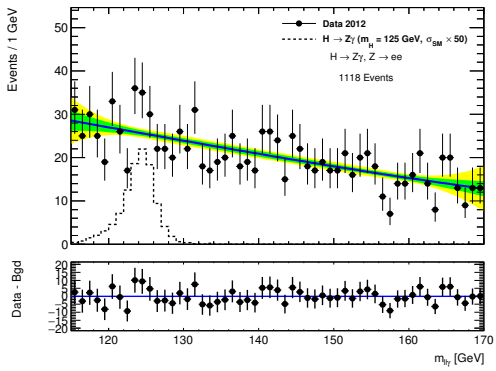

(a) $ee\gamma$ final state, High-p_T^t

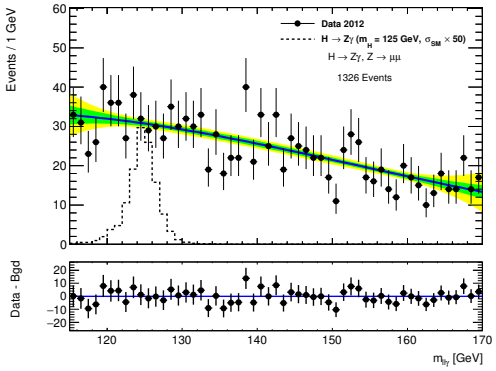

(d) $\mu\mu\gamma$ final state, High-p_T^t

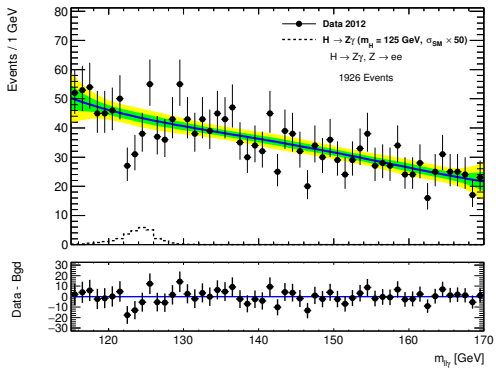

(b) $ee\gamma$ final state, Low-p_T^t, High-$\Delta\eta$

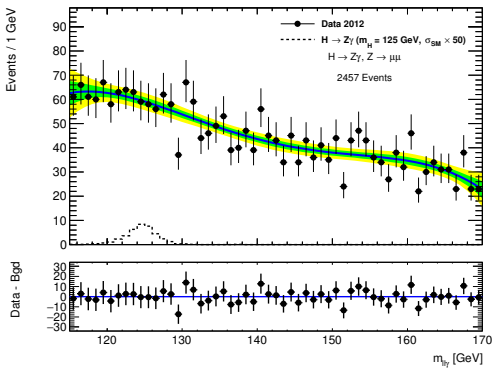

(e) $\mu\mu\gamma$ final state, Low-p_T^t, High-$\Delta\eta$

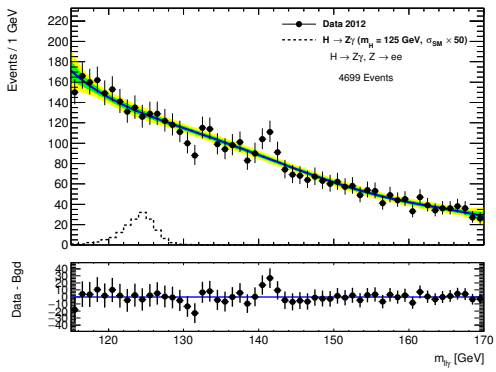

(c) $ee\gamma$ final state, Low-p_T^t, High-$\Delta\eta$

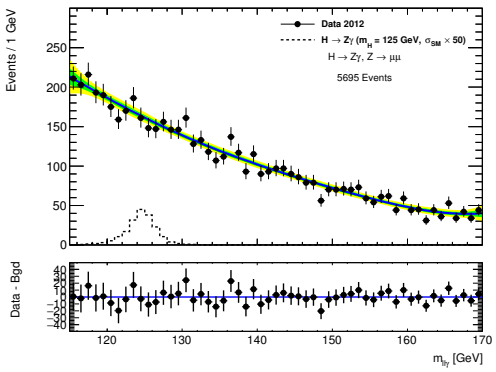

(f) $\mu\mu\gamma$ final state, Low-p_T^t, High-$\Delta\eta$

Figure 6.17: Background-only fit to the $m_{\ell\ell\gamma}$ distribution of events selected from 8 TeV data. The blue line is the fit result, while the green and yellow bands represent the 1σ and 2σ error bands from the uncertainties on the parameters of the fitted functions. The black dashed line is the total expected signal for a Higgs boson of mass 125 GeV, scaled by a factor of 50 for visibility.

6.2.4.1 Theoretical uncertainties

Higgs boson production cross section and branching fraction

The production cross-sections for the Higgs boson were studied by the LHC Higgs Cross-Section Working Group, and have been compiled in Refs. [21, 22]. These sources provide production cross-sections, branching fractions and the corresponding uncertainties for many possible Higgs masses with high granularity.

The theoretical uncertainties on the production cross-section include two components: a scale uncertainty related to energy scales used for the fixed order calculation; and a combined uncertainty from the parton distribution functions and the value of α_s used in the perturbative calculation. The uncertainties provided in Refs. [21, 22] were used for each Higgs mass point considered in this analysis, but for reference the uncertainties at 120 and 150 GeV are summarised in Table 6.11.

Background processes

Theoretical uncertainties on the background cross-section do not apply to this analysis, since the normalisation and model parameters of the background were obtained by directly fitting the observed data. The uncertainties only affect comparisons between data and MC, since the $t\bar{t}$ and WZ background normalisation was obtained from the MC cross-sections. The normalisations for Z + jet and $Z + \gamma$ backgrounds in comparisons between data and MC were extracted directly from data, and were therefore unaffected by the uncertainties on the respective cross-sections [23].

6.2.4.2 Experimental uncertainties

Tables 6.12 and 6.13 list the main sources of systematic uncertainties, together with their contributions to the expected $H \to Z\gamma$ signal yield or the parameters of the signal models, for 7 and 8 TeV respectively. The treatment of the uncertainties as correlated or uncorrelated between the $ee\gamma$ and $\mu\mu\gamma$ final states is also presented in these tables. It should also be noted that all systematic uncertainties are considered to be fully correlated between the 7 and 8 TeV data sets, apart from the uncertainty on the luminosity.

Luminosity

The overall normalisation uncertainty of the integrated luminosity was 1.8% and 2.8% for 7 TeV data and 8 TeV data, respectively (as noted in Section 4.1.1) [71, 72].

Photon reconstruction and identification

An uncertainty on the photon reconstruction efficiency exists because of the presence of additional material in the real detector whose nature and distribution cannot be well modelled in the computer simulations. This uncertainty was ignored since the

Uncertainty source	Relative uncertainty (%)			
	7 TeV, $m_H =$		8 TeV, $m_H =$	
	120 GeV	150 GeV	120 GeV	150 GeV
$\sigma(gg \to H)$ (scale)	$^{+7.2}_{-7.9}$	$^{+6.6}_{-7.4}$	$^{+7.3}_{-7.9}$	$^{+6.7}_{-7.4}$
$\sigma(gg \to H)$ (PDF)	$^{+7.6}_{-7.0}$	$^{+7.6}_{-7.5}$	$^{+7.5}_{-6.9}$	$^{+7.4}_{-7.0}$
σ(VBF) (scale)	$^{+0.3}_{-0.4}$	$^{+0.2}_{-0.1}$	$^{+0.2}_{-0.2}$	$^{+0.3}_{-0.2}$
σ(VBF) (PDF)	$^{+2.4}_{-2.1}$	$^{+2.7}_{-2.1}$	$^{+2.6}_{-2.8}$	$^{+2.5}_{-2.7}$
$\sigma(WH)$ (scale)	$^{+0.9}_{-0.9}$	$^{+0.9}_{-0.9}$	$^{+1.0}_{-1.0}$	$^{+1.0}_{-1.0}$
$\sigma(WH)$ (PDF)	$^{+2.6}_{-2.6}$	$^{+3.6}_{-3.6}$	$^{+2.5}_{-2.5}$	$^{+2.5}_{-2.6}$
$\sigma(ZH)$ (scale)	$^{+2.8}_{-2.8}$	$^{+3.0}_{-3.0}$	$^{+3.0}_{-3.0}$	$^{+3.9}_{-3.9}$
$\sigma(ZH)$ (PDF)	$^{+2.8}_{-2.8}$	$^{+3.7}_{-3.7}$	$^{+2.5}_{-2.5}$	$^{+2.7}_{-2.7}$
$\sigma(t\bar{t}H)$ (scale)	$^{+3.4}_{-9.3}$	$^{+2.8}_{-9.1}$	$^{+3.9}_{-9.3}$	$^{+3.4}_{-9.1}$
$\sigma(t\bar{t}H)$ (PDF)	$^{+8.4}_{-8.4}$	$^{+8.5}_{-8.5}$	$^{+8.1}_{-8.1}$	$^{+8.2}_{-8.2}$
$\mathcal{B}(H \to Z\gamma)$	$^{+9.4}_{-9.3}$	$^{+6.4}_{-6.5}$	$^{+9.4}_{-9.3}$	$^{+6.4}_{-6.5}$

Table 6.11: Theoretical systematic uncertainties for the SM Higgs boson production cross section and branching fraction of the $H \to Z\gamma$ decay at the boundaries of the tested Higgs boson mass range (120 and 150 GeV) [23].

Systematic Uncertainty	$H \to Z(\mu\mu)\gamma$(%)	$H \to Z(ee)\gamma$(%)	Uncertainty Treatment
Signal Yield			
Luminosity	1.8	1.8	correlated
Trigger	0.74	0.17	uncorrelated
	0.70	0.14	
γ ID efficiency	2.59	2.57	correlated
	3.01	2.98	
electron reco+ID efficiency	–	2.57$\oplus$1.18	uncorrelated
	–	1.75$\oplus$1.06	
μ reco+ID efficiency	0.69	–	uncorrelated
	0.65	–	
e/γ Energy Scale	0.3	0.4	correlated
	0.2	0.4	
e/γ isolation	0.38	0.19	correlated
	0.17	0.31	
e/γ energy resolution	0.13	0.20	correlated
	0.12	0.39	
μ momentum scale	0.28	–	correlated
	0.06	–	
μ momentum resolution	0.3	–	correlated
	0.2	–	
Signal $m_{\ell\ell\gamma}$ resolution			
e/γ Energy Resolution	3.25	9.95	correlated
μ momentum Resolution	1.5	–	
Signal $m_{\ell\ell\gamma}$ peak position			
e/γ Energy Scale	0.2 GeV	0.2 GeV	correlated
muon momentum scale	negligible	–	negligible

Table 6.12: Summary of the systematic uncertainties on the signal yield and invariant mass distribution for $m_H = 125$ GeV, at $\sqrt{s} = 7$ TeV. The numbers are listed in two categories: high-p_T^t (top), low-p_T^t (bottom) [23].

Systematic Uncertainty	$H \to Z(\mu\mu)\gamma(\%)$	$H \to Z(ee)\gamma(\%)$	Uncertainty Treatment
Signal Yield			
Luminosity	2.8	2.8	correlated
Trigger	0.87	0.44	uncorrelated
	0.83	0.41	
	0.67	0.36	
γ ID efficiency	2.51	2.53	correlated
	3.10	3.09	
	3.13	3.07	
electron reco+ID efficiency	–	1.46$\oplus$2.41	uncorrelated
	–	1.42$\oplus$2.46	
	–	1.36$\oplus$2.08	
μ reco+ID efficiency	0.65	–	uncorrelated
	0.64	–	
	0.65	–	
e/γ Energy Scale	0.6	1.6	correlated
	0.2	1.7	
	0.7	2.6	
e/γ isolation	0.34	0.40	correlated
	0.38	0.35	
	0.59	0.32	
e/γ energy resolution	0.19	0.26	correlated
	0.09	0.05	
	0.31	1.25	
μ momentum scale	0.35	–	correlated
	0.03	–	
	0.03	–	
μ momentum resolution	0.30	–	correlated
	0.20	–	
	0.30	–	
Signal $m_{\ell\ell\gamma}$ resolution			
e/γ energy resolution	2.69	10.62	correlated
μ momentum resolution	0.5	–	negligible
Signal $m_{\ell\ell\gamma}$ peak position			
e/γ energy scale	0.2 GeV	0.2 GeV	correlated
muon momentum scale	negligible	–	negligible

Table 6.13: Summary of the systematic uncertainties on the signal yield and invariant mass distribution for $m_H = 125\,\text{GeV}$, at $\sqrt{s} = 8\,\text{TeV}$. The numbers are listed in three categories: high p_{Tt} (top), low p_{Tt} & low $\Delta\eta$ (medium), low p_{Tt} & high $\Delta\eta$ (bottom) [23].

efficiencies computed using MC samples produced with nominal and distorted detector geometries were found to be in good agreement within statistical uncertainties.

The photon identification efficiency was measured in data and compared against the value obtained from MC samples, in order to assign a systematic uncertainty on this efficiency as a function of the photon transverse energy, pseudorapidity, and status as a converted or unconverted photon. The photon efficiency was then shifted by its uncertainty, as per official recommendations [157], and the relative variation in the signal yield was taken as a systematic uncertainty.

Photon and electron isolation requirements

Differences of around 100 MeV (500 MeV) between data and simulation were observed for topological-cluster (standard cell) based isolation of photons, selected from di-photon enriched events, and electrons, selected from a $Z \to ee$ control sample. In signal MC samples, the photon and electron isolation was shifted by ± 100 MeV (± 500 MeV for electrons from 7 TeV samples) on an event-by-event basis and the full event selection was performed again. The relative variation in the signal yield with respect to the nominal result was used as the corresponding systematic uncertainty.

Photon and electron energy scale

A difference exists between the electromagnetic energy scales in data and MC samples that gives rise to an uncertainty on the signal efficiency (which then propagates to an uncertainty on the expected signal yield) and the mean position of the $m_{\ell\ell\gamma}$ signal peak. The e/γ working group EnergyRescalerUpgrade tool [107, 158] was used to vary the energy scale within its uncertainties, and the efficiency and yield were then recalculated to allow evaluation of this systematic uncertainty. The $m_{\ell\ell\gamma}$ distribution was also reconstructed, and the relative shift of the peak position was taken as the systematic uncertainty on the signal PDF.

Photon and electron energy resolution

A difference exists between the constant term of the electromagnetic calorimeter resolution in data and MC samples, which gives rise to an uncertainty on the signal yield (albeit a small one) and on the width of the $m_{\ell\ell\gamma}$ signal peak. As noted in Section 4.2.1.3, the MC samples are already corrected by smearing the energy resolution to match data. The e/γ working group EnergyRescalerUpgrade tool [107, 158] was used to vary that correction within its uncertainties, and the relative variation of the signal yield was taken as a systematic uncertainty. The $m_{\ell\ell\gamma}$ distribution was also reconstructed and the relative variation in the width of the signal PDF was taken as another systematic uncertainty.

Electron trigger, reconstruction and identification efficiency

Trigger, reconstruction and efficiency scale factors were used to correct the MC samples to match the data selection efficiency, as noted in Section 4.2.1.3, but this gives rise to an uncertainty on the signal yield. These efficiency scale factors were varied within their uncertainties in accordance with official recommendations [158, 159], and the relative variation of the signal yield was taken as a systematic uncertainty. A scale factor of 1 was assumed for the additional requirements on the b-layer hits and the longitudinal impact parameter that were applied on top of the standard "Loose" cut-based selection criteria (described in Section 5.3.2).

Muon momentum

The uncertainty on the muon momentum selection requirement of $p_{\mathrm{T}} > 10\,\mathrm{GeV}$ (or $p_{\mathrm{T}} > 15\,\mathrm{GeV}$ in the case of CT muons, see Section 5.4), was estimated by varying the MC muon momentum corrections by their uncertainties. The muon momentum was varied by the uncertainty on its resolution, in accordance with official recommendations [160]. The resultant variations in the signal yields and resolution were then taken as systematic uncertainties.

Muon trigger, reconstruction and identification efficiency

As in the case of electrons described above, a set of trigger, reconstruction and efficiency scale factors were used to correct the MC samples to match the data selection efficiency. These efficiency scale factors were varied within their uncertainties in accordance with official recommendations [160], and the relative variation of the signal yield was taken as a systematic uncertainty.

Background modelling

The method to estimate the bias in the signal arising from the choice of background model (the spurious signal) was discussed in Section 6.2.3. This is treated as a correction to the expected signal yield, as described in Section 6.2.5.

6.2.5 Exclusion Limits and p-values

Likelihood-based statistical tests were used to search for evidence of a SM Higgs boson decaying to a $Z\gamma$ final state within the selected data samples. The tests were similar to those used in searches for the Higgs decaying to other final states and gave results which can be expressed in terms of a signal-strength parameter μ:

$$\mu = \frac{N_S}{N_S^{SM}}, \tag{6.9}$$

which is the ratio of the measured number of signal events to the SM expectation. For a SM Higgs boson undergoing the decay $H \to Z\gamma$, the value of μ from each of

the categories into which the data was subdivided should be consistent with a single overall value of unity (within statistical uncertainties).

6.2.5.1 Evaluating the Likelihood

The Modified Frequentist method (CL_s method) [161] was used to interpret the data, as per official recommendations from the ATLAS Collaboration. The results were obtained using an unbinned maximum likelihood that depended solely on the three-body invariant mass $m_{\ell\ell\gamma}$, which is denoted as x in the following to simplify the notation and provide clarity. There was only one parameter of interest, μ, but the likelihood also depends on several additional "nuisance" parameters, such as the number of background events or parameters describing the signal or background models. For some of these nuisance parameters there may be additional prior information available (for example, from theoretical calculations or from measurements performed using control samples), in which case the corresponding probability density function for those parameters was incorporated into the full likelihood function.

The data set was split into ten categories (as defined in Figure 6.7) and a simultaneous unbinned maximum likelihood fit to the distribution of x in all categories was then performed. The likelihood is defined as:

$$L\left(\mu, \boldsymbol{\theta} = \bigcup_{c=1}^{n_{cat}} \boldsymbol{\theta} \middle| \boldsymbol{x} = \bigcup \boldsymbol{x}_c\right) = \prod_{c=1}^{n_{cat}} L_c\left(\mu, \boldsymbol{\theta}_c \middle| \boldsymbol{x}_c\right), \tag{6.10}$$

where n_{cat} is the number of categories (10) that the data was subdivided into, $\boldsymbol{\theta}_c$ is the set of nuisance parameters used to describe the model in category c, and $\boldsymbol{x}_c$ is the set of measurements of x in category c. The term L_c is the likelihood for the individual category c:

$$L_c\left(\mu, \boldsymbol{\theta}_c \middle| \boldsymbol{x}_c\right) = e^{-N_{SB,c}} {N_{SB,c}}^{N_c} \prod_{k=1}^{N_c} \mathcal{L}_c\left(x_k \middle| \mu, \boldsymbol{\theta}_c\right), \tag{6.11}$$

where N_c is the number of selected events, x_k is the value of x in event k, and $N_{SB,c}$ is the sum of the numbers of signal and background events ($N_{S,c}$ and $N_{B,c}$, respectively). The term $e^{-N_{SB,c}} {N_{SB,c}}^{N_c}$ is a Poisson probability factor that, when the likelihood is maximised with respect to it, forces the estimates of the signal and background yields to satisfy $\hat{N}_{S,c} + \hat{N}_{B,c} = N_c$. The term $\mathcal{L}_c(x|\mu, \boldsymbol{\theta}_c)$ is the per-event likelihood, which describes the probability of measuring $x = x_k$ in category c for the given values of μ and $\boldsymbol{\theta}_c$. It is defined as:

$$\mathcal{L}_c(x|\mu, \boldsymbol{\theta}_c) = \frac{N_{S,c}\left(\mu, \boldsymbol{\theta}_c^{yield}\right)}{N_{S,c} + N_{B,c}} f_{S,c}\left(x \middle| \boldsymbol{\theta}_c^{sig}\right) + \frac{N_{B,c}}{N_{S,c} + N_{B,c}} f_{B,c}\left(x \middle| \boldsymbol{\theta}_c^{bgd}\right), \tag{6.12}$$

where $f_{S,c}$ and $f_{B,c}$ are the signal and background probability density functions, respectively. The terms $\boldsymbol{\theta}_c^{yield}$, $\boldsymbol{\theta}_c^{sig}$, $\boldsymbol{\theta}_c^{bgd}$ are the nuisance parameters used to describe the expected signal yield, the signal PDF, and the background PDF respectively. The full set of nuisance parameters is therefore defined as $\boldsymbol{\theta}_c = \boldsymbol{\theta}_c^{yield} \cup \boldsymbol{\theta}_c^{sig} \cup \boldsymbol{\theta}_c^{bgd} \cup \{N_{B,c}\}$.

The number of signal events in each category c is given by:

$$N_{S,c}\left(\mu, \boldsymbol{\theta}_c^{yield}\right) = \left[\mu \times \left(\sum^{i} N_{i,c}^{SM}\left(\boldsymbol{\theta}^i\right)\right) \times f\left(\boldsymbol{\theta}_\varepsilon\right)\right] + \sigma_{spurious,c}\theta_{spurious,c}, \quad (6.13)$$

where $N_{i,c}^{SM}\left(\boldsymbol{\theta}^i\right)$ $(i = ggF, VBF, WH, ZH, t\bar{t}H)$ is the expected number of SM $H \to Z\gamma$ decays for a Higgs boson produced through production mechanism i, and $\boldsymbol{\theta}^i$ is the set of nuisance parameters affecting the theoretical production cross-sections σ_i. The term $f\left(\boldsymbol{\theta}_{\varepsilon,BF}\right)$ is a function of nuisance parameters that take into account the systematic uncertainties on the branching fraction and event selection efficiencies, described in more detail in the following subsection. It would equal one and $N_{i,c}^{SM}$ would then be a constant if the $H \to Z\gamma$ branching fraction and the efficiency could be perfectly known. The final term $\sigma_{spurious,c}\theta_{spurious,c}$ represents the number of events due to the bias on the choice of background model, and is also discussed in the following subsection.

6.2.5.2 Systematic Uncertainties and Nuisance Parameters

The systematic uncertainties described in Section 6.2.4 were introduced to the likelihood calculation by adding a nuisance parameter θ for each uncertainty, such that the affected quantities (the yields or model parameters for signal and background) became functions of θ. A constraint term was then included in the likelihood so that the systematic uncertainty would be held close to the value that had been estimated for it. The nuisance parameters were then fitted, or profiled, to the data together with the parameter of interest, μ, when maximising the likelihood.

The constraint term took a Gaussian form for uncertainties on the model shape parameters or event migrations between categories. The affected quantity in the likelihood was multiplied by a term of the form:

$$(1 + \sigma\theta), \quad (6.14)$$

where θ is the nuisance parameter and σ is the best estimate of the relative uncertainty. The likelihood was then multiplied by a normal distribution $G(\theta)$ of mean zero and width unity - this construction meant that the PDF for $(1 + \sigma\theta)$ was therefore a Gaussian with mean one and width of σ. In the cases of a few asymmetric theoretical uncertainties, the Gaussian constraints were replaced with bifurcated Gaussians. The value σ was treated as the negative uncertainty, the right width was assigned the ratio of positive to negative uncertainties, and the left width was taken to be unity.

More generally, a log-normal constraint was adopted and the affected quantity in the likelihood was multiplied by a term of the form:

$$\exp\left(\sqrt{\log\left(1 + \sigma^2\right)}\theta\right), \quad (6.15)$$

where θ and σ are again the nuisance parameter and best estimate of the relative uncertainty, respectively. The likelihood was then multiplied by a normal distribution $G(\theta)$, which meant that the logarithm of the above term therefore had a Gaussian form of mean zero and width one.

The theoretical uncertainties (see Section 6.2.4.1) on the Higgs production cross-sections were accounted for by using log-normal constraints for the scale uncertainties and Gaussian constraints for the uncertainties from variations of the PDF set's eigenvalues. This affected the expected signal yields in each Higgs production mechanism, modifying the following terms from Equation 6.13:

$$\begin{aligned}
N^{SM}_{\mathrm{gg},c}(\theta^{gg}) &= N^{SM}_{\mathrm{gg},c} \exp\left(\sqrt{\log(1+\sigma^2_{gg_scale})}\theta_{gg_scale}\right)(1+\sigma_{gg_PDF,gg}\theta_{gg_PDF}),\\
N^{SM}_{\mathrm{VBF},c}(\theta^{VBF}) &= N^{SM}_{\mathrm{VBF},c} \exp\left(\sqrt{\log(1+\sigma^2_{VBF_scale})}\theta_{VBF_scale}\right)(1+\sigma_{q\bar{q}_PDF,VBF}\theta_{q\bar{q}_PDF}),\\
N^{SM}_{\mathrm{WH},c}(\theta^{WH}) &= N^{SM}_{\mathrm{WH},c} \exp\left(\sqrt{\log(1+\sigma^2_{WH_scale})}\theta_{WH_scale}\right)(1+\sigma_{q\bar{q}_PDF,WH}\theta_{q\bar{q}_PDF}),\\
N^{SM}_{\mathrm{ZH},c}(\theta^{ZH}) &= N^{SM}_{\mathrm{ZH},c} \exp\left(\sqrt{\log(1+\sigma^2_{ZH_scale})}\theta_{ZH_scale}\right)(1+\sigma_{q\bar{q}_PDF,ZH}\theta_{q\bar{q}_PDF}),\\
N^{SM}_{\mathrm{ttH},c}(\theta^{ttH}) &= N^{SM}_{\mathrm{ttH},c} \exp\left(\sqrt{\log(1+\sigma^2_{ttH_scale})}\theta_{ttH_scale}\right)(1+\sigma_{gg_PDF,ttH}\theta_{gg_PDF}).
\end{aligned} \tag{6.16}$$

The likelihood was then multiplied by a collection of normal distributions:

$$G(\theta_{gg\_scale})G(\theta_{VBF\_scale})G(\theta_{WH\_scale})G(\theta_{ZH\_scale})G(\theta_{ttH\_scale})G(\theta_{gg\_PDF})G(\theta_{q\bar{q}\_PDF}). \tag{6.17}$$

It should be noted that while there are five scale uncertainties σ_{i_scale} and five PDF uncertainties σ_{i_PDF} corresponding to the five Higgs production mechanisms, only seven nuisance parameters and constraints were applied. Production of the Higgs boson through the ggF and $t\bar{t}$ mechanisms involves the interaction of two gluons, where uncertainty arises due to limited knowledge of the gluon PDF. The PDF uncertainties for both of these mechanisms are therefore fully correlated, and can be described by a single nuisance parameter, θ_{gg_PDF}. Production of the Higgs boson through the VBF, WH and ZH mechanisms involve $q\bar{q}$ interactions, where uncertainty arises due to limited knowledge of the quark PDFs. By the same logic, the PDF uncertainties for these three mechanisms are fully correlated and can be described by a single nuisance parameter, $\theta_{q\bar{q}\_PDF}$.

In order to take into account the experimental systematic uncertainties (described in Section 6.2.4), the following term was added in Equation 6.13:

$$\begin{aligned} f\left(\boldsymbol{\theta}_{\varepsilon}\right) = & \exp\left(\sqrt{\log\left(1+\sigma^2_{luminosity}\right)}\theta_{luminosity}\right) \\ & \exp\left(\sqrt{\log\left(1+\sigma^2_{trigger}\right)}\theta_{trigger}\right) \\ & \exp\left(\sqrt{\log\left(1+\sigma^2_{generator}\right)}\theta_{generator}\right) \\ & \exp\left(\sqrt{\log\left(1+\sigma^2_{\gamma-ID}\right)}\theta_{\gamma-ID}\right) \\ & \exp\left(\sqrt{\log\left(1+\sigma^2_{lepton-ID}\right)}\theta_{lepton-ID}\right) \\ & \exp\left(\sqrt{\log\left(1+\sigma^2_{e\gamma-ES}\right)}\theta_{e\gamma-ES}\right) \\ & \exp\left(\sqrt{\log\left(1+\sigma^2_{e\gamma-ISO}\right)}\theta_{e\gamma-ISO}\right) \\ & \exp\left(\sqrt{\log\left(1+\sigma^2_{e\gamma-smear}\right)}\theta_{e\gamma-smear}\right), \end{aligned} \tag{6.18}$$

where the uncertainties σ_j are those described in Section 6.2.4 and summarised in Tables 6.12 and 6.13. The asymmetric systematic uncertainty on the $H \to Z\gamma$ branching fraction is also taken into account.

Finally, the systematic uncertainty for the spurious signal (described in Section 6.2.3) was included by adding the following term to the expected signal yield given in Equation 6.13, as noted previously:

$$\sigma_{spurious,c}\theta_{spurious,c}, \tag{6.19}$$

The likelihood was then multiplied by a normal distribution, $G\left(\theta_{spurious,c}\right)$, and the nuisance parameter $\theta_{spurious,c}$ was profiled in the same manner as the other uncertainties.

6.2.5.3 Calculating p-values

In order to evaluate the compatibility of the data with the background-only (B-only) hypothesis, where $\mu = 0$, the likelihood was used to compute the p_0 value of the data. This gives the probability for a dataset generated under the B-only hypothesis to be in the same or worse agreement with that hypothesis. The p_0 computation begins with the evaluation of the test statistics q_0:

$$q_0 = \begin{cases} -2\ln\frac{L\left(0,\hat{\hat{\boldsymbol{\theta}}}(0)\right)}{L\left(\hat{\mu},\hat{\boldsymbol{\theta}}\right)} & \hat{\mu} \geq 0 \\ +2\ln\frac{L\left(0,\hat{\hat{\boldsymbol{\theta}}}(0)\right)}{L\left(\hat{\mu},\hat{\boldsymbol{\theta}}\right)} & \hat{\mu} < 0 \end{cases}, \tag{6.20}$$

where L is the likelihood function, $\hat{\mu}$ and $\hat{\boldsymbol{\theta}}$ are the best fit values for μ and $\boldsymbol{\theta}$ when all parameters are floating, and $\hat{\hat{\boldsymbol{\theta}}}\left(0\right)$ is the best fit value of $\boldsymbol{\theta}$ in the B-only hypothesis. The numerator is the best value of the likelihood in the B-only hypothesis and the denominator is the best value in the S+B hypothesis, which contains both signal and

background. In datasets which are compatible with the B-only hypothesis, these two values should be of comparable size and q_0 will be small. If a signal is present, however, the denominator will be greater than the numerator and so q_0 will be large. The p-value of the B-only hypothesis is then:

$$p_0 = \int_{q_{0,\text{obs}}}^{\infty} f(q_0|0, m_H, \hat{\boldsymbol{\theta}}(0))dq_0, \tag{6.21}$$

where f is the distribution of the test statistic q_0.

Only deviations from the B-only hypothesis corresponding to a positive signal strength have been considered here. If a positive signal is present then q_0 will be large and positive, and p_0 will be small. Large p_0 values are therefore indicative of a good agreement between the dataset and the B-only hypothesis. Negative signal fluctuations are assigned p_0 values in the range $[0.5, 1.0]$, with small negative fluctuations giving p_0 close to 0.5 and large negative fluctuations giving p_0 close to 1.

In the following, the observed p_0 was computed using real data and the expected p_0 was computed from an Asimov dataset [162] generated in the S+B hypothesis where $\mu = 1$.

6.2.5.4 Setting Limits

Upper limits on μ were set using a modified frequentist (CL_s) [161] method, using a CL_{s+b} that was based on the $\tilde{q}_\mu$ test statistic which is defined as:

$$q_0 = \begin{cases} -2\ln\frac{L\left(\mu,\hat{\boldsymbol{\theta}}(\mu)\right)}{L\left(\hat{\mu},\hat{\boldsymbol{\theta}}\right)} & 0 \leq \hat{\mu} \leq \mu \\ 0 & \hat{\mu} > \mu \\ -2\ln\frac{L\left(0,\hat{\boldsymbol{\theta}}(0)\right)}{L\left(\hat{\mu},\hat{\boldsymbol{\theta}}\right)} & \hat{\mu} < 0 \end{cases}, \tag{6.22}$$

where L is the likelihood function, $\hat{\mu}$ and $\hat{\boldsymbol{\theta}}$ are the best fit values for μ and $\boldsymbol{\theta}$ when all parameters are floating, and $\hat{\boldsymbol{\theta}}(\mu)$ is the best fit value of $\boldsymbol{\theta}$ for the given value of μ. The compatibility of the data with the μ hypothesis is done using the ratio of likelihoods for the cases of floating and fixed values of μ. If $\hat{\mu} > \mu$ then $\tilde{q}_\mu$ is assigned a value of zero, as was done in the case of q_0. Finally, if $\hat{\mu} < 0$ then the $\mu = 0$ hypothesis is used to prevent complications from negative PDFs.

The p-value corresponding to CL_{s+b} is defined as:

$$p_\mu = \int_{q_{\mu,\text{obs}}}^{\infty} f\left(\tilde{q}_\mu|\mu, m_H, \hat{\boldsymbol{\theta}}(\mu)\right) d\tilde{q}_\mu, \tag{6.23}$$

and the p-value corresponding to CL_s is defined as:

$$p'_\mu = \frac{p_\mu}{1 - p_b}, \tag{6.24}$$

where

$$p_\mu = 1 - \int_{q_{\mu,\mathrm{obs}}}^{\infty} f\left(\tilde{q}_\mu | 0, m_H, \hat{\boldsymbol{\theta}}\,(0)\right) d\tilde{q}_\mu. \tag{6.25}$$

The value of p'_μ and the corresponding CL_s exclusion were obtained using either the asymptotic formula or psuedo-data generation. In order to set limits on the value of μ at 95% confidence level, values of μ were scanned to identify the one for which the corresponding CL_s exclusion was 0.05.

Observed limits were computed using real data, expected limits were computed using an Asimov dataset generated in the $\mu = 0$ hypothesis.

6.2.6 Results

Figure 6.18 shows the expected and observed p_0 values as a function of the Higgs boson mass. Higgs boson mass hypotheses between 120 and 150 GeV were tested, using 4.5 fb^{-1}of pp collisions at 7 TeV and 20.3 fb^{-1}of pp collisions at 8 TeV. The expected p_0 was found to range from 0.35 to 0.43, which corresponds to significances of approximately 0.4σ. The observed p_0 was found to range from 0.98 (-2.08σ) to 0.027 (0.313σ), with the largest significance occurring for $m_H = 142$ GeV. For a Higgs boson of mass 125 GeV, the expected and observed p_0 values were 0.41 (0.22σ) and 0.27 (0.62σ), respectively.

Since no significant excess above background was observed, upper limits were set on the production cross section of a SM Higgs boson decaying to $Z\gamma$ (normalised by the SM expectation). Figure 6.19 shows the expected and observed limits as a function of the Higgs boson mass over the range 120 to 150 GeV. The expected 95% CL limits varies between 5.11 and 15.80, while the observed limit varies between 3.12 and 17.63. For a Higgs boson of mass 125 GeV, the expected and observed limits were 9.01 and 10.95, respectively.

6.3 Optimising VBF selection criteria

When an SM Higgs boson is produced through the VBF production mechanism, the event is characterised by the production of two forward hadronic jets (as noted in Section 2.5). An attempt was therefore made to exploit this feature by introducing a VBF category for events produced in this manner. Any events containing two or more jets were initially considered as VBF candidates. The jets were searched to identify the pair with the highest total invariant mass, and all other jets were discarded.

Table 6.14 provides a brief description of the variables that were investigated. Those variables connected to the dijet system (such as $|\Delta\eta_{jj}|$ or m_{jj}) were obvious choices for study, while others (such as η_{Zep} or p_T^t) were considered due to their use in similar VBF studies for the $H \to \gamma\gamma$ analysis.

The Toolkit for Multivariate Data Analysis (TMVA) package [163] was configured to perform a cut-based multi-variate analysis on the chosen signal and background samples, using various combinations of some or all of the selected variables. The result

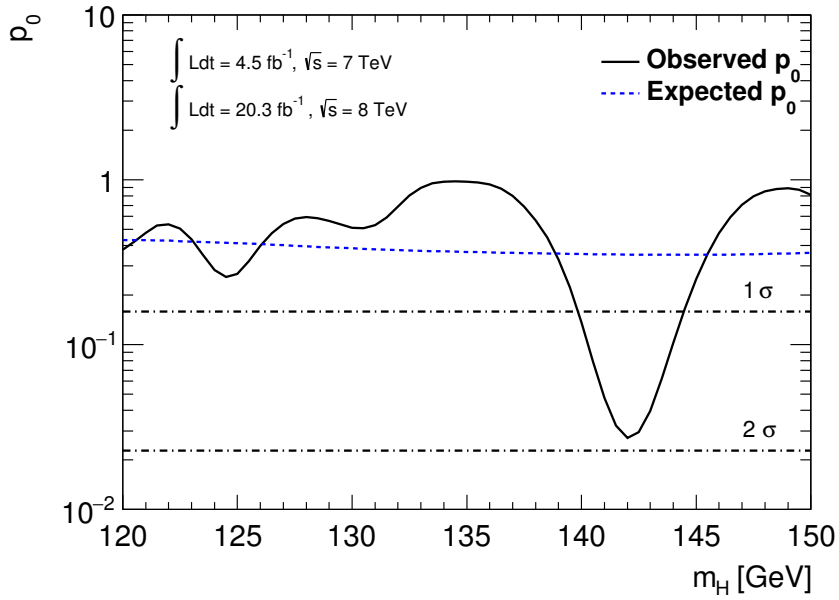

Figure 6.18: Observed and expected p_0 (solid and dashed blue lines, respectively) as a function of the Higgs boson mass, using the kinematic event categorisation. The results were obtained using $4.5\,\text{fb}^{-1}$ of pp collision data at $\sqrt{s} = 7\,\text{TeV}$ and $4.5\,\text{fb}^{-1}$ of pp collision data at $\sqrt{s} = 8\,\text{TeV}$.

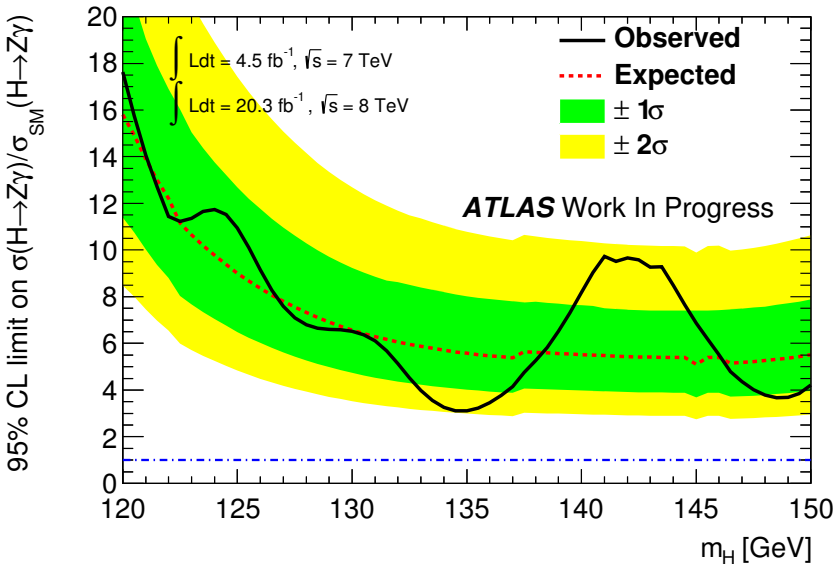

Figure 6.19: Observed and expected 95% C. L. limits (solid and dashed blue lines, respectively) on the production cross section of a SM Higgs boson decaying to $Z\gamma$ (normalised by the SM expectation), as a function of the Higgs boson mass, using the kinematic event categorisation. The results were obtained using $4.5\,\text{fb}^{-1}$ of pp collision data at $\sqrt{s} = 7\,\text{TeV}$ and $20.3\,\text{fb}^{-1}$ of pp collision data at $\sqrt{s} = 8\,\text{TeV}$. The green and yellow bands correspond to the $\pm 1\sigma$ and $\pm 2\sigma$ intervals. For reference, the observed and expected 95% C. L. limits obtained using the kinematic event categorisation are overlaid (solid and dashed lines, respectively) with their uncertainties.

Variable	Description
$\lvert\Delta\eta_{jj}\rvert$	Absolute value of difference in η between the two VBF jets
m_{jj}	Invariant mass of the summed VBF jet four-vectors
$\lvert\Delta\phi_{H,jj}\rvert$	Absolute value of the difference in ϕ between the Higgs boson and the dijet system
$\lvert\eta_H - \frac{\eta_{j1}+\eta_{j2}}{2}\rvert$	Zeppenfield variable, η_{Zep}, calculated from the Higgs boson and jet η components
$\min(\Delta R_{j\gamma})$	Minimum of the values of ΔR between the photon and each jet
Higgs p_T^t	Component of the $Z\gamma$ p_{T} that is transverse to the thrust axis
$\max(\eta_j)$	Maximum of the η components of the individual jets
p_{T}^H	Transverse momentum of the Higgs boson

Table 6.14: Overview of variables considered for optimising the VBF category event selection.

for each combination was a function giving the Signal-to-Background ratio (SBR) in terms of the signal efficiency, where the SBR was evaluated using Equation 6.26:

$$R_{SB} = \frac{S}{\sqrt{S+B}}. \tag{6.26}$$

Here, R_{SB} denotes the SBR, S denotes the number of events in the signal region $120 < m_{\ell\ell\gamma} < 130\,\mathrm{GeV}$ and B denotes the combined number of events in the background regions $115 < m_{\ell\ell\gamma} < 120\,\mathrm{GeV}$ and $130 < m_{\ell\ell\gamma} < 135\,\mathrm{GeV}$. The background region was defined in this manner because in this study it was extracted directly from data where the signal region is expected to contain some small signal, whereas the 5 GeV signal region sidebands should be free of signal and contain an equivalent number of background events. Previous unpublished work [1] showed that, in the vast majority of cases, the low statistics in the available MC and data samples caused TMVA to recommend cuts for a maximum SBR that were strong enough to reduce the level of signal, background, or both to zero. This was problematic since some signal should always be preserved, and it was deemed that a minimum of approximately 9 events would be required in the background to allow it to be modelled reliably. To avoid these issues, this study was restricted to examine only the m_{jj}, $\Delta\eta_{jj}$ and $\Delta\phi_{H,jj}$ variables. It is hoped that the other variables will be examined again when higher statistics samples become available in the future, in order to determine what, if any, enhancements they can bring to this analysis.

TMVA was again used to perform a cut-based, multi-variate analysis of the three remaining variables, and a distribution showing how the signal purity, background efficiency and SBR changed as a function of the signal efficiency was produced (Figure 6.20). The requirement of nine background events was met by selecting cuts that corresponded to a background efficiency of around 6%. Study of Figure 6.20 showed that such a background efficiency corresponds to a signal efficiency of around 34-35%. The signal efficiency was therefore advanced from 34.1% to 34.8% in steps of 0.1% and

[1] undertaken by Dr. S. Burdin

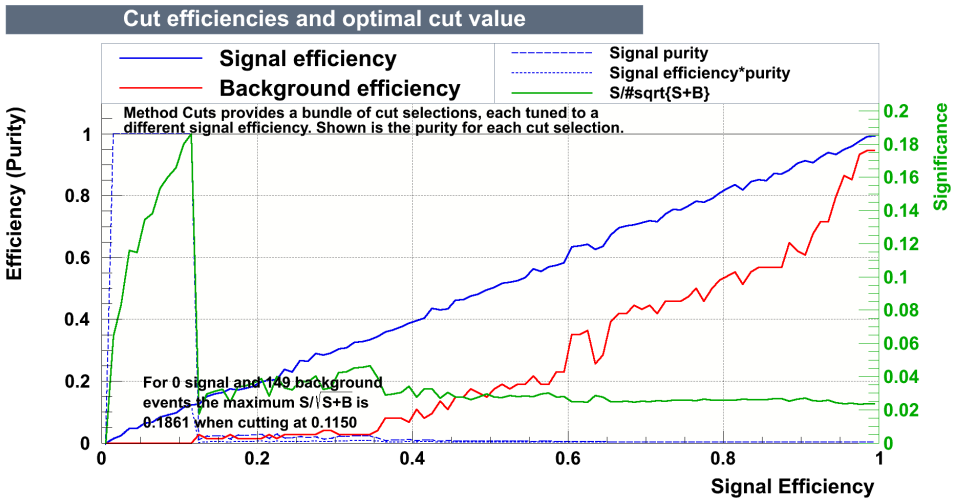

Figure 6.20: Output from the TMVA package for a cut-based multi-variate analysis showing the variations in signal purity, background efficiency and signal-to-background ratio as a function of the signal efficiency. The background is taken from the signal region sidebands in data, while the signal is normalised to the data luminosity of 21 fb^{-1}. Note that there are actually 0.28 signal events on a background of 149 events, but the output values displayed on the plot were truncated to integers.

the selection criteria recommended by TMVA for each efficiency are presented in Table 6.15.

To examine the selection criteria for a single signal efficiency, histograms of each variable from both the signal and background samples were plotted after all of the proposed cuts had been applied, except for the cut on the variable being plotted. The signal and background histograms for a given variable were then examined, and the SBR that would result from a cut applied to the centre of each bin was calculated using Equation 6.26. Since the cuts on all three variables under investigation require the selection of events where the value of the variable is greater than some limit, the parameters S and B in these calculations were assigned the values of the integrals from the current bin up to the last bin of the signal and background distributions, respectively.[2]

This process was repeated for all of the signal efficiencies, and it was found that the SBR was a maximum for the selection criteria associated with a signal efficiency of 34.2%. The SBR distributions for this signal efficiency for the variables $|\Delta\eta_{jj}|$, m_{jj} and $|\Delta\phi_{H,jj}|$ are shown in Figure 6.21. These figures also include the signal and background distributions for reference.

The limited numbers of available statistics, especially in the background sample, made it difficult to identify the optimal selection criteria since the presence of each event in the background sample was typically characterised by a sharp spike in the SBR distribution.

[2]Note that if the cut requires the selection of events where the value of the variable is less than some limit, the parameters S and B would be assigned the values of the integrals from the first bin up to the current bin of the signal and background distributions, respectively.

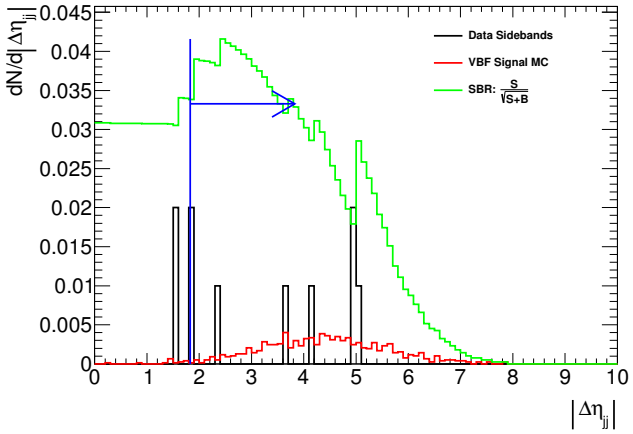

(a) $|\Delta\eta_{jj}|$

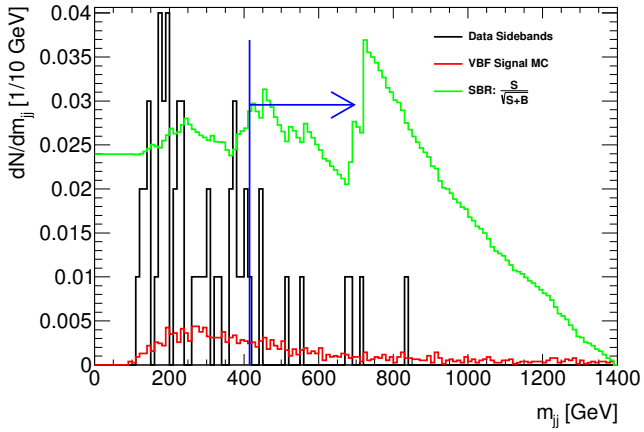

(b) m_{jj}

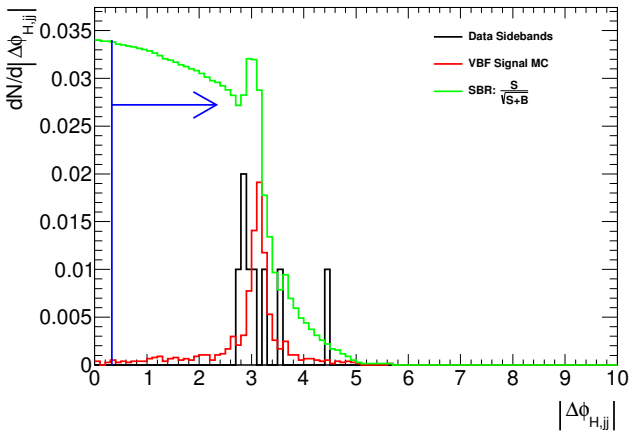

(c) $|\Delta\phi_{H,jj}|$

Figure 6.21: SBR distributions for the (a) $|\Delta\eta_{jj}|$, (b) m_{jj} and (c) $|\Delta\phi_{H,jj}|$ variables. The SBR (green) is evaluated for each variable after the cuts recommended by TMVA for the other two variables are applied. Signal (red) and background (black) distributions are included for reference, with the background scaled by a factor of 1/100 for visibility. The blue line marks the location of the cut recommended by TMVA, with the arrow indicating the region in which events are retained. The TMVA cuts correspond to a signal efficiency of 34.2%.

	$\lvert\Delta\eta_{jj}\rvert$	m_{jj} (GeV)	$\lvert\Delta\phi_{H,jj}\rvert$
HCP $\gamma\gamma$	2.8	400	2.6
VBF (30% Sig Eff)	2.4	447	0.08
VBF (34.1% Sig Eff)	2.1	410	0.57
VBF (34.2% Sig Eff)	1.8	415	0.33
VBF (34.3% Sig Eff)	2.4	400	0.20
VBF (34.4% Sig Eff)	2.2	406	0.25
VBF (34.5% Sig Eff)	2.4	313	2.45
VBF (34.6% Sig Eff)	2.7	316	1.75
VBF (34.6% Sig Eff)	2.1	407	0.26
VBF (34.6% Sig Eff)	2.0	409	-0.03
VBF (40% Sig Eff)	2.1	307	1.5
VBF (Optimal)	2.4	410	(No Cut)

Table 6.15: Assorted selection criteria for choosing VBF events with specific signal efficiencies.

For the variable $|\Delta\eta_{jj}|$, the TMVA cut was not optimal as a higher SBR could be obtained if the cut $|\Delta\eta_{jj}| > 2.4$ was applied instead. For the variable m_{jj}, the TMVA cut appeared to be acceptable since it provided a reasonable SBR while retaining 8 background events. Moving the cut limit to a higher value would clearly yield a higher SBR, but could not be done without leaving the background distribution with too few events for accurate modelling. For the variable $|\Delta\phi_{H,jj}|$, the TMVA cut was superfluous as it removed a small amount of signal and made no impact on the background. No cut should therefore be applied on this variable, which is also advantageous as it removes complications in theoretical calculations by decoupling the Higgs from the dijet system. The final cuts for the optimal selection criteria in the VBF channel are shown in Table 6.15.

However, the limited statistics available within this category mean that it is unlikely to make any meaningful difference to the expected limit. A VBF category has not therefore been pursued any further, although it will be examined again in Run 2 once more statistics become available (especially since the higher beam energy will increase the production cross-section in this channel).

6.4 Z Mass Slice Event Classification

In an effort to improve the sensitivity of the analysis, an alternative event classification was examined where events were separated into categories based on the mass of the reconstructed Z boson. Figure 6.22 shows 2D plots of $m_{\ell\ell\gamma}$ against $m_{\ell\ell}$ in 8 TeV data and ggF signal MC. The signal MC has a very different distribution to the data, which is essentially pure background, and shows that the $m_{\ell\ell\gamma}$ resolution has a clear dependence on $m_{\ell\ell}$. This dependence is made more explicit in Figure 6.23, which shows the $m_{\ell\ell\gamma}$ distribution within the ranges $85 < m_{\ell\ell} < 86$, $90 < m_{\ell\ell} < 91$ and $94 < m_{\ell\ell} < 95$ GeV. Higgs boson candidates reconstructed from Z candidates close to the true Z mass have a significantly better resolution than those reconstructed from Z

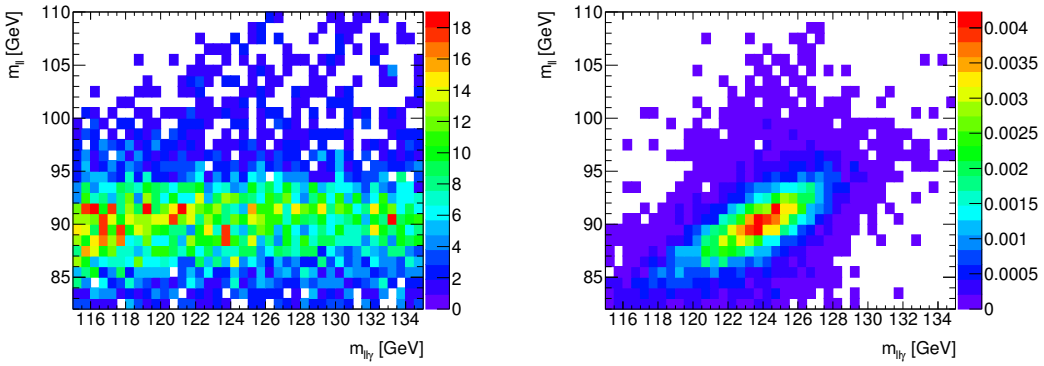

Figure 6.22: Plot of $m_{\ell\ell\gamma}$ against $m_{\ell\ell}$ for selected Higgs boson candidates from 8 TeV data (left) and 8 TeV ggF signal MC at $m_H = 125\,\text{GeV}$ (right) with an $ee\gamma$ final state.

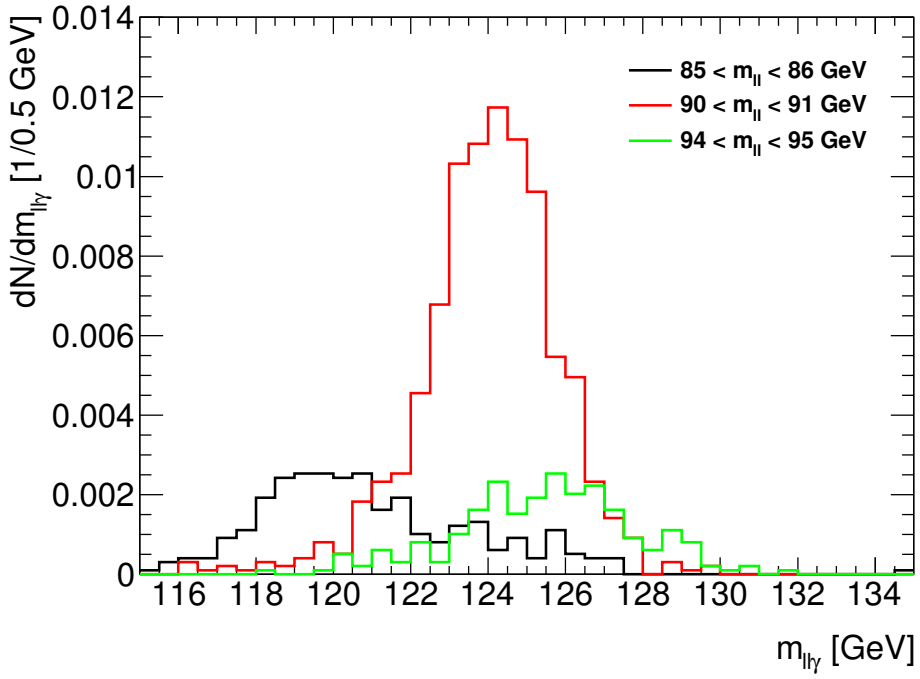

Figure 6.23: Plot of $m_{\ell\ell\gamma}$ in 7 TeV ggF Signal MC with an $ee\gamma$ final state for three different $m_{\ell\ell}$ slices: $85 < m_{\ell\ell} < 86$, $90 < m_{\ell\ell} < 91$, and $94 < m_{\ell\ell} < 95\,\text{GeV}$.

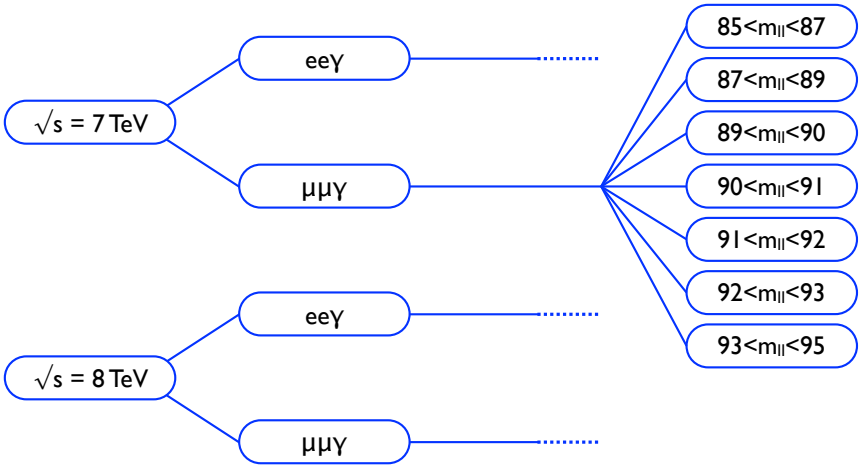

Figure 6.24: Overview of the Z slices event categorisation. Events are classified by centre-of-mass energy, final state, and $m_{\ell\ell}$. Note that events in each final state and centre-of-mass energy are separated into the Z mass categories that are listed.

candidates in the tails of the $m_{\ell\ell}$ distribution. Placing events into categories covering different $m_{\ell\ell}$ ranges, termed Z slices hereafter, means that those slices close to the true Z mass will make a greater contribution to the expected limit, and therefore improve the sensitivity of the analysis.

For this study, Z and Higgs boson candidates were reconstructed as described in Section 6.1 but without all of the corrections described in Section 6.1.1 being applied. The Z mass constraint was removed because although it enhances the $m_{\ell\ell}$ resolution, it does so by manipulating the four-vectors of the leptons making up the Z candidate to allow events from the tails of the $m_{\ell\ell}$ distribution to migrate back into the central peak. This feature is both inappropriate and undesirable here, since it is performed by separating events into the Z slices and it is also important to preserve events in the tails of the $m_{\ell\ell}$ distribution to facilitate signal and background modelling. The FSR constraint was observed to affect just over 1% of all 8 TeV data and was also removed in order to simplify the study. However, the correction of the photon origin to the location of the primary vertex was retained because this has no dependence on the parameters of the Z boson.

Events in each final state and at each centre-of-mass energy were initially subdivided into a total of seven categories, or slices, based on the reconstructed Z mass. These slices typically have a width of 1 GeV, except in the tails of the Z mass distribution where the slice width was changed to 2 GeV to increase the available statistics for signal and background modelling in these regions. A graphical overview of this categorisation is presented in Figure 6.24.

However, the analysis in Section 6.2 used categories based on the kinematic variables $|\Delta\eta_{Z\gamma}|$ and Higgs p_T^t that should be independent of $m_{\ell\ell}$. The increase in sensitivity that these brought to the kinematic analysis should therefore be cumulative with any enhancement obtained through use of the Z slices, and so a second Z slices

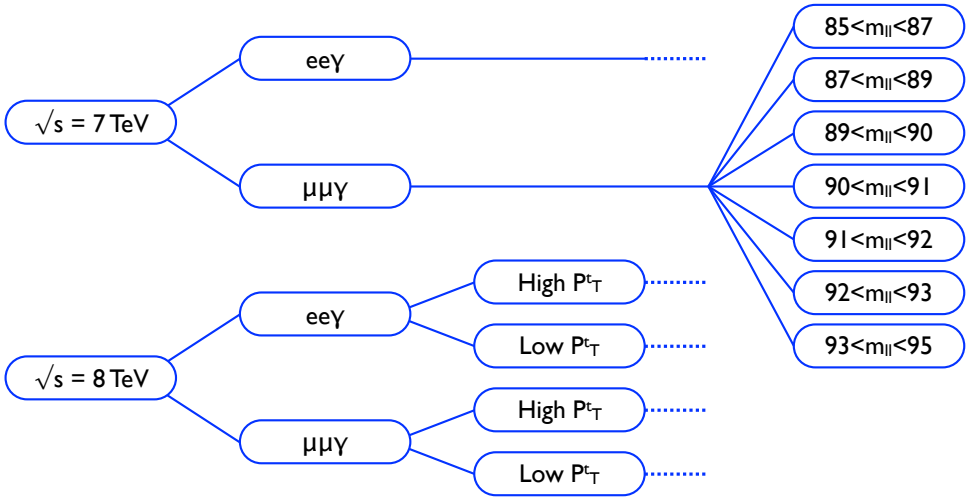

Figure 6.25: Overview of the Z slices with p_T^t event categorisation. Events are classified by centre-of-mass energy, final state, $m_{\ell\ell}$ and p_T^t. High and Low p_T^t denote $p_T^t > 30$ and $p_T^t < 30\,\text{GeV}$, respectively. Note that all categories are subdivided into the Z mass slices listed.

categorisation was tested. It was originally intended that each of the ten kinematic event categories be further subdivided into the seven Z slices described above. Unfortunately, in 7 TeV data it was found that many of the Z slices with high-p_T^t contained fewer than 5 events, which made it impossible to use the data-driven background estimation technique with any reliability. A reoptimisation of the threshold for high- and low-p_T^t events was beyond the scope of this study, and so events at 7 TeV were subdivided into Z slices only. The 8 TeV data contained enough statistics to allow all six kinematic categories to be subdivided into Z slices, but many of the $|\Delta\eta_{Z\gamma}|$ categories in signal MC samples had too few events to allow the signal peak to be accurately modelled with a Crystal Ball plus Gaussian function (see Section 6.4.2). For this reason, events could not be subdivided into categories based on $|\Delta\eta_{Z\gamma}|$. The final categorisation, termed the Z slices with p_T^t categorisation, therefore consisted of 7 TeV events in each final state being separated into Z slices and 8 TeV events separated into high- and low-p_T^t, which were each further subdivided into Z slices. The threshold for high- and low-p_T^t was kept at 30 GeV, using the same value determined for the kinematic analysis. A graphical overview of this categorisation is presented in Figure 6.25.

6.4.1 Proof of concept

In order to verify that the use of a Z slices event categorisation improved sensitivity in the search for $H \to Z\gamma$ decays, a proof of concept study was performed that evaluated the Poisson upper limits at 95% CL given the expected number of signal and background events around $m_H = 125\,\text{GeV}$. Tests were performed using a greatly simplified version of the technique described in Section 6.2.5, where systematic uncertainties were neglected and functional forms for the signal and background distributions were not

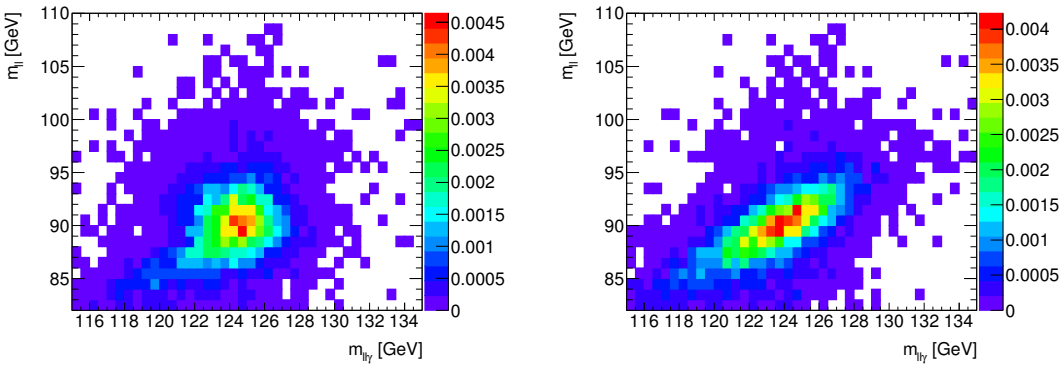

(a) $ee\gamma$ channel

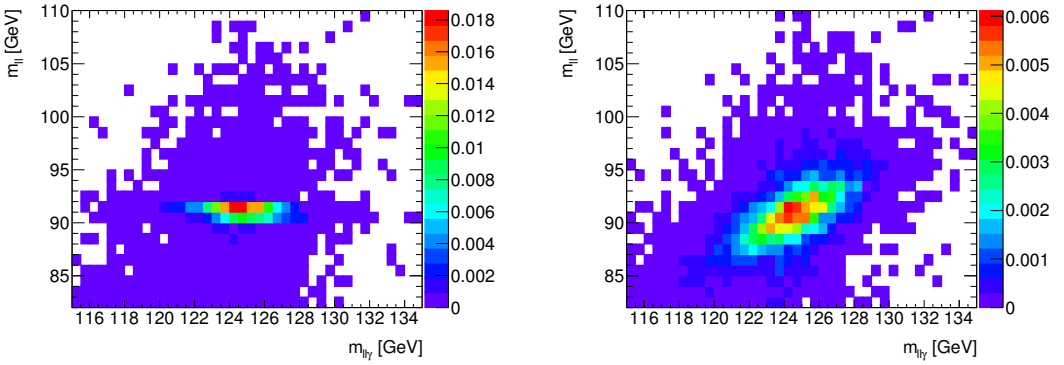

(b) $\mu\mu\gamma$ channel

Figure 6.26: Plots of $m_{\ell\ell\gamma}$ against $m_{\ell\ell}$ for selected Higgs boson candidates from 8 TeV ggF signal MC at $m_H = 125\,\text{GeV}$ in the $ee\gamma$ and $\mu\mu\gamma$ final states, with (left) and without (right) the application of the Z mass constraint and the FSR correction.

required. The calculation of the likelihood (Equation 6.10) was therefore altered as Equation 6.12 changed to depend solely on the expected number of signal (N_S) and background (N_B) events - each event is assigned a weight of $\log(1 + N_S/N_B)$. This analysis technique therefore serves as merely a first-order approximation.

Four different event categorisations were evaluated: inclusive, kinematic, Z slices and Z slices with p_T^t. The inclusive categorisation separates event based on the centre-of-mass energy and final state only, and is included here only for reference. The kinematic, Z slices and Z slices with p_T^t categorisations separate events as described in Figures 6.7, 6.24, and 6.25, respectively. To ensure a fair evaluation of the capabilities of the Z slices classification, the inclusive and kinematic categorisations select events where the Z mass constraint and FSR corrections have been applied, while the Z slices event categorisations do not include these corrections.

Figure 6.26 shows 2D plots of $m_{\ell\ell\gamma}$ against $m_{\ell\ell}$ in 8 TeV ggF signal MC for $m_H = 125\,\text{GeV}$, both with and without the application of the FSR correction and Z mass constraint. In order to enclose all of the signal when neither of these corrections was applied, a relatively wide window of $125 \pm 5.5\,\text{GeV}$ was chosen.

The expected number of signal events in each category was evaluated by summing

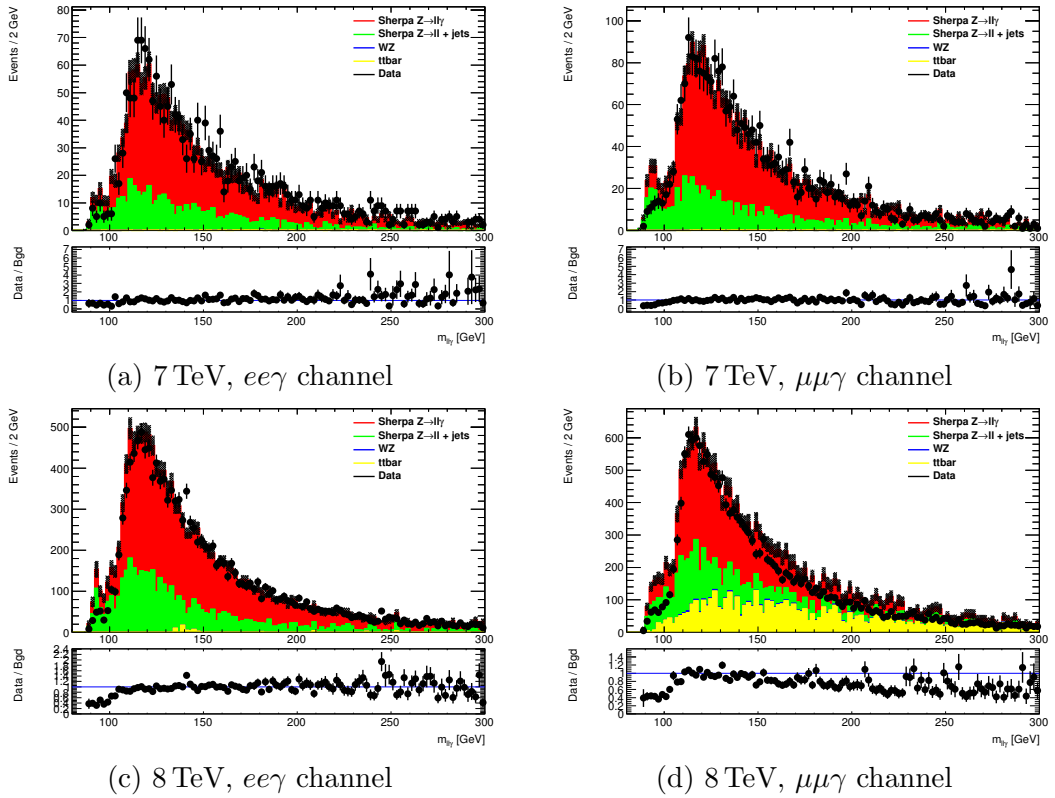

(a) 7 TeV, $ee\gamma$ channel

(b) 7 TeV, $\mu\mu\gamma$ channel

(c) 8 TeV, $ee\gamma$ channel

(d) 8 TeV, $\mu\mu\gamma$ channel

Figure 6.27: Data distributions and background composition for selected events separated into categories based on the centre-of-mass energy and final state.

the number of events found in signal MC within the region 125 ± 5.5 GeV in all production mechanisms, after normalising them according to their production cross-sections. The expected number of background events in each category was evaluated by normalising the Sherpa $Z \to \ell\ell\gamma$, Sherpa $Z \to \ell\ell$, WZ and $t\bar{t}$ background samples to their respective cross-sections and combining them. The number of events in the signal region sidebands at $100 < m_{\ell\ell\gamma} < 120$ and $130 < m_{\ell\ell\gamma} < 150$ GeV were then evaluated in data, and the total background was scaled to match. Figure 6.27 shows the distributions of data and the background components in the four inclusive categories at this point. The events in the rescaled background were then separated into the required categories, and the expected number of background events was determined by summing the number of events within the region 125 ± 5.5 GeV. The expected numbers of signal and background events at $m_H = 125$ GeV for each of the event categorisations being examined are listed in Tables 6.16 to 6.19.

The first test evaluated the compatibility of the background-only case with a signal plus background hypothesis. The level of signal in the hypothesis was increased in steps of 0.1 times the SM expectation, and the corresponding CL_s value at each step was calculated. The CL_s values were then plotted against the injected signal and fitted with a Gaussian function, as shown in Figure 6.28, to precisely identify where the CL_s value fell below 5%. At this point, any greater level of signal is excluded since it would otherwise be visible at a 2σ level. The levels of injected signal for which this occurs

$\sqrt{s}$	Final State	Background	Signal
7 TeV	$ee\gamma$	283.9	0.751
	$\mu\mu\gamma$	414.3	1.04
8 TeV	$ee\gamma$	2197.9	5.50
	$\mu\mu\gamma$	2656.4	6.81

Table 6.16: Number of expected signal and background events for the inclusive event categorisation, taken from the region $m_{\ell\ell\gamma} = 125 \pm 5.5\,\text{GeV}$. The Higgs boson was reconstructed using the Z mass constraint and FSR corrections.

$\sqrt{s}$	Final State	p_T^t	$\lvert\Delta\eta_{Z\gamma}\rvert$	Background	Signal
7 TeV	$ee\gamma$	High		36.58	0.290
		Low		247.3	0.461
	$\mu\mu\gamma$	High		56.32	0.388
		Low		358.0	0.652
8 TeV	$ee\gamma$	High		317.5	1.967
		Low	High	1447.6	2.981
			Low	432.8	0.556
	$\mu\mu\gamma$	High		577.6	2.390
		Low	High	1574.7	3.664
			Low	504.1	0.757

Table 6.17: Number of expected signal and background events for the kinematic event categorisation, taken from the region $m_{\ell\ell\gamma} = 125 \pm 5.5\,\text{GeV}$. The Higgs boson was reconstructed using the Z mass constraint and FSR corrections.

$\sqrt{s}$	Final State	Z Slice	Background	Signal
7 TeV	$ee\gamma$	$85 < m_{\ell\ell} < 87\,\text{GeV}$	28.01	0.066
		$87 < m_{\ell\ell} < 89\,\text{GeV}$	43.84	0.142
		$89 < m_{\ell\ell} < 90\,\text{GeV}$	27.46	0.103
		$90 < m_{\ell\ell} < 91\,\text{GeV}$	28.58	0.106
		$91 < m_{\ell\ell} < 92\,\text{GeV}$	27.26	0.094
		$92 < m_{\ell\ell} < 93\,\text{GeV}$	21.28	0.076
		$93 < m_{\ell\ell} < 95\,\text{GeV}$	25.64	0.071
	$\mu\mu\gamma$	$85 < m_{\ell\ell} < 87\,\text{GeV}$	25.50	0.063
		$87 < m_{\ell\ell} < 89\,\text{GeV}$	49.85	0.146
		$89 < m_{\ell\ell} < 90\,\text{GeV}$	35.27	0.128
		$90 < m_{\ell\ell} < 91\,\text{GeV}$	49.11	0.148
		$91 < m_{\ell\ell} < 92\,\text{GeV}$	48.45	0.154
		$92 < m_{\ell\ell} < 93\,\text{GeV}$	43.37	0.121
		$93 < m_{\ell\ell} < 95\,\text{GeV}$	56.66	0.143
8 TeV	$ee\gamma$	$85 < m_{\ell\ell} < 87\,\text{GeV}$	174.8	0.460
		$87 < m_{\ell\ell} < 89\,\text{GeV}$	301.9	0.987
		$89 < m_{\ell\ell} < 90\,\text{GeV}$	214.3	0.720
		$90 < m_{\ell\ell} < 91\,\text{GeV}$	219.1	0.733
		$91 < m_{\ell\ell} < 92\,\text{GeV}$	233.8	0.662
		$92 < m_{\ell\ell} < 93\,\text{GeV}$	174.8	0.473
		$93 < m_{\ell\ell} < 95\,\text{GeV}$	226.5	0.542
	$\mu\mu\gamma$	$85 < m_{\ell\ell} < 87\,\text{GeV}$	138.6	0.396
		$87 < m_{\ell\ell} < 89\,\text{GeV}$	273.5	0.959
		$89 < m_{\ell\ell} < 90\,\text{GeV}$	213.2	0.826
		$90 < m_{\ell\ell} < 91\,\text{GeV}$	262.0	0.953
		$91 < m_{\ell\ell} < 92\,\text{GeV}$	275.8	0.970
		$92 < m_{\ell\ell} < 93\,\text{GeV}$	265.9	0.758
		$93 < m_{\ell\ell} < 95\,\text{GeV}$	308.6	0.873

Table 6.18: Number of expected signal and background events for the Z slices categorisation, taken from the region $m_{\ell\ell\gamma} = 125 \pm 5.5\,\text{GeV}$. The Higgs boson was reconstructed without the Z mass constraint and FSR corrections.

$\sqrt{s}$	Final State	p_T^t	Z Slice	Background	Signal
7 TeV	$ee\gamma$		$85 < m_{\ell\ell} < 87\,\text{GeV}$	28.01	0.066
			$87 < m_{\ell\ell} < 89\,\text{GeV}$	43.84	0.142
			$89 < m_{\ell\ell} < 90\,\text{GeV}$	27.46	0.103
			$90 < m_{\ell\ell} < 91\,\text{GeV}$	28.58	0.106
			$91 < m_{\ell\ell} < 92\,\text{GeV}$	27.26	0.094
			$92 < m_{\ell\ell} < 93\,\text{GeV}$	21.28	0.076
			$93 < m_{\ell\ell} < 95\,\text{GeV}$	25.64	0.071
	$\mu\mu\gamma$		$85 < m_{\ell\ell} < 87\,\text{GeV}$	25.50	0.063
			$87 < m_{\ell\ell} < 89\,\text{GeV}$	49.85	0.146
			$89 < m_{\ell\ell} < 90\,\text{GeV}$	35.27	0.128
			$90 < m_{\ell\ell} < 91\,\text{GeV}$	49.11	0.148
			$91 < m_{\ell\ell} < 92\,\text{GeV}$	48.45	0.154
			$92 < m_{\ell\ell} < 93\,\text{GeV}$	43.37	0.121
			$93 < m_{\ell\ell} < 95\,\text{GeV}$	56.66	0.143
8 TeV	$ee\gamma$	High	$85 < m_{\ell\ell} < 87\,\text{GeV}$	17.70	0.158
			$87 < m_{\ell\ell} < 89\,\text{GeV}$	35.38	0.355
			$89 < m_{\ell\ell} < 90\,\text{GeV}$	26.79	0.248
			$90 < m_{\ell\ell} < 91\,\text{GeV}$	35.90	0.273
			$91 < m_{\ell\ell} < 92\,\text{GeV}$	36.07	0.237
			$92 < m_{\ell\ell} < 93\,\text{GeV}$	24.40	0.171
			$93 < m_{\ell\ell} < 95\,\text{GeV}$	37.53	0.203
		Low	$85 < m_{\ell\ell} < 87\,\text{GeV}$	157.1	0.302
			$87 < m_{\ell\ell} < 89\,\text{GeV}$	266.5	0.632
			$89 < m_{\ell\ell} < 90\,\text{GeV}$	187.5	0.472
			$90 < m_{\ell\ell} < 91\,\text{GeV}$	183.2	0.460
			$91 < m_{\ell\ell} < 92\,\text{GeV}$	197.7	0.425
			$92 < m_{\ell\ell} < 93\,\text{GeV}$	150.4	0.303
			$93 < m_{\ell\ell} < 95\,\text{GeV}$	189.0	0.339
	$\mu\mu\gamma$	High	$85 < m_{\ell\ell} < 87\,\text{GeV}$	27.4	0.134
			$87 < m_{\ell\ell} < 89\,\text{GeV}$	47.2	0.329
			$89 < m_{\ell\ell} < 90\,\text{GeV}$	29.7	0.302
			$90 < m_{\ell\ell} < 91\,\text{GeV}$	41.8	0.336
			$91 < m_{\ell\ell} < 92\,\text{GeV}$	46.0	0.342
			$92 < m_{\ell\ell} < 93\,\text{GeV}$	55.6	0.253
			$93 < m_{\ell\ell} < 95\,\text{GeV}$	63.0	0.309
		Low	$85 < m_{\ell\ell} < 87\,\text{GeV}$	111.2	0.262
			$87 < m_{\ell\ell} < 89\,\text{GeV}$	226.4	0.630
			$89 < m_{\ell\ell} < 90\,\text{GeV}$	183.5	0.524
			$90 < m_{\ell\ell} < 91\,\text{GeV}$	220.2	0.618
			$91 < m_{\ell\ell} < 92\,\text{GeV}$	229.8	0.628
			$92 < m_{\ell\ell} < 93\,\text{GeV}$	210.3	0.505
			$93 < m_{\ell\ell} < 95\,\text{GeV}$	245.6	0.565

Table 6.19: Number of expected signal and background events for the Z slices with p_T^t categorisation, taken from the region $m_{\ell\ell\gamma} = 125 \pm 5.5\,\text{GeV}$. High and Low p_T^t is denoted by $p_T^t > 30$ and $p_T^t < 30\,\text{GeV}$, respectively. The Higgs boson was reconstructed without the Z mass constraint and FSR corrections.

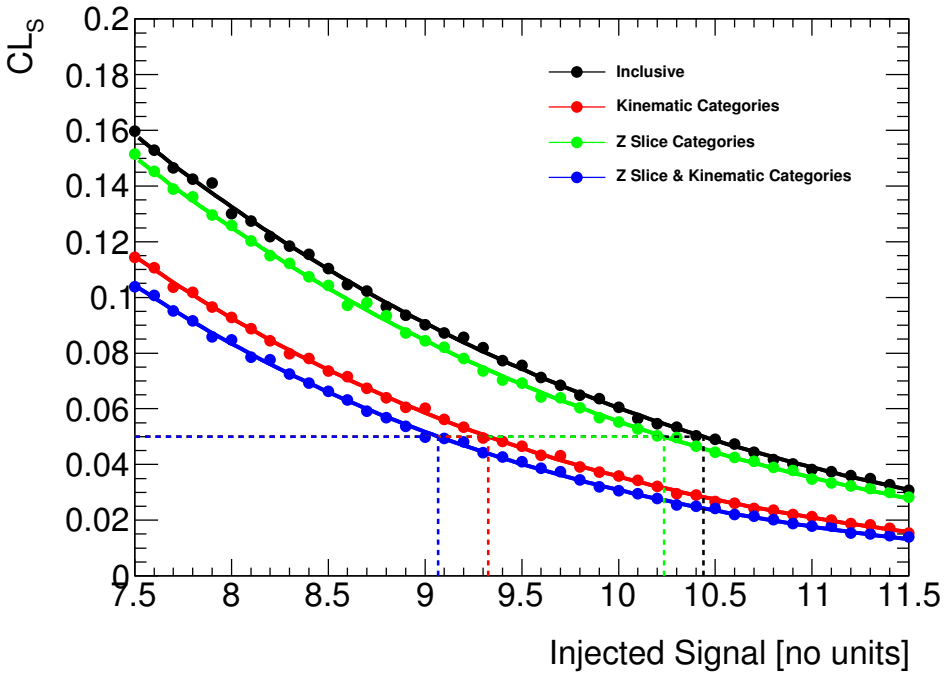

Figure 6.28: Distributions of CL_s values for given amounts of injected signal under the Background-only hypothesis. Results are shown for the Inclusive, Kinematic, Z slices and Z slices with p_T^t categorisations.

Event Categorisation	Injected Signal ($n \times$ SM)
Inclusive	10.44
Kinematic	9.33
Z slices	10.24
Z slices with p_T^t	9.07

Table 6.20: Level of injected signal corresponding to $CL_s = 0.05$ in the inclusive, kinematic, Z slices and Z slices with p_T^t event categorisations.

with each of the four event categorisations are presented in Table 6.20.

The second test evaluated the compatibility of the signal plus background case with a background-only hypothesis. The level of signal was again increased in steps of 0.1 times the SM expectation, and the corresponding CL_b values were calculated. The CL_b values were plotted against the injected signal and fitted with a second order polynomial, as shown in Figure 6.29. The fitted function was then used to identify the level of signal for which the CL_b value rose above 95%, at which point the signal plus background case becomes incompatible with the background-only hypothesis. The levels of injected signal for which this occurs with each of the four event categorisations are presented in Table 6.21.

In both cases, the inclusive event categorisation is the worst and the Z slices categorisation offers a slight improvement - this demonstrates that Z slices technique can successfully replace and improve on the use of the Z mass constraint. The Z slices with

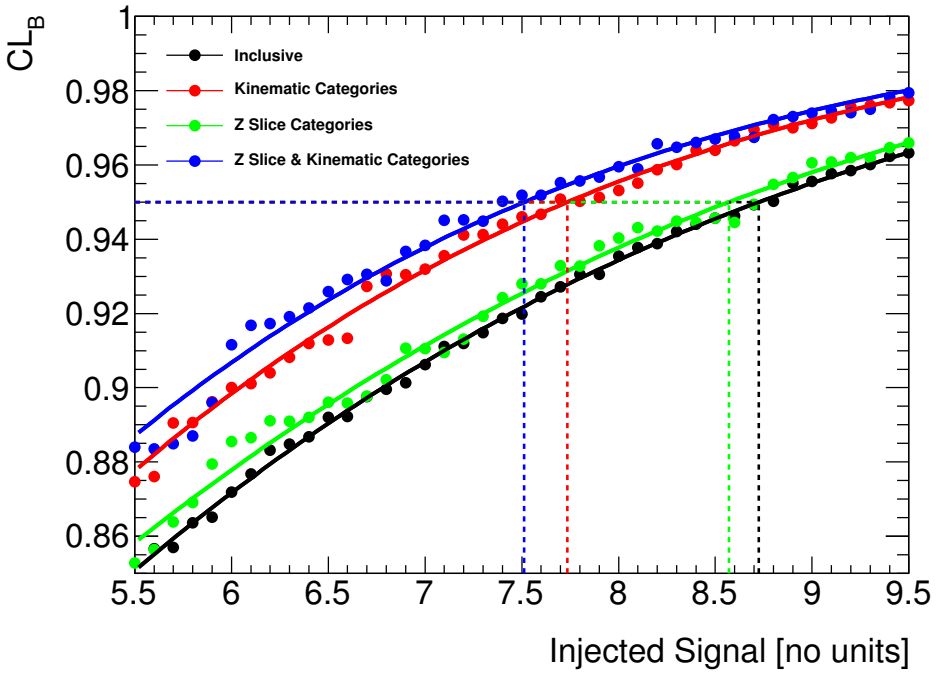

Figure 6.29: Distributions of CL_b values for given amounts of injected signal under the Signal plus Background hypothesis. Results are shown for the Inclusive, Kinematic, Z slices and Z slices with p_T^t categorisations.

Event Categorisation	Injected Signal ($n \times$ SM)
Inclusive	8.73
Kinematic	7.74
Z slices	8.57
Z slices with p_T^t	7.51

Table 6.21: Level of injected signal corresponding to $CL_b = 0.95$ in the inclusive, kinematic, Z slices and Z slices with p_T^t event categorisations.

p_T^t event categorisation provides the best limit, although it only improves on the kinematic analysis by 3%. However, the fixed width window in which events were selected had to be very wide in order to accommodate the entire Z slices signal distribution, and this included a significant proportion of background for minimal gains in signal. Both Z slices categorisations could therefore have distorted signal-to-background ratios that reduce their apparent impact on the sensitivity. The use of a sliding window to select events might improve the results, but this is not really necessary as the proof of concept study has served its purpose and demonstrated that gains can be made using this new technique.

6.4.2 Z Slices Event Categorisation

A better approach than the one adopted in the previous section is to utilise the full limit setting procedure developed for the kinematic analysis, where modelling of the signal and background can account for the distribution of events and give more accurate values for the expected limit. Events were separated according to the Z slices categorisation described in Figure 6.24, and processed largely as described in Section 6.2.

The signal for each category and production mechanism was modelled by simultaneously fitting the MC samples at all mass points with a function composed of a Crystal Ball lineshape summed with a Gaussian distribution (as defined by Equation 6.8 in Section 6.2.2). The parameters n_{CB} and f_{CB} were held constant across all mass points, while the others were allowed to vary linearly with mass. As with the kinematic analysis, the Crystal Ball and Gauss functions shared a common mean. The seed values and ranges for all of the parameters were hand optimised to facilitate good quality fits to the MC distributions. The resultant signal models for events produced through the ggF production mechanism are shown in Figures 6.30 to 6.33.

The background was again modelled by fitting a function directly to the observed data. However, in view of the low statistics available in many of the Z slices, the decision was made to fit events in each category with a simple exponential function:

$$N = A \exp B m_{\ell\ell\gamma}, \tag{6.27}$$

where A is a normalisation parameter and B is a constant to be determined. The results of fitting this exponential to the data in each category are shown in Figures 6.34 to 6.37, together with the corresponding expected signal distribution for a Higgs boson of mass 125 GeV (scaled by a factor of 50 for visibility).

The expected and observed limits were then evaluated following the same procedure adopted for the kinematic analysis, except that in this case no systematic uncertainties were included. The analysis is dominated by statistical uncertainties, and the impact of systematics is therefore expected to be minimal. The results are shown in Figure 6.38, together with the results of the kinematic analysis for comparison. For a Higgs boson of mass 125 GeV, the expected limit is $9.01 \times$ SM under the kinematic categorisation and $9.63 \times$SM under the Z slices categorisation. However, this deterioration of around 6.5%

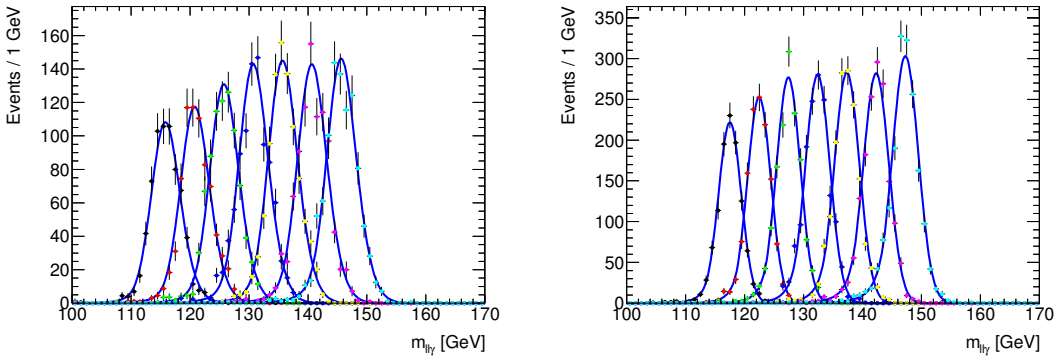

(a) $85 < m_{\ell\ell} < 87\,\text{GeV}$

(b) $87 < m_{\ell\ell} < 89\,\text{GeV}$

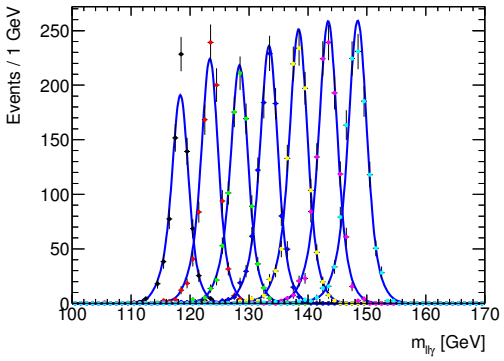

(c) $89 < m_{\ell\ell} < 90\,\text{GeV}$

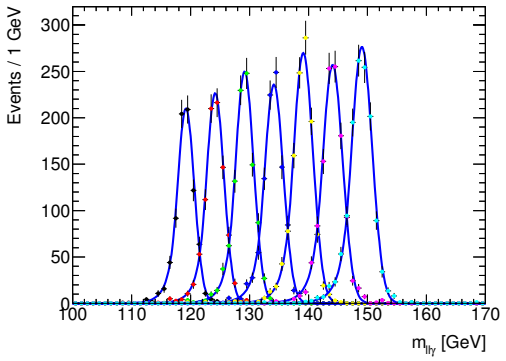

(d) $90 < m_{\ell\ell} < 91\,\text{GeV}$

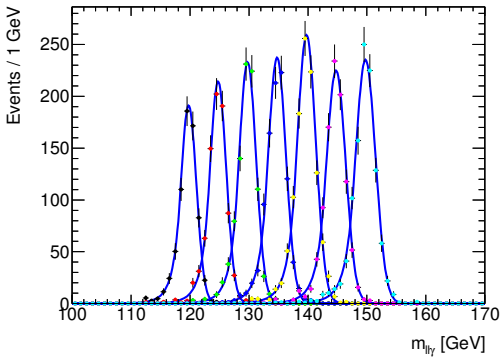

(e) $91 < m_{\ell\ell} < 92\,\text{GeV}$

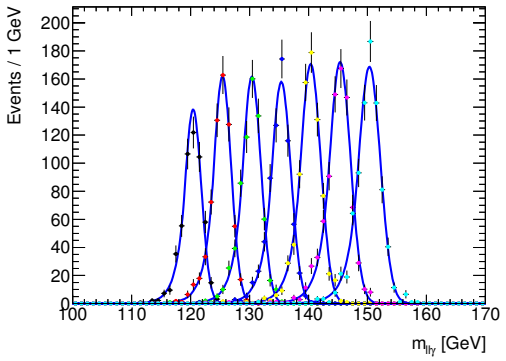

(f) $92 < m_{\ell\ell} < 93\,\text{GeV}$

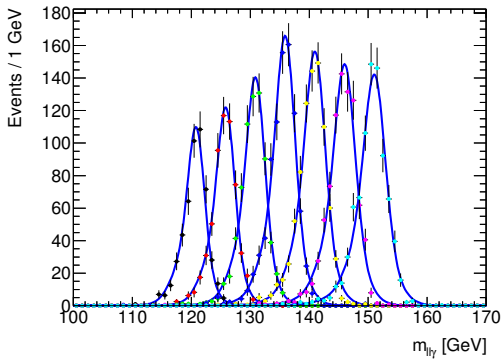

(g) $93 < m_{\ell\ell} < 95\,\text{GeV}$

Figure 6.30: Signal models for the $H \to Z\gamma$, 7 TeV ggF MC samples in the $ee\gamma$ channel, for seven different mass points. All mass points were simultaneously fitted with a model composed of a Crystal Ball function summed with a Gaussian function.

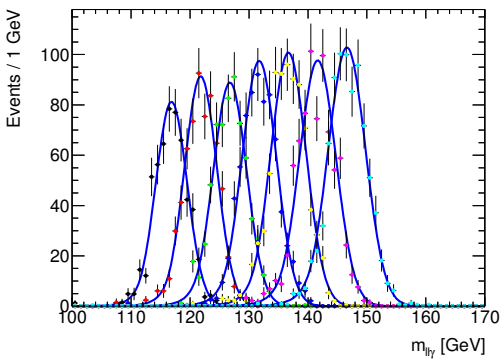

(a) $85 < m_{\ell\ell} < 87\,\text{GeV}$

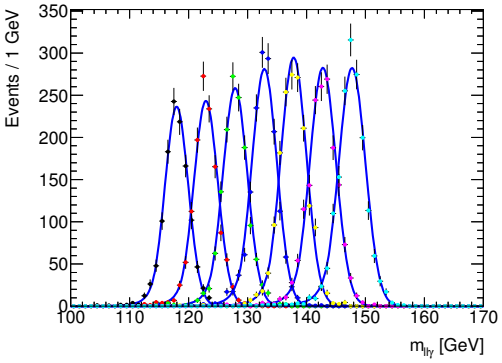

(b) $87 < m_{\ell\ell} < 89\,\text{GeV}$

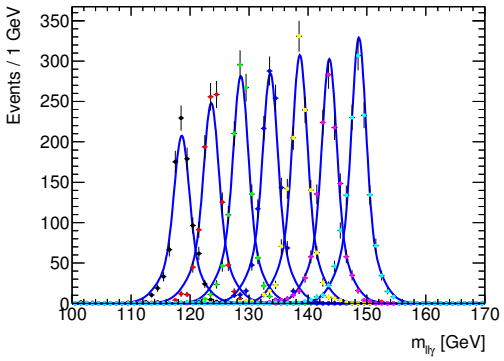

(c) $89 < m_{\ell\ell} < 90\,\text{GeV}$

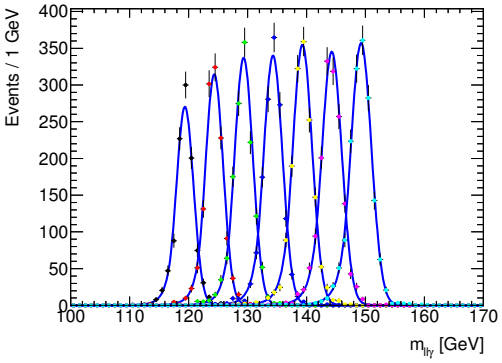

(d) $90 < m_{\ell\ell} < 91\,\text{GeV}$

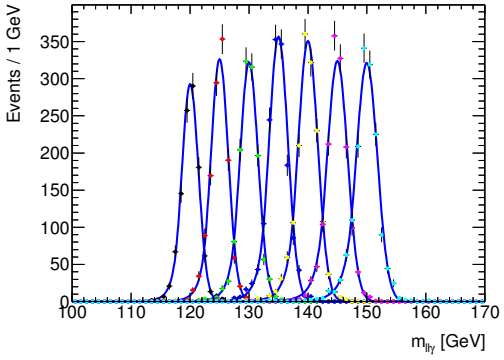

(e) $91 < m_{\ell\ell} < 92\,\text{GeV}$

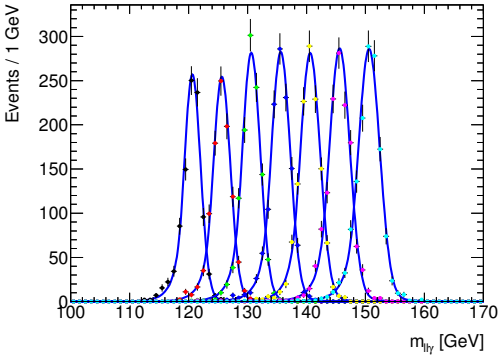

(f) $92 < m_{\ell\ell} < 93\,\text{GeV}$

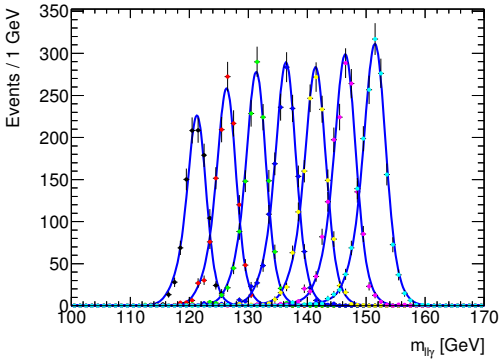

(g) $93 < m_{\ell\ell} < 95\,\text{GeV}$

Figure 6.31: Signal models for the $H \to Z\gamma$, 7 TeV ggF MC samples in the $\mu\mu\gamma$ channel, for seven different mass points. All mass points were simultaneously fitted with a model composed of a Crystal Ball function summed with a Gaussian function.

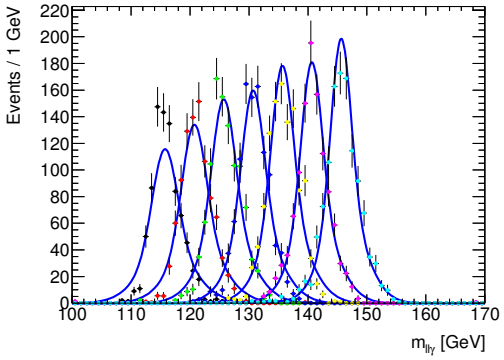

(a) $85 < m_{\ell\ell} < 87\,\text{GeV}$

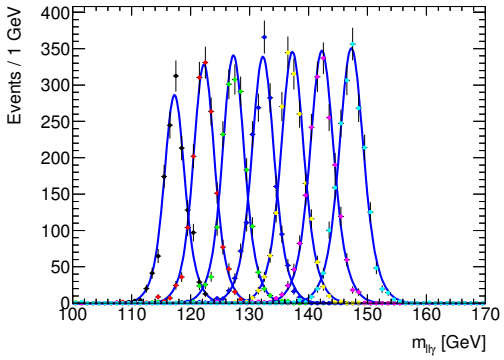

(b) $87 < m_{\ell\ell} < 89\,\text{GeV}$

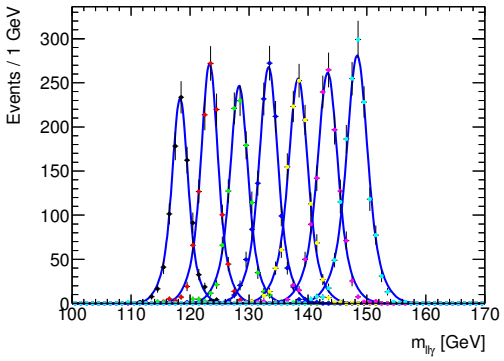

(c) $89 < m_{\ell\ell} < 90\,\text{GeV}$

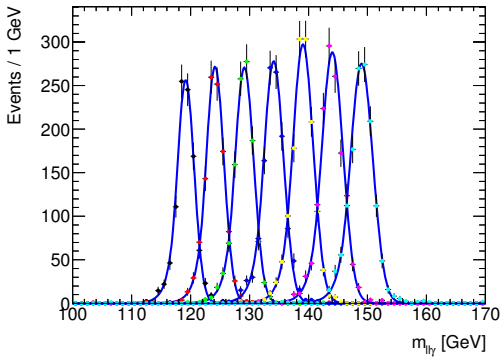

(d) $90 < m_{\ell\ell} < 91\,\text{GeV}$

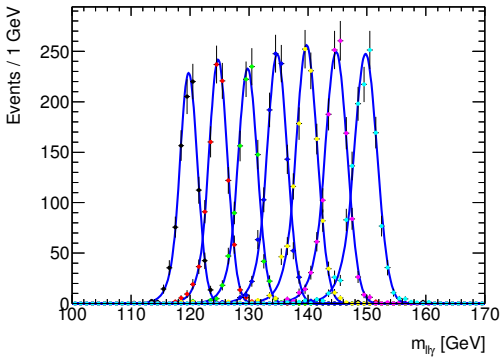

(e) $91 < m_{\ell\ell} < 92\,\text{GeV}$

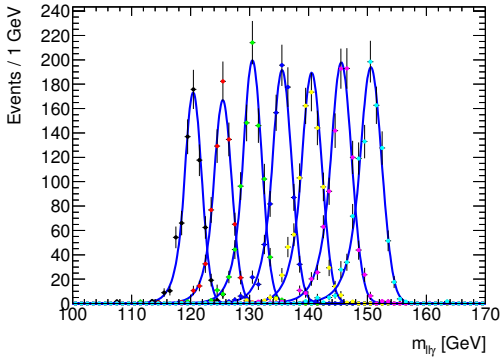

(f) $92 < m_{\ell\ell} < 93\,\text{GeV}$

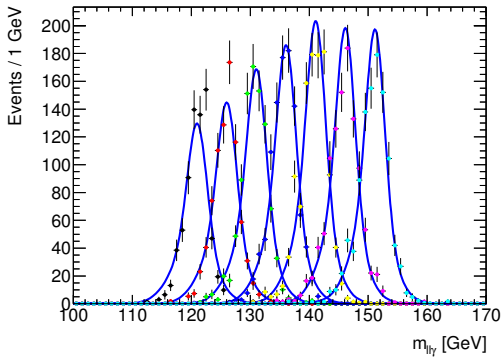

(g) $93 < m_{\ell\ell} < 95\,\text{GeV}$

Figure 6.32: Signal models for the $H \to Z\gamma$, 8 TeV ggF MC samples in the $ee\gamma$ channel, for seven different mass points. All mass points were simultaneously fitted with a model composed of a Crystal Ball function summed with a Gaussian function.

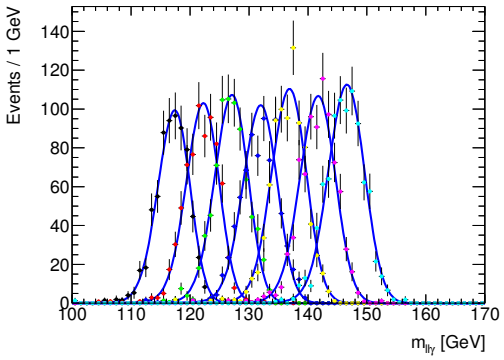

(a) $85 < m_{\ell\ell} < 87\,\text{GeV}$

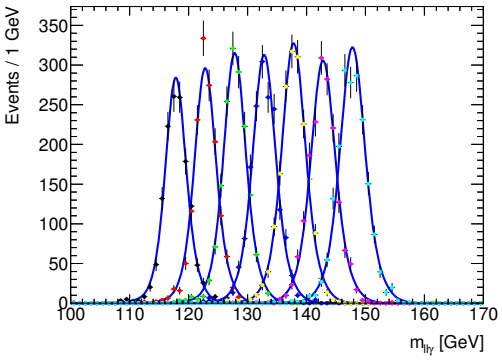

(b) $87 < m_{\ell\ell} < 89\,\text{GeV}$

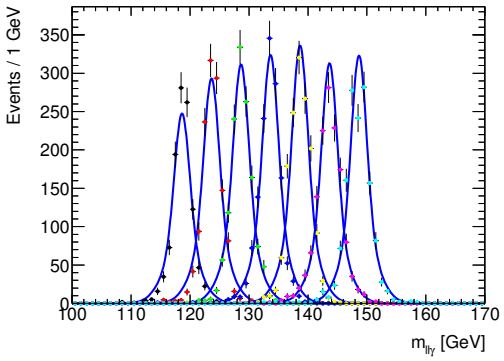

(c) $89 < m_{\ell\ell} < 90\,\text{GeV}$

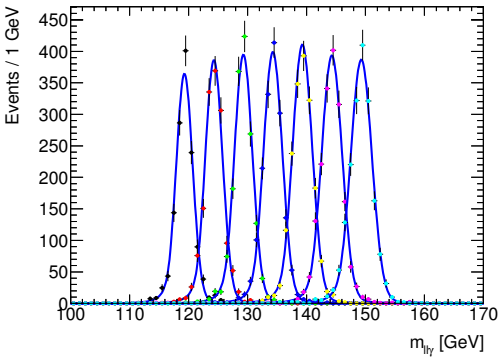

(d) $90 < m_{\ell\ell} < 91\,\text{GeV}$

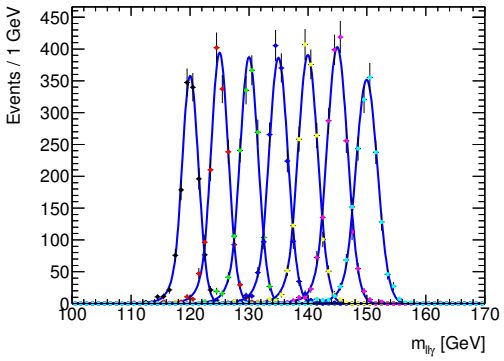

(e) $91 < m_{\ell\ell} < 92\,\text{GeV}$

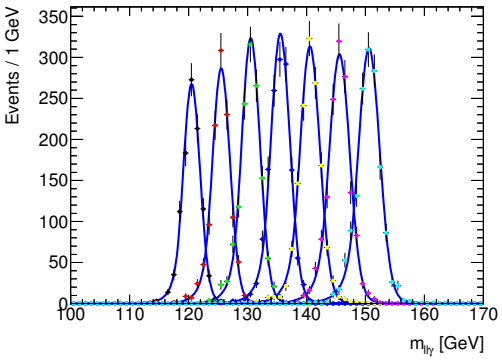

(f) $92 < m_{\ell\ell} < 93\,\text{GeV}$

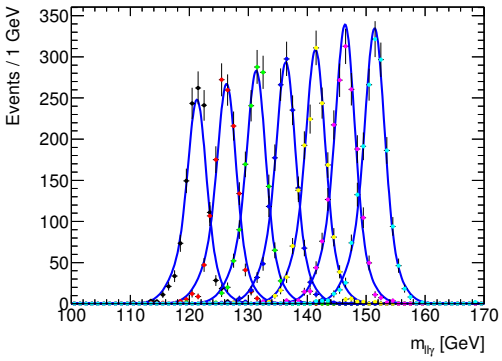

(g) $93 < m_{\ell\ell} < 95\,\text{GeV}$

Figure 6.33: Signal models for the $H \to Z\gamma$, 8 TeV ggF MC samples in the $\mu\mu\gamma$ channel, for seven different mass points. All mass points were simultaneously fitted with a model composed of a Crystal Ball function summed with a Gaussian function.

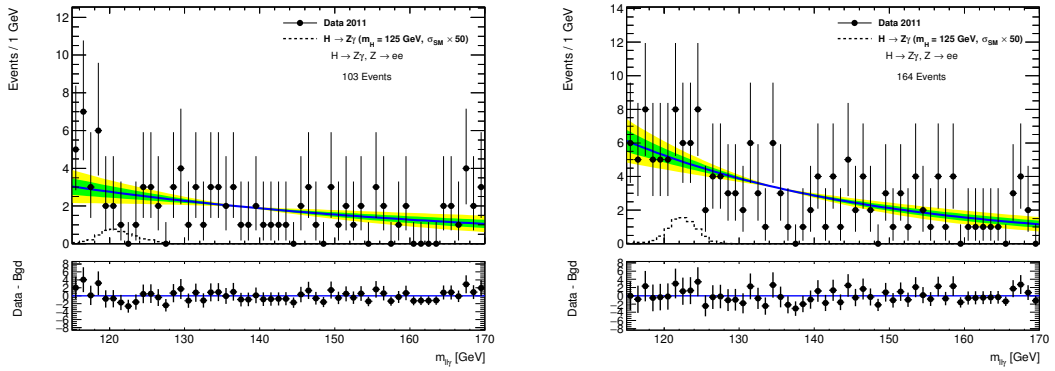

(a) $85 < m_{\ell\ell} < 87\,\text{GeV}$

(b) $87 < m_{\ell\ell} < 89\,\text{GeV}$

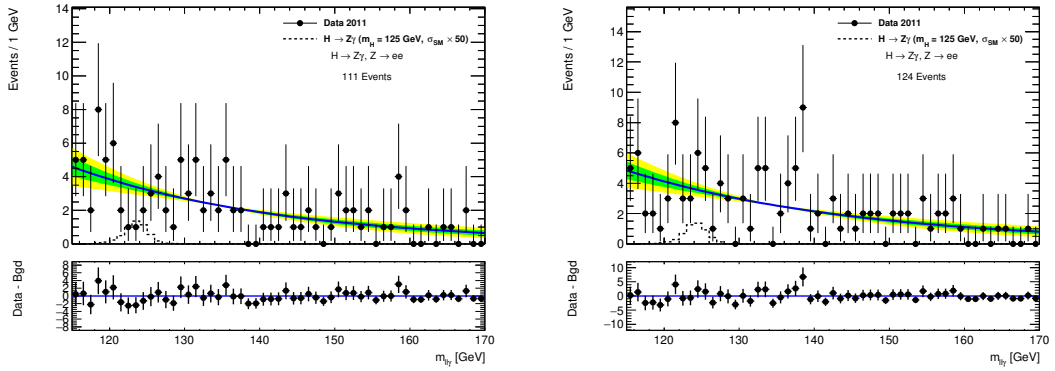

(c) $89 < m_{\ell\ell} < 90\,\text{GeV}$

(d) $90 < m_{\ell\ell} < 91\,\text{GeV}$

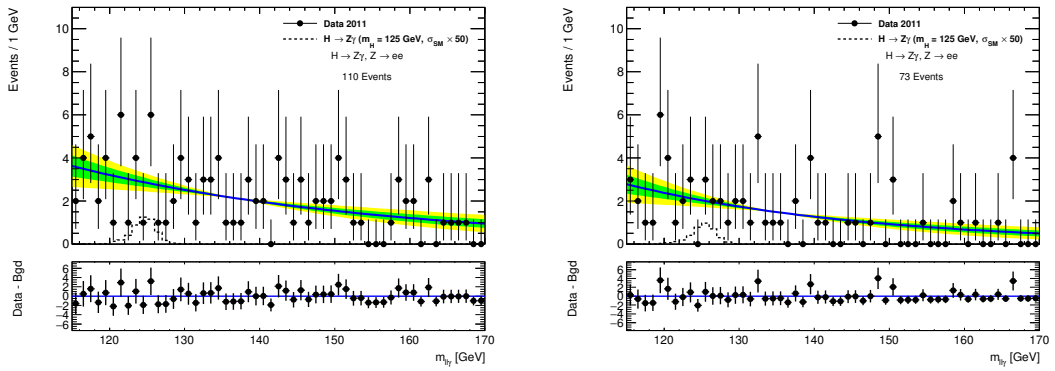

(e) $91 < m_{\ell\ell} < 92\,\text{GeV}$

(f) $92 < m_{\ell\ell} < 93\,\text{GeV}$

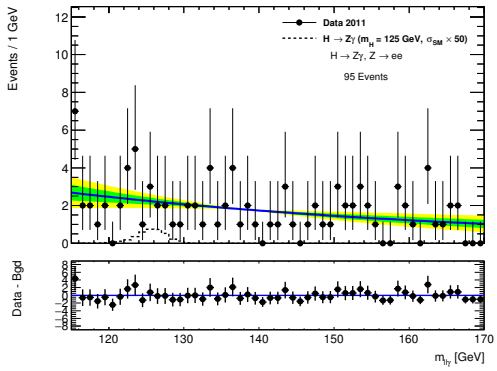

(g) $93 < m_{\ell\ell} < 95\,\text{GeV}$

Figure 6.34: Background-only fit to the $m_{\ell\ell\gamma}$ distribution of events selected from 7 TeV data in the $ee\gamma$ channel. The blue line is the fit result, while the green and yellow bands represent the 1σ and 2σ error bands from the uncertainties on the parameters of the fitted exponentials. The black dashed line is the total expected signal for a Higgs boson of mass 125 GeV, scaled by a factor of 50 for visibility.

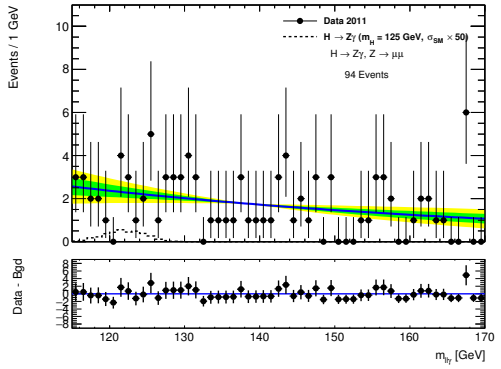

(a) $85 < m_{\ell\ell} < 87\,\text{GeV}$

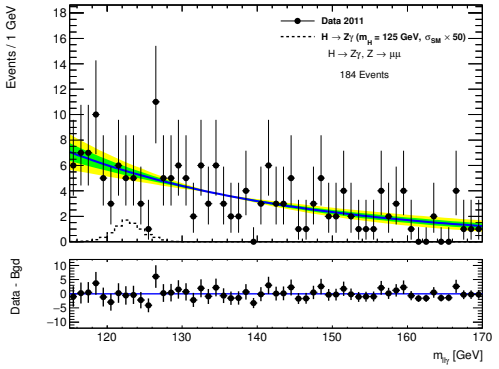

(b) $87 < m_{\ell\ell} < 89\,\text{GeV}$

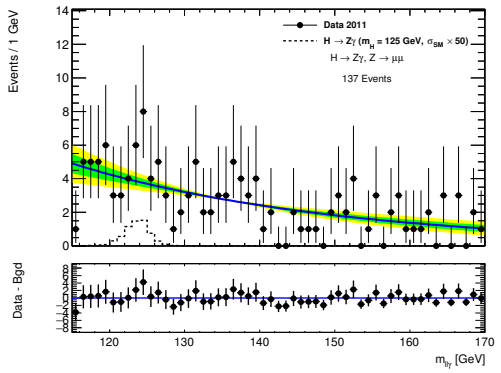

(c) $89 < m_{\ell\ell} < 90\,\text{GeV}$

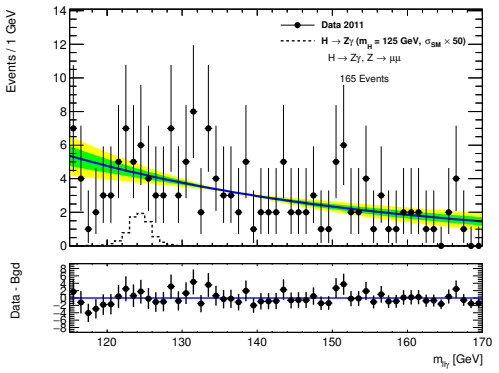

(d) $90 < m_{\ell\ell} < 91\,\text{GeV}$

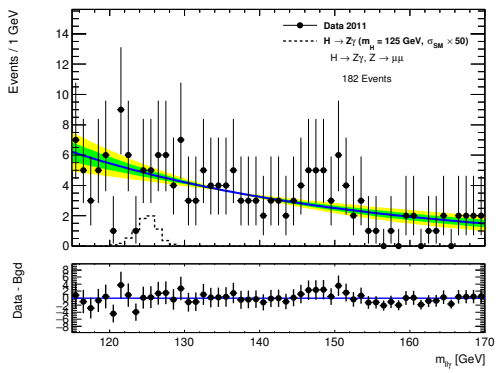

(e) $91 < m_{\ell\ell} < 92\,\text{GeV}$

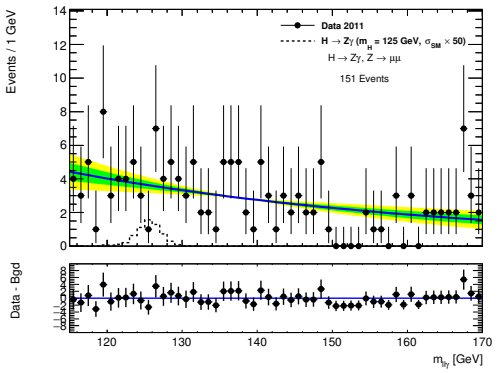

(f) $92 < m_{\ell\ell} < 93\,\text{GeV}$

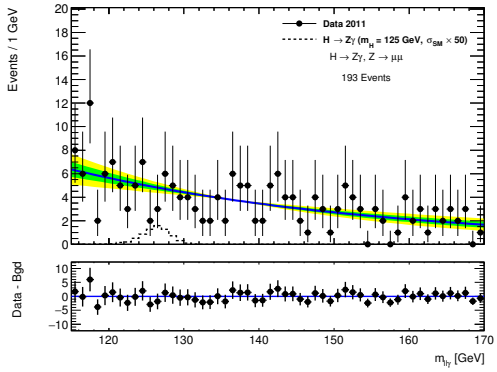

(g) $93 < m_{\ell\ell} < 95\,\text{GeV}$

Figure 6.35: Background-only fit to the $m_{\ell\ell\gamma}$ distribution of events selected from 7 TeV data in the $\mu\mu\gamma$ channel. The blue line is the fit result, while the green and yellow bands represent the 1σ and 2σ error bands from the uncertainties on the parameters of the fitted exponentials. The black dashed line is the total expected signal for a Higgs boson of mass 125 GeV, scaled by a factor of 50 for visibility.

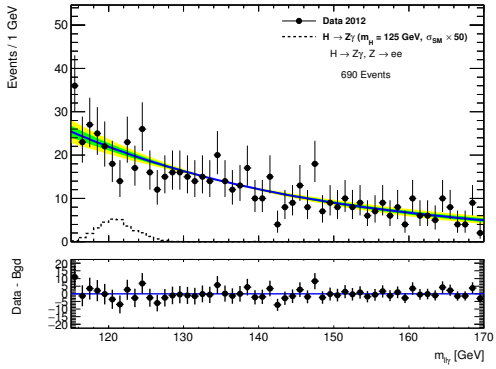

(a) $85 < m_{\ell\ell} < 87\,\text{GeV}$

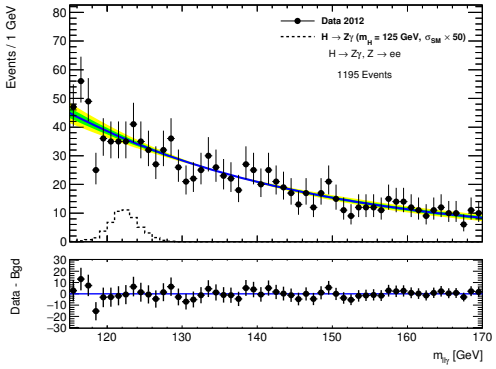

(b) $87 < m_{\ell\ell} < 89\,\text{GeV}$

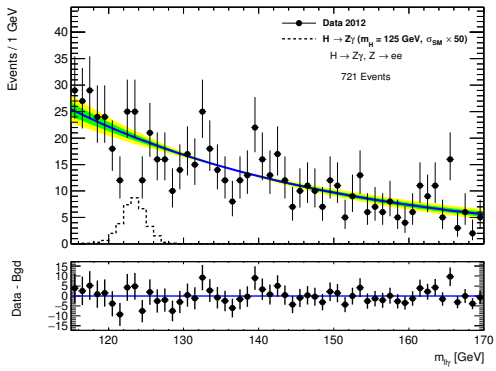

(c) $89 < m_{\ell\ell} < 90\,\text{GeV}$

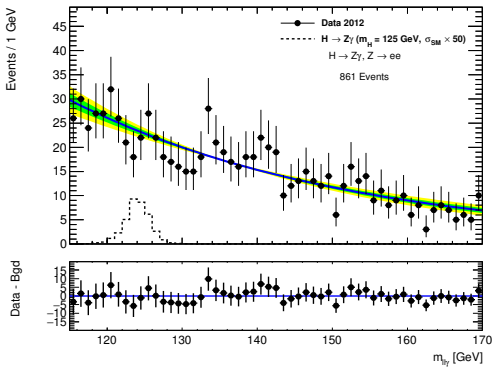

(d) $90 < m_{\ell\ell} < 91\,\text{GeV}$

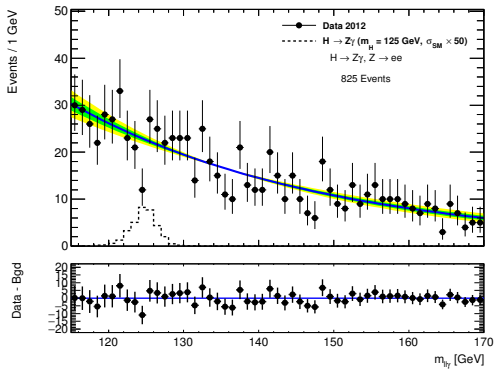

(e) $91 < m_{\ell\ell} < 92\,\text{GeV}$

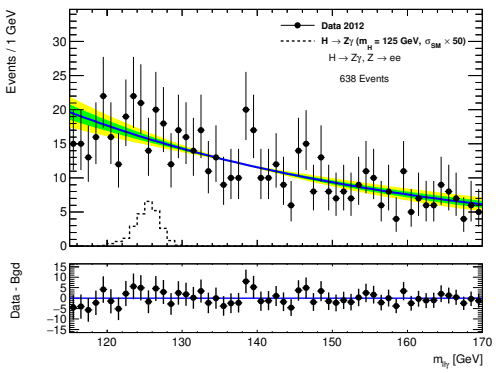

(f) $92 < m_{\ell\ell} < 93\,\text{GeV}$

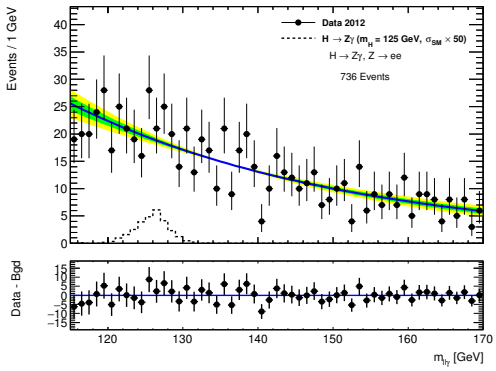

(g) $93 < m_{\ell\ell} < 95\,\text{GeV}$

Figure 6.36: Background-only fit to the $m_{\ell\ell\gamma}$ distribution of events selected from 8 TeV data in the $ee\gamma$ channel. The blue line is the fit result, while the green and yellow bands represent the 1σ and 2σ error bands from the uncertainties on the parameters of the fitted exponentials. The black dashed line is the total expected signal for a Higgs boson of mass 125 GeV, scaled by a factor of 50 for visibility.

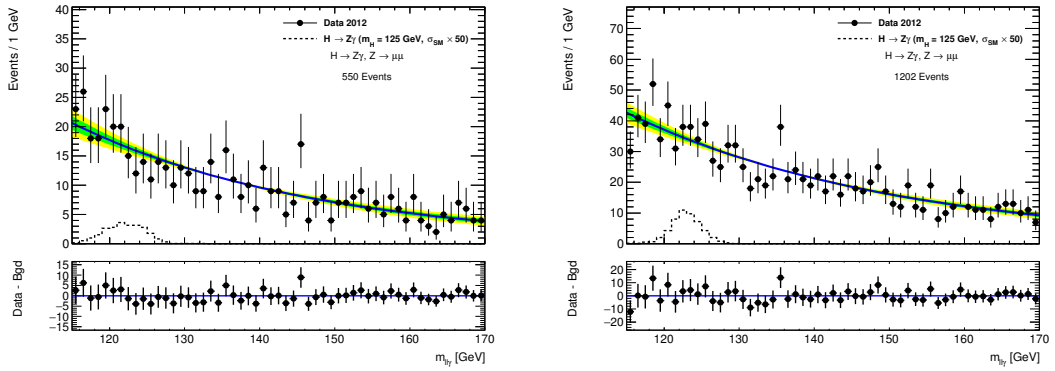

(a) $85 < m_{\ell\ell} < 87\,\text{GeV}$

(b) $87 < m_{\ell\ell} < 89\,\text{GeV}$

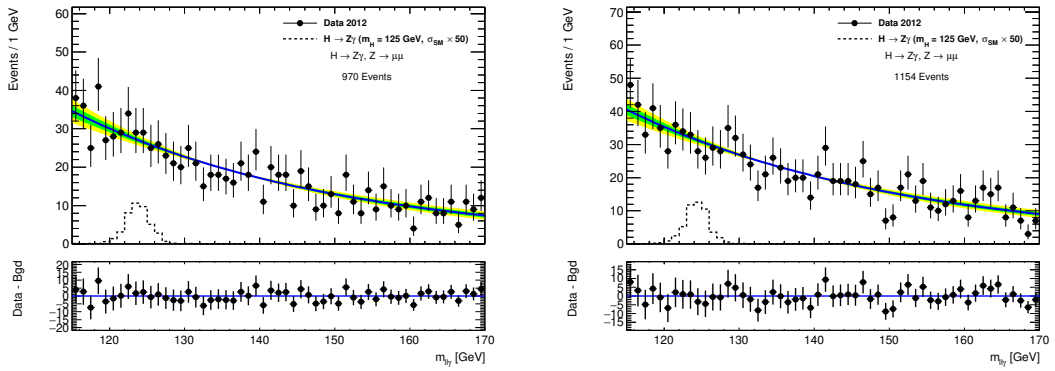

(c) $89 < m_{\ell\ell} < 90\,\text{GeV}$

(d) $90 < m_{\ell\ell} < 91\,\text{GeV}$

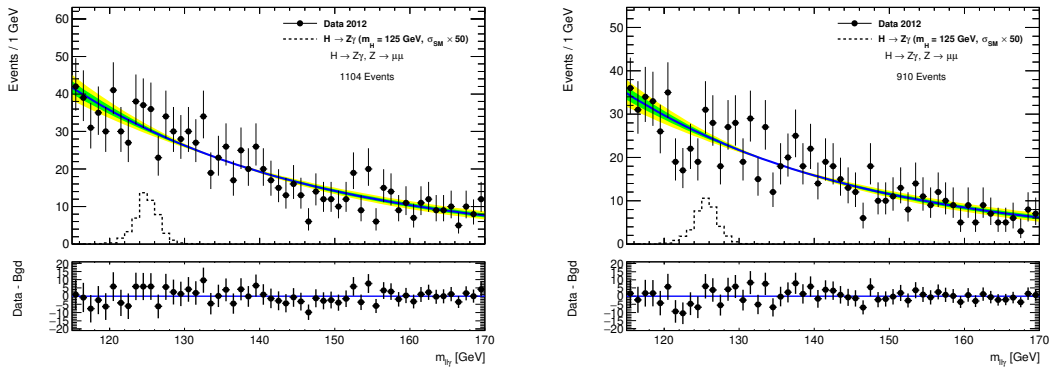

(e) $91 < m_{\ell\ell} < 92\,\text{GeV}$

(f) $92 < m_{\ell\ell} < 93\,\text{GeV}$

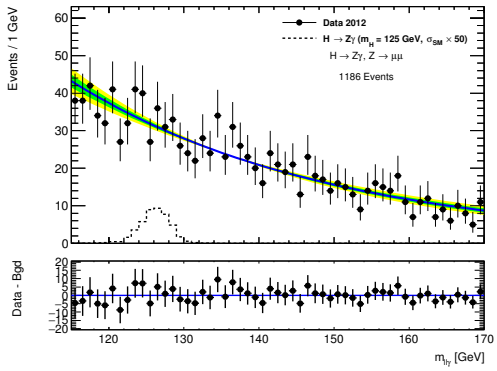

(g) $93 < m_{\ell\ell} < 95\,\text{GeV}$

Figure 6.37: Background-only fit to the $m_{\ell\ell\gamma}$ distribution of events selected from 8 TeV data in the $\mu\mu\gamma$ channel. The blue line is the fit result, while the green and yellow bands represent the 1σ and 2σ error bands from the uncertainties on the parameters of the fitted exponentials. The black dashed line is the total expected signal for a Higgs boson of mass 125 GeV, scaled by a factor of 50 for visibility.

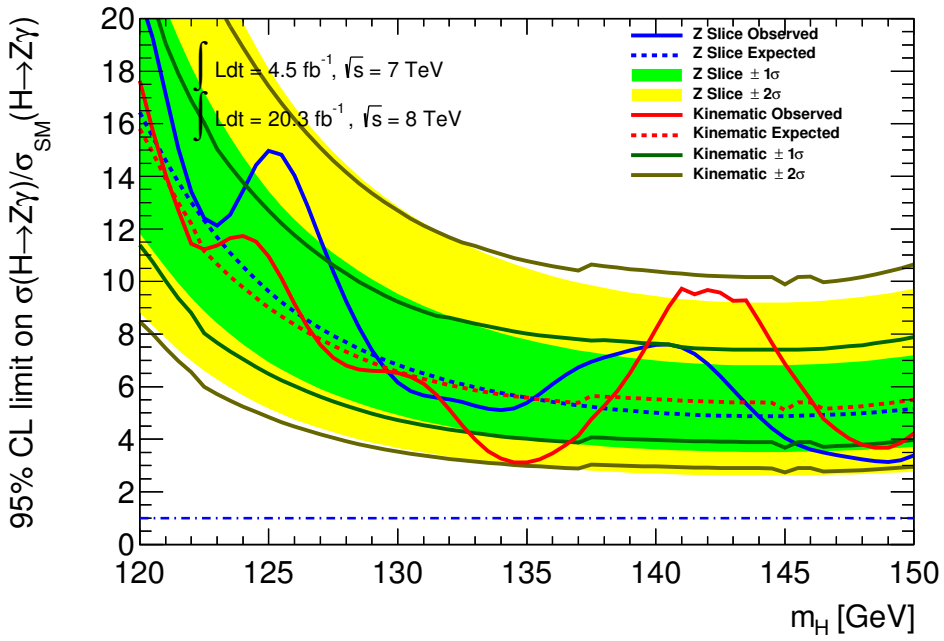

Figure 6.38: Observed and expected 95% C. L. limits (solid and dashed blue lines, respectively) on the production cross section of a SM Higgs boson decaying to $Z\gamma$ (normalised by the SM expectation), as a function of the Higgs boson mass, using the Z slices categorisation. The results were obtained using $4.5\,\text{fb}^{-1}$ of pp collision data at $\sqrt{s} = 7\,\text{TeV}$ and $20.3\,\text{fb}^{-1}$ of pp collision data at $\sqrt{s} = 8\,\text{TeV}$. The green and yellow bands correspond to the $\pm 1\sigma$ and $\pm 2\sigma$ intervals. For reference, the observed and expected 95% C. L. limits obtained using the kinematic event categorisation are overlaid (solid and dashed red lines, respectively) with their uncertainties.

is expected because the Z slices categorisation is only fulfilling and slightly improving on the role of the Z mass constraint (as noted in the previous section). The Z slices categorisation is incapable of matching the enhancements brought to the kinematic categorisation through the use of the p_T^t and $|\Delta\eta_{Z\gamma}|$ variables, and must therefore be extended to include these variables.

6.4.3 Z Slices with p_T^t Event Categorisation

For this study, events were separated according to the Z slices with p_T^t event categorisation described in Figure 6.25, and the analysis described in the previous section was repeated. The signal in each category and production mechanism was modelled by simultaneously fitting the MC samples at all mass points with a function composed of a Crystal Ball lineshape summed with a Gaussian distribution, and the results for events produced through the ggF production mechanism are shown in Figures 6.39 to 6.42. Since the Z slices and Z slices with p_T^t event categorisations contain identical 7 TeV categories, the signal models for these categories are unchanged from those shown in Figures 6.34 and 6.35.

The limited statistics available in data again required that the background in each category be modelled by fitting a simple exponential to the data. The results of these fits in the 8 TeV categories, together with the expected signal scaled by a factor of 50, are shown in Figures 6.43 to 6.46. The results of the fits to 7 TeV categories are unchanged from those shown in Figures 6.34 and 6.35.

The expected and observed limits were then evaluated, without including the systematic uncertainties, and Figure 6.47 shows the results together with those from the kinematic analysis. For a Higgs boson of mass 125 GeV, the expected limit is $9.01 \times$ SM under the kinematic categorisation and 8.05 under the Z slices with p_T^t categorisation. The enhancement in sensitivity due to the p_T^t variable adds to the enhancements from replacing the Z mass constraint with the Z slices selection criteria, yielding an improvement in the expected limit that is just over 10%.

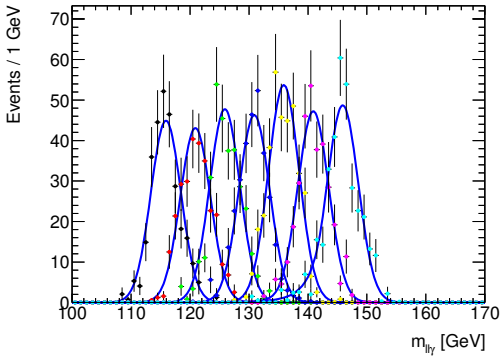

(a) $85 < m_{\ell\ell} < 87\,\text{GeV}$

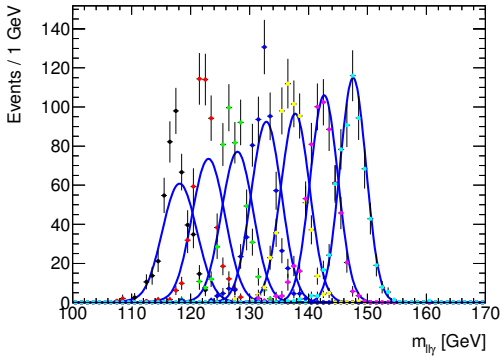

(b) $87 < m_{\ell\ell} < 89\,\text{GeV}$

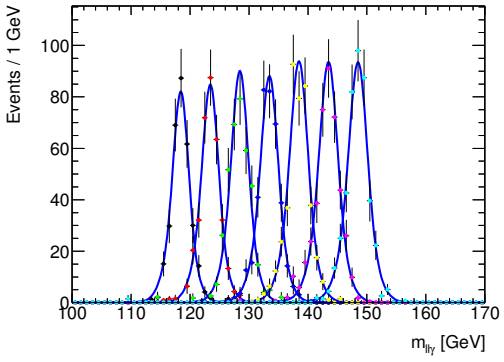

(c) $89 < m_{\ell\ell} < 90\,\text{GeV}$

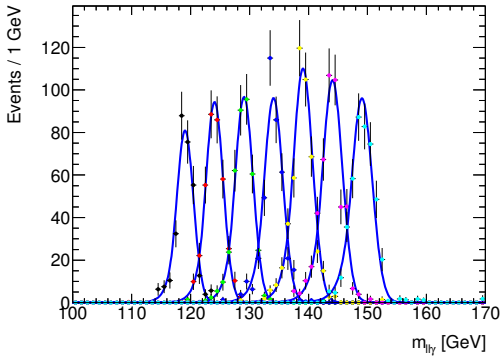

(d) $90 < m_{\ell\ell} < 91\,\text{GeV}$

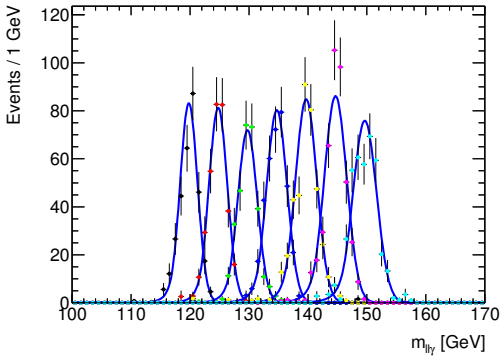

(e) $91 < m_{\ell\ell} < 92\,\text{GeV}$

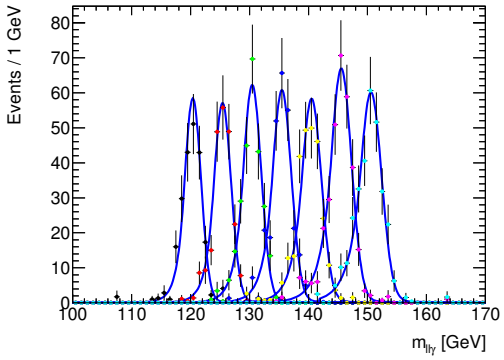

(f) $92 < m_{\ell\ell} < 93\,\text{GeV}$

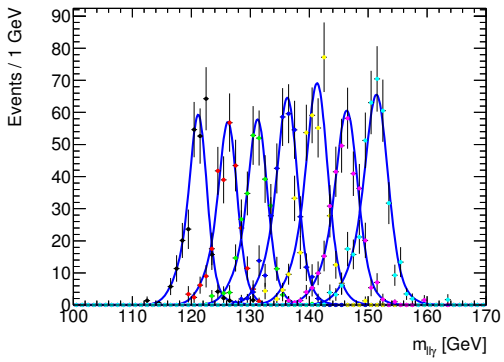

(g) $93 < m_{\ell\ell} < 95\,\text{GeV}$

Figure 6.39: Signal models for the $H \to Z\gamma$, 8 TeV ggF MC samples in the $ee\gamma$ channel and high-p_T^t category, for seven different mass points. All mass points were simultaneously fitted with a model composed of a Crystal Ball function summed with a Gaussian function.

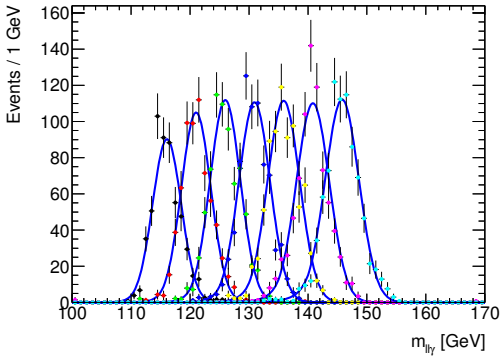

(a) $85 < m_{\ell\ell} < 87\,\text{GeV}$

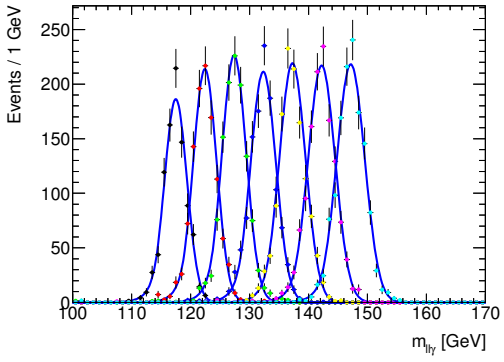

(b) $87 < m_{\ell\ell} < 89\,\text{GeV}$

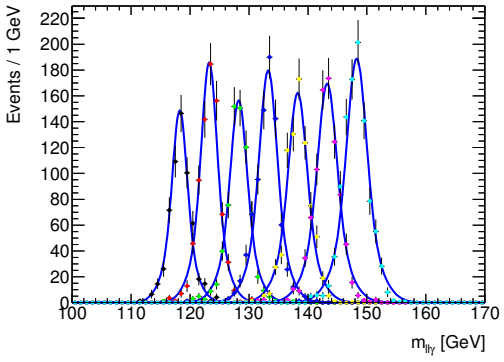

(c) $89 < m_{\ell\ell} < 90\,\text{GeV}$

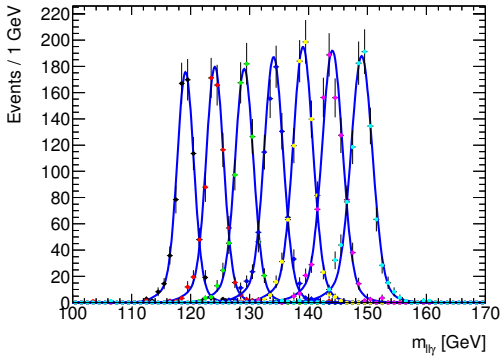

(d) $90 < m_{\ell\ell} < 91\,\text{GeV}$

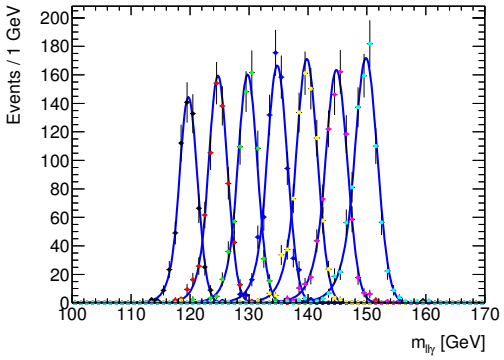

(e) $91 < m_{\ell\ell} < 92\,\text{GeV}$

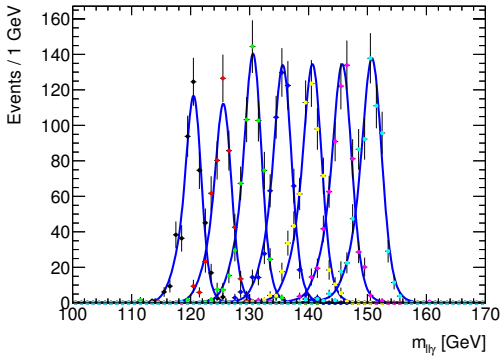

(f) $92 < m_{\ell\ell} < 93\,\text{GeV}$

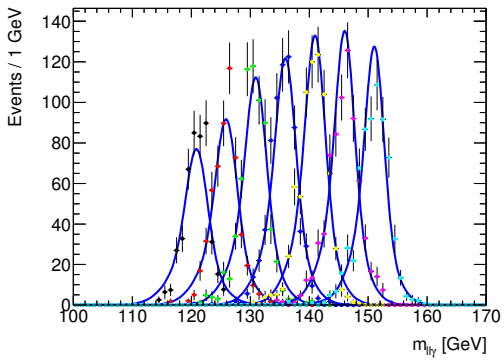

(g) $93 < m_{\ell\ell} < 95\,\text{GeV}$

Figure 6.40: Signal models for the $H \to Z\gamma$, 8 TeV ggF MC samples in the $ee\gamma$ channel and low-p_T^t category, for seven different mass points. All mass points were simultaneously fitted with a model composed of a Crystal Ball function summed with a Gaussian function.

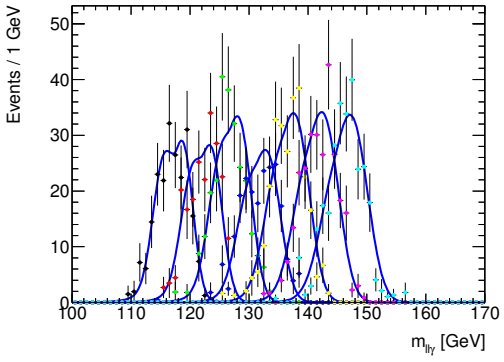

(a) $85 < m_{\ell\ell} < 87\,\text{GeV}$

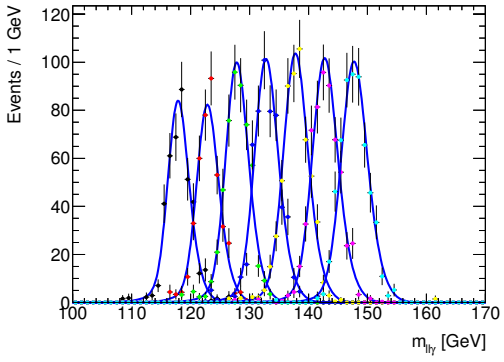

(b) $87 < m_{\ell\ell} < 89\,\text{GeV}$

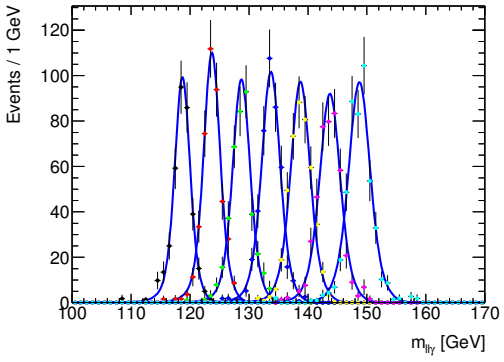

(c) $89 < m_{\ell\ell} < 90\,\text{GeV}$

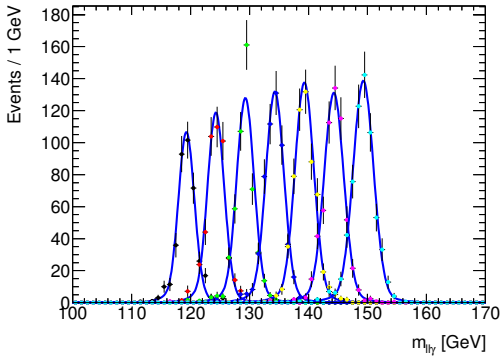

(d) $90 < m_{\ell\ell} < 91\,\text{GeV}$

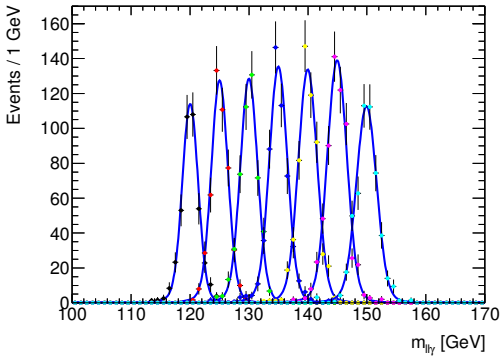

(e) $91 < m_{\ell\ell} < 92\,\text{GeV}$

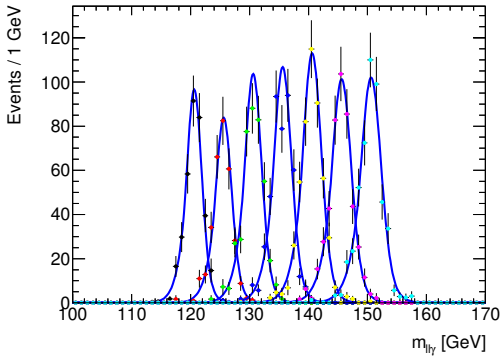

(f) $92 < m_{\ell\ell} < 93\,\text{GeV}$

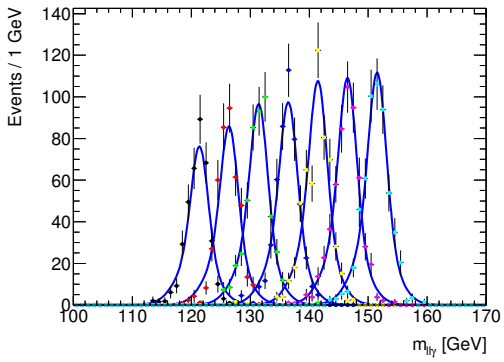

(g) $93 < m_{\ell\ell} < 95\,\text{GeV}$

Figure 6.41: Signal models for the $H \to Z\gamma$, 8 TeV ggF MC samples in the $\mu\mu\gamma$ channel and high-p_T^t category, for seven different mass points. All mass points were simultaneously fitted with a model composed of a Crystal Ball function summed with a Gaussian function.

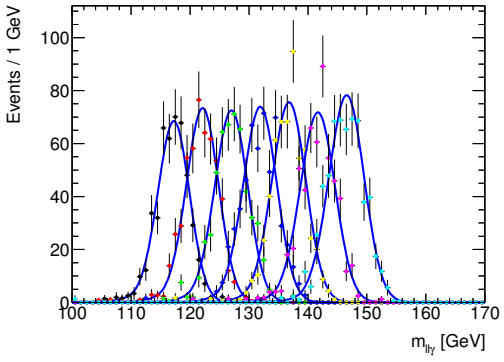

(a) $85 < m_{\ell\ell} < 87\,\text{GeV}$

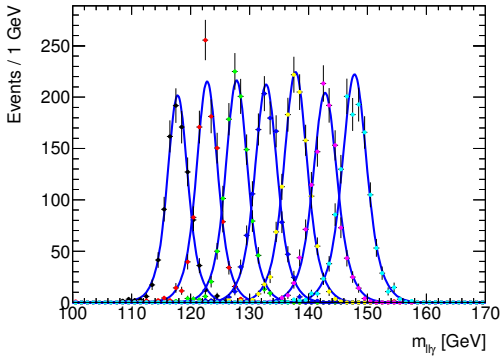

(b) $87 < m_{\ell\ell} < 89\,\text{GeV}$

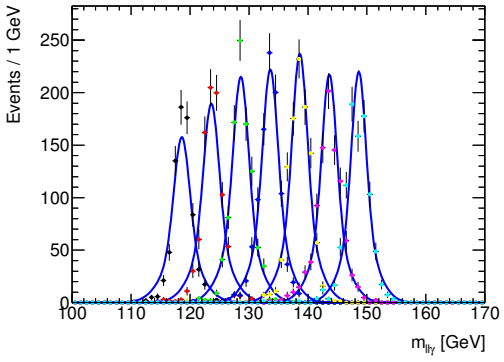

(c) $89 < m_{\ell\ell} < 90\,\text{GeV}$

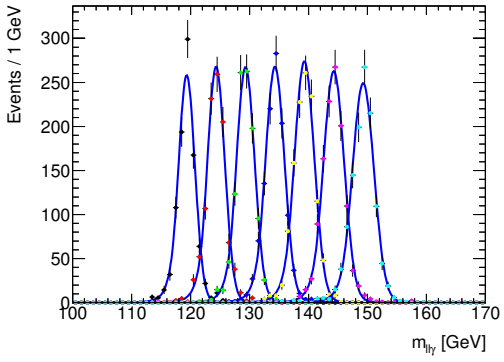

(d) $90 < m_{\ell\ell} < 91\,\text{GeV}$

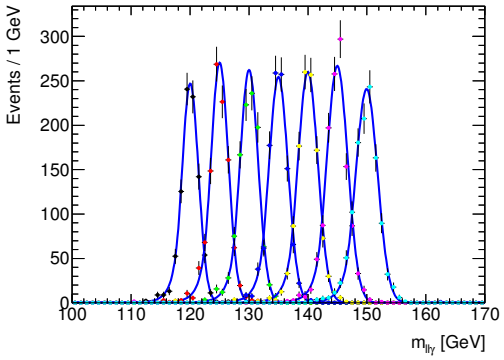

(e) $91 < m_{\ell\ell} < 92\,\text{GeV}$

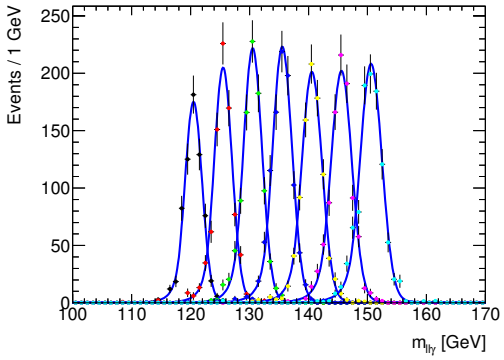

(f) $92 < m_{\ell\ell} < 93\,\text{GeV}$

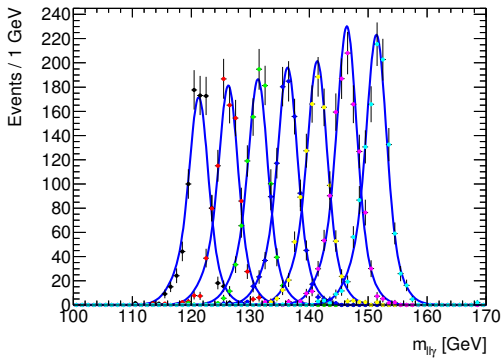

(g) $93 < m_{\ell\ell} < 95\,\text{GeV}$

Figure 6.42: Signal models for the $H \to Z\gamma$, 8 TeV ggF MC samples in the $\mu\mu\gamma$ channel and low-p_T^t category, for seven different mass points. All mass points were simultaneously fitted with a model composed of a Crystal Ball function summed with a Gaussian function.

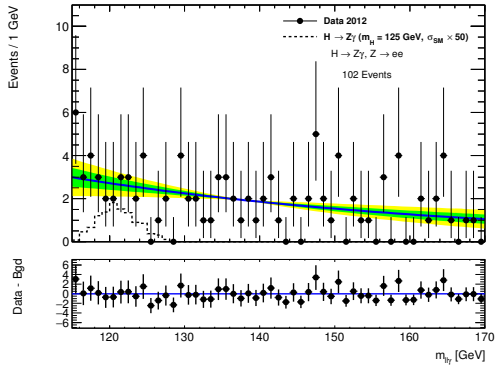

(a) $85 < m_{\ell\ell} < 87\,\text{GeV}$

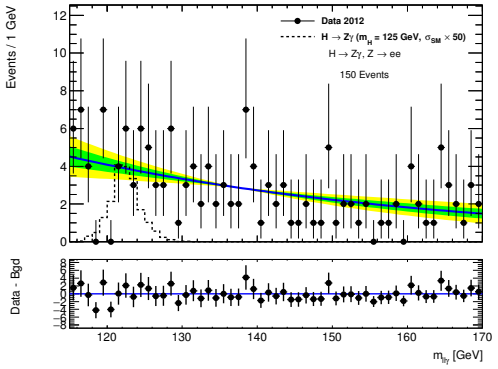

(b) $87 < m_{\ell\ell} < 89\,\text{GeV}$

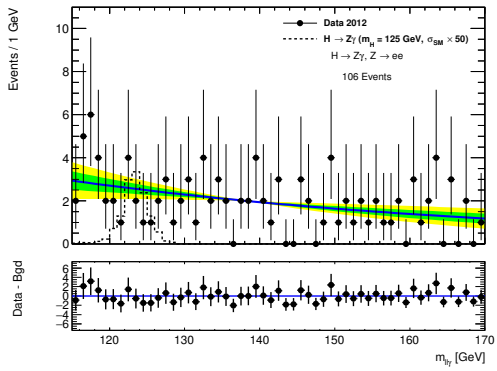

(c) $89 < m_{\ell\ell} < 90\,\text{GeV}$

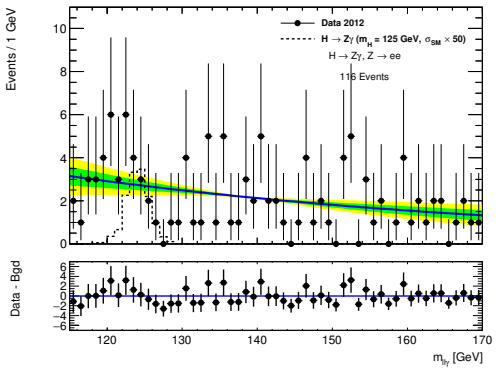

(d) $90 < m_{\ell\ell} < 91\,\text{GeV}$

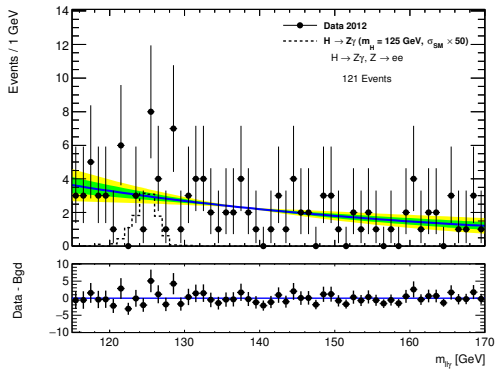

(e) $91 < m_{\ell\ell} < 92\,\text{GeV}$

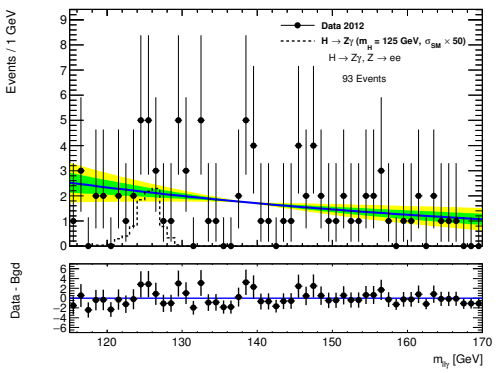

(f) $92 < m_{\ell\ell} < 93\,\text{GeV}$

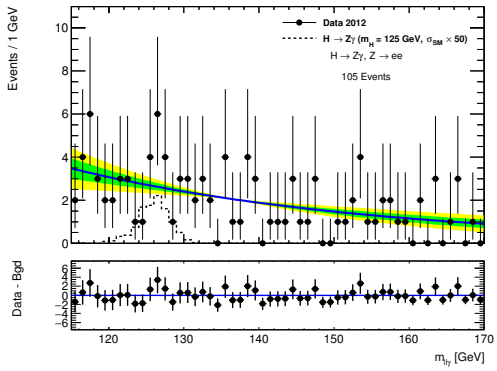

(g) $93 < m_{\ell\ell} < 95\,\text{GeV}$

Figure 6.43: Background-only fit to the $m_{\ell\ell\gamma}$ distribution of events selected from 8 TeV data in the $ee\gamma$ channel and high-p_T^t category. The blue line is the fit result, while the green and yellow bands represent the 1σ and 2σ error bands from the uncertainties on the parameters of the fitted exponentials. The black dashed line is the total expected signal for a Higgs boson of mass 125 GeV, scaled by a factor of 50 for visibility.

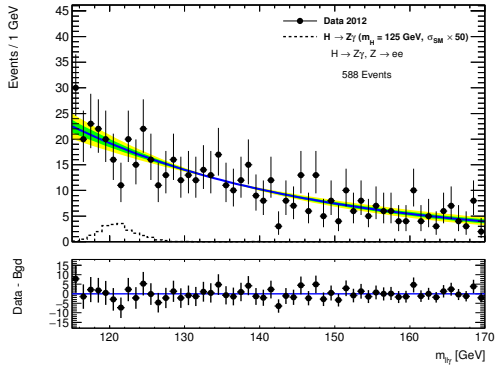

(a) $85 < m_{\ell\ell} < 87\,\text{GeV}$

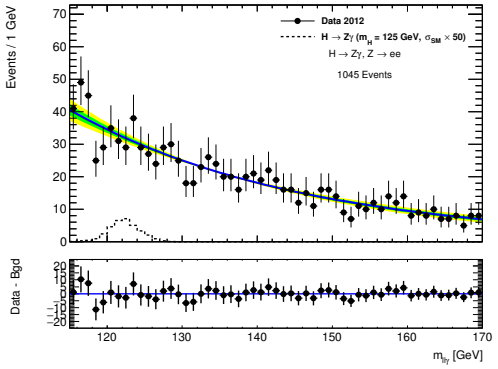

(b) $87 < m_{\ell\ell} < 89\,\text{GeV}$

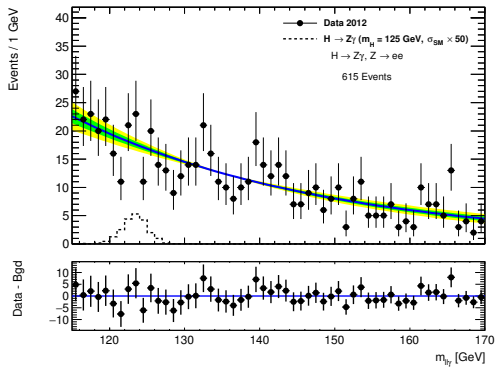

(c) $89 < m_{\ell\ell} < 90\,\text{GeV}$

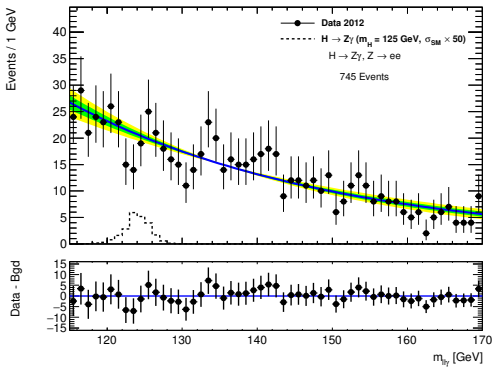

(d) $90 < m_{\ell\ell} < 91\,\text{GeV}$

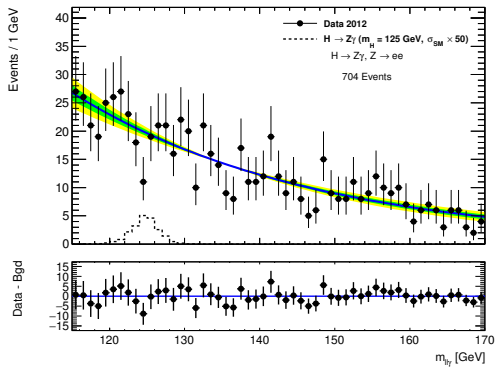

(e) $91 < m_{\ell\ell} < 92\,\text{GeV}$

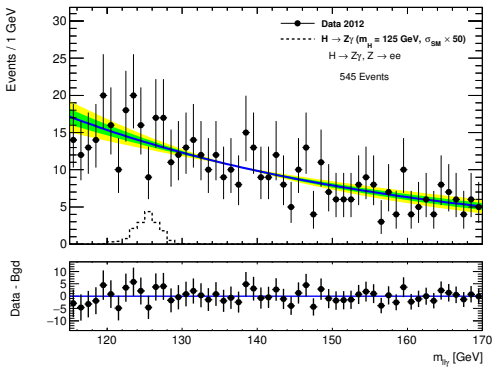

(f) $92 < m_{\ell\ell} < 93\,\text{GeV}$

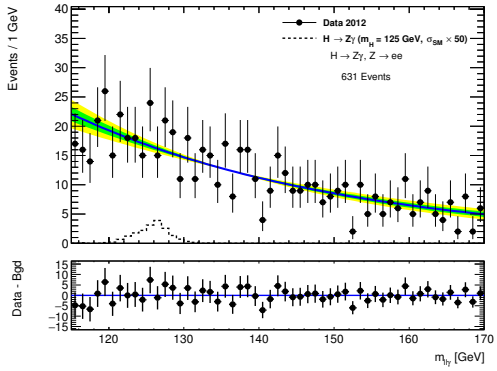

(g) $93 < m_{\ell\ell} < 95\,\text{GeV}$

Figure 6.44: Background-only fit to the $m_{\ell\ell\gamma}$ distribution of events selected from 8 TeV data in the $ee\gamma$ channel and low-p_T^t category. The blue line is the fit result, while the green and yellow bands represent the 1σ and 2σ error bands from the uncertainties on the parameters of the fitted exponentials. The black dashed line is the total expected signal for a Higgs boson of mass 125 GeV, scaled by a factor of 50 for visibility.

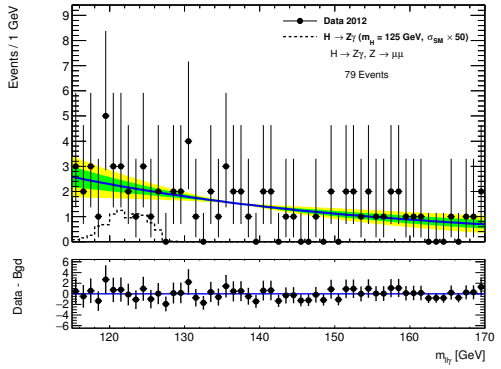

(a) $85 < m_{\ell\ell} < 87\,\text{GeV}$

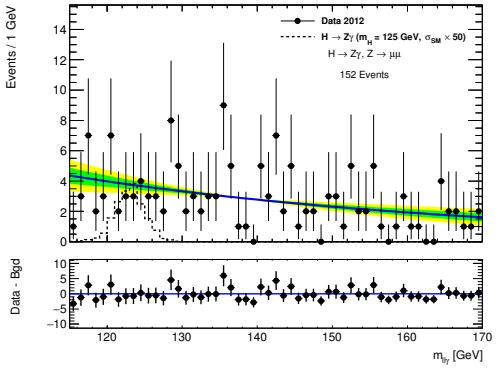

(b) $87 < m_{\ell\ell} < 89\,\text{GeV}$

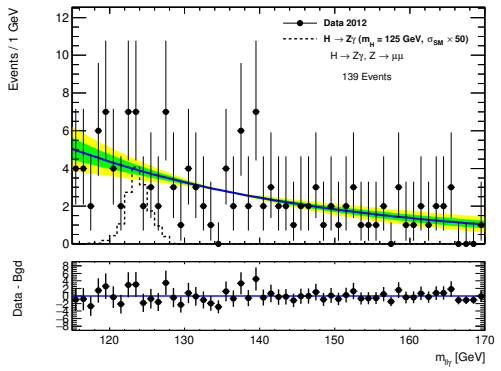

(c) $89 < m_{\ell\ell} < 90\,\text{GeV}$

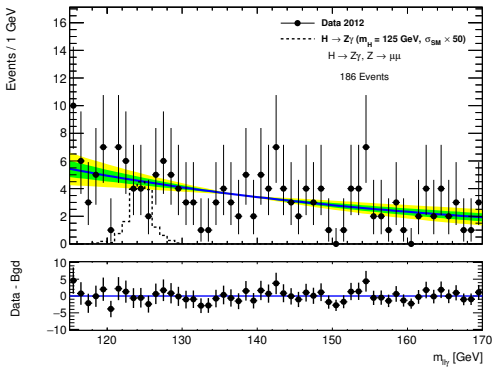

(d) $90 < m_{\ell\ell} < 91\,\text{GeV}$

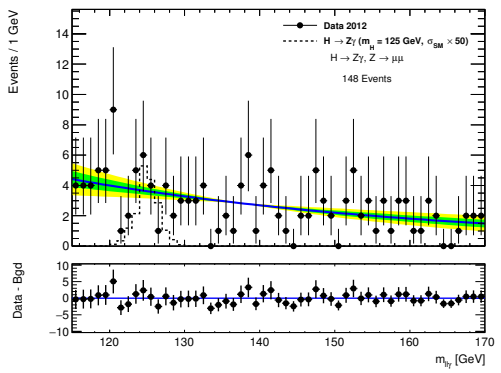

(e) $91 < m_{\ell\ell} < 92\,\text{GeV}$

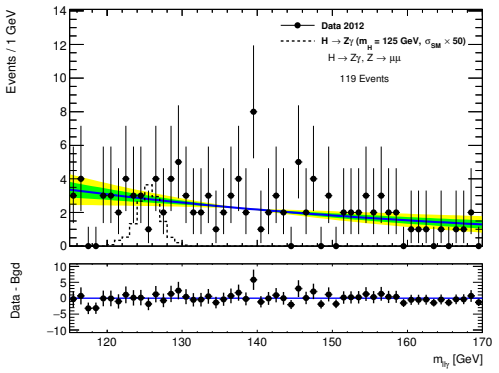

(f) $92 < m_{\ell\ell} < 93\,\text{GeV}$

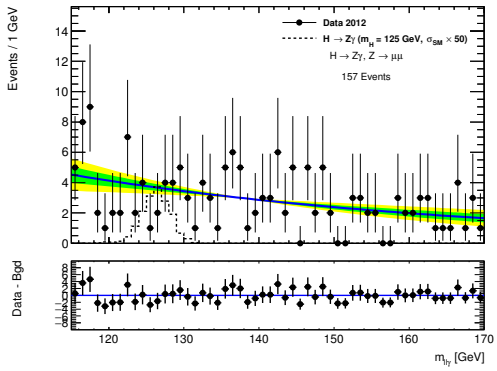

(g) $93 < m_{\ell\ell} < 95\,\text{GeV}$

Figure 6.45: Background-only fit to the $m_{\ell\ell\gamma}$ distribution of events selected from 8 TeV data in the $\mu\mu\gamma$ channel and high-p_T^t category. The blue line is the fit result, while the green and yellow bands represent the 1σ and 2σ error bands from the uncertainties on the parameters of the fitted exponentials. The black dashed line is the total expected signal for a Higgs boson of mass 125 GeV, scaled by a factor of 50 for visibility.

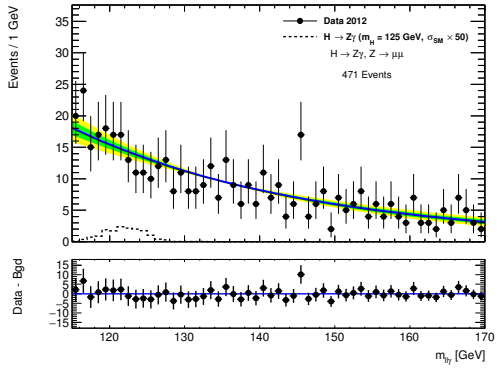

(a) $85 < m_{\ell\ell} < 87\,\text{GeV}$

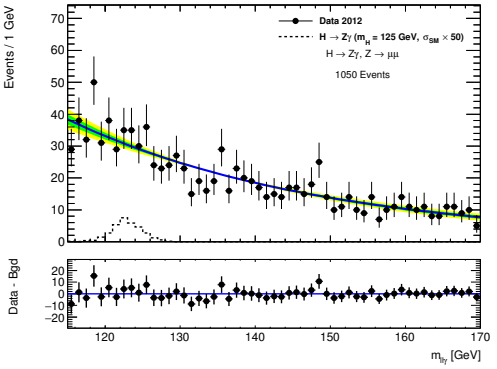

(b) $87 < m_{\ell\ell} < 89\,\text{i GeV}$

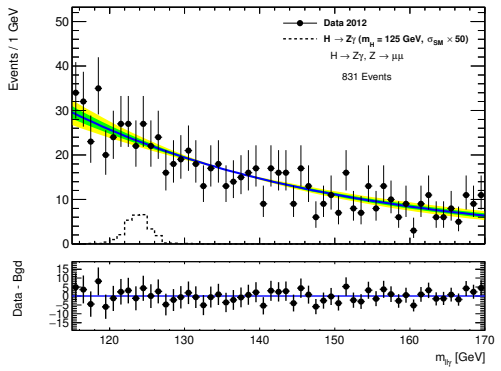

(c) $89 < m_{\ell\ell} < 90\,\text{GeV}$

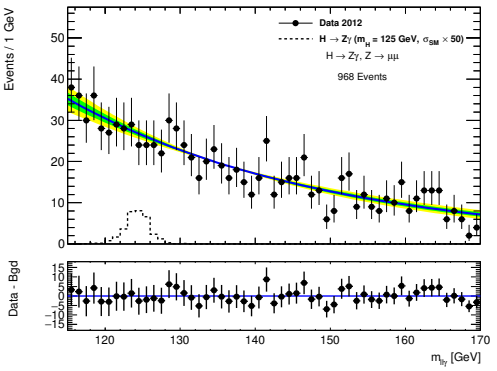

(d) $90 < m_{\ell\ell} < 91\,\text{GeV}$

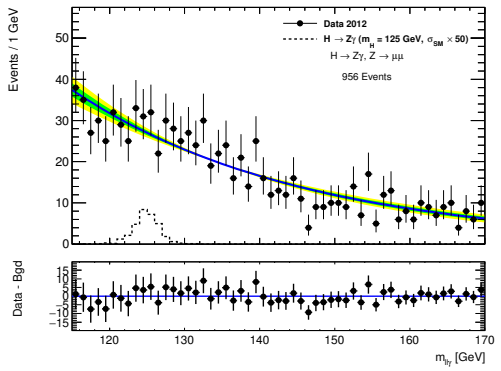

(e) $91 < m_{\ell\ell} < 92\,\text{GeV}$

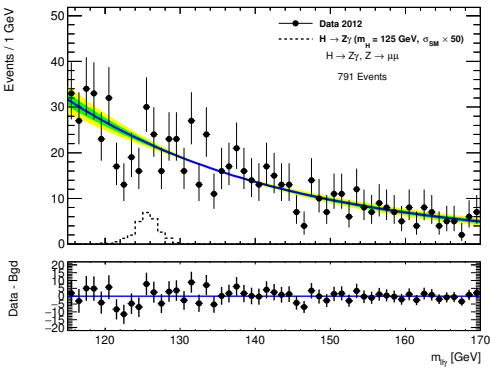

(f) $92 < m_{\ell\ell} < 93\,\text{GeV}$

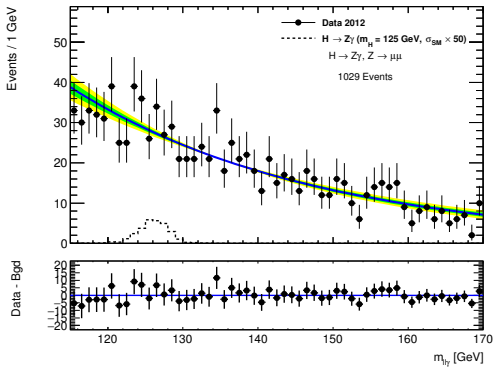

(g) $93 < m_{\ell\ell} < 95\,\text{GeV}$

Figure 6.46: Background-only fit to the $m_{\ell\ell\gamma}$ distribution of events selected from 8 TeV data in the $\mu\mu\gamma$ channel and low-p_T^t category. The blue line is the fit result, while the green and yellow bands represent the 1σ and 2σ error bands from the uncertainties on the parameters of the fitted exponentials. The black dashed line is the total expected signal for a Higgs boson of mass 125 GeV, scaled by a factor of 50 for visibility.

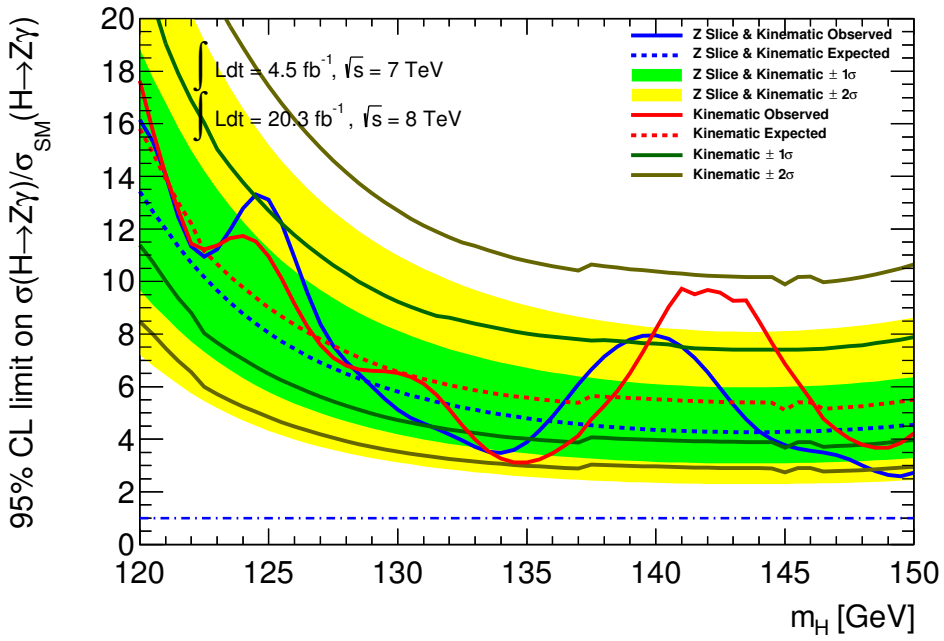

Figure 6.47: Observed and expected 95% C. L. limits (solid and dashed blue lines, respectively) on the production cross section of a SM Higgs boson decaying to $Z\gamma$ (normalised by the SM expectation), as a function of the Higgs boson mass, using the Z Slices with p_T^t categorisation. The results were obtained using $4.5\,\text{fb}^{-1}$ of pp collision data at $\sqrt{s} = 7\,\text{TeV}$ and $20.3\,\text{fb}^{-1}$ of pp collision data at $\sqrt{s} = 8\,\text{TeV}$. The green and yellow bands correspond to the $\pm 1\sigma$ and $\pm 2\sigma$ intervals. For reference, the observed and expected 95% C. L. limits obtained using the kinematic event categorisation are overlaid (solid and dashed red lines, respectively) with their uncertainties.

Event Categorisation	Expected Limit
10 slices (1 GeV width)	9.51
5 slices (2 GeV width)	9.67
3 slices (various width)	9.77
Z slices categorisation	9.63

Table 6.22: Expected limit for the Z slices categorisation with slices of varying width.

6.4.4 Event Migration Between Z Slices

Owing to the narrow width of the Z slices, it is possible that uncertainties in the reconstruction of Higgs and Z candidates may result in events being incorrectly assigned to a slice. In order to asses the impact of such an event migration, the expected limit at $m_H = 125\,\text{GeV}$ was evaluated using three variants of the Z slices categorisation. For each centre-of-mass energy and final state, events satisfying $85 < m_{\ell\ell} < 95\,\text{GeV}$ were separated into:

- 10 slices of width 1 GeV
- 5 slices of width 2 GeV
- 3 slices covering $85 < m_{\ell\ell} < 89$, $89 < m_{\ell\ell} < 91$, and $91 < m_{\ell\ell} < 95\,\text{GeV}$

The expected limits are presented in Table 6.22, together with those of the actual Z slices event categorisation (1 GeV slices, except for the tails with 2 GeV slices) for reference.

When moving from 10 slices to 5 slices, five sets of neighbouring slices are merged together to remove boundaries that events could have migrated across. Any difference in the expected limit can therefore be assumed to come from the migration of events across those missing boundaries. In this case, the variation is relatively small at 1.6%. Moving from 5 to 3 slices similarly reduces the number of boundaries across which events could migrate, giving a change in the expected limit of 1.04%. A conservative estimate of the systematic uncertainty due to event migration would therefore be 2%.

A more refined approach was then taken by smearing the reconstructed Z mass to deliberately introduce a migration of events across slices. The kinematic analysis included a 5% systematic uncertainty on the $m_{\ell\ell\gamma}$ resolution, and so it was considered appropriate to apply this level of smearing to $m_{\ell\ell}$. A random number thrown from a Gaussian distribution of mean zero and σ such that the resultant $m_{\ell\ell}$ distribution would be 5% wider was added to the reconstructed mass of each Z boson. The four-vector of each Z boson was then updated and combined with the unaffected photon candidate, and a corresponding smeared $m_{\ell\ell\gamma}$ value was calculated. The expected limit was then evaluated for the Z slices and Z slices with p_T^t event categorisations, following the same procedures described in Sections 6.4.2 and 6.4.3, but using these smeared reconstructed Z and Higgs boson masses. Comparisons of the limits from smeared and unsmeared variables from both categorisations are presented in Figures 6.48 and 6.49.

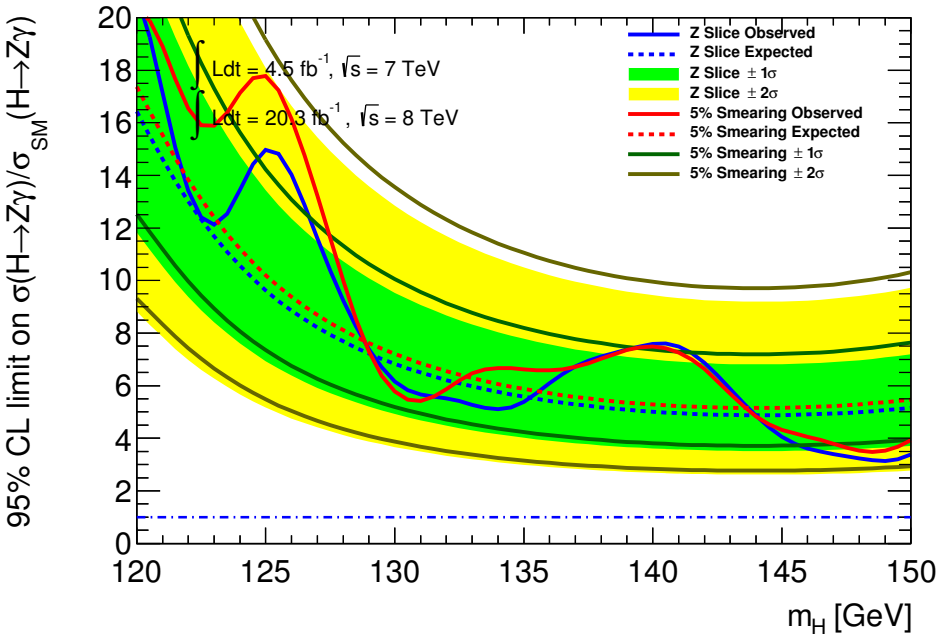

Figure 6.48: Observed and expected 95% C. L. limits (solid and dashed blue lines, respectively) on the production cross section of a SM Higgs boson decaying to $Z\gamma$ (normalised by the SM expectation), as a function of the Higgs boson mass, using the Z Slices categorisation. The observed and expected limits from smearing the Z mass (and propagating this to the Higgs boson mass) are shown by the solid and dashed red lines, respectively.

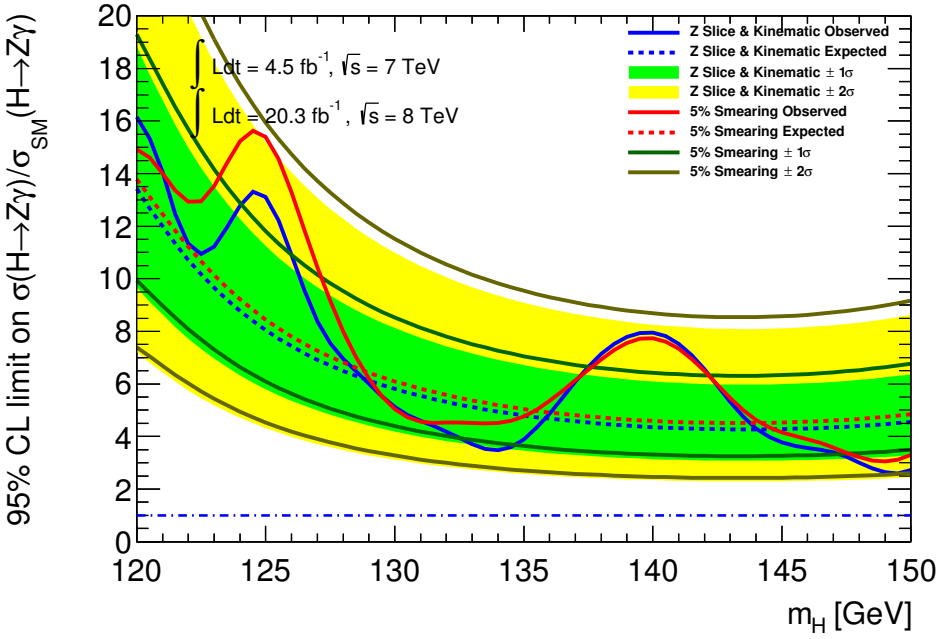

Figure 6.49: Observed and expected 95% C. L. limits (solid and dashed blue lines, respectively) on the production cross section of a SM Higgs boson decaying to $Z\gamma$ (normalised by the SM expectation), as a function of the Higgs boson mass, using the Z slices with p_T^t categorisation. The observed and expected limits from smearing the Z mass (and propagating this to the boson Higgs mass) are shown by the solid and dashed red lines, respectively.

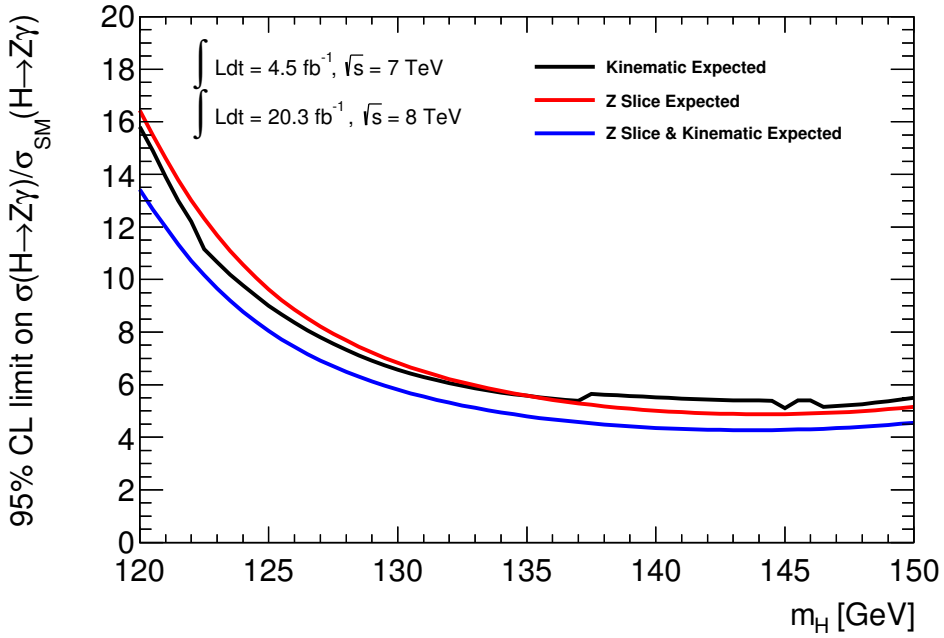

Figure 6.50: Expected 95% C. L. limits for the Kinematic, Z slices, and Z slices with p_T^t event categorisations, normalised by the SM expectation.

Applying smearing when using either of the Z slices categorisations causes the limit to shift by approximately 5%. It should be noted that this value does not represent a systematic uncertainty, but is rather a figure-of-merit for a worst-case scenario.

6.4.5 Comparison of Limits

Figure 6.50 shows a comparison of the expected limits obtained using the kinematic, Z slices, and Z slices with p_T^t event categorisations. As noted in the previous section, any event migration between Z slices would be minimal and not affect the basic conclusions that using this technique provides a significant enhancement in the sensitivity of the analysis. While Z slices alone can only fulfil and improve the role of the Z mass constraint, improvements from additional subcategories based on kinematic variables bring further enhancements and reduce the expected limit by just over 10%. It may be possible to further increase the sensitivity by reoptimising the threshold between high- and low-p_T^t in the 8 TeV categories, but such a study is beyond the scope of this analysis. The analysis should also be repeated using 13 TeV data obtained in Run 2, to verify the effect of this improvement, and the $|\Delta\eta_{Z\gamma}|$ categories could be reintroduced once sufficient statistics were available.

Chapter 7

Search for $X \to Z\gamma$ Decays

This chapter describes a search for new high mass resonances with a $Z\gamma$ final state, and Section 7.1 provides a brief overview of the analysis and its motivation. Chapter 5 described how standard objects are reconstructed and identified using the ATLAS detector, and Section 7.2 builds on this to describe the final event selection criteria imposed during evaluation of the three-body invariant mass $m_{\ell\ell\gamma}$. The analysis follows the procedure adopted for the search for an SM Higgs boson decaying to a $Z\gamma$ final state (see Chapter 6), where the signal and background distributions are modelled using analytic functions as described in Section 7.3. The main sources of systematic uncertainty are summarised in Section 7.4, and the expected and observed limits computed using the 95% CL_s method are presented in Section 7.5.

7.1 Overview

The LHC was successfully restarted in July 2015 following a lengthy shutdown, during which the machine received maintenance and upgrades that enabled it to begin colliding protons at a centre-of-mass energy of $\sqrt{s} = 13\,\text{TeV}$. At this unprecedented energy, the production cross-sections of heavy particles are greatly enhanced (for example, moving from $\sqrt{s} = 8\,\text{TeV}$ to 13 TeV increases the ggF production cross-section of the SM Higgs boson by a factor of 2.3) and it becomes possible to perform direct searches for new physics in higher mass ranges than ever before.

It was discussed in Chapter 2 how there are many BSM models that introduce new bosons through additional gauge fields or extensions of the Higgs sector, and so searches for any new bosons can therefore help identify models to pursue and provide a broad indication of physics beyond the SM. As with the search for the SM Higgs boson, decays involving $\gamma\gamma$, ZZ and $Z\gamma$ states are excellent for study owing to relatively low backgrounds from SM processes and numerous final states where all particles can be reconstructed. Such features are essential in determining the properties of any new resonances that are observed, especially given the limited statistics that are available in high mass regions.

In a recent search performed by the ATLAS collaboration for heavy resonances decaying to a diphoton final state, using $3.2\,\text{fb}^{-1}$ of pp collision data collected at $\sqrt{s} = 13\,\text{TeV}$ in 2015, a slight excess of events was observed around a diphoton mass of 750 GeV [42, 164]. The results of this analysis are presented in Figure 7.1, which

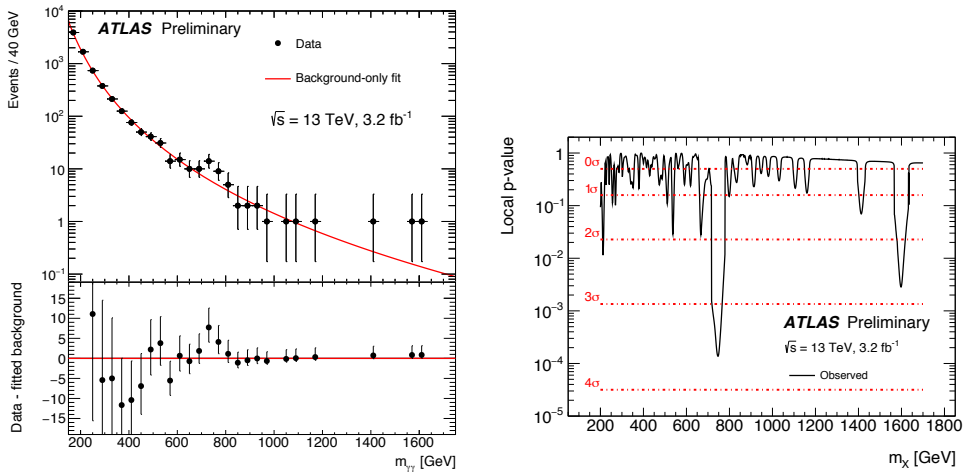

Figure 7.1: Left: selected diphoton invariant mass distribution, fitted with a background-only hypothesis, in the ATLAS high-mass diphoton resonance search with the 2015 data. Right: scan of the null hypothesis p-value as a function of the resonance mass [42].

.

shows the diphoton invariant mass distribution of the selected events fitted with a background-only hypothesis, together with a scan of the null hypothesis p-value. The observed excess was found to have a local significance of 3.5σ and a global significance of 2.5σ.

The CMS collaboration performed a similar search and also reported an excess near the same mass, albeit one of slightly smaller significance [43]. They used $2.6\,\text{fb}^{-1}$ of pp collision data collected at $\sqrt{s} = 13\,\text{TeV}$ in 2015 and their results are shown in Figure 7.2.

These tantalising results may prove to be nothing more than a statistical fluctuation, but could equally represent the first hints of a new particle. Theorists have therefore put forward numerous possible interpretations of this excess (see Ref. [165] and its references) and many of these theories also predict significant decays to a $Z\gamma$ final state with a similar branching ratio.

Previous searches for a new high-mass boson, X, decaying to a Z boson and a photon were carried out at both the Tevatron and the LHC. The D0 collaboration set limits on $X \to Z\gamma$ production using $p\bar{p}$ collisions at $\sqrt{s} = 1.96\,\text{TeV}$ [166], while the ATLAS [44, 167] and CMS [168] collaborations used pp collision data collected at 7 and 8 TeV in 2011 and 2012 to extend the mass range and sensitivity. These studies assumed a narrow intrinsic width for the X boson and examined decays that produced an $ee\gamma$ or $\mu\mu\gamma$ final state. No signals were observed and so limits were ultimately placed on $\sigma(pp \to X) \times BR(X \to Z\gamma)$ for an X boson of mass between 200 and 1 000 GeV.

The search performed by ATLAS using the 8 TeV data is of particular relevance since it has been used as a template for this analysis. This study selected events using the following requirements:

- Exactly two opposite-sign charged leptons, with $p_{\text{T}} > 25\,\text{GeV}$ and $|\eta| < 2.47$.

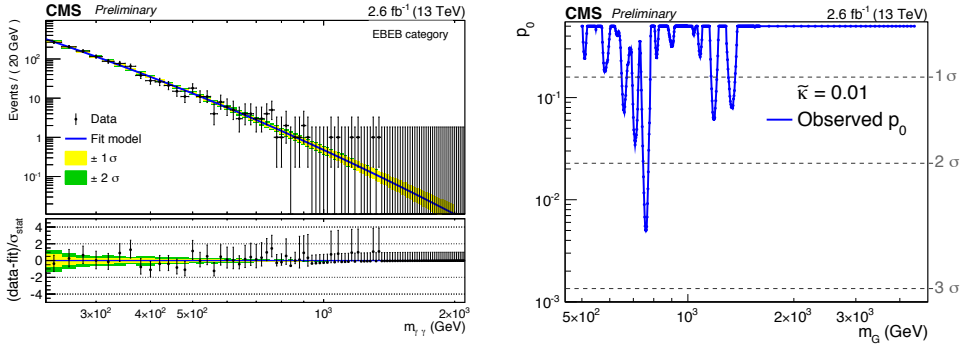

Figure 7.2: Left: selected diphoton invariant mass distribution, fitted with a background-only hypothesis, in the CMS high-mass diphoton resonance search with the 2015 data, for both photons reconstructed in the barrel calorimeter. Right: scan of the null hypothesis p-value as a function of the resonance mass, in the hypothesis of a narrow signal [43].

.

- Dilepton invariant mass between 65 and 115 GeV.
- A photon with $p_{\mathrm{T}} > 40\,\mathrm{GeV}$, $|\eta| < 2.37$, separated from the leptons by $\Delta R > 0.7$ and with a relative particle-level isolation that is below 0.5 when evaluated in a cone of radius 0.4.

Figure 7.3 shows the limits that were set on the fiducial cross section using the 8 TeV data, which range between approximately 2 fb at a mass of 200 GeV and 0.1 fb at masses above 1 TeV.

This analysis describes the search for high-mass $Z\gamma$ resonances, where Z boson candidates were reconstructed from pairs of electrons or muons. As in Run 1, the branching fraction $BR(Z \to ee, \mu\mu) = 6.7\%$ reduces the final yield with respect to that of an analysis reconstructing hadronic decays of the Z. However, the sensitivity remains similar or better since hadronic decays have large QCD backgrounds and this final state is cleaner, which results in a better signal-to-background ratio. The analysis draws heavily on the experience gained in the search for the SM Higgs boson in the $H \to Z\gamma$ decay mode described in Chapter 6 and is fully data-driven. The background is a smooth and continuous distribution that is modelled by an analytic function and a search is performed for any excesses in the data distribution. Owing to the limited available statistics, events were not filtered into categories as was done in the Run 1 SM Higgs boson search and a fully inclusive analysis was performed instead.

7.2 $X \to Z\gamma$ Reconstruction and Selection

Following the identification of a Z candidate satisfying the selection criteria outlined in Section 5.7, it was further required that the Z candidate have an invariant mass $m_{\ell\ell} > 45\,\mathrm{GeV}$. This was done in order to avoid a threshold effect from the derivation selection, described in Section 4.1.2, which only retains events with $m_{\ell\ell} > 40\,\mathrm{GeV}$. The Z candidate was then required to have a mass within 15 GeV of the true Z mass. Once

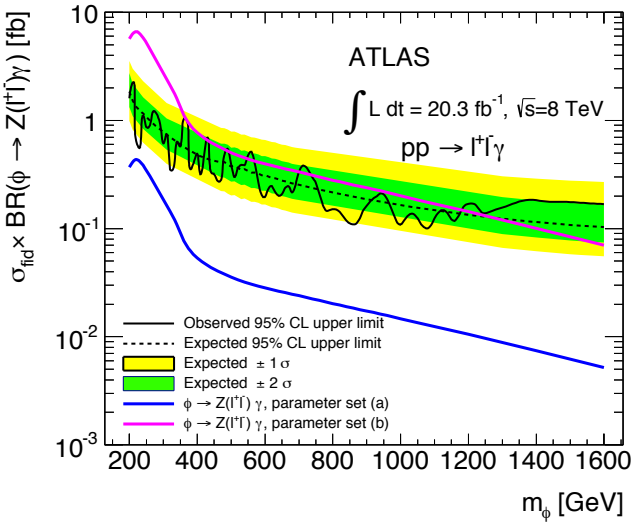

Figure 7.3: Upper limit on the production cross section times branching ratio to $Z(\ell\ell)\gamma$ as a function of the resonance mass using the full 8 TeV ATLAS dataset. The black line is the observed limit. The dashed black line is the expected limit, the yellow and green bands are the one and two σ uncertainties on the expectation. The blue and magenta lines show the theoretical cross sections for an effective field theory model of a scalar singlet ϕ (S in Equation 2.43) coupling to gauge bosons with two different parameter sets [44].

Cut	Electrons	Muons	Photons
p_{T}	$> 10\,\mathrm{GeV}$	$> 10\,\mathrm{GeV}$	$> 10\,\mathrm{GeV}$
$\lvert\eta\rvert$	$\lvert\eta\rvert < 1.37$, $1.52 < \lvert\eta\rvert < 2.47$	$\lvert\eta\rvert < 2.7$	$\lvert\eta\rvert < 1.37$, $1.52 < \lvert\eta\rvert < 2.37$
$\lvert d_0\rvert/\sigma_{d_0}$	< 6.5	< 3.5	-
Identification	Medium	Medium	Loose
Isolation	Loose	GradientLoose	-

Table 7.1: Summary of the lepton selection criteria and the photon preselection criteria, as described in Chapter 5.

a Z candidate was identified that satisfied these additional criteria, it was combined with the highest p_{T} photon to create an $m_{\ell\ell\gamma}$ candidate. The lepton and photon object selection criteria are summarised in Table 7.1.

The invariant mass of the $m_{\ell\ell\gamma}$ candidate was then recalculated using many of the corrections that were applied in the Run 1 analysis, in order to improve the resolution of signal events and enhance the signal-to-background ratio:

- The origin of the selected photon was set to the dilepton origin, and the photon four-vector recalculated.
- The four-momenta of muons were corrected for collinear FSR.
- The four-vectors of all leptons were recomputed by applying a Z mass constraint.

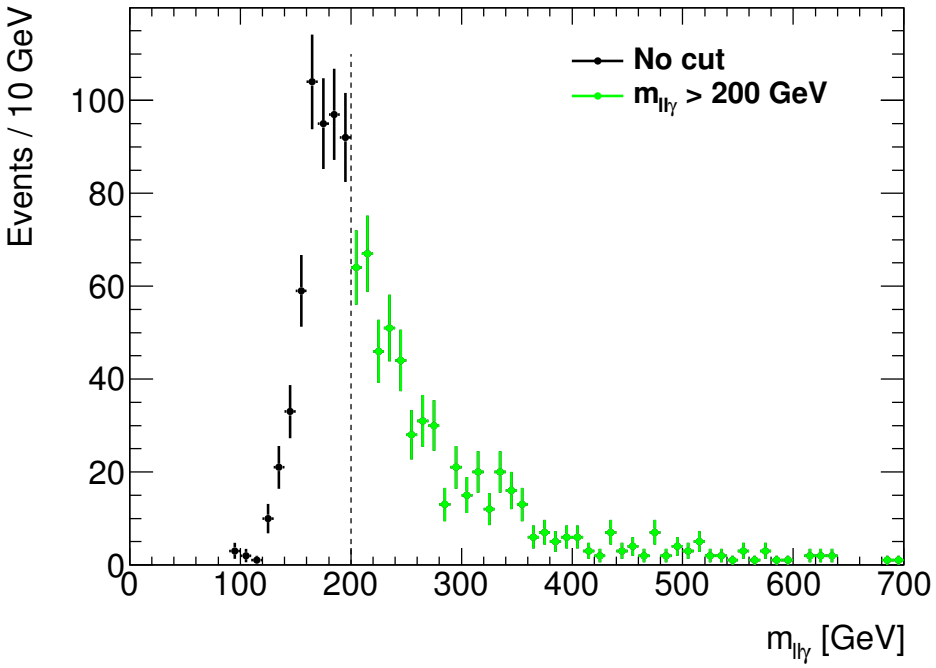

Figure 7.4: Three-body invariant mass distribution in 13 TeV data for events with $m_{\ell\ell\gamma} < 700\,\text{GeV}$, showing the threshold effect below 200 GeV due to the Z mass and photon p_{T} requirements.

Details of these corrections have already been given in Section 6.1.1, although the precise corrections applied in this analysis were obtained from control samples that used early 13 TeV data or the complete 8 TeV data from Run 1 (using additional systematic uncertainties to take into account the different conditions in which Run 1 and Run 2 data is obtained). In order to avoid a threshold effect in the data due to the Z mass and photon p_{T} requirements, as shown in Figure 7.4, only candidates with $m_{\ell\ell\gamma} > 200\,\text{GeV}$ were considered.

A final set of selection criteria were then applied to the photons, which are tighter than those used for the object selection (outlined in Section 5.3). Photons were required to pass a "Tight" identification criterion based on the shower shape profiles recorded in the electromagnetic calorimeter, as opposed to the initial "Loose" criteria. The background due to hadronic jets was then suppressed by requiring that the photon transverse isolation energy, $E_{\text{T}}^{\text{iso}}$, in a cone of radius $\Delta R = 0.4$ around the photon direction to be less than $(2.45 + 0.022 \times p_{\text{T}})$ GeV [137].

Finally, a cut was applied on the relative p_{T} of the photon, $p_{\text{T}}^{\gamma}/m_{\ell\ell\gamma} > 0.3$. Figures 7.5 and 7.6 show distributions of the photon p_{T} and the ratio $p_{\text{T}}^{\gamma}/m_{\ell\ell\gamma}$ for signals with different m_X, before the photon relative p_{T} cut was applied. The distribution of events in data, which are dominated by the background processes, are also shown for reference. The photon p_{T} distributions show considerable variation as a function of m_X, and it is impossible to choose a single cut on the photon p_{T} that suppresses the background and remains efficient over the full mass range. However, the distributions of $p_{\text{T}}/m_{\ell\ell\gamma}$ remain similar for all mass points and it is therefore more effective to cut

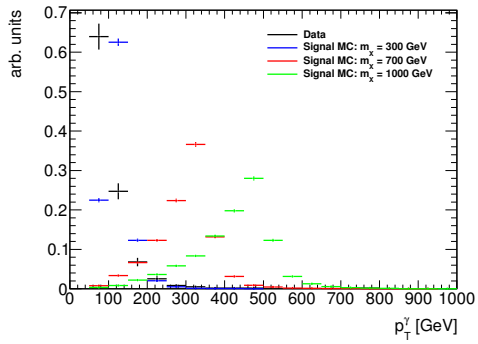

Figure 7.5: Transverse momentum distribution for photons from $Z\gamma$ candidates in data and a selection of signal MC samples. All distributions are normalised to have an integral of unity.

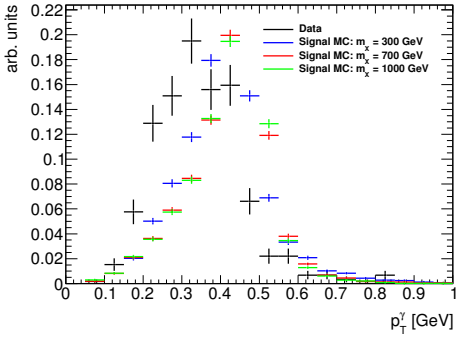

Figure 7.6: Distribution of the relative transverse momentum $p_{\mathrm{T}}^{\gamma}/m_{\ell\ell\gamma}$ for photons from $Z\gamma$ candidates in data and a selection of signal MC samples. All distributions are normalised to have an integral of unity.

on this variable instead of the raw p_{T}. The best cut is one that maximises the relative sensitivity:

$$\frac{\varepsilon_S}{\sqrt{\varepsilon_B}}, \tag{7.1}$$

where ε_S and ε_B are the efficiencies for signal and background, respectively, identified by examining the number of events in a 3% window around each mass point.

Figure 7.7 shows the relative sensitivity for different cuts, while Figure 7.8 shows the relative change in the signal efficiency. Study of these plots reveal that the optimal cut is $p_{\mathrm{T}}^{\gamma}/m_{\ell\ell\gamma} > 0.3$, which maximises the sensitivity but is responsible for a 15% loss in signal efficiency.

The event selection efficiencies in data and in the 750 GeV MC signal sample are summarised in Table 7.2. Comparisons between the electron and muon channels are presented for data and the 750 GeV MC signal sample in Tables 7.3 and 7.4, respectively.

7.3 Signal and Background Modelling

The signal and background yields from the selected events were determined through a maximum-likelihood fit to the three-body invariant mass distribution. Both the signal and background distributions were modelled using analytical functions - the signal model parameters are fixed constants determined through fitting the function to simulated signal samples, while the background model parameters were determined by a direct fit to the data distribution.

7.3.1 Signal Modelling

Study of the signal MC samples has shown that the three body invariant mass distribution, $m_{\ell\ell\gamma}$, for a particle of mass m_X can be well described by a double-sided Crystal

Selection	$gg \to H$ MC, $m_X = 750\,\text{GeV}$			Data		
	Number of Events	Efficiency [%]	Relative efficiency [%]	Number of Events	Efficiency [%]	Relative efficiency [%]
All events	13448	100.0	100.0	5694392	100.00	100.00
GRL (data only)	13448	100.0	100.0	5436689	95.47	95.47
Primary vertex	13448	100.0	100.0	5436675	95.47	100.00
Event Quality	13448	100.0	100.0	5435297	95.45	99.97
Trigger	9946.1	74.0	74.0	1757278	30.86	32.33
At least two good leptons	6389.5	47.5	64.2	661976	11.63	37.67
Two leptons with opposite charge and $m_{\ell\ell} > 45\,\text{GeV}$	6215.6	46.2	97.3	647494	11.37	97.81
One loose photon passing preselection	5200.9	38.7	83.7	108426	1.90	16.75
At least one Higgs candidate	4951.1	36.8	95.2	108426	1.90	100.00
Trigger Matching	4949.0	36.8	100.0	108384	1.90	99.96
$\lvert m_{\ell\ell} - m_Z \rvert < 15\,\text{GeV}$	4606.5	34.3	93.1	69999	1.23	64.58
γ (tight) identification	4362.6	32.4	94.7	1697	0.03	2.42
γ isolation	4233.1	31.5	97.0	1108	0.02	65.29
$m_{\ell\ell\gamma} > 200\,\text{GeV}$	4232.3	31.5	100.0	591	0.01	53.34
$p_{\text{T}}^{\gamma}/m_{\ell\ell\gamma} > 0.3$	3668.4	27.3	86.7	382	0.01	64.64

Table 7.2: Event selection efficiency in signal MC at $m_X = 750\,\text{GeV}$ and in data.

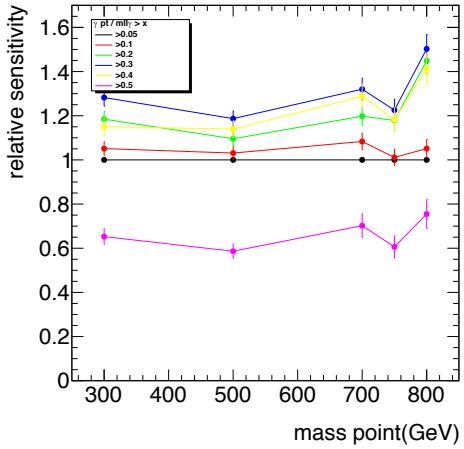

Figure 7.7: Relative variation in $\varepsilon_S/\sqrt{\varepsilon_B}$ as a function of the resonance mass for given $p_{\mathrm{T}}^{\gamma}/m_{\ell\ell\gamma}$ cut values [119].

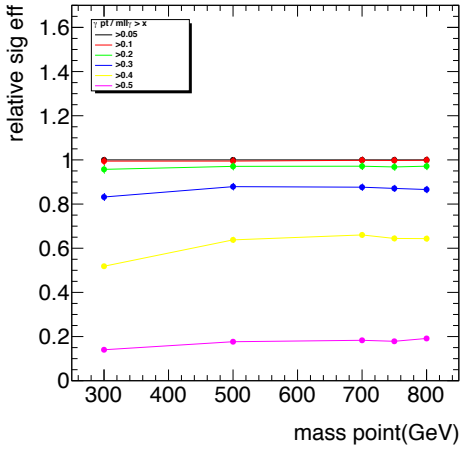

Figure 7.8: Relative variation in signal efficiency as a function of the resonance mass for given $p_{\mathrm{T}}^{\gamma}/m_{\ell\ell\gamma}$ cut values [119].

Selection	$ee\gamma$		$\mu\mu\gamma$	
	Number of Events	Relative efficiency (%)	Number of Events	Relative efficiency (%)
Trigger Matching	2371.8	100.0	2577.2	100.0
$\lvert m_{\ell\ell} - m_Z \rvert < 15\,\mathrm{GeV}$	2222.1	93.7	2384.4	92.5
γ (tight) identification	2108.8	94.9	2253.8	94.5
γ isolation	2043.3	96.9	2189.8	97.2
$m_{\ell\ell\gamma} > 200\,\mathrm{GeV}$	2042.4	100.0	2189.8	100.0
$p_{\mathrm{T}}^{\gamma}/m_{\ell\ell\gamma} > 0.3$	1806.4	88.4	1861.9	85.0

Table 7.3: Event selection efficiencies in signal MC at $m_X = 750\,\mathrm{GeV}$ for separate $ee\gamma$ and $\mu\mu\gamma$ channels.

Selection	$ee\gamma$		$\mu\mu\gamma$	
	Number of Events	Relative efficiency (%)	Number of Events	Relative efficiency (%)
Trigger Matching	45692	100.0	62692	100.0
$\lvert m_{\ell\ell} - m_Z \rvert < 15\,\mathrm{GeV}$	29754	65.1	40245	64.2
γ (tight) identification	746	2.5	951	2.4
γ isolation	473	63.4	635	66.8
$m_{\ell\ell\gamma} > 200\,\mathrm{GeV}$	262	55.4	329	51.8
$p_{\mathrm{T}}^{\gamma}/m_{\ell\ell\gamma} > 0.3$	168	64.1	214	65.0

Table 7.4: Event selection efficiencies in data for separate $ee\gamma$ and $\mu\mu\gamma$ channels.

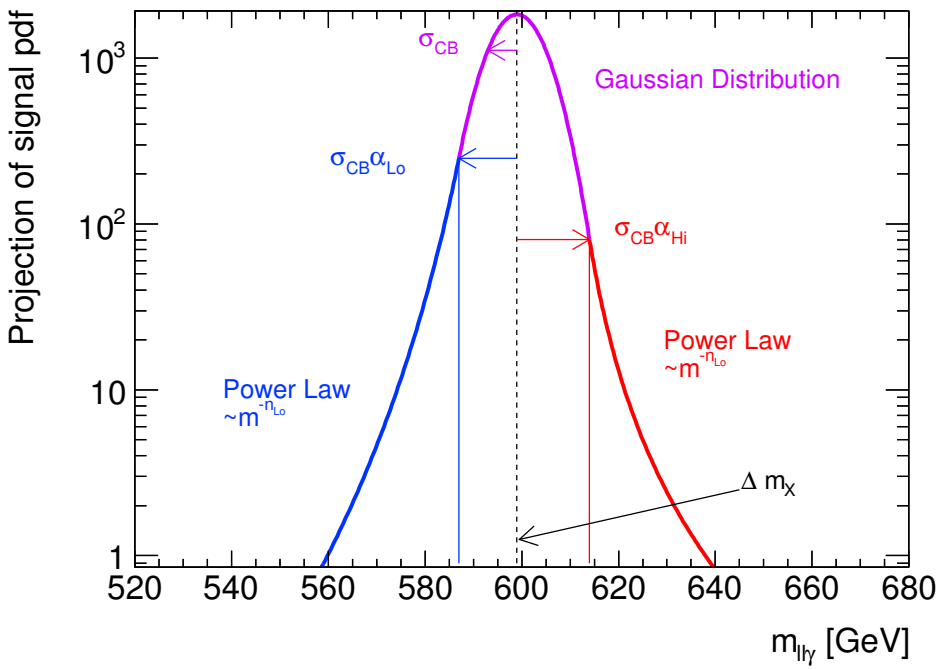

Figure 7.9: Definition of the Double-Sided Crystal Ball function.

Ball (DSCB) function. Such a function comprises a Gaussian core with asymmetric power tails, and is defined as:

$$N \cdot \begin{cases} e^{-t^2/2} & \text{if } -\alpha_{\text{Lo}} \leq t \leq \alpha_{\text{Hi}} \\ \frac{e^{-0.5\alpha_{\text{Lo}}^2}}{\left[\frac{\alpha_{\text{Lo}}}{n_{\text{Lo}}}\left(\frac{n_{\text{Lo}}}{\alpha_{\text{Lo}}} - \alpha_{\text{Lo}} - t\right)\right]^{n_{\text{Lo}}}} & \text{if } t < -\alpha_{\text{Lo}} \\ \frac{e^{-0.5\alpha_{\text{Hi}}^2}}{\left[\frac{\alpha_{\text{Hi}}}{n_{\text{Hi}}}\left(\frac{n_{\text{Hi}}}{\alpha_{\text{Hi}}} - \alpha_{\text{Hi}} + t\right)\right]^{n_{\text{Hi}}}} & \text{if } t > \alpha_{\text{Hi}}, \end{cases} , \tag{7.2}$$

where $t = \Delta m_X / \sigma_{\text{CB}}$, $\Delta m_X = m_{\ell\ell\gamma} - m_X - \mu_{\text{CB}}$, N is a normalisation parameter, μ_{CB} is the mean of the Gaussian distribution, σ_{CB} represents the width of the core Gaussian, α_{Lo} (α_{Hi}) is the point where the Gaussian is replaced by a power law on the low (high) mass side, and n_{Lo} (n_{Hi}) is the exponent of this power law. Figure 7.9 shows a graphical representation of the function shape and parameter definitions.

In order to construct a signal model at any arbitrary mass point, and not just those for which MC samples have been generated, several of the DSCB parameters were given functional forms that vary with m_X:

$$\mu_{\text{CB}} = a_\mu + b_\mu x + c_\mu x^2 + m_X, \tag{7.3}$$

$$\sigma_{\text{CB}} = a_\sigma + b_\sigma x, \tag{7.4}$$

$$\alpha_{\text{Lo}} = a_{\alpha_{\text{Lo}}} + \frac{b_{\alpha_{\text{Lo}}}}{(x + c_{\alpha_{\text{Lo}}})}, \tag{7.5}$$

$$\alpha_{\text{Hi}} = a_{\alpha_{\text{Hi}}} + \frac{b_{\alpha_{\text{Hi}}}}{(x + c_{\alpha_{\text{Hi}}})}, \tag{7.6}$$

$$x = \frac{(m_X - 100\text{GeV})}{100\ \text{GeV}}. \tag{7.7}$$

m_X [GeV]	200	300	500	700	750	800	1000	1500
FWHM [GeV]	4.5	6.4	10.4	14.3	15.3	16.3	20.2	30.0

Table 7.5: Full Width at Half-Maximum height (FWHM) of the reconstructed invariant mass distribution of fully simulated signal samples in the range $200 \leq m_X \leq 1\,500$ GeV.

The DSCB function was then fitted to all signal MC samples simultaneously, allowing the coefficients of the above functions to be determined. These parameters then describe how the DSCB functional form evolves with m_X, allowing a model to be interpolated for any given mass point. Figure 7.10 shows the results of a simultaneous fit to the invariant mass distributions of the simulated signal samples for combined $ee\gamma$ and $\mu\mu\gamma$ final states. The variations of the model parameters as a function of m_X are presented in Figures 7.11 to 7.14. For reference, Figures 7.15 and 7.16 show the results of a simultaneous fit in the $ee\gamma$ and $\mu\mu\gamma$ channels, respectively. A plot of a DSCB fitted to the simulated signal distribution at $m_X = 750$ GeV is shown in Figure 7.17, and separate fits to events with $ee\gamma$ and $\mu\mu\gamma$ final states are presented in Figure 7.18. The full-width at half-maximum (FWHM) of the invariant mass distribution for the signal, obtained from the fully simulated samples between 200 GeV and 1.5 TeV, varies between 4.3 GeV (2.2%) and 30 GeV (2%), as shown in Table 7.5.

The signal efficiency at masses between 200 GeV and 1.5 TeV was evaluated by fitting an exponential function:

$$a + b \exp(c \cdot m_X). \tag{7.8}$$

The results of this fit are shown in Figure 7.19, and the efficiencies vary from 17% at $m_X = 200$ GeV to around 29% at $m_X = 1\,500$ GeV. It should be noted that the efficiency is calculated as the number of selected $ee\gamma$ and $\mu\mu\gamma$ candidates in signal samples that also contain $Z \to \tau\tau$ decays. The efficiency with respect to only dielectron and dimuon decays is therefore 50% larger, ranging between 26% and 43%.

A study was performed [119] in order to assess the quality of the DSCB signal model. Asimov datasets [162] were generated by throwing a distribution from the selected background model (see Section 7.3.2) and injecting a fixed level of signal MC. The resultant distribution was then fitted with the combined signal and background model, and the fitted signal peak mean and yield were compared to those of the injected signal. The study tested all values of m_X between 200 and 1 000 GeV for which MC samples existed. For $m_X = 750$ GeV, the Crystal Ball plus Gaussian signal model adopted in the Run 1 analysis (Section 6.2.2) gave a bias of 6.6% whereas the DSCB function gave a bias of only 0.6%. Further, the bias on the signal yield when using the DSCB model was less than 1% for all tested m_X values. The DSCB model was therefore an excellent choice for modelling the signal.

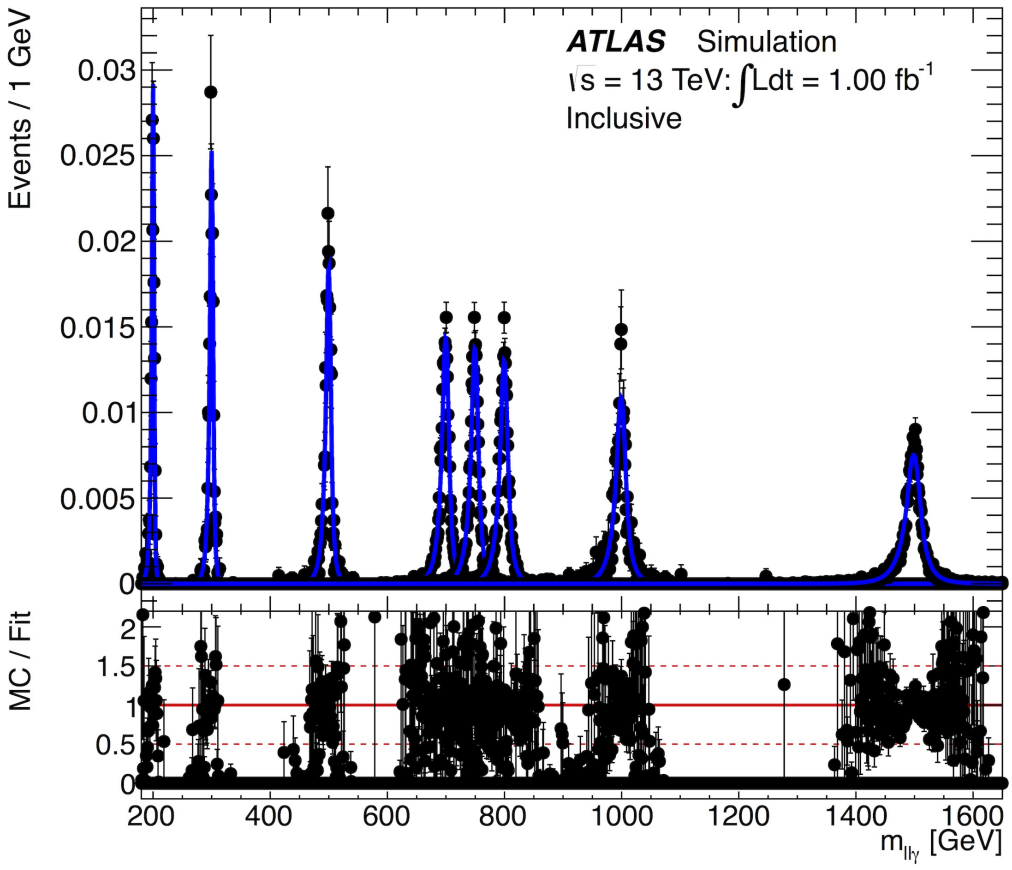

Figure 7.10: Result of the simultaneous DSCB fit to the signal MC samples with generated masses between 200 and 1 500 GeV.

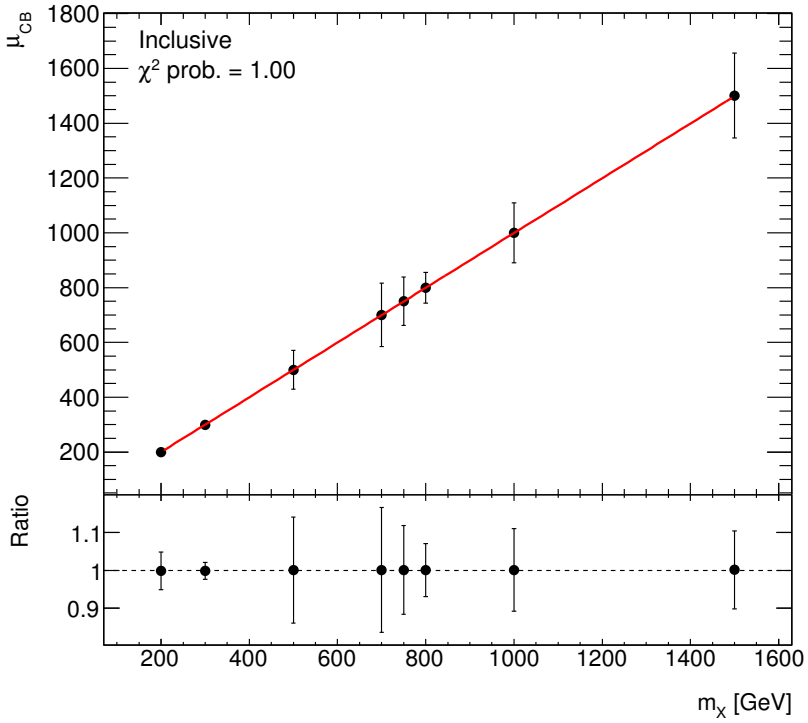

Figure 7.11: Parameterisation of μ_{CB} as a function of m_X. The data points (black) are the values of μ_{CB} retrieved from individual fits of a DSCB function to each mass point, while the line (red) shows the functional form determined through the simultaneous fit of a DSCB function to all mass points.

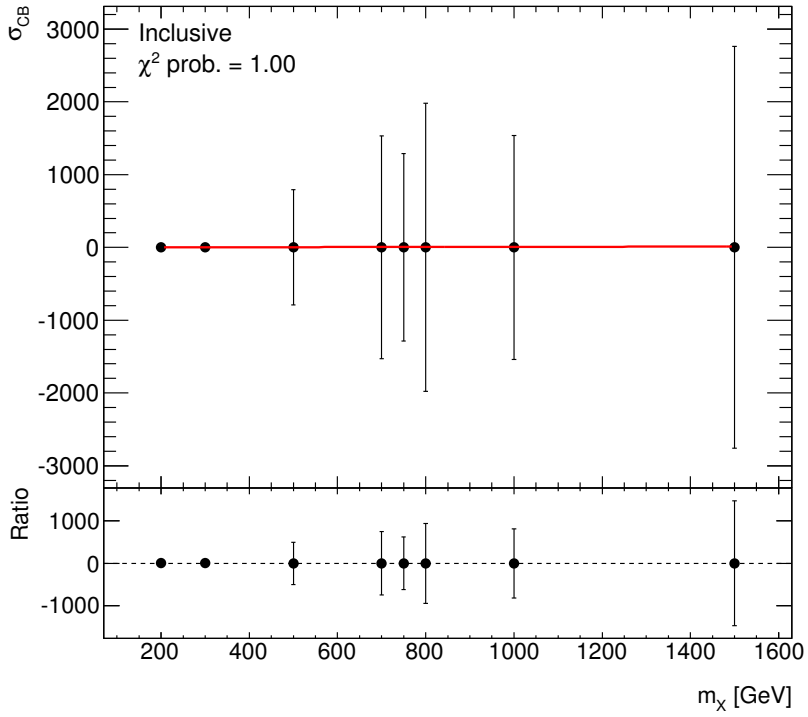

Figure 7.12: Parameterisation of σ_{CB} as a function of m_X. The data points (black) are the values of σ_{CB} retrieved from individual fits of a DSCB function to each mass point, while the line (red) shows the functional form determined through the simultaneous fit of a DSCB function to all mass points.

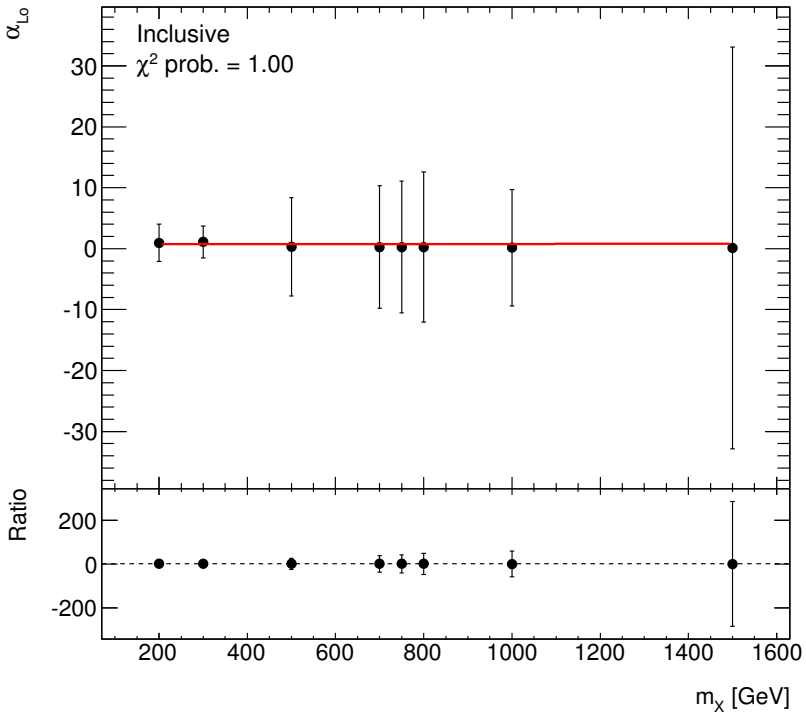

Figure 7.13: Parameterisation of α_{Lo} as a function of m_X. The data points (black) are the values of α_{Lo} retrieved from individual fits of a DSCB function to each mass point, while the line (red) shows the functional form determined through the simultaneous fit of a DSCB function to all mass points.

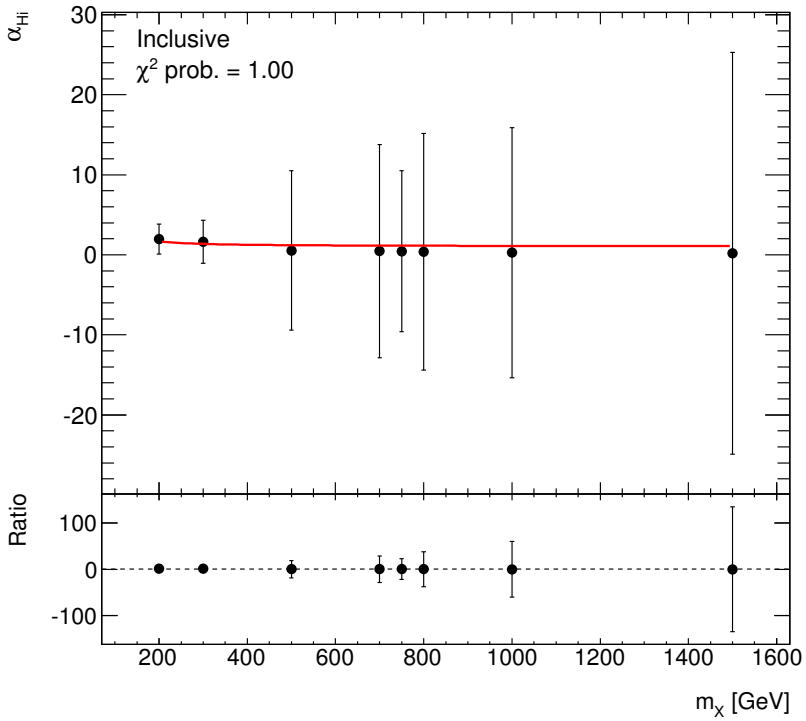

Figure 7.14: Parameterisation of α_{Hi} as a function of m_X. The data points (black) are the values of α_{Hi} retrieved from individual fits of a DSCB function to each mass point, while the line (red) shows the functional form determined through the simultaneous fit of a DSCB function to all mass points.

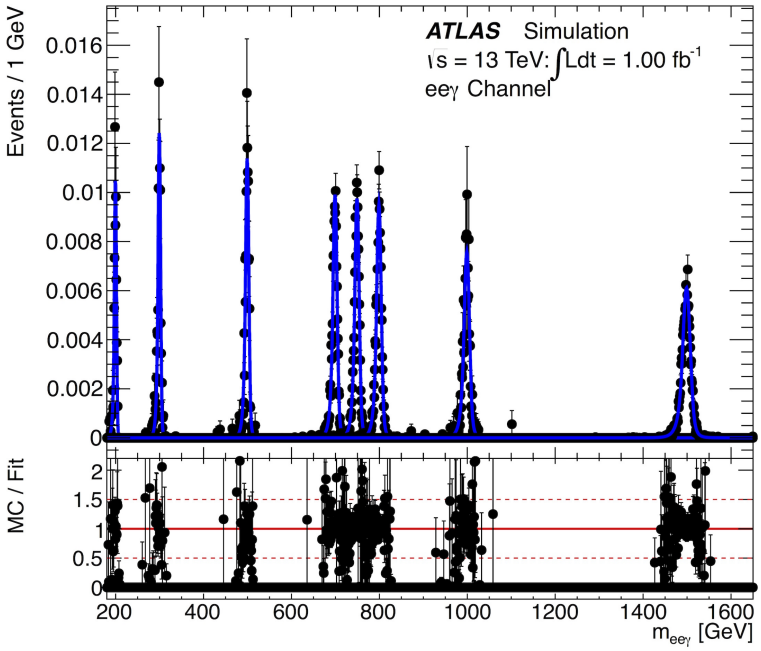

Figure 7.15: Result of the simultaneous DSCB fit to the signal MC samples with generated masses between 200 and 1 500 GeV, in the $ee\gamma$ channel.

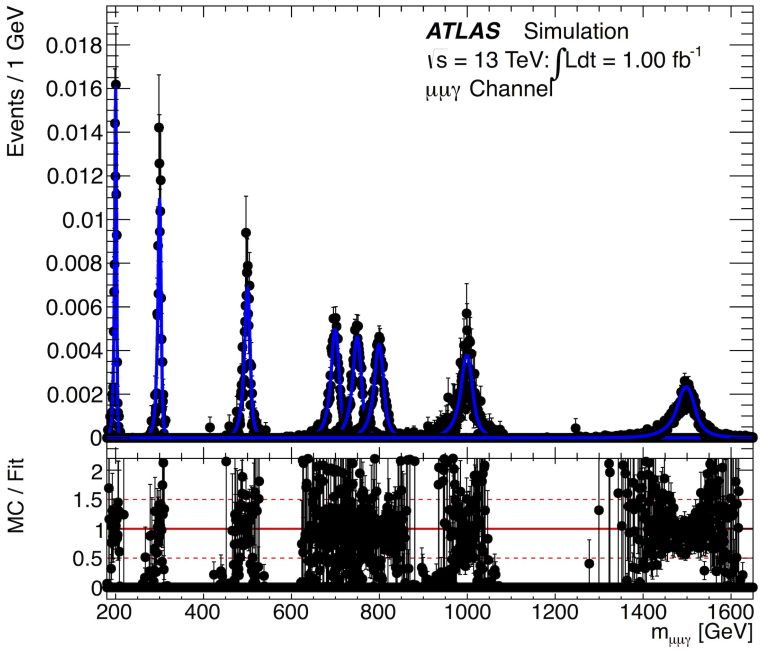

Figure 7.16: Result of the simultaneous DSCB fit to the signal MC samples with generated masses between 200 and 1 500 GeV, in the $\mu\mu\gamma$ channel.

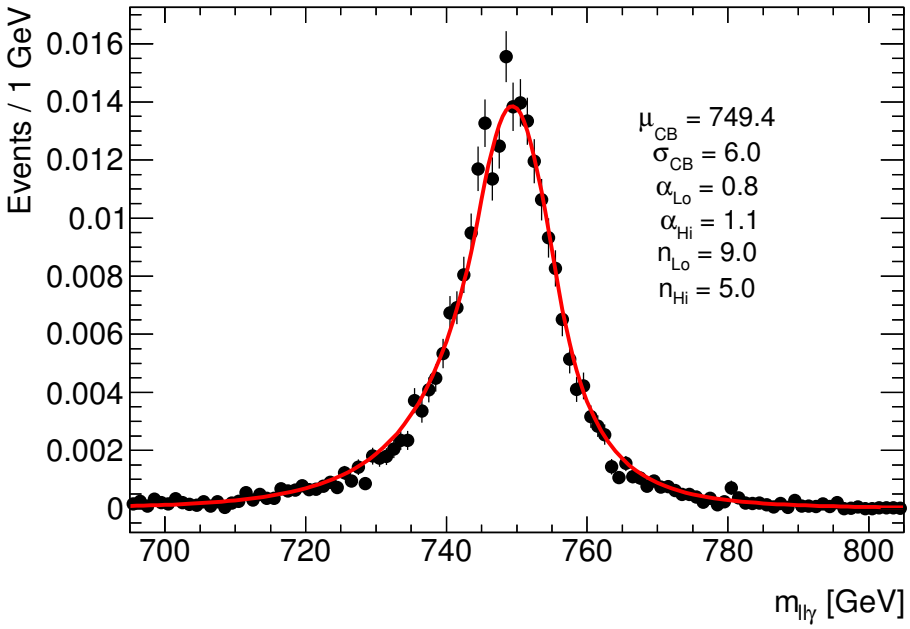

Figure 7.17: Fit to the invariant mass distribution for the signal generated at $m_X = 750\,\text{GeV}$

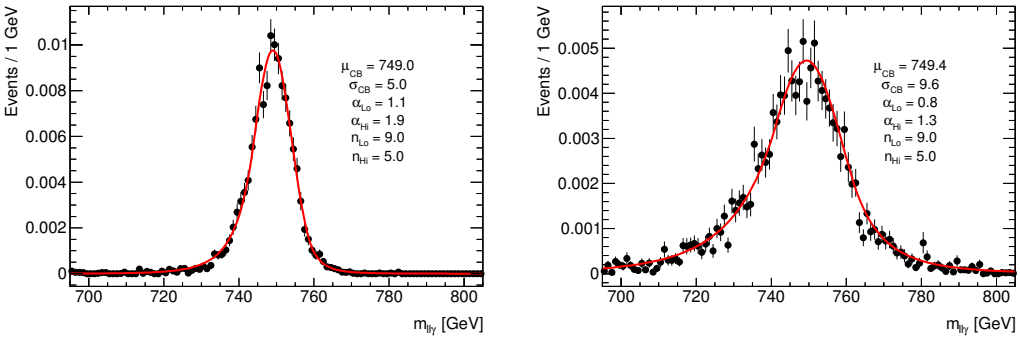

Figure 7.18: Fit to the invariant mass distribution for the signal generated at $m_X = 750\,\text{GeV}$: (left) $ee\gamma$, (right) $\mu\mu\gamma$ channels.

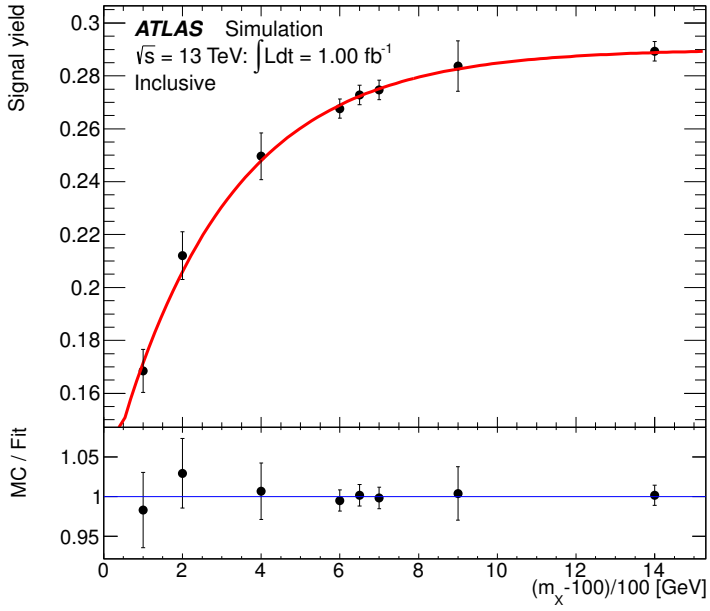

Figure 7.19: Parameterised signal efficiency calculated from the fit to the DSCB to each mass point.

7.3.2 Background Modelling

The invariant mass distributions from the main backgrounds of $Z + \gamma$ and Z + jet combine into a smoothly falling distribution that can be described by an analytical function. As in Run 1, the background model was fitted directly to the data in order to remove sources of systematic uncertainty such as the selection efficiencies and the normalisation of individual samples that arise when combining multiple MC background samples.

It was first necessary to identify a suitable function for the background that accurately described the data compared to alternative functions with more degrees of freedom, and that minimised any bias on the signal yield. The class of functions shown by Equation 7.9 was eventually selected owing to its successful use in other studies with γ+jet and diphoton final states [42, 169]:

$$f_{k;d}(x; b, \{a_k\}) = (1 - x^d)^b x^{\sum_{j=0}^{k} a_j \log(x)^j}, \tag{7.9}$$

where $x = \frac{m_{\ell\ell\gamma}}{\sqrt{s}}$ and the exponent d is held at a constant of 1/3. The simplest possible function is produced by setting $k = 0$ as follows:

$$f_{k=0;d=1/3}(x; b, d, \{a_k\}) = (1 - x^{1/3})^b x^{a_0}, \tag{7.10}$$

where b and a_0 are parameters to be determined.

A study was performed [119] to assess the bias on the fitted signal due to the choice of background model, following the same procedure adopted in the Run 1 $H \to Z\gamma$ analysis (outline in Section 6.2.3). A background-only MC sample was produced by

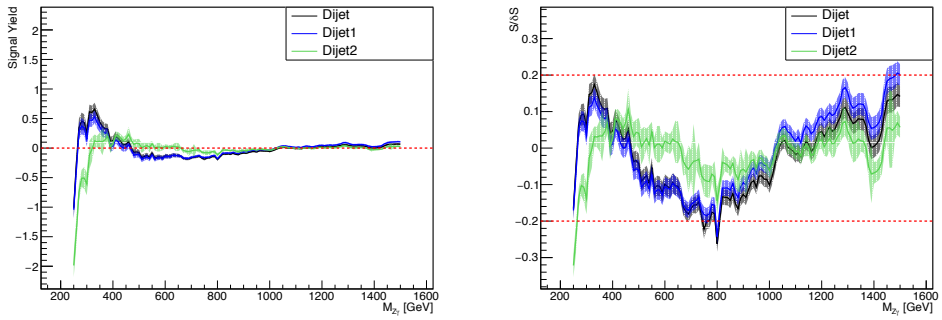

Figure 7.20: Absolute amount of spurious signal (left) and the relative spurious signal with respect to the statistical uncertainty on the background (right) when considering an integrated luminosity of $3.2\,\text{fb}^{-1}$. Dijet denotes the function $f_{k=0;d=1/3}(x;b,d,\{a_k\}) = (1-x^{1/3})^b x^{a_0}$ Dijet1 denotes $f_{k=1;d=1/3}(x;b,d,\{a_k\}) = (1-x^{1/3})^b x^{a_0+a_1 log(x)}$, and Dijet2 denotes $f_{k=2;d=1/3}(x;b,d,\{a_k\}) = (1-x^{1/3})^b x^{a_0+a_1 log(x)+a_2 log(x)^2}$ [119].

combining $Z+\gamma$ and Z + jet MC samples of SM background processes, which were normalised according to the relative fractions observed in data of 90% and 10%, respectively. To ensure high-statistics for this study, the $Z+\gamma$ sample was generated by simulating events with the Sherpa generator and passing them through a fast simulation of the calorimeter response [170]. This process replaces the detailed full simulation of the detector response with approximations that are less computationally expensive, thus allowing large samples to be generated quickly. Quality is not significantly affected and the $m_{\ell\ell\gamma}$ distributions from full and fast simulations were found to be in good agreement. A high-statistics Z + jet sample was produced by reweighting the $Z+\gamma$ sample. A combined signal and background model was then constructed and an unbinned likelihood fit to the $m_{\ell\ell\gamma}$ distribution was performed over the range $250 < m_{\ell\ell\gamma} < 1\,500\,\text{GeV}$. Figure 7.20 shows the absolute level of spurious signal identified at each mass point, and the relative spurious signal with respect to the statistical uncertainty on the background. As before, the selected background model was taken to be the one with the fewest degrees of freedom for which the level of spurious signal was less than 20% of the fitted uncertainty. The function given in Equation 7.10 satisfies these criteria and was therefore adopted for this analysis.

Figure 7.21 shows the three-body invariant mass spectrum for the electron and muons channels combined, together with the fitted background function. An additional fit was performed for each channel separately and these are shown in Figure 7.22. The 1σ and 2σ error bands show the statistical uncertainty on the background arising from the uncertainties on the fit parameters.

7.4 Systematic Uncertainties

This analysis is dominated by large statistical uncertainties due to the small number of events that pass the full selection criteria, and the systematic uncertainties only

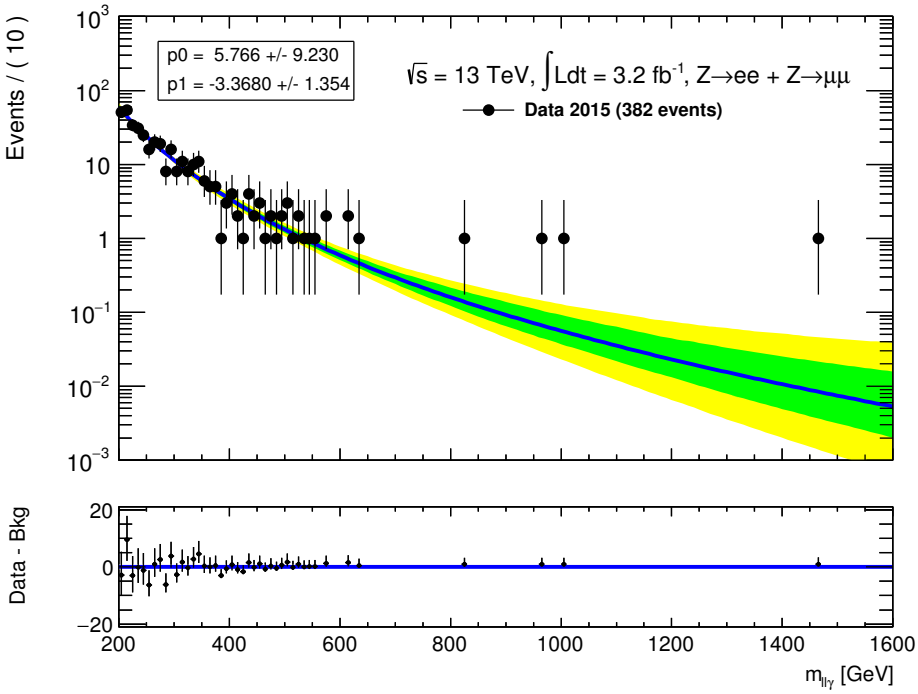

Figure 7.21: Three-body invariant mass distribution ($m_{\ell\ell\gamma}$) in data in the region 200 to 1 600 GeV. The background fit result from Equation 7.10 is shown with a solid line. The coloured green and yellow bands show the 1σ and 2σ uncertainty bands on the background from the uncertainties of the fitted parameters.

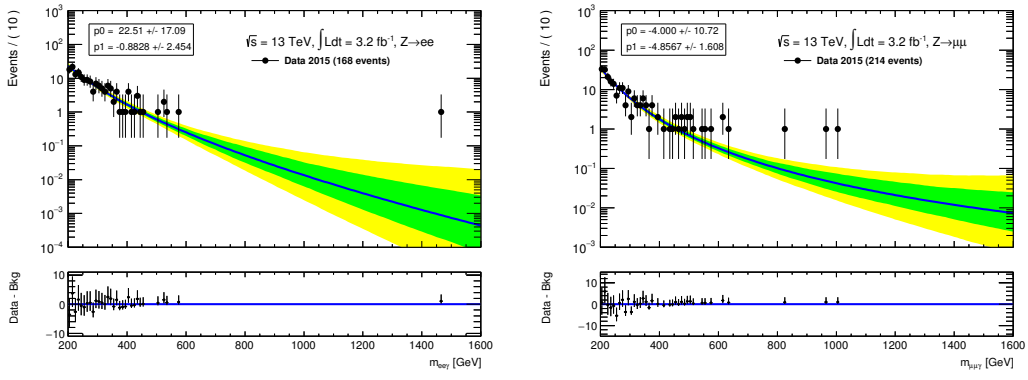

Figure 7.22: The three-body invariant mass distribution ($m_{\ell\ell\gamma}$) in data in the region of 200 to 1 600 GeV: (left) electron, (right) muon channels. The background fit result from Equation 7.10 is shown with a solid line. The coloured green and yellow bands show the 1σ and 2σ uncertainty bands on the background from the uncertainties of the fitted parameters.

Source	Uncertainty on $\sigma(pp \to X) \times BR(X \to Z\gamma)$
Luminosity	$\pm 5\%$
Signal efficiency	
Efficiency dependence vs pileup	$\sim 0.1\%$
Photon ID efficiency	$\sim 1\%$
Photon isolation efficiency	$< 0.1\%$
Electron ID efficiency	$\sim 2\%$
Electron isolation efficiency	$\sim 2\%$
Electron reconstruction efficiency	$\sim 0.5\%$
Electron trigger efficiency	$< 0.01\%$
Muon efficiency (Stat. Lowpt)	$\sim 0\%$
Muon efficiency (Stat.)	$\sim 0.3\%$
Muon efficiency (Sys. Lowpt)	$\sim 0\%$
Muon efficiency (Sys.)	$\sim 2\%$
Muon Trigger efficiency (Stat.)	$\sim 0.8\%$
Muon Trigger efficiency (Sys.)	$\sim 0.3\%$
Signal modeling	
Bias from choice of DCSB model	0.6%
e/γ energy scale	
e/γ energy resolution	
muon momentum scale	
muon momentum resolution	
Background modeling	
Spurious signal	

Table 7.6: Summary of the main sources of systematic uncertainty for the measurement of $\sigma(pp \to X) \times BR(X \to Z\gamma)$ and of their contribution to the measurement uncertainty [5].

make a small contribution overall. The systematic uncertainties affecting this analysis consist of uncertainty on the luminosity of the data, bias in the background model, and various sources affecting both the signal model parameters and the expected yield. These uncertainties are summarised in Table 7.6 [5] and described in more detail below.

The integrated luminosity was found to be 3.2 fb^{-1} with a relative uncertainty of 5%. This uncertainty was evaluated from a preliminary calibration of the luminosity scale derived from beam-separation scans performed in August 2015, following a similar method to the one described in [72].

As in the SM $H \to Z\gamma$ analysis, the background was data-driven and modelled with an analytic function. The only source of systematic uncertainty was therefore due to the bias, or spurious signal, in the model as discussed in Section 7.3.2.

The identified sources of uncertainty affecting the signal $m_{\ell\ell\gamma}$ distribution were the e/γ energy scale, e/γ energy resolution, muon momentum scale and muon momentum resolution, for which values and corresponding uncertainties were provided by the ATLAS e/γ and muon working groups [171–173]. The identified sources of systematic uncertainty affecting the signal efficiency were the lepton reconstruction,

identification, trigger and isolation scale factors, and also the photon isolation and identification efficiency scale factors - these were used to correct the MC samples to match the data selection efficiency but carry uncertainties themselves. Each of these listed parameters and scale factors was independently varied within its uncertainty, the three-body invariant mass reevaluated, and the signal model fitted again to determine the revised model parameters. The relative difference between each updated model and the nominal results were then used to estimate the systematic uncertainties.

7.5 Results

An unbinned-maximum likelihood fit was performed on the $m_{\ell\ell\gamma}$ distribution to assess the compatibility of the data with a background-only hypothesis and evaluate the asymptotic limits on $\sigma \cdot \mathrm{BR}(X \to Z\gamma)$, following the same general procedure adopted for the SM $H \to Z\gamma$ analysis (as described in Chapter 6).

The invariant mass distribution of $Z(\ell\ell)\gamma$ candidates in data was shown in Figure 7.21, and only 4 $Z(\ell\ell)\gamma$ candidates were found with $m_{\ell\ell\gamma} > 700\,\mathrm{GeV}$. In order to improve the quality of the background fit in the largely empty signal region, a flat distribution of "ghost events" with a weight of order 10^{-5} was inserted into the data. The presence of these events assisted the minimisation process, while the low weight ensured that the result is not distorted.

Figure 7.23 shows the expected and observed p_0 values for a narrow width scalar Higgs-like resonance as a function of the mass hypothesis m_X. Mass hypotheses between 250 and 1 500 GeV were tested, using $3.2\,\mathrm{fb}^{-1}$ of pp collisions at $\sqrt{s} = 13\,\mathrm{TeV}$. The expected p_0 was found to range from 0.43 (0.19σ) to 0.50 (0.02σ), while the observed p_0 was found to range from 0.04 (-1.40σ) to 0.98 (-2.07σ), with the largest significance occurring for $m_X = 345\,\mathrm{GeV}$.

Figure 7.24 shows the expected and observed limits for a narrow width scalar Higgs-like resonance as a function of mass hypothesis m_X. The expected limits were found to vary between 26.9 and 211.6 while the observed limits varied between 23.8 and 323.3.

Following publication of this analysis, the CMS collaboration released their own study of the $X \to Z\gamma$ decay using $2.7\,\mathrm{fb}^{-1}$ of data recorded at 13 TeV [174]. Their analysis proceeded in a similar manner to the one presented here and set limits on $\sigma \cdot \mathrm{BR}(X \to Z\gamma)$ as shown in Figure 7.25. These results are in good agreement with those reported by ATLAS, and no significant excesses were found.

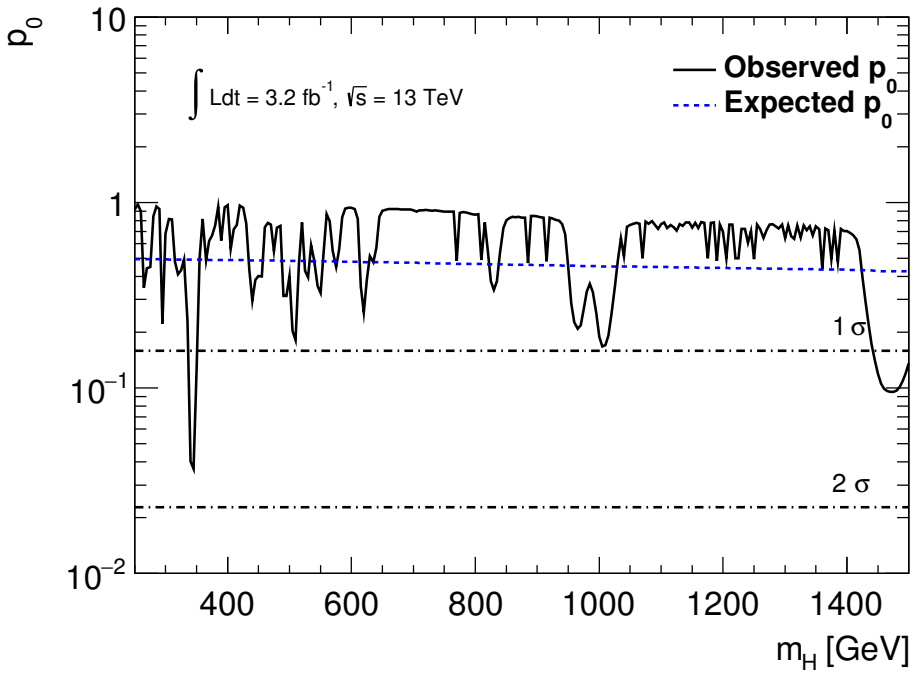

Figure 7.23: Observed p_0 (compatibility of the data with the background-only hypothesis) as a function of the resonance mass m_X.

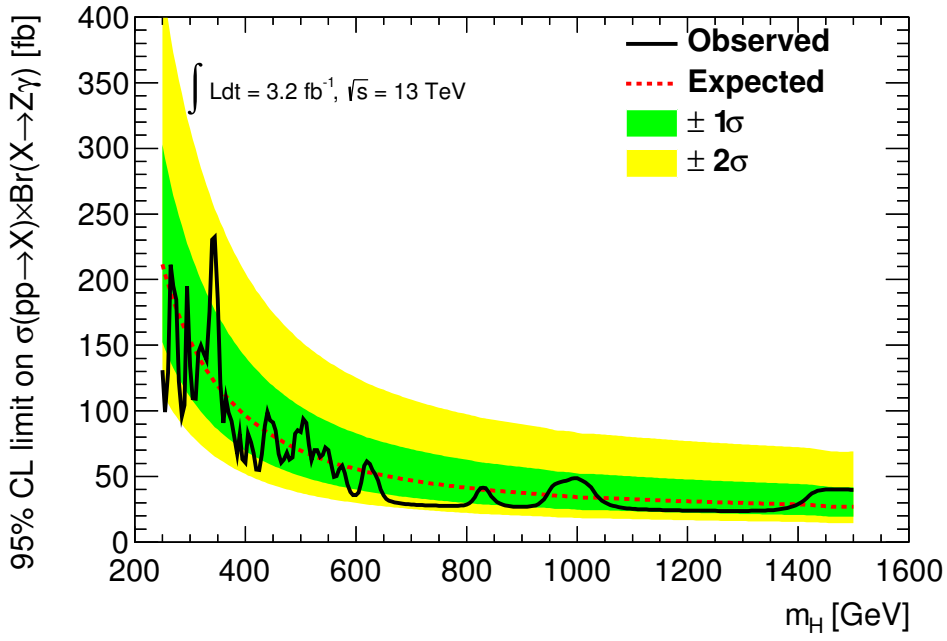

Figure 7.24: Expected and observed 95% *C.L.* limits on $\sigma \cdot \mathrm{BR}(X \to Z\gamma)$ of a narrow resonance as a function of the resonance mass m_X.

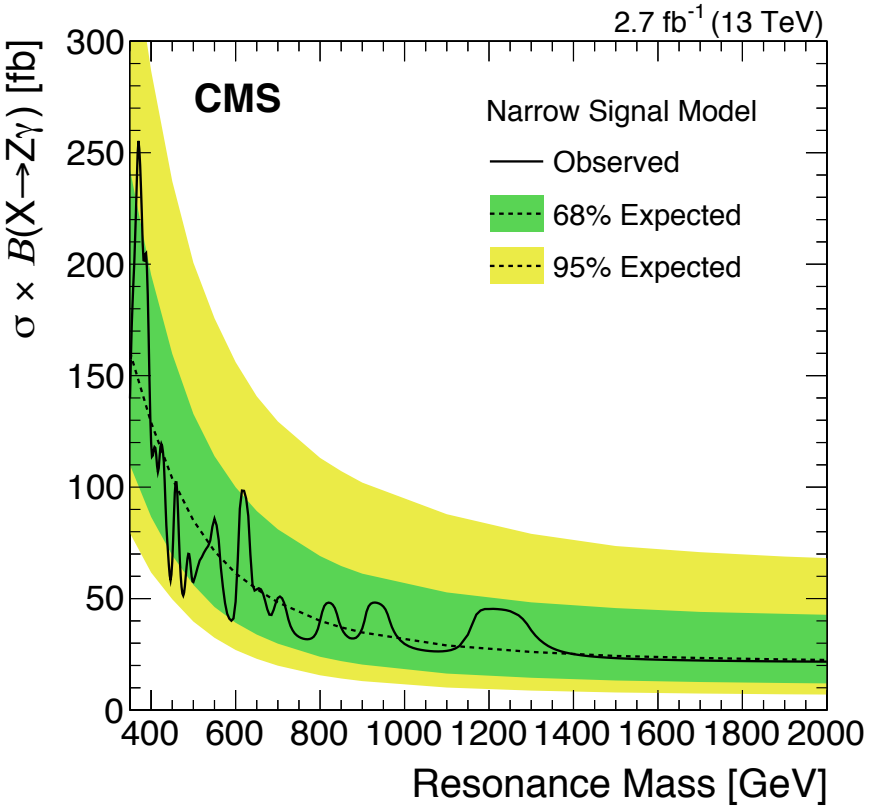

Figure 7.25: Expected and observed 95% *C.L.* limits on $\sigma \cdot \mathrm{BR}(X \to Z\gamma)$ of a narrow resonance as a function of the resonance mass m_X from the CMS collaboration [174].

Chapter 8

Conclusions

A search for evidence of a Standard Model Higgs boson in the decay channel $H \to Z\gamma$, $Z \to \ell\ell$ where $\ell = e$ or μ at the ATLAS detector has been presented in this thesis. This search was performed using data gathered from proton-proton collisions provided by the Large Hadron Collider at CERN: 4.5 fb^{-1} of data obtained at a centre-of-mass energy $\sqrt{s} = 7$ TeV and 20.3 fb^{-1} of data obtained at a centre-of-mass energy $\sqrt{s} = 8$ TeV.

In the available data, no significant excess over the Standard Model prediction was observed and so the results were used to set exclusion limits on the production cross-section of an SM Higgs boson decaying to $Z\gamma$ at 95% confidence level: production of the Higgs at 9.0 $\times$ SM predictions was excluded.

Further refinements to the method using a novel alternative event categorisation based on the mass of the reconstructed Z boson yielded an improvement of around 10% in the sensitivity of the analysis: production of the Higgs boson at 8.0 $\times$ SM predictions was excluded. This technique could be investigated more fully in Run 2 when more data is available.

A further search for new Higgs-like bosons with high mass and decaying through $Z\gamma$ to an $\ell\ell\gamma$ final state is also presented. This search used 3.2 fb^{-1} of data obtained at a centre-of-mass energy $\sqrt{s} = 13$ TeV. No significant excesses above the SM background were observed and so limits were set at 95% confidence level.

Bibliography

[1] G. Aad et al., *Search for Higgs boson decays to a photon and a Z boson in pp collisions at $\sqrt{s}$=7 and 8 TeV with the ATLAS detector*, Phys. Lett. **B732** (2014) 8, arXiv: 1402.3051 [hep-ex].

[2] M. Aaboud et al., *Search for heavy resonances decaying to a Z boson and a photon in pp collisions at $\sqrt{s} = 13$ TeV with the ATLAS detector* (2016), arXiv: 1607.06363 [hep-ex].

[3] G. Aad et al., *Observation of a new particle in the search for the Standard Model Higgs boson with the ATLAS detector at the LHC*, Phys. Lett. **B716** (2012) 1, arXiv: 1207.7214 [hep-ex].

[4] S. Chatrchyan et al., *Observation of a new boson at a mass of 125 GeV with the CMS experiment at the LHC*, Phys. Lett. **B716** (2012) 30, arXiv: 1207.7235 [hep-ex].

[5] ATLAS Collaboration, *Search for heavy resonances decaying to a Z boson and a photon in pp collisions at $\sqrt{s} = 13$ TeV with the ATLAS detector*, tech. rep. ATLAS-CONF-2016-010, CERN, 2016, URL: https://cds.cern.ch/record/2139795.

[6] S. L. Glashow, *Partial Symmetries of Weak Interactions*, Nucl. Phys. **22** (1961) 579.

[7] S. Weinberg, *A Model of Leptons*, Phys. Rev. Lett. **19** (1967) 1264.

[8] A. Salam, *Weak and Electromagnetic Interactions*, Proceedings of the 8th Nobel symposium, Ed. N. Svartholm, Almqvist & Wiskell, 1968, Conf. Proc. **C680519** (1968) 367, URL: {http://inspirehep.net/record/53083}.

[9] G. 't Hooft and M. J. G. Veltman, *Regularization and Renormalization of Gauge Fields*, Nucl. Phys. **B44** (1972) 189.

[10] K. A. Olive et al., *Review of Particle Physics*, Chin. Phys. **C38** (2014) 090001.

[11] F. Englert and R. Brout, *Broken symmetry and the mass of gauge vector mesons*, Phys. Rev. Lett. **13** (1964) 321.

[12] P. W. Higgs, *Broken symmetries and the masses of gauge bosons*, Phys. Rev. Lett. **13** (1964) 508.

[13] G. Guralnik, C. Hagen and T. Kibble,
Global conservation laws and massless particles,
Phys. Rev. Lett. **13** (1964) 585.

[14] E. Noether, *Invariant variation problems*,
Transport Theory and Statistical Physics **1**.3 (1971) 186,
eprint: http://dx.doi.org/10.1080/00411457108231446,
URL: http://dx.doi.org/10.1080/00411457108231446.

[15] Q. R. Ahmad et al., *Direct Evidence for Neutrino Flavor Transformation from Neutral-Current Interactions in the Sudbury Neutrino Observatory*,
Phys. Rev. Lett. **89** (1 2002) 011301,
URL: http://link.aps.org/doi/10.1103/PhysRevLett.89.011301.

[16] G. Arnison et al., *Experimental observation of isolated large transverse energy electrons with associated missing energy at $\sqrt{s}$=540 GeV*,
Physics Letters B **122**.1 (1983) 103 , ISSN: 0370-2693, URL: http://www.sciencedirect.com/science/article/pii/0370269383911772.

[17] M. Banner et al., *Observation of single isolated electrons of high transverse momentum in events with missing transverse energy at the CERN pp collider*,
Physics Letters B **122**.5 (1983) 476 , ISSN: 0370-2693, URL: http://www.sciencedirect.com/science/article/pii/0370269383916052.

[18] G. Arnison et al., *Experimental observation of lepton pairs of invariant mass around 95 GeV/c^2 at the CERN SPS collider*,
Physics Letters B **126**.5 (1983) 398 , ISSN: 0370-2693, URL: http://www.sciencedirect.com/science/article/pii/0370269383901880.

[19] P. Bagnaia et al., *Evidence for $Z^0 \to e^+e^-$ at the CERN pp collider*,
Physics Letters B **129**.1 (1983) 130 , ISSN: 0370-2693, URL: http://www.sciencedirect.com/science/article/pii/037026938390744X.

[20] L. Alvarez-Gaume and J. Ellis, *Eyes on a prize particle*,
Nat Phys **7**.1 (Jan. 2011) 2, URL: http://dx.doi.org/10.1038/nphys1874.

[21] S. Dittmaier et al.,
Handbook of LHC Higgs Cross Sections: 1. Inclusive Observables (2011),
arXiv: 1101.0593 [hep-ph].

[22] S. Dittmaier et al.,
Handbook of LHC Higgs Cross Sections: 2. Differential Distributions (2012),
arXiv: 1201.3084 [hep-ph].

[23] T Barklow et al., *Search for the Standard Model Higgs boson in the $H \to Z\gamma$ decay mode with 20.3 fb^{-1} of pp collisions at $\sqrt{s} = 8$ TeV and 4.6 fb^{-1} of pp collisions at $\sqrt{s} = 7$ TeV*, tech. rep. ATL-COM-PHYS-2013-1397,
CERN, 2013, URL: https://cds.cern.ch/record/1605669.

[24] A. Djouadi, *The Anatomy of electro-weak symmetry breaking. II. The Higgs bosons in the minimal supersymmetric model*, Phys. Rept. **459** (2008) 1, arXiv: hep-ph/0503173 [hep-ph].

[25] S. P. Martin, *A Supersymmetry primer* (1997), [Adv. Ser. Direct. High Energy Phys.18,1(1998)], arXiv: hep-ph/9709356 [hep-ph].

[26] P. Bechtle, T. Plehn and C. Sander, 'Supersymmetry', *The Large Hadron Collider: Harvest of Run 1*, ed. by T. Schörner-Sadenius, 2015 421, arXiv: 1506.03091 [hep-ex], URL: https://inspirehep.net/record/1375491/files/arXiv:1506.03091.pdf.

[27] G. Bertone and D. Hooper, *A History of Dark Matter*, Submitted to: Rev. Mod. Phys. (2016), arXiv: 1605.04909 [astro-ph.CO].

[28] V. C. Rubin, W. K. J. Ford and N. . Thonnard, *Rotational properties of 21 SC galaxies with a large range of luminosities and radii, from NGC 4605 /R = 4kpc/ to UGC 2885 /R = 122 kpc/*, Astrophys.J. **238** (June 1980) 471.

[29] R. Massey, T. Kitching and J. Richard, *The dark matter of gravitational lensing*, Rept. Prog. Phys. **73** (2010) 086901, arXiv: 1001.1739 [astro-ph.CO].

[30] M. Markevitch et al., *Direct constraints on the dark matter self-interaction cross-section from the merging galaxy cluster 1E0657-56*, Astrophys. J. **606** (2004) 819, arXiv: astro-ph/0309303 [astro-ph].

[31] G. R. Blumenthal et al., *Formation of galaxies and large-scale structure with cold dark matter*, Nature **311**.5986 (Oct. 1984) 517, URL: http://dx.doi.org/10.1038/311517a0.

[32] R. Adam et al., *Planck 2015 results. I. Overview of products and scientific results* (2015), arXiv: 1502.01582 [astro-ph.CO].

[33] G. Bertone, D. Hooper and J. Silk, *Particle dark matter: Evidence, candidates and constraints*, Phys. Rept. **405** (2005) 279, arXiv: hep-ph/0404175 [hep-ph].

[34] D. Bauer et al., *Dark Matter in the Coming Decade: Complementary Paths to Discovery and Beyond*, Phys. Dark Univ. **7-8** (2015) 16, arXiv: 1305.1605 [hep-ph].

[35] T. Marrodán Undagoitia and L. Rauch, *Dark matter direct-detection experiments*, J. Phys. **G43**.1 (2016) 013001, arXiv: 1509.08767 [physics.ins-det].

[36] U. Amaldi, W. de Boer and H. Fürstenau, *Comparison of grand unified theories with electroweak and strong coupling constants measured at LEP*, Physics Letters B **260**.3 (1991) 447 , ISSN: 0370-2693, URL: http://www.sciencedirect.com/science/article/pii/0370269391916418.

[37] C.-W. Chiang and K. Yagyu, *Higgs boson decays to $\gamma\gamma$ and $Z\gamma$ in models with Higgs extensions*, Phys. Rev. **D87**.3 (2013) 033003, arXiv: 1207.1065 [hep-ph].

[38] I. Low, J. Lykken and G. Shaughnessy, *Singlet scalars as Higgs imposters at the Large Hadron Collider*, Phys. Rev. **D84** (2011) 035027, arXiv: 1105.4587 [hep-ph].

[39] M. Carena, I. Low and C. E. M. Wagner, *Implications of a Modified Higgs to Diphoton Decay Width*, JHEP **08** (2012) 060, arXiv: 1206.1082 [hep-ph].

[40] M. Aoki, S. Kanemura and K. Yagyu, *Testing the Higgs triplet model with the mass difference at the LHC*, Phys. Rev. **D85** (2012) 055007, arXiv: 1110.4625 [hep-ph].

[41] M. Carena, L. Da Rold and E. Pontón, *Minimal Composite Higgs Models at the LHC*, JHEP **06** (2014) 159, arXiv: 1402.2987 [hep-ph].

[42] ATLAS Collaboration, *Search for resonances decaying to photon pairs in 3.2 fb^{-1} of pp collisions at $\sqrt{s}$ = 13 TeV with the ATLAS detector*, ATLAS-CONF-2015-081 (2015), URL: https://cds.cern.ch/record/2114853.

[43] CMS Collaboration, *Search for new physics in high mass diphoton events in proton-proton collisions at $\sqrt{s} = 13$ TeV*, CMS-PAS-EXO-15-004 (2015), URL: https://cds.cern.ch/record/2114808.

[44] ATLAS Collaboration, *Search for new resonances in $W\gamma$ and $Z\gamma$ final states in pp collisions at $\sqrt{s} = 8$ TeV with the ATLAS detector*, Phys. Lett. **B738** (2014) 428, arXiv: 1407.8150 [hep-ex].

[45] G. Aad et al., *The ATLAS Experiment at the CERN Large Hadron Collider*, JINST **3** (2008) S08003.

[46] L. Evans and P. Bryant, *LHC Machine*, JINST **3** (2008) S08001.

[47] S. Chatrchyan et al., *The CMS experiment at the CERN LHC*, JINST **3** (2008) S08004.

[48] K Aamodt et al., *The ALICE experiment at the CERN LHC*, Journal of Instrumentation **3**.08 (2008) S08002, URL: http://stacks.iop.org/1748-0221/3/i=08/a=S08002.

[49] A. A. A. Jr et al., *The LHCb Detector at the LHC*, Journal of Instrumentation **3**.08 (2008) S08005, URL: http://stacks.iop.org/1748-0221/3/i=08/a=S08005.

[50] V Berardi et al., *Total cross-section, elastic scattering and diffraction dissociation at the Large Hadron Collider at CERN: TOTEM Technical Design Report*, Technical Design Report TOTEM, Geneva: CERN, 2004, URL: https://cds.cern.ch/record/704349.

[51] J. Pinfold et al., *Technical Design Report of the MoEDAL Experiment*, tech. rep. CERN-LHCC-2009-006. MoEDAL-TDR-001, CERN, 2009, URL: https://cds.cern.ch/record/1181486.

[52] O Adriani et al., *LHCf experiment: Technical Design Report*, Technical Design Report LHCf, Geneva: CERN, 2006, URL: https://cds.cern.ch/record/926196.

[53] P. Mouche, *Overall view of the LHC. Vue d'ensemble du LHC* (2014), General Photo, URL: http://cds.cern.ch/record/1708847.

[54] J. Haffner, *The CERN accelerator complex. Complexe des accélérateurs du CERN* (2013), General Photo, URL: http://cds.cern.ch/record/1621894.

[55] G. Aad et al., *Improved luminosity determination in pp collisions at $\sqrt{s} = 7$ TeV using the ATLAS detector at the LHC*, Eur. Phys. J. **C73**.8 (2013) 2518, arXiv: 1302.4393 [hep-ex].

[56] ATLAS Collaboration, *ATLAS public results on luminosity measurements*, 2015, URL: https://twiki.cern.ch/twiki/bin/view/AtlasPublic/LuminosityPublicResults.

[57] ATLAS Collaboration, *ATLAS public results on luminosity measurements for Run 2*, 2015, URL: https://twiki.cern.ch/twiki/bin/view/AtlasPublic/LuminosityPublicResultsRun2.

[58] J. Pequenao, 'Computer generated image of the whole ATLAS detector', 2008, URL: http://cds.cern.ch/record/1095924.

[59] J. Pequenao, 'Computer generated image of the ATLAS inner detector', 2008, URL: http://cds.cern.ch/record/1095926.

[60] G Aad et al., *Expected performance of the ATLAS experiment: detector, trigger and physics*, Geneva: CERN, 2009, URL: https://cds.cern.ch/record/1125884.

[61] A. La Rosa, *ATLAS Pixel Detector: Operational Experience and Run-1 to Run-2 Transition*, PoS **Vertex2014** (2015) 001, arXiv: 1410.6347 [physics.ins-det].

[62] J. Pequenao, 'Computer Generated image of the ATLAS calorimeter', 2008, URL: http://cds.cern.ch/record/1095927.

[63] M Aharrouche et al., *Energy Linearity and Resolution of the ATLAS Electromagnetic Barrel Calorimeter in an Electron Test-Beam*, Nucl. Instrum. Methods Phys. Res., A **568**.physics/0608012 (2006) 601, URL: http://cds.cern.ch/record/976098.

[64] T Davidek, M Volpi and T Zenis, *Response of the ATLAS Tile Calorimeter to Hadrons in Stand-Alone Testbeam Data*, tech. rep. ATL-TILECAL-PUB-2009-004. ATL-COM-TILECAL-2009-002, The note has been updated using comments received by both referees.: CERN, 2009, URL: http://cds.cern.ch/record/1161351.

[65] 2013, URL: https://twiki.cern.ch/twiki/bin/view/AtlasPublic/ApprovedPlotsDAQ.

[66] 2015, URL: https://twiki.cern.ch/twiki/bin/viewauth/Atlas/LowestUnprescaled2011.

[67] 2016, URL: https://twiki.cern.ch/twiki/bin/viewauth/Atlas/LowestUnprescaled2012.

[68] 2011, URL: https://twiki.cern.ch/twiki/bin/view/Atlas/TriggerMenuConvention.

[69] ATLAS Collaboration, *Atlas Muon Trigger Performance on cosmics and p-p collisions at $\sqrt{s}$ = 900 GeV*, tech. rep. ATLAS-CONF-2010-013, CERN, 2010, URL: https://cds.cern.ch/record/1276547.

[70] 2013, URL: https://atlas.web.cern.ch/Atlas/GROUPS/DATAPREPARATION/DQSummary/Run1/.

[71] ATLAS Collaboration, *Luminosity Determination in pp Collisions at $\sqrt{s} = 7$ TeV Using the ATLAS Detector at the LHC*, Eur. Phys. J. C **71** (2011) 1630, arXiv: 1101.2185 [hep-ex].

[72] ATLAS Collaboration, *Improved luminosity determination in pp collisions at $\sqrt{s} = 7$ TeV using the ATLAS detector at the LHC* (2013), arXiv: 1302.4393 [hep-ex].

[73] T Hryn'ova and K Nagano, *Trigger Menu Strategy for Run 2*, tech. rep. ATL-COM-DAQ-2014-054, CERN, 2014, URL: https://cds.cern.ch/record/1703730.

[74] ATLAS Collaboration, *Electron identification measurements in ATLAS using $\sqrt{s}$ = 13 TeV data with 50 ns bunch spacing*, tech. rep. ATL-PHYS-PUB-2015-041, CERN, 2015, URL: http://cds.cern.ch/record/2048202.

[75] A. Ruiz-Martinez and A. Collaboration, *The Run-2 ATLAS Trigger System*, tech. rep. ATL-DAQ-PROC-2016-003, CERN, 2016, URL: https://cds.cern.ch/record/2133909.

[76] S. Alioli, P. Nason, C. Oleari and E. Re, *NLO Higgs boson production via gluon fusion matched with shower in POWHEG*, JHEP **04** (2009) 002, arXiv: 0812.0578 [hep-ph].

[77] P. Nason and C. Oleari, *NLO Higgs boson production via vector-boson fusion matched with shower in POWHEG*, JHEP **02** (2010) 037, arXiv: 0911.5299 [hep-ph].

[78] T. Sjöstrand, S. Mrenna, P. Skands, *A brief introduction to PYTHIA 8.1*, Comput.Phys.Commun. **178** (2008) 852, arXiv: 0710.3820 [hep-ph].

[79] H.-L. Lai et al., *New parton distributions for collider physics*, Phys. Rev. D **82** (2010) 074024, arXiv: 1007.2241 [hep-ph].

[80] J. Pumplin et al., *New generation of parton distributions with uncertainties from global QCD analysis*, JHEP **07** (2002) 012.

[81] R. V. Harlander and W. B. Kilgore, *Next-to-next-to-leading order Higgs production at hadron colliders*, Phys. Rev. Lett. **88** (2002) 201801, arXiv: hep-ph/0201206.

[82] C. Anastasiou and K. Melnikov, *Higgs boson production at hadron colliders in NNLO QCD*, Nucl. Phys. **B 646** (2002) 220, arXiv: hep-ph/0207004.

[83] V. Ravindran, J. Smith and W. L. van Neerven, *NNLO corrections to the total cross section for Higgs boson production in hadron hadron collisions*, Nucl. Phys. **B 665** (2003) 325, arXiv: hep-ph/0302135.

[84] C. Anastasiou et al., *Inclusive Higgs boson cross-section for the LHC at 8 TeV*, JHEP **1204** (2012) 004, arXiv: 1202.3638 [hep-ph].

[85] D. de Florian and M. Grazzini, *Higgs production at the LHC: updated cross sections at* $\sqrt{s} = 8$ *TeV*, Phys. Lett. **B718** (2012) 117, arXiv: 1206.4133 [hep-ph].

[86] U. Aglietti et al., *Two-loop light fermion contribution to Higgs production and decays*, Phys. Lett. **B 595** (2004) 432, arXiv: hep-ph/0404071.

[87] S. Actis et al., *NLO Electroweak Corrections to Higgs Boson Production at Hadron Colliders*, Phys. Lett. **B 670** (2008) 12, arXiv: 0809.1301 [hep-ph].

[88] M. Ciccolini, A. Denner and S. Dittmaier, *Strong and electroweak corrections to the production of Higgs+2jets via weak interactions at the LHC*, Phys. Rev. Lett. **99** (2007) 161803, arXiv: 0707.0381 [hep-ph].

[89] M. Ciccolini, A. Denner and S. Dittmaier, *Electroweak and QCD corrections to Higgs production via vector-boson fusion at the LHC*, Phys. Rev. **D 77** (2008) 013002, arXiv: 0710.4749 [hep-ph].

[90] K. Arnold et al., *VBFNLO: A parton level Monte Carlo for processes with electroweak bosons*, Comput. Phys. Commun. **180** (2009) 1661, arXiv: 0811.4559 [hep-ph].

[91] P. Bolzoni et al., *Higgs production via vector-boson fusion at NNLO in QCD*, Phys. Rev. Lett. **105** (2010) 011801, arXiv: 1003.4451 [hep-ph].

[92] O. Brein, A. Djouadi and R. Harlander, *NNLO QCD corrections to the Higgs-strahlung processes at hadron colliders*, Phys. Lett. **B 579** (2004) 149, arXiv: hep-ph/0307206.

[93] M. L. Ciccolini, S. Dittmaier and M. Kramer, *Electroweak radiative corrections to associated WH and ZH production at hadron colliders*, Phys. Rev. **D 68** (2003) 073003, arXiv: hep-ph/0306234.

[94] W. Beenakker et al., *NLO QCD corrections to t anti-t H production in hadron collisions.* , Nucl. Phys. **B 653** (2003) 151, arXiv: hep-ph/0211352.

[95] S. Dawson et al., *Associated Higgs production with top quarks at the Large Hadron Collider: NLO QCD corrections*, Phys. Rev. **D 68** (2003) 034022, arXiv: hep-ph/0305087.

[96] A. Djouadi, J. Kalinowski and M. Spira, *HDECAY: A program for Higgs boson decays in the standard model and its supersymmetric extension*, Comput. Phys. Commun. **108** (1998) 56, arXiv: hep-ph/9704448.

[97] A. Bredenstein et al., *Precise predictions for the Higgs-boson decay $H \to WW/ZZ \to 4$leptons*, Phys. Rev. **D 74** (2006) 013004, arXiv: hep-ph/0604011.

[98] S. Actis et al., *NNLO Computational Techniques: the Cases $H \to \gamma\gamma$ and $H \to gg$*, Nucl. Phys. **B 811** (2009) 182, arXiv: 0809.3667 [hep-ph].

[99] T Gleisberg et al., *SHERPA 1.alpha, a proof-of-concept version*, JHEP **02** (2004) 056, arXiv: hep-ph/0311263 [hep-ph].

[100] T. Gleisberg et al., *Event generation with SHERPA 1.1*, JHEP **02** (2009) 007, arXiv: 0811.4622 [hep-ph].

[101] S. Hoeche, S. Schumann and F. Siegert, *Hard photon production and matrix-element parton-shower merging*, Phys. Rev. D **81** (2010) 034026, arXiv: 0912.3501 [hep-ph].

[102] G. Corcella et al., *HERWIG 6: an event generator for hadron emission reactions with interfering gluons (including super-symmetric processes)* , JHEP **01** (2001) 010.

[103] J. M. Butterworth, J. R. Forshaw and M. H. Seymour, *Multiparton interactions in photoproduction at HERA*, Z. Phys. **C 72** (1996) 637, arXiv: hep-ph/9601371.

[104] 2011, URL: https://twiki.cern.ch/twiki/bin/view/AtlasProtected/PileupReweighting.

[105] 2011, URL: https://twiki.cern.ch/twiki/bin/viewauth/AtlasProtected/PhotonFudgeFactors.

[106] ATLAS Collaboration, *Measurements of the photon identification efficiency with the ATLAS detector using 4.9 fb^{-1} of pp collision data collected in 2011*, ATLAS-CONF-2012-123 (2012), URL: http://cdsweb.cern.ch/record/1473426/.

[107] 2014, URL: https://twiki.cern.ch/twiki/bin/view/AtlasProtected/EGammaCalibrationGEO20.

[108] G. Aad et al., *Measurement of the muon reconstruction performance of the ATLAS detector using 2011 and 2012 LHC proton–proton collision data*, The European Physical Journal C **74**.11 (2014) 1, ISSN: 1434-6052, URL: http://dx.doi.org/10.1140/epjc/s10052-014-3130-x.

[109] W. Lukas et al., *Charged-particle multiplicities in pp interactions at $\sqrt{s} = 8$ TeV measured with the ATLAS detector at the LHC*, tech. rep. ATL-COM-PHYS-2014-449, CERN, 2014, URL: https://cds.cern.ch/record/1700840.

[110] 2016, URL: https://twiki.cern.ch/twiki/bin/view/AtlasProtected/TrackingCPMC11#Impact_parameter_resolution.

[111] 2016, URL: https://twiki.cern.ch/twiki/bin/view/AtlasProtected/AtlasProductionGroupMC15a.

[112] S. Alioli et al., *A general framework for implementing NLO calculations in shower Monte Carlo programs: the POWHEG BOX*, JHEP **06** (2010) 043, arXiv: 1002.2581 [hep-ph].

[113] E. Bagnaschi et al., *Higgs production via gluon fusion in the POWHEG approach in the SM and in the MSSM*, JHEP **02** (2012) 088, arXiv: 1111.2854 [hep-ph].

[114] ATLAS Collaboration, *Measurement of the Z/γ^* boson transverse momentum distribution in pp collisions at $\sqrt{s} = 7$ TeV with the ATLAS detector*, JHEP **09** (2014) 145, arXiv: 1406.3660 [hep-ex].

[115] ATLAS Collaboration, *Summary of ATLAS Pythia 8 tunes*, ATL-PHYS-PUB-2012-003 (2012), URL: https://cds.cern.ch/record/1474107.

[116] A. D. Martin et al., *Parton distributions for the LHC*, Eur. Phys. J. **C63** (2009) 189, arXiv: 0901.0002 [hep-ph].

[117] GEANT4 Collaboration, S. Agostinelli et al., *GEANT4 - a simulation toolkit*, Nucl. Instrum. Methods A **506** (2003) 250.

[118] ATLAS Collaboration, *The ATLAS Simulation Infrastructure*, Eur. Phys. J. **C70** (2010) 823, arXiv: 1005.4568 [physics.ins-det].

[119] S. Burdin et al., *Support Note : Search for high-mass $Z + \gamma$ resonances in di-lepton plus photon final states with 3.2 fb^{-1} of pp collisions at $\sqrt{s} = 13$ TeV*, tech. rep. ATL-COM-PHYS-2016-086, CERN, 2016, URL: https://cds.cern.ch/record/2128141.

[120] ATLAS Collaboration, *Supporting note: Selection and performance for the $H \to \gamma\gamma$ and $H \to Z\gamma$ analyses*, tech. rep. ATL-COM-PHYS-2016-109, CERN, 2015, URL: http://cdsweb.cern.ch/record/2130656.

[121] 2016, URL: https://twiki.cern.ch/twiki/bin/view/AtlasProtected/EGammaIdentificationRun2.

[122] 2016, URL: https://twiki.cern.ch/twiki/bin/viewauth/AtlasProtected/ElectronPhotonFourMomentumCorrection.

[123] G. Aad et al., *Muon reconstruction performance of the ATLAS detector in proton–proton collision data at $\sqrt{s}$ =13 TeV*, Eur. Phys. J. **C76**.5 (2016) 292, arXiv: 1603.05598 [hep-ex].

[124] ATLAS Collaboration, *Electron and photon energy calibration with the ATLAS detector using data collected in 2015 at $\sqrt{s} = 13$ TeV*, tech. rep. ATL-PHYS-PUB-2016-015, CERN, 2016, URL: https://cds.cern.ch/record/2203514.

[125] C. Anastopoulos et al., *Photon identification pre-recommendations for run 2*, tech. rep. ATL-COM-PHYS-2015-496, CERN, 2015, URL: https://cds.cern.ch/record/2022342.

[126] J. Pequenao and P. Schaffner, 'An computer generated image representing how ATLAS detects particles', 2013, URL: https://cds.cern.ch/record/1505342.

[127] ATLAS Collaboration, *Performance of the ATLAS Inner Detector Track and Vertex Reconstruction in High Pile-Up LHC Environment*, ATLAS-CONF-2012-042, 2012, URL: http://cdsweb.cern.ch/record/1435196.

[128] ATLAS Collaboration, *Early Inner Detector Tracking Performance in the 2015 data at $\sqrt{s} = 13$ TeV*, tech. rep. ATL-PHYS-PUB-2015-051, CERN, 2015, URL: http://cds.cern.ch/record/2110140.

[129] ATLAS Collaboration,
The Optimization of ATLAS Track Reconstruction in Dense Environments,
tech. rep. ATL-PHYS-PUB-2015-006, CERN, 2015,
URL: http://cds.cern.ch/record/2002609.

[130] T Cornelissen et al.,
Concepts, Design and Implementation of the ATLAS New Tracking (NEWT),
tech. rep. ATL-SOFT-PUB-2007-007. ATL-COM-SOFT-2007-002,
CERN, 2007, URL: https://cds.cern.ch/record/1020106.

[131] ATLAS Collaboration, *Performance of primary vertex reconstruction in proton-proton collisions at $\sqrt{s}$ =7 TeV in the ATLAS experiment*,
tech. rep. ATLAS-CONF-2010-069, CERN, 2010,
URL: https://cds.cern.ch/record/1281344.

[132] G. Aad et al.,
Electron reconstruction and identification efficiency measurements with the ATLAS detector using the 2011 LHC proton-proton collision data,
Eur. Phys. J. **C74**.7 (2014) 2941, arXiv: 1404.2240 [hep-ex].

[133] ATLAS Collaboration, *Electron efficiency measurements with the ATLAS detector using the 2012 LHC proton-proton collision data*,
tech. rep. ATLAS-CONF-2014-032, CERN, 2014,
URL: https://cds.cern.ch/record/1706245.

[134] W Lampl et al.,
Calorimeter Clustering Algorithms: Description and Performance,
tech. rep. ATL-LARG-PUB-2008-002. ATL-COM-LARG-2008-003,
CERN, 2008, URL: https://cds.cern.ch/record/1099735.

[135] M. Levchenko, *Photons in ATLAS from Run1 to Run2*,
tech. rep. ATL-PHYS-PROC-2015-166, CERN, 2015,
URL: https://cds.cern.ch/record/2110695.

[136] ATLAS Collaboration, *Improved electron reconstruction in ATLAS using the Gaussian Sum Filter-based model for bremsstrahlung*,
tech. rep. ATLAS-CONF-2012-047, CERN, 2012,
URL: https://cds.cern.ch/record/1449796.

[137] G. Aad et al., *Measurement of isolated-photon pair production in pp collisions at $\sqrt{s} = 7$ TeV with the ATLAS detector*, JHEP **01** (2013) 086,
arXiv: 1211.1913 [hep-ex].

[138] G. Aad et al., *Measurement of the inclusive isolated prompt photon cross section in pp collisions at $\sqrt{s} = 7$ TeV with the ATLAS detector*,
Phys. Rev. **D83** (2011) 052005, arXiv: 1012.4389 [hep-ex].

[139] M. Cacciari, G. P. Salam and G. Soyez, *The Catchment Area of Jets*,
JHEP **04** (2008) 005, arXiv: 0802.1188 [hep-ph].

[140] M. Cacciari, G. P. Salam and S. Sapeta,
On the characterisation of the underlying event, JHEP **04** (2010) 065,
arXiv: 0912.4926 [hep-ph].

[141] G. Aad et al., *Electron performance measurements with the ATLAS detector using the 2010 LHC proton-proton collision data*,
Eur. Phys. J. **C72** (2012) 1909, arXiv: 1110.3174 [hep-ex].

[142] ATLAS Collaboration, *Muon Reconstruction Performance*,
tech. rep. ATLAS-CONF-2010-064, CERN, 2010,
URL: http://cds.cern.ch/record/1281339.

[143] ATLAS Collaboration,
Measurement of the muon reconstruction performance of the ATLAS detector using 2011 and 2012 LHC proton–proton collision data,
Eur. Phys. J. C **74** (2014) 3130, arXiv: 1407.3935 [hep-ex].

[144] S. Hassani et al., *A muon identification and combined reconstruction procedure for the ATLAS detector at the LHC using the (MUONBOY, STACO, MuTag) reconstruction packages*, Nuclear Instruments and Methods in Physics Research Section A: Accelerators, Spectrometers, Detectors and Associated Equipment **572**.1 (2007) 77 , Frontier Detectors for Frontier PhysicsProceedings of the 10th Pisa Meeting on Advanced Detectors,
ISSN: 0168-9002, URL: http://www.sciencedirect.com/science/article/pii/S0168900206019863.

[145] T Lagouri et al., *A Muon Identification and Combined Reconstruction Procedure for the ATLAS Detector at the LHC at CERN*
(2003), revised version number 1 submitted on 2003-10-30 18:34:15,
URL: https://cds.cern.ch/record/681410.

[146] 2016, URL:
https://twiki.cern.ch/twiki/bin/viewauth/Atlas/MuonSelectionTool.

[147] ATLAS Collaboration,
Muon reconstruction performance in early $\sqrt{s}$=13 TeV data,
tech. rep. ATL-PHYS-PUB-2015-037, CERN, 2015,
URL: https://cds.cern.ch/record/2047831.

[148] G. Aad et al., *Jet energy measurement with the ATLAS detector in proton-proton collisions at $\sqrt{s} = 7$ TeV*,
The European Physical Journal C **73**.3 (2013) 1, ISSN: 1434-6052,
URL: http://dx.doi.org/10.1140/epjc/s10052-013-2304-2.

[149] M. Cacciari, G. P. Salam and G. Soyez, *The anti-k_t jet clustering algorithm*,
JHEP **04** (2008) 063, arXiv: 0802.1189 [hep-ph].

[150] ATLAS Collaboration, *Pile-up corrections for jets from proton-proton collisions at $\sqrt{s} = 7$ TeV in ATLAS in 2011*, tech. rep. ATLAS-CONF-2012-064, CERN, 2012, URL: https://cds.cern.ch/record/1459529.

[151] ATLAS Collaboration, *Pile-up subtraction and suppression for jets in ATLAS*, tech. rep. ATLAS-CONF-2013-083, CERN, 2013, URL: https://cds.cern.ch/record/1570994.

[152] 2014, URL: https://twiki.cern.ch/twiki/bin/viewauth/AtlasProtected/HowToCleanJets2011.

[153] ATLAS Collaboration, *Reconstruction of collinear final-state-radiation photons in Z decays to muons in $\sqrt{s} = 7$ TeV proton-proton collisions.*, tech. rep. ATLAS-CONF-2012-143, CERN, 2012, URL: http://cds.cern.ch/record/1491697.

[154] ATLAS Collaboration, *Measurements of the properties of the Higgs-like boson in the four lepton decay channel with the ATLAS detector using 25 fb-1 of proton-proton collision data*, tech. rep. ATLAS-CONF-2013-013, CERN, 2013, URL: http://cds.cern.ch/record/1523699.

[155] G. Aad et al., *Measurements of Higgs boson production and couplings in the four-lepton channel in pp collisions at center-of-mass energies of 7 and 8 TeV with the ATLAS detector*, Phys. Rev. **D91**.1 (2015) 012006, arXiv: 1408.5191 [hep-ex].

[156] M. Vesterinen and T. R. Wyatt, *A Novel Technique for Studying the Z Boson Transverse Momentum Distribution at Hadron Colliders*, Nucl. Instrum. Meth. **A602** (2009) 432, arXiv: 0807.4956 [hep-ex].

[157] 2014, URL: https://twiki.cern.ch/twiki/bin/viewauth/AtlasProtected/PhotonIdentificationEfficiency.

[158] J.-B. Blanchard, J.-B. de Vivie and P Mastrandrea, *In situ scales and smearings from Z and J/Ψ events*, tech. rep. ATL-COM-PHYS-2013-1653, CERN, 2013, URL: https://cds.cern.ch/record/1637533.

[159] 2016, URL: https://twiki.cern.ch/twiki/bin/viewauth/AtlasProtected/EfficiencyMeasurements.

[160] 2014, URL: https://twiki.cern.ch/twiki/bin/viewauth/AtlasProtected/MCPAnalysisGuidelinesData2012.

[161] A. L. Read, *Presentation of search results: The CL(s) technique*, J. Phys. **G28** (2002) 2693.

[162] G. Cowan et al., *Asymptotic formulae for likelihood-based tests of new physics*, Eur. Phys. J. **C 71** (2011) 1554, arXiv: 1007.1727 [physics.data-an].

[163] A. Hoecker et al., *TMVA: Toolkit for Multivariate Data Analysis*, PoS **ACAT** (2007) 040, arXiv: physics/0703039.

[164] ATLAS Collaboration, *Search for scalar diphoton resonances with the ATLAS detector at* $\sqrt{s} = 13$ *TeV*, tech. rep. ATL-COM-PHYS-2015-1437, CERN, 2015, URL: https://cds.cern.ch/record/2109707.

[165] Y.-J. Zhang, B.-B. Zhou and J.-J. Sun, *The Fourth Generation Quark and the 750 GeV Diphoton Excess* (2016), arXiv: 1602.05539 [hep-ph].

[166] D0 Collaboration, V. M. Abazov et al, *Search for a scalar or vector particle decaying into* $Z\gamma$ *in* $p\bar{p}$ *collisions at* $\sqrt{s}$*=1.96 TeV*, Phys. Lett. **B671** (2009) 349, arXiv: 0806.0611 [hep-ex].

[167] ATLAS Collaboration, *Measurements of* $W\gamma$ *and* $Z\gamma$ *production in pp collisions at* $\sqrt{s} = 7$ *TeV with the ATLAS detector at the LHC*, Phys. Rev. **D87**.11 (2013) 112003, [Erratum: Phys. Rev.D91,no.11,119901(2015)], arXiv: 1302.1283 [hep-ex].

[168] CMS Collaboration, *Search for scalar resonances in the 200-500 GeV mass range decaying into a Z and a photon in pp collisions at* $\sqrt{s} = 8$ *TeV*, CMS-PAS-HIG-14-031 (2015), URL: https://cds.cern.ch/record/1997885.

[169] G. Aad et al., *Search for new phenomena in photon + jet events collected in proton–proton collisions at with the ATLAS detector*, Physics Letters B **728** (2014) 562 , ISSN: 0370-2693, URL: http://www.sciencedirect.com/science/article/pii/S0370269313010046.

[170] ATLAS Collaboration, *The simulation principle and performance of the ATLAS fast calorimeter simulation FastCaloSim*, ATL-PHYS-PUB-2010-013 (2010), URL: https://cds.cern.ch/record/1300517.

[171] 2015, URL: https://twiki.cern.ch/twiki/bin/viewauth/AtlasProtected/EGammaCalibrationRun2.

[172] ATLAS Collaboration, *The ElectronPhotonFourMomentumCorrection tool* (2015), URL: https://twiki.cern.ch/twiki/bin/view/AtlasProtected/ElectronPhotonFourMomentumCorrection.

[173] ATLAS Collaboration, *The MCP Moriond 2016 Recommendation* (2016), URL: https://twiki.cern.ch/twiki/bin/view/AtlasProtected/MCPAnalysisGuidelinesMC15.

[174] V. Khachatryan et al., *Search for high-mass* $Z\gamma$ *resonances in* $e^+e^-\gamma$ *and* $\mu^+\mu^-\gamma$ *final states in proton-proton collisions at* $\sqrt{s}$*=8 and 13 TeV* (2016), arXiv: 1610.02960 [hep-ex].